Thermal Evaporation for Perovskite Films and Photovoltaic Devices

Yan, J.

DOI
10.4233/uuid:fdc60afc-2e6e-43f2-a44e-793f5a1f2795

Publication date
2025

Document Version
Final published version

Citation (APA)
Yan, J. (2025). *Thermal Evaporation for Perovskite Films and Photovoltaic Devices*. [Dissertation (TU Delft), Delft University of Technology]. https://doi.org/10.4233/uuid:fdc60afc-2e6e-43f2-a44e-793f5a1f2795

Thermal Evaporation for Perovskite Films and Photovoltaic Devices

Jin YAN

闫锦

Thermal Evaporation for Perovskite Films and Photovoltaic Devices

Dissertation

ter verkrijging van de graad van doctor
aan de Technische Universiteit Delft,
op gezag van de Rector Magnificus Prof.dr.ir. T.H.J.J. van der Hagen,
voorzitter van het College voor Promoties,
in het openbaar te verdedigen op 6 maart 2025.

door

Jin YAN

Dit proefschrift is goedgekeurd door de promotoren.

Samenstelling promotiecommissie bestaat uit:

Rector Magnificus	voorzitter
Prof.dr.ir. O. Isabella	Technische Universiteit Delft, promotor
Dr. T. J. Savenije	Technische Universiteit Delft, promotor
Dr. L. Mazzarella	Technische Universiteit Delft, co-promotor

Onafhankelijke leden:

Keywords: perovskite solar cells, thermal evaporation, sequential deposition, orientation growth

Printed by: XX

ISBN: 000-00-0000-000-0

An electronic version of this dissertation is available at
`http://repository.tudelft.nl/`.

Contents

Summary

For centuries, society has relied on fossil fuels for development, leading to the problem of global warming and significant environmental changes. To address these environmental issues, cleaner and more cost-effective energy productions are required. Solar energy, harnessed through well-developed photovoltaic (PV) technology, offers a promising solution. In the PV research field, perovskite (PVK)-based devices offer a feasible processing and have exhibited a fast increase in efficiency. Despite advancements in both the efficiency and stability of perovskite solar cells, there still is a long way to go towards industrialization due to the formation of pinholes during large area film deposition, non-uniformity, and poor reproducibility. Thermal evaporation technology has shown potential for the commercialization of perovskite solar cells, owing to its compatibility with large areas and textured substrates. In this thesis, we focused on the sequential thermal evaporation of perovskite. Through this approach, post-annealing and precursor mixing processes were investigated. Additionally, crystal orientation was tuned by applying different intermediate annealing temperatures. The optimized process was then applied to upscale both absorber films and cells from 0.09 cm^2 to 1 cm^2.

An introduction is provided in Chapter 1, briefly discussing PV technology, the properties of perovskite materials, thermally deposited perovskite films, and corresponding devices.

Chapter 2 summarizes recent progress in large-area perovskite solar cells from three main perspectives: material properties, fabrication technologies, and industrialization challenges. Moreover, this chapter evaluates the latest advances in large-area perovskite/silicon monolithic tandem devices, focusing on aspects such as efficiency, stability and optical design.

In Chapter 3, we propose an approach involving a single-cycle deposition (SCD) of three thick layers of precursors to obtain high-quality $Cs_{0.15}FA_{0.85}PbI_{2.85}Br_{0.15}$ films. After annealing, the optimized PVK film exhibits properties comparable to those deposited by multi-cycle deposition in terms of crystal structure, in-depth uniformity, and opto-electrical properties for 100-nm and 250-nm thick PVK films. The 250-nm thick SCD PVK film demonstrates a half-intensity lifetime of approximately 650 ns with a carrier mobility close to 10 $cm^2V^{-1}s^{-1}$. We also studied the precursor reaction during post-deposition annealing, as well as the crystal structure and opto-electrical properties as a function of different annealing times using Incidence X-Ray Diffraction and Time-Resolved Photoluminescence. Our findings reveal that the structural and optical properties of these SCD PVKs are asynchronous with electrical properties during annealing, and this phenomenon is strongly influenced by film thickness due to precursor mixing and reacting. Additionally, $FAPbI_3$ was introduced to elucidate the role of CsBr in precursor mixing during annealing. The presence of CsBr facilitates fast precursor reaction and PVK conversion.

In Chapter 4, we manipulated the crystal orientation of 450 nm-thick

$Cs_{0.15}FA_{0.85}PbI_{2.85}Br_{0.15}$ films, which were deposited with two cycles of sequential thermal evaporation of the individual precursors. By applying different intermediate annealing temperatures between the cycles, we achieved tunable crystal orientation from a mixed (110)/(100) orientation to a complete (100) orientation. We link these differences in crystal growth to the degree of conversion of the precursors in the first layer. Our findings suggest that the level of conversion plays a critical role in directing the orientation of the entire layer, due to the template guided crystal growth of PVKs. Regarding the relationship between crystal orientation and opto-electronic properties, we found that bulk properties such as charge carrier mobility, lifetime, and trap densities are minimally affected. On the contrary, the (100) oriented layer exhibited lower trap densities at the film surface compared to the mixed (110)/(100) sample. In addition, Kelvin Probe Force Microscopy (KPFM) measurements revealed that the (100) oriented layer had a more homogeneous local contact potential difference distribution than the mixed orientation sample. These observations suggest that well oriented crystal growth may enhance charge extraction at the device level.

In Chapter 5, based on multi-cycle sequential thermal evaporation, we systematically investigated the effects of annealing temperature on PVK properties in terms of morphology, opto-electronic, and device performance. The grain size increases to almost 1 μm with carrier mobility exceeding 50 cm^2/Vs when the annealing temperature is enhanced to 170 °C. With the optimized annealing temperature, little $PbCl_2$ is introduced in the multi-cycle sequential deposition to improve the absorber crystallinity, as evidenced by the XRD and PL. The resulting PSCs yield a PCE of 18.5% with a cell area of 0.09 cm^2. With the same deposition parameters, the cell area is scaled up to 0.36 cm^2, and 1 cm^2, achieving the champion PCEs of 17.3% and 11%, respectively. Notably, there is almost no drop in open circuit voltage drop as the cell area increases.

In conclusion, this thesis mainly focuses on the preparation of perovskite films and solar cells via sequential thermal evaporation. Chapter 2 provides a literature review summarizing recent progress in large-area perovskite solar cells, scalable top cells for tandem devices, and industrialization challenges. Chapter 3 demonstrates comparable crystal structural and opto-electrical properties of single-cycle deposited perovskite to those deposited via multi-cycle deposition. Chapter 4 explores the manipulation of crystal orientation in $Cs_{0.15}FA_{0.85}PbI_{2.85}Br_{0.15}$ films, demonstrating template-guided crystal growth through thermal evaporation. Besides, this chapter also highlights that well oriented crystal growth can enhance charge extraction at the device level. In Chapter 5, sequentially thermally deposited perovskites exhibit high cell efficiency and demonstrates non-drop in open circuit voltage as the cell area increases. The large-area perovskite films exhibit good uniformity with less than 10% thickness variation, highlighting the potential application of this technology for the future commercialization of PSCs.

Samenvatting

Translated by Jasmine Apawti

Eeuwenlang heeft de samenleving vertrouwd op fossiele brandstoffen voor ontwikkeling, wat heeft geleid tot de opwarming van de aarde en aanzienlijke milieuveranderingen. Om deze milieuproblemen aan te pakken, zijn schonere en kosteneffectievere energieproductiemethoden vereist. Zonne-energie, benut door goed ontwikkelde fotovoltaïsche (PV) technologie, biedt een veelbelovende oplossing. In het PV-onderzoeksveld bieden perovskiet-gebaseerde apparaten een haalbare verwerking en vertonen zij een snelle toename in efficiëntie. Ondanks de vooruitgang in zowel de efficiëntie als de stabiliteit van perovskiet zonnecellen, is er nog een lange weg te gaan richting industrialisatie vanwege de vorming van pinholes tijdens de depositie van grote filmoppervlakken, niet-uniformiteit en problemen met slechte reproduceerbaarheid. Thermische evaporatietechnologie heeft potentie getoond voor de commercialisering van perovskiet zonnecellen, dankzij de compatibiliteit met grote oppervlakken en getextureerde substraten. In dit proefschrift richten we ons op de sequentiële thermische evaporatie van perovskiet. Via deze benadering werden nabehandelings- en precursor-mengprocessen onderzocht. Bovendien werd de kristaloriëntatie afgestemd door het toepassen van verschillende tussentijdse annealing-temperaturen. Het geoptimaliseerde proces werd vervolgens toegepast om zowel absorberende films als cellen op te schalen van 0.09 cm^2 tot 1 cm^2. In hoofdstuk 1 wordt een inleiding gegeven waarin kort fotovoltaïsche (PV) technologie, de eigenschappen van perovskiet materialen, thermisch gedeponeerde perovskiet lagen, en bijbehorende apparaten worden besproken. Hoofdstuk 2 vat recente vooruitgang samen in grootschalige perovskiet zonnecellen (PSCs) vanuit drie hoofdperspectieven: materiaaleigenschappen, fabricagetechnologieën, en uitdagingen bij de industrialisatie. Bovendien evalueert dit hoofdstuk de laatste ontwikkelingen in grootschalige perovskiet/silicium monolithische tandemapparaten, met een focus op aspecten zoals efficiëntie, stabiliteit, en optisch ontwerp. In hoofdstuk 3 stellen we een aanpak voor waarbij gebruik wordt gemaakt van een enkelvoudige cyclus depositie (SCD) van drie dikke precursorlagen om hoogwaardige $Cs_{0.15}FA_{0.85}PbI_{2.85}Br_{0.15}$ films te verkrijgen. Na annealing vertoont de geoptimaliseerde PVK laageigenschappen die vergelijkbaar zijn met die van lagen gedeponeerd via multicycle depositie, wat betreft kristalstructuur, dieptegelijkmatigheid en opto-elektrische eigenschappen voor PVK films van 100 nm en 250 nm dikte. De 250 nm dikke SCD PVK lagen vertoont een half-intensiteit levensduur van ongeveer 650 ns met een ladingsmobiliteit van buna 10 $cm^2V^{-1}s^{-1}$. We hebben ook de reactie van de precursor bestudeerd tijdens post-depositie annealing, evenals de kristalstructuur en opto-elektrische eigenschappen als functie van verschillende annealing tijden met behulp van Röntgen diffractie onder invallende straling (Incidence X-Ray Diffraction) en tijd-afhankelijh fotoluminescentie (Time-Resolved Photoluminescence). Onze bevindingen tonen aan dat de

structurele en optische eigenschappen van deze SCD PVK's asynchroon zijn met elektrische eigenschappen tijdens het annealingproces, en dat dit fenomeen sterk wordt beïnvloed door de filmdikte als gevolg van precursor menging en reactie. Bovendien werd $FAPbI_3$ geïntroduceerd om de rol van CsBr in precursor menging tijdens het annealing proces te verduidelijken. De aanwezigheid van CsBr vergemakkelijkt een snelle precursorreactie en PVK omzetting. In hoofdstuk 4 hebben we de kristaloriëntatie van 450 nm dikte $Cs_{0.15}FA_{0.85}PbI_{2.85}Br_{0.15}$ gemanipuleerd. Deze lagen zijn gedeponeerd met twee cycli van sequentiële thermische verdamping van de individuele precursors. Door verschillende tussentijdse annealing temperaturen toe te passen tussen de cycli, hebben we een verstelbare kristaloriëntatie bereikt van een gemengde (110)/(100) oriëntatie naar een volledige (100) oriëntatie. We brengen deze verschillen in kristalgroei in verband met de mate van omzetting van de precursors in de eerste laag. Onze bevindingen suggereren dat de mate van omzetting een cruciale rol speelt bij het sturen van de oriëntatie van de gehele laag, vanwege de sjabloon-geleide kristalgroei van PVKs. Wat betreft de relatie tussen kristaloriëntatie en opto-elektronische eigenschappen, hebben we gevonden dat bulk eigenschappen zoals ladingsdrager mobiliteit, levensduur en vangst dichtheden minimaal worden beïnvloed. Daarentegen vertoonde de (100) georiënteerde laag lagere vangst dichtheden aan het oppervlak van de laag in vergelijking met het gemengde (110)/(100) monster. Bovendien onthulden metingen met Kelvin Probe Force Microscopy (KPFM) dat de (100) georiënteerde laag een meer homogene verdeling van het lokale contact potentiaalverschil had dan het monster met gemengde oriëntatie. Deze waarnemingen suggereren dat sterk georiënteerde kristalgroei de ladingsextractie op apparaar niveau kan verbeteren. In hoofdstuk 5 hebben we op basis van multi-cycle sequentiële thermische verdamping systematisch de effecten van annealingstemperatuur onderzocht op de eigenschappen van perovskiet in termen van morfologie, opto-elektronische kenmerken en apparaatprestaties. De korrelgrootte neemt toe tot bijna 1 µm, met een ladingsmobiliteit van meer dan 50 cm^2/Vs wanneer de annealingstemperatuur wordt verhoogd tot 170 °C. Met de geoptimaliseerde annealingstemperatuur wordt een kleine hoeveelheid $PbCl_2$ geïntroduceerd tijdens de multi-cycle sequentiële depositie om de kristalliniteit van de absorber te verbeteren, zoals aangetoond door XRD en PL metingen. De resulterende perovskiete zonnecellen behalen een efficientie van 18.5% met een celoppervlakte van 0.09 cm^2. Met dezelfde depositieparameters wordt het celoppervlak vergroot tot 0.36 cm^2 en 1 cm^2, waarbij respectievelijk topprestaties van 17.3% en 15% efficientie worden bereikt. Opmerkelijk is dat er bijna geen daling van de open-klemspanning optreedt naarmate het celoppervlak toeneemt. In conclusie richt dit proefschrift zich voornamelijk op de voorbereiding van perovskiet lagen en zonnecellen via sequentiële thermische verdamping. Hoofdstuk 2 biedt een literatuuroverzicht dat recente vooruitgang samenvat in grootschalige perovskiet zonnecellen, schaalbare topcellen voor tandemapparaten, en uitdagingen bij de industrialisatie. Hoofdstuk 3 toont vergelijkbare kristalstructuur en opto-elektrische eigenschappen van perovskiet gedeponeerd in één cyclus ten opzichte van die gedeponeerd via meercyclische depositie. Hoofdstuk 4 onderzoekt de manipulatie van de kristaloriëntatie in $Cs_{0.15}FA_{0.85}PbI_{2.85}Br_{0.15}$ lagen, waarbij sjabloon-geleide kristalgroei door thermische verdamping wordt gedemonstreerd. Bovendien benadrukt dit hoofdstuk dat sterk georiënteerde kristalgroei de ladingsextractie op het apparaatniveau kan

verbeteren. In Hoofdstuk 5 vertonen sequentieel thermisch gedeponeerde perovskieten hoge cel efficiëntie en vertonen geen daling in open-klemspanning bij toenemend celoppervlak. De grootschalige perovskiet lagen vertonen goede uniformiteit met minder dan 10% variatie in dikte, wat de potentie van deze technologie onderstreept voor toekomstige commercialisatie van perovskiete zonnecellen.

Nomenclature

Abbreviations

Ag	Silver
BCP	Bathocuproine
c-Si	Crystal silicon
C60	Fullerene
CPD	Contact potential difference
CsBr	Caesium bromide
CTL	Charge transporting layer
CVD	Chemical vapour deposition
ETL	Electron transporting layer
FAI	Formamidinium iodide
FWHM	Full width at half maximum
GI-XRD	Grazing incidence XRD
HCVD	Hybride chemical vapour deposition
HTL	Hole transporting layer
ITO	Indium doped tin oxide
IV	Current voltage
KPFM	Kelvin probe force microscopy
MCD	Multicycle deposition
$PbCl_2$	Lead chloride
PbI_2	Lead iodide
PCE	Power conversion efficiency
PL	Photoluminescence
PLD	Pulsed laser deposition

PSC	Perovskite solar cell
PTAA	Poly(triaryl amine)
PV	Photovoltaic
PVK	Perovskite
SCD	Single-cycle deposition
SEM	Scanning electron microscope
TRMC	Time-resolved mirowave conductivity
TRPL	Time-resolved photoluminescence
UV-vis	Ultraviolet-visible spectrosco
XPS	X-ray photoelectron spectroscopy
XRD	X-ray diffraction

Symbols

η	Efficiency
μ	Mobility
τ	Lifetime
FF	Fill factor
J_{sc}	Short-circuit current density
V_{oc}	Open-circuit voltage

1

Introduction

1.1. Climate change and renewable energy

Fossil fuels - including coal, oil, and natural gas - have served as the predominant catalysts of contemporary global climate change, contributing to over 75% of global greenhouse gas emissions and accounting for nearly 90% of all carbon dioxide emissions [1, 2]. These emissions form a layer of so-called greenhouse gases in the Earth's atmosphere, which act as a thermal blanket, trapping solar radiation and resulting in the phenomenon of global warming and subsequent climate alterations. The current pace of global warming surpasses any historical precedent. In October 2018, the Intergovernmental Panel on Climate Change (IPCC) published its Special Report on Global Warming, as shown in Figure 1.1 [3]. Over time, this increase of temperature contributes to climate change altering weather patterns and disrupting the Earth's natural equilibrium. This effect poses numerous risks to both humanity and all other forms of life on Earth. Therefore, the development of a clean and sustainable energy system is the greatest challenges humanity faces today.

To tackle climate change, various renewable energy technologies are currently under development, among them the top three are: wind, hydro and solar energy. Solar energy is particularly interesting due to its inexhaustible and ubiquitous nature. Solar energy is available virtually everywhere on Earth, typically offering around 1000 W/m^2 on the Earth's surface and 1367 W/m^2 in space for satellite applications [4, 5]. Solar energy has therefore an enormous potential and will largely contribute to our electrified and sustainable future society.

1.2. Photovoltaic technology

Photovoltaic (PV) devices convert solar irradation into electrical power. This process is achieved in two steps: 1) The radiation from the sun is absorbed in the so-called absorber material, populations of electrons and holes; 2) These photo-generated electrons and holes are separated and selectively transported to their respective electrodes.

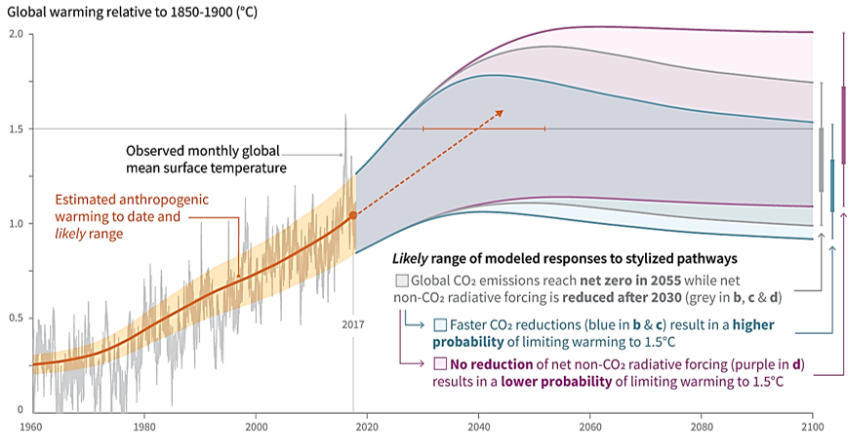

Figure 1.1: Aiming to limit temperature increase to 1.5 °C [3]

1.2.1. Evolution of solar cells

As the first-generation PV technology, the wafer-based crystalline silicon (c-Si) solar cells have been dominating the PV industry with more than 90% of the market share [6]. c-Si solar cell exhibits high stability and long-term reliability in commercial applications. With continuous improvement in silicon PV technology, a remarkable reduction in manufacturing cost has been realized, making c-Si solar cells increasingly favorable for large-scale utilization. However, c-Si solar cells are currently reaching their fundamental efficiency limit and are experiencing a relatively slow efficiency increment [7]. According to the Shockley-Queisser (SQ) detailed-balanced model, a maximum achievable efficiency limit of 29.4% can be extracted from a single-junction c-Si solar cell [8]. Currently, the record laboratory-scale efficiency for a c-Si solar cell is 26.7% [9], as shown in Figure 1.2. The second generation of solar cells is based on thin-film technology. Similar to the first generation of PV technologies, thin-film solar cells are also based on a single junction and therefore they obey the SQ limit. Aiming at lower manufacturing costs and simpler production processes [10], the second-generation technologies are developed, including amorphous-Si (a-Si), CuIn(Ga)Se_2 (CIGS), Cadmium Telluride (CdTe) or polycrystalline-Si (poly-Si) [11–13]. However, compared to c-Si solar cells, these cells have relatively lower power conversion efficiency (PCE). The emerging PV is referring to PV technologies that are at the precommercial stage and are aiming to overcome the SQ limit [14]. The emerging PV technology is covering a range from technologies under demonstration, such as multi-junction PV, to novel PV technologies that still require basic research and development investigations. The novel technologies provide innovative techniques and materials to achieve absorber materials with tunable bandgap and other opto-electronic properties. Some of the emerging technologies are dye-sensitized cells, quantum dot cells, organic cells and organic-inorganic hybrid perovskite cells [15–19].

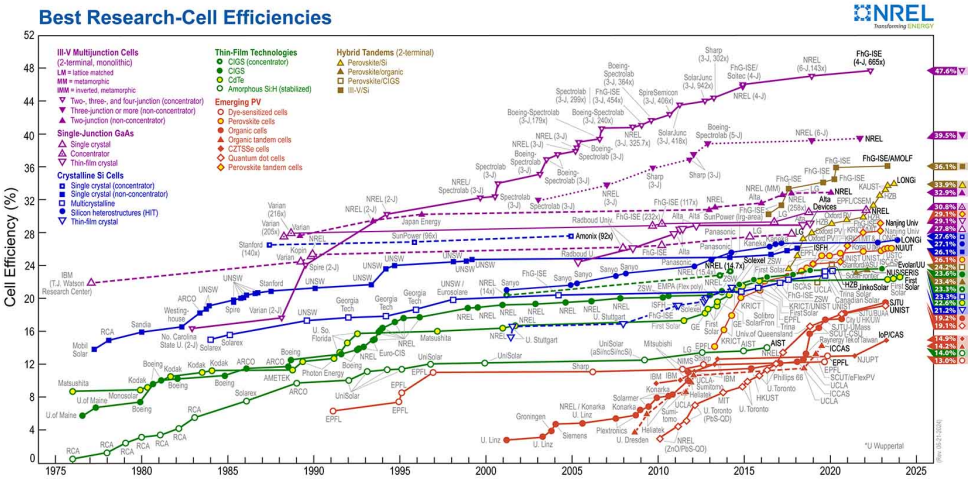

Figure 1.2: Best solar solar cells conversion efficiency evolution chart from NREL by 08/2024 [20].

1.2.2. Perovskite materials and solar cells

Perovskite (PVK) has ABX_3 structure, A is a monovalent cation, B is a bivalent cation, and X is an anion. The commonly used A-site cations are methylammonium, formamidium, or caesium; lead and tin are generally in the B-site; while the X-site is mostly occupied by halides, as shown in Figure 1.3. Methylammonium lead iodide ($MAPbI_3$) was the first reported metal halide PVK to be successfully used as the absorber in a photovoltaic device. Perovskites' bandgap can be manipulated from 1.4 eV to 2.3 eV by changing the halide or the monovalent cation [21, 22]. Because of the tunable bandgap of the perovskite, it enables the relatively straightforward tandem solar cells, such as PVK/c-Si tandem solar cells or all-PVK tandem solar cells. In addition to the tunable bandgap, PVK material exhibits many other favorable properties for applications in opto-electronics, for example, high optical absorption coefficient at UV-vis wavelength range ($\approx 10^5$ cm^{-1}) [23], balanced electron/hole mobility and long diffusion length (above 1 µm) [24]. These properties allow efficient harvest of the incident light and charge transport with limited recombination. In a working PVK solar cell (PSC), the photo-generated carriers are extracted from the absorber to transporting layers and then collected by the electrodes, as illustrated in Figure 1.3. Therefore, to minimize the energy loss during charge transfer, less traps and band energy alignment are very important. However, as in many types of solar cells, the loss of photo-generated charges due to non-radiative recombination prevents PSCs from approaching their theoretical limits [25, 26]. The very first report of PSCs was demonstrated by Kojima and co-workers in 2009 [27]. They introduced $MAPbI_3$ as sensitizers in liquid-electrolyte-based dye-sensitized solar cells and achieved a PCE of 3.8 % [27]. However, they reported rapid performance degradation hydrolysis of $MAPbI_3$. That extreme instability problem was not improved until 2012, when the first solid-state PSCs appeared [28]. By replacing the liquid electrolyte by the solid state, p-type hole conductor spiro-MeOTAD, previously used in solid-state dye sensitized solar cells [29], a PCE of 10.9% was achieved. At the time, mesoporous TiO_2 was used as a n-type layer,

1

spiro-MeOTAD as a p-type layer, and $MAPbI_3$ as the absorber. Since then, a great number of researchers started working in this field and various developments were demonstrated [30–36]. Different PVK materials and device structures are introduced to further improve the device performance *via* composition engineering [37–39], interfacial engineering [40, 41], solvent engineering [42–44]. To date, the common device structures are either conventional (n-i-p) including both mesoporous and planar architectures or inverted (p-i-n) planar configurations. From material perspective, bandgap energies for different transporting layers are studied [19, 45–48]. To date, the highest recorded PCEs for single junction PSCs have achieved 26.1% [49] in conventional n-i-p structures and 24.6% [50] with an inverted p-i-n configuration. Although PSCs with p-i-n structures currently demonstrate lower performance compared to regular n-i-p structures, they exhibit enhanced stability which is related to the undoped hole transport layers [51]. In only two decades, the PCE demonstrated a rapid increase from 3.8% to above 26%, motivating the industrialization of PSCs. Therefore, the research direction of the PSCs community is now mainly focused on 1) Up-scaling, 2) Improving of PCE in both single-junction and multi-junction devices, and 3) Stability [51]. The recent development and challenges of PSCs are discussed in detail in Chapter 2.

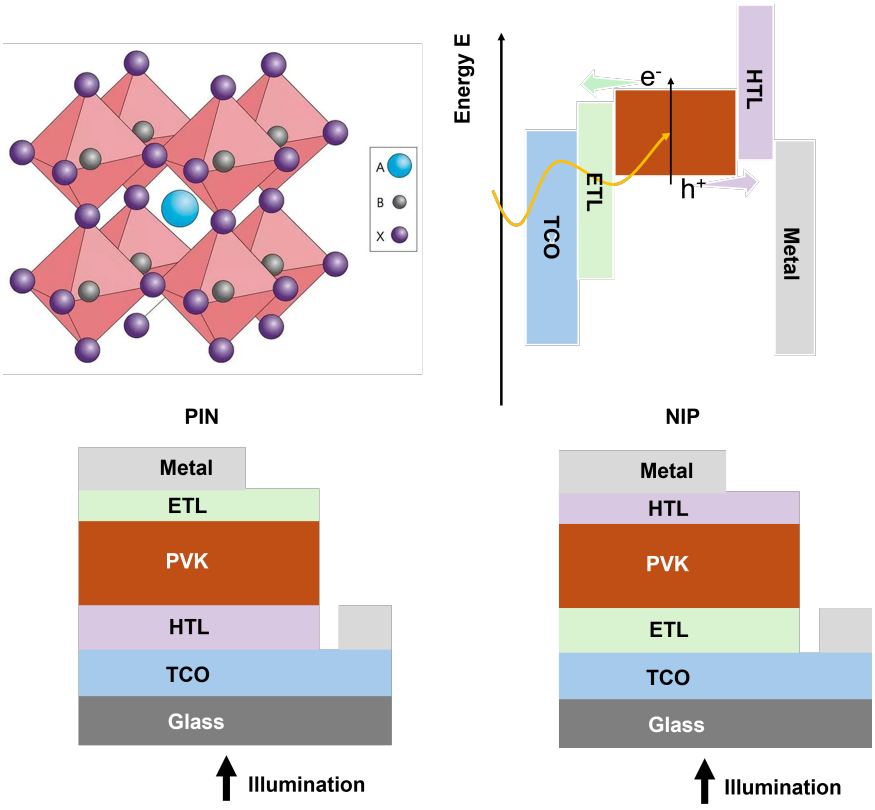

Figure 1.3: Crystal structure of PVK [52] and the energy band diagram of a typical PSC.

1.2.3. Thermally evaporated perovskite for device preparation

The deposition of PVK can be performed using several methods such as solution, vacuum, or hybrid, as described in Chapter 2. As one of the vacuum-based deposition, thermal evaporation of PVK shows potential application for scaling up and compatibility with textured substrate, such as textured c-Si solar cells for tandem applications. Since 2013, Liu firstly applied thermal evaporation of PVK absorber to realize 16% of PCE [53], the thermal deposition approach attracts much attention. Vacuum deposition techniques are classified into co-evaporation and sequential evaporation depending on different deposition process, as shown in Figure 1.4.

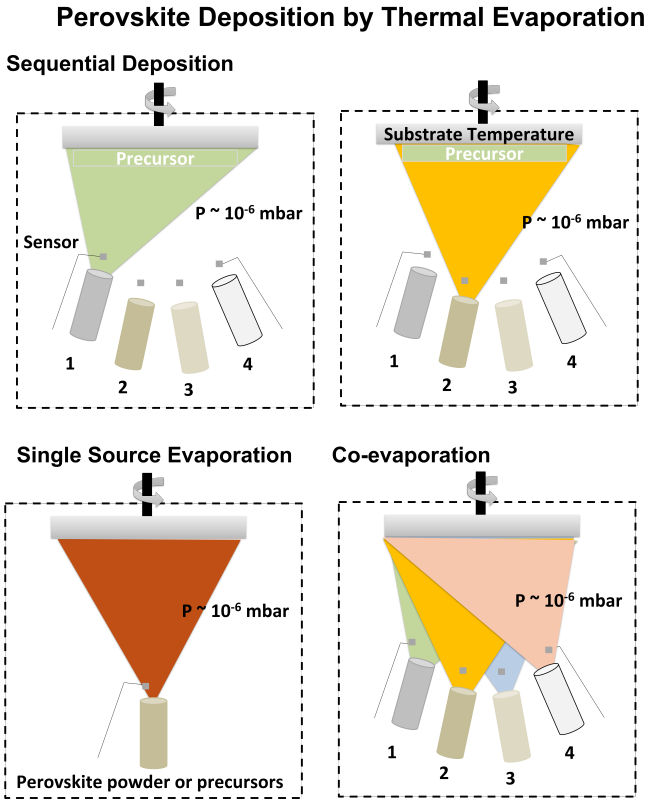

Figure 1.4: Schematic of PVK deposition methods based on thermal evaporation.

In co-evaporation, the organic and inorganic halides are simultaneously thermally sublimed under high vacuum. To obtain multi-cation and/or multi-halide perovskite films, multiple sources are introduced during deposition, making the process more complicated. Bolink's group at University of Valencia firstly reported the multiple thermal evaporation using 3 and 4 sources to form wide-bandgap PVK films and yielding stable and high PCE devices [54–58]. While in the sequential deposition, the precursors are deposited one after the other. By controlling the thickness of each precursor, PVK films

with target composition and thickness are obtained. Differently from co-evaporation, in sequential deposition most of the PVK is converted during a post-annealing treatment. In this thesis, sequential vacuum deposition will be employed in all experiments, and the details of each process will be discussed in the corresponding chapters.

1.3. Aim and outline of this thesis

This thesis aims at understanding and developing vacuum deposited PVK films and corresponding PSCs preparation. Firstly, the development of PVK films *via* thermal evaporation following the sequential layer approach is explored. Then, optimized PVK films are tested in HTL/PVK/ETL-based PSCs because of further tandem application in the future. Develop PVK films with thermal deposition approach, apply the film for PSCs preparation, and scale up to 1 cm^2 of cells area. This thesis is outlined in the following way.

Chapter 1. Introduction. This chapter gives a general introduction to the requirement of renewable energy, evolution of PV technologies and PSCs. Besides, the development and challenges of thermally deposited PSCs are introduced.

Chapter 2. Progress and Challenges on Scaling-up of Perovskite Solar Cell Technology. This chapter focuses on reviewing the challenges and progresses related to scaling up of large area PSCs, which includes an overview of the most widely utilized deposition approaches and their comparison. Finally, this chapter addresses the very current topic of developing of PSCs towards their commercialization.

Chapter 3. Crystallization Process for High-Quality $Cs_{0.15}FA_{0.85}PbI_{2.85}Br_{0.15}$ Film Deposited via Simplified Sequential Vacuum Evaporation. This chapter proposes a simplified approach to deposit PVK material consisting of a single-cycle deposition (SCD) of three thick layers of precursors to obtain high-quality $Cs_{0.15}FA_{0.85}PbI_{2.85}Br_{0.15}$ films. The role of post-deposition annealing on the opto-electronic properties of the PVK absorber is investigated and optimized to minimize the number of subsequent cycle to obtain high quality material. Furthermore, we discuss the role of CsBr in the PVK formation during the post-deposition annealing and propose a conversion mechanism to explain our findings. Besides, the formation and evolution of SCD PVK during annealing are investigated.

Chapter 4. Vacuum Deposited Perovskites with a Controllable Crystal Orientation. This chapter uses different intermediate annealing temperatures (T_{inter}) between two sequential evaporation cycles to control the $Cs_{0.15}FA_{0.85}PbI_{2.85}Br_{0.15}$ orientation of the final PVK layer. XRD and 2D-XRD measurements reveal that when using no T_{inter}, primarily the (110) orientation is obtained, while when using T_{inter} = 100 °C a nearly isotropic orientation is found. Most interestingly for T_{inter} > 130 °C, a highly oriented PVK (100) is formed. We found that although bulk electronic properties like photoconductivity are independent from the preferential orientation, surface related properties differ substantially for samples with different crystal orientation.

Chapter 5. Scalable Perovskites for Perovskite Solar Cells *via* Simplified Sequential Vacuum Deposition. This chapter discusses the sequentially deposited PVKs and corresponding device preparation. We systematically investigated the effects of annealing temperature on PVK properties in terms of morphology, opto-electronic, and device performance. The grain size increases to almost 1 µm with carrier mobility more than

50 cm^2/Vs when the annealing temperature is enhanced to 170 °C. With the optimized annealing temperature, a trace of $PbCl_2$ is introduced in the sequential deposition to improve the absorber crystallinity, as evidenced by the XRD and PL. The resulting PSCs yield a PCE of 18.5% with a cell area of 0.09 cm^2. With the same deposition parameters, the cell area is scaled up to 0.36 cm^2, and 1 cm^2, achieving the champion PCEs of 17.3% and 11.6%, respectively.

Chapter 6. Conclusions and outlook. This chapter summarizes the key results of this thesis and gives an outlook about future research on high performance evaporated PVK development, deployment into PSCs, and the potential application in tandem solar cells.

1.4. Main contribution to the field

This work contributes to the advancement of research and development of thermally evaporated PVK materials and the implementation of sequentially deposited PVK in solar cells, aiming at application of thermally evaporated PVK for PSCs preparation and scaling up to 1 cm^2 cell area. Several aspects are addressed below:

1. Review about the progress and challenges on scaling up of evaporated perovskite solar cell technology. This review summarizes most relevant recent progress in large-scale PSCs and focuses on the challenges for commercialization of PSCs. In the review, different scalable deposition methods of every PSCs layers (charge transporting layers, absorbing layer, electrode, and encapsulation) are discussed based on different materials. Besides, the advances of large area PVK/c-Si monolithic tandem devices are systematically reviewed.

2. Simplified sequential vacuum evaporation approach for PVKs. We demonstrated a simple sequential evaporation technique to prepare high-quality PVK films based on multi-source deposition. Besides, we found that the presence of cesium bromide can assist the precursor mixing during annealing of the sequentially deposited film, which is beneficial to the fast precursor reaction and PVK conversion.

3. Manipulation of the orientation growth of thermally deposited PVKs. Manipulating the preferential orientation of the PVK crystal growth in layers prepared by thermal evaporation has hardly been addressed in literature, due to lacking solvent and additives. We propose an intermediate post-annealing approach between two subsequent stacks of the sequential evaporation to manipulate the crystal orientation ranging from primarily (110) to near isotropic to predominantly (100). Besides, our finding suggests that the variation of crystal orientation shows no effects on the bulk opto-electrical properties for the thermally evaporated $Cs_{0.15}FA_{0.85}PbI_{2.85}Br_{0.15}$.

4. Scalable PVKs and PSCs *via* simplified sequential vacuum evaporation. Most of the literature reported thermally deposited PSCs are based on co-evaporation approaches. We applied the simplified sequential vacuum deposition approach mentioned in Chapter 3 and Chapter 4 into device preparation. With optimized post-annealing temperature and the introduction of $PbCl_2$, the solar cell shows a maximum power conversion efficiency of 18.5% with V_{oc} and *FF* equal to 1.01 V and 78.5%, respectively, for device area of 0.09 cm^2. Building on these optimized parameters, we scaled the device size up from 0.09 cm^2 to 0.36 cm^2 and 1 cm^2, showing almost unaffected open circuit voltage of above 1 V despite the increase in cell area. These results show the possibility of this

technology to scale the device area up to 1 cm^2 and further application as the top cell in tandem devices.

2

Progress and challenges on scaling up of perovskite solar cell technology

This chapter was published in Sustainable Energy & Fuels *

Abstract

Since the first application of a metal halide perovskite (PVK) absorber in a solar cell, these materials have drawn a great deal of attention in the photovoltaic (PV) community, showing exceptional rapid progress in power conversion efficiency. The potential advantages of low-cost, high efficiency, easy processability, and wide range of applications make PVK solar cells (PSCs) a desirable candidate for future uptake in the PV market over traditional semiconductors such as silicon. Furthermore, PVK thin-film technology holds a concrete potential to closely approach the theoretical efficiency limit for single-junction solar cells *via* unique control of the opto-electronic properties. However, for a disruptive breakthrough of PVK technology from fundamental research to industry, systematic research efforts are required to unravel the poor long-term stability and to reach a reliable large area fabrication process. In this review, we examine in detail recent progress on large-scale PSCs and we discuss challenges for commercialization touching upon the following aspects: material properties, fabrication technology, and industrialization challenges. Besides, the long-term stability and efficiency of large-area PSCs as well as PVK-based two-terminal tandem devices are discussed. In addition, strategies for PSC upscaling are further studied for scalable deposition technologies.

*This chapter is based on the following publication: **J. Yan**, T. J. Savenije, L. Mazzarella, O. Isabella, *Progress and challenges on scaling up of perovskite solar cell technology*, Sustainable Energy Fuels, 2022,6, 243-266

2.1. Introduction

Photovoltaic (PV) technology converts solar energy into electricity. Over the last seventy years, many different absorber materials and device architectures have been developed resulting in high power conversion efficiencies (PCEs). Among them, crystalline silicon (c-Si) and so-called III-V solar cells have demonstrated high efficiencies and a mature level of development. Currently, c-Si solar cells dominate more than 90% of the PV market share because of cheap raw materials, long stability, and well-established technology. However, the limitation of c-Si PV is the complex fabrication process as well as high requirements for wafer quality, which increase the fabrication cost and hinder further commercialization of high-efficiency architectures [59, 60]. The promise of emerging thin-film PV technology is to cost-effectively fabricate high-quality semiconductor materials by simpler deposition processes and reducing the amount of material used. Over the last decade, organic-inorganic metal halide PVK has attracted much attention in the PV research community, after Kojima *et al.* [27] discovered in 2009 the ability of PVK to convert the energy carried by sunlight into electricity. The reasons behind the success of PVK can be ascribed to its exceptional electrical properties with direct bandgap and high absorption coefficient, long carrier diffusion length, tuneable bandgap by compositional engineering, and simplified deposition process. With these outstanding properties, PSCs have been developed rapidly, demonstrating in only a decade, albeit on a sensibly smaller device area, PCEs approaching those recorded by solar cells based on c-Si [61].

However, compared to c-Si, PVK technology still has two main drawbacks namely device stability and device upscaling. These two factors directly determine the steps toward commercialization. Pinholes and defects existing in thin films have a negative impact on photoelectric properties [62, 63] and their influence becomes more severe for an effective lab-to-fab transition [30]. To address this problem, various scalable deposition strategies are employed for each layer of the PSC to obtain high-quality films and excellent device properties. Challenges in device stability, as well as cost are all crucial topics of relevance for the PV industry.

In fact, PVKs suffer from different degradation pathways related to temperature [64, 65], humidity [66, 67], composition [68], and light [69, 70]. This leads to decomposition of the material and decrease of performance as time goes on. Several approaches [71–74] have been explored to prevent this reduction in performance. Recently, PVK degradation mechanisms have been reported [75] and different materials are tested to replace less stable systems [76] Up to now, large-scale (100 cm^2) PSCs show promising stabilities [77, 78]. Nevertheless, there is still a long way towards commercialization, especially compared with c-Si PV. An approach to control degradation deals with tailoring the nature of the PVK lattice by using various cations [79] and halide anions [80, 81]. Other strategies comprise functionalizing the PVK material to improve stability [82].

Although there are numerous challenges, the progress of PSCs towards commercialization is unprecedented in the PV community. Many technologies are demonstrated to be suitable for scalable film deposition, which can produce each layer of PSC with high film quality. With the application of various strategies, such as precursor engineering and interfacial engineering, the efficiency for large area devices has been largely improved. PSCs with an active area of more than 57 cm^2 have been fabricated with a certi-

fied PCE of 14.6% [83].

Besides, PVK is also employed as at least one of the absorbers in double and triple-junction solar cells fully based on PVK PV technology [84–86] or in combination with c-Si PV technology. For their promising PCEs, the PVK-based tandem solar cells provide a valuable economic approach to break through the Shockley and Queisser (SQ) limit [87] for single-junction devices. Currently, the world record PCE for PVK/c-Si tandem solar cell has achieved 34.6% [88]. Apart from efficiency, long-term stability has also been improved in the last years with the introduction of inorganic cations, such as cesium (Cs). Nowadays, large-area devices are reported to work consistently for 1000 h under the condition of 25 °C and 85% humidity with an area of 25 cm^2 [89]. With further development of encapsulation technology and device optimization, the device stability aims at fulfilling the test requirements for commercialization in near future.

In this chapter, we discuss recent progress in large-scale PSCs and focus on the challenges for commercialization. Section 2.2 summarizes several high-volume manufacturing technologies which are suitable for scalable deposition of PVK film. Section 2.3 summarizes the challenges of up-scaling for different PVK layers. Section 2.4 provides an overview of efficiency and stability for large area PVK-based monolithic tandem solar cells.

2.2. Progress for scalable techniques

Fabrication of uniform and pinhole-free large-area PVK films can be realized by employing suitable deposition methods, such as blade coating, slot die coating, spray deposition and more. In this section, we review some deposition methods enabling scalable processes for PVK film fabrication.

2.2.1. Solution based processes

Blade coating

In the blade coating process, the precursor solution is spread onto a substrate by a moving blade, forming a wet film, as shown in Figure 2.1a. The film quality depends on the properties of the substrate surface [90], velocity of the blade, solvent properties (for example composition [91] concentration, solvent viscosity) [92, 93], annealing temperature [94], and atmosphere. As an example, Figure 2.1b illustrates the relationship between coating speed, film thickness, and solvent evaporation [83]. Since the first PVK film was formed with blade coating in 2015, many studies have been reported ranging from in situ observations to technical optimization [95, 96]. In situ GI-XRD measurements are employed for blade coating to observe the ink-to-solid phase transformation of PVK films during preparation [97]. The composition, solvate phase, and intermediate complexes are observed under low processing temperatures; the crystallization process takes place directly without forming intermediate phases, leading to a successful method for large-area film fabrication [97]. Apart from the in situ observation of PVK crystallization, various basic technical parameters are also optimized. Temperature and solvent evaporation rate are of critical importance to control the film formation [98]. Kim *et al.* [99] found that a slow solvent drying process could encourage the formation of large crystals, which were formed immediately after solution blading.

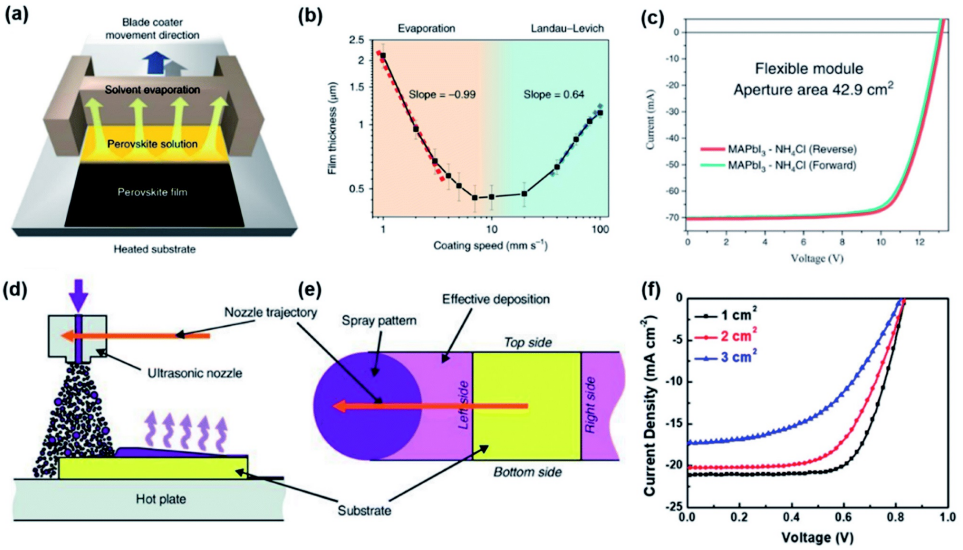

Figure 2.1: (a) Diagram of blade coating of PVK film [83]; (b) the film thickness as a function of coating speed for blade coating [83]; (c) *J-V* curves for flexible PSCs with a record aperture area of 42.9 cm^2 and PCE of 15.86% (ref. [90]); (d) diagram of the spray coating process [83]; (e) diagram of the magnified structure of nozzle trajectory [83]; (f) *J-V* curves for PSCs with different active areas [100].

In Mallajosyula's work [94], a temperature-controlled blading technique was employed for the growth of large-grain PVK thin films. Apart from temperature, other parameters, like coating speed, is found to have a relationship with film thickness [101]. Besides, a combination of blade coating and rapid thermal processing has been demonstrated to exhibit high PVK film quality [94]. Devices with a PCE over 17% for an active area of 2.7 cm^2 were reported [90]. The interaction between the ink and the substrate was also investigated. Dai *et al.* [102] introduced ammonium chloride as an additive into precursor solution to reduce film trap density, flexible PSCs with a record PCE of 15.86% was obtained for an aperture area of 42.9 cm^2 (see Figure 2.1c). Similarly, Chen *et al.* [90] recently partially replaced dimethyl sulfoxide with solid-state carbohydrazide to avoid the formation of voids at perovskite-substrate interfaces. Based on the research mentioned above, this technique shows a high sensitivity towards temperature and towards the interaction between the ink and the substrate. In the recent report from Bu's group [103], the nucleation process is facilitated by controlling the suitable substrate temperature. In this way, they demonstrated a 205 cm^2 sub-module with a PCE of 15.3%. Blade coating approach is also flexible to combine with other methods to prepare PVK films, such as roll-to-roll setups, rapid thermal processing [94], and sequential deposition [92], which provides more possibility for the future commercial application.

Spray coating

The spray coating technology was firstly used for PVK preparation in 2014 (ref. [104]) and developed rapidly from then on with various ways of creating the spray droplets.

In this process, tiny liquid droplets are formed with a nozzle and then dispersed onto a substrate, as shown in Figure 2.1d and 2.1e. According to the investigation of Chen *et al.* [105], the spray process is classified into three stages: atomization process, droplet flight, and film deposition. Each of them was discussed in detail from principles to parameters in ref. [105]. The flying route of these tiny droplets during spray has a strong influence on the final film quality. Ishihara *et al.* [106] studied the fluid dynamics of droplets, and Girotto *et al.* [107] described the relationship between spray velocity and precursor solution spreading capabilities. Besides, factors affecting the deposition were systematically optimized, such as precursor solution (viscosity, concentration, compositions) [108, 109], substrate (wettability, roughness, temperature) [110, 111], boiling point of solution [112], distance between the nozzle and substrate [113]. Park *et al.* [110] prepared high-quality PVK layers by controlling the flow rate of precursor solution and the reaction temperature. As a result, larger-scale PVK film with an area of 7.5 × 7.5 cm^2 showed excellent photovoltaic properties and uniformity [110]. Chou *et al.* [100] realized a PCE of 7.01% with an aperture area up to 3 cm^2 by controlling precursor solution concentration and spray passes, the corresponding $J-V$ curves are shown in Figure 2.1f. Recently, Heo *et al.*[114] successfully prepared $CsPbI_{3-x}Br_x$ sub-module by spray coating with an efficiency of 13.82% (112 cm^2 aperture area). A graded PVK absorber structure is created and it shows only 9% degradation after 1-sun light soaking for 1000 h [114]. All-spray coating PSCs (CTLs and PVK) have also been reported [115], and PCEs are in the range of 10–12% with an aperture area of about 1 cm^2. Spray coating of PVK PV shows an increasing PCE situation in the recent few years and the future experiments can concern more about low volatility controlling, new additives for PVK solution and novel transport materials [113].

Slot-die coating

Slot-die coating can be applied for film deposition of different layers, especially the PVK layer. During the process, the coating head is positioned close to substrate and there is a narrow slit on the coating head. Precursor solution is pumped into the coating head and is forced to flow out of the narrow slit onto the moving substrate. The film quality is extremely sensitive to the processing parameters such as the substrate temperature, wettability, moving speed, and width of the slit. Besides, the wettability, viscosity of precursor solution also influences the degree of PVK crystallinity [118, 119]. In Cotella's work [120], the preheated substrate combining with air-knife led to a temperature gradient in the wet film which plays a crucial role in controlling the crystallization. By selecting low boiling solvents and employing multifunctional additives, the processing window time can be widened. The Dutch institute Solliance, which is specialized in the roll-to-roll slot die production process of PVK layers [121], has modified the ink with a co-solvent and additive, avoiding efficiency losses with the increase of area during the drying process. They demonstrated a 144 cm^2 module with a PCE of 14.5% [122]. Apart from the physical property influence of precursor solution, chemical properties such as additive [123, 124], and precursors composition [125, 126], can also lead to excellent film properties. By applying additive method, Yang *et al.* [127] prepared large-area FACs-based PVK films with a certified quasi-stabilized PCE of 16.63% (20.77 cm^2). In additional to several basic parameters, models and principles are also introduced to further explain

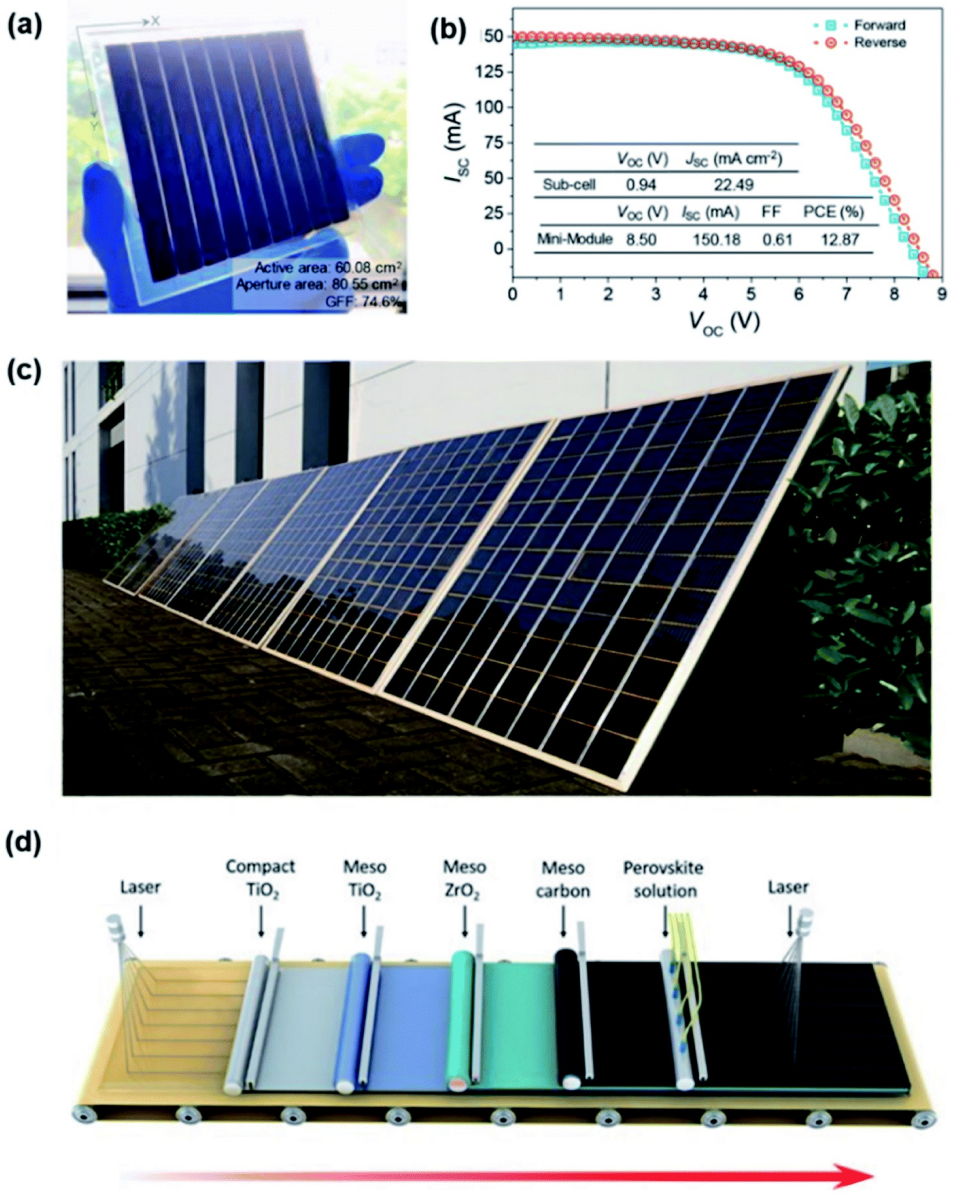

Figure 2.2: (a) Image of slot die coated PSC-based mini-module with an active area of 60.08 cm^2 [116]; (b) the $J-V$ curves of the device shown in (a) [116]; (c) image of 7 m^2 fully printed PSC-based modules [117]; (d) diagram of fabrication process for fully printed PSCs [117].

the slot die coating process. Xu *et al.* [116] investigated the infiltration process of the precursor solution into a mesoporous titanium oxide (TiO_2) [128]. Under the guidance of the model, coating parameters were optimized and a PCE of 12.87% was obtained with an active area of 60.08 cm^2 [116]. Figure 2.2a and 2.2b show the device structure and corresponding *J-V* curves [116]. Bu *et al.* [129] prepared 65 cm^2 FACs-based PSCs with a certificated PCE of 19.54%. In their work, avoiding the formation of PVK intermediate complex is the key point to obtain high quality PVK film. Not only for PVK film formation, but deposition of CTLs can be also realized with slot-die coating. All-slot-die coating devices with PCEs around 11% have been successfully fabricated [130–132]. Among all-slot-die coating works, Di Giacomo *et al.* [133] in Solliance fabricated PVK solar modules; the highest PCE exceeded 10% with a power output of 1.7 W for an area of 168.75 cm^2. Slot-die coating shows a great potential toward industrialization because it is one of the most used techniques for the roll-to-roll fabrication of PSCs [134].

Inkjet printing

In terms of inkjet printing, precursor solution is dispersed by nozzles. The influence of some basic factors (such as substrate wettability, temperature, ink droplet wetting behavior, viscosity, and solvent evaporation rate) on PVK film quality was investigated. Properties of the precursor solution play an important role in controlling PVK film formation [135]. Li *et al.* [136] reported a new ink system, whose solvent was composed of *n*-methyl pyrrolidone (NMP) and dimethylformamide (DMF), the corresponding devices were fabricated with PCEs of 14.5% (4.04 cm^2) [136]. As the most basic factor, temperature is also taken into consideration. In Liang's work [137], inkjet printing combined with vacuum-assisted thermal annealing was employed for scaling up. High-performance PSCs based on printed $MAPbI_3$ were demonstrated to obtain a PCE of 13.3% with an active area of 4.0 cm^2 [137]. Recently, the emerging of all-inkjet-printed PSCs accelerates the process of industrialization. Hu *et al.* [117] fabricated a large-area (49 cm^2) PVK module that exhibited a PCE of 10.4% with a fully printable process. Besides, a 7 m^2 fully printed PSC-based module has been successfully prepared (see Figure 2.2c and 2.2d), showing promising potential in the practical photovoltaic application.

2.2.2. Vacuum based processes

As an alternative to solution-based processes, vacuum deposition has been explored to grow thin-film PVK from dry sources. There are two unique advantages of vacuum-based process. Firstly, the process does not involve the use of toxic solvents which may have a negative effect on the environment.Secondly, the conformal growth onto rough substrates allowing the use of textured substrates in devices to improve light in-coupling [138]. This opens the integration of PVK cells on textured c-Si bottom cells for further applications [138–140].

Thermal evaporation

In thermal evaporation process, the precursors are sublimated by heating in high vacuum conditions. They are deposited onto substrates to form different material layers as shown in Figure 2.3a. According to the evaporation temperature of different source

materials, a PVK film can be grown using two methods: co-evaporation [53, 141] and sequential vacuum deposition [142].

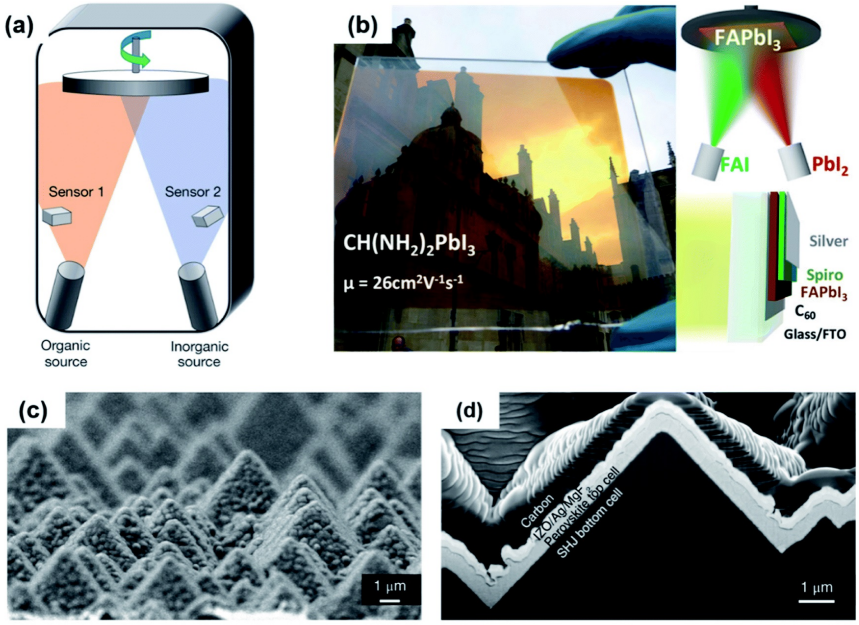

Figure 2.3: (a) Schematic diagram of the co-evaporation of PVK film [53]; (b) image of 64 cm^2 $FAPbI_3$ thin film and corresponding fabrication process [143]; (c) SEM image of the PVK film fully covering the silicon pyramids [144]; (d) a cross-section of the PVK/SHJ monolithic tandem solar cell [144].

Liu et al.[53] firstly reported PSCs with high PCEs, which were prepared by the dual-source co-evaporation method. Large area PVKs have also been reported. Borchert *et al.* [143] applied the co-evaporation method for large-area PVK deposition. Formamidinium lead triiodide ($FAPbI_3$) thin films were obtained with an area of 64 cm^2, as shown in Figure 2.3b. Up to now, $MAPbI_3$ layer deposited by thermal evaporation demonstrates a PCE of 18.13% with 21 cm^2 active area (mini-modules) [145]. A challenge for PVK deposition with thermal evaporation is the control of the organic precursors, such as the MAI and FAI. Apart from two source co-evaporation, multi-source co-depositions and sequential thermal evaporation are also applied for PVK fabrication [146, 147]. For multi-source deposition, Bolink's group from University of Valencia reported several studies focused on fully thermal evaporated PSCs [58], wide-bandgap absorber [147], and device stability [54]. In terms of sequential thermal evaporation, Feng *et al.* [148] successfully deposited some superior FA-based PVK films using low temperature annealing in vacuum. Zhou *et al* [149] from Tsinghua University reported solar cells fabricated with thermally deposited absorber with record PCE of 26.4%. Compared with other solution based methods, thermal evaporation has been demonstrated to allow PVK deposition onto textured substrates [144], and this feature provides a promising future for further applications. Sahli *et al.* [144] applied the sequential two-step method to deposit the PVK layer for a monolithic tandem device. The PVK film fully covered the μm-sized sil-

icon pyramids (see Figure 2.3c and 2.3d), and the tandem device achieved an efficiency as high as 25.2% [144]. Following the same approach, the same group demonstrated a PVK/PVK/c-Si monolithic triple-junction solar cell [146]. All-vacuum-processable PSCs are also obtained recently [150, 151], Lei *et al.* reported an all-evaporation method to achieve PCEs beyond 13% with an active area of 16 cm^2 [152]. The recently reported improved results based on thermal evaporation indicate the potential application in PSCs scaling up, especially for scalability and the compatibility with textured device-Si bottom cells.

Pulsed laser deposition

Pulsed laser deposition (PLD) is a versatile technique for stoichiometric deposition of various inorganic materials independently of vapour pressure to form thin films. The PLD configuration and deposition process are shown in Figure 2.4a. Different from other vacuum-based approaches, PLD exhibits stoichiometric mass transfer of materials from the target to the substrate [153]. This unique advantage offers a potential application for PVK film formation. PLD consists of two main stages, namely formation of the target plasma and material deposition. In the first stage, the focused laser strikes the surface of the target material for a short time, ablating material that forms a so-called plasma plume containing ions and atoms. In the second stage, these excited ions directly impinge the substrate in front of the target. Film properties can be optimized by controlling the laser parameters [154], substrate temperature [154], and chamber pressure [155].

The first deposition of $MAPbI_3$ film based on PLD was reported by Bansode *et al.* [155] in 2015. Following the same method, they successfully deposited PVK films on silicon showing good crystal quality. The corresponding SEM-based top view and cross-sectional images are shown in Figure 2.4b and 2.4c [155], respectively. From then on, several PLD-grown inorganic metal halide PVKs have been successfully prepared, showing good photovoltaic properties and film stability [156–158]. Wang *et al.* [156]. fabricated a dense $CsPbBr_3$ film *via* PLD. No significant decomposition was observed when the sample was placed in a highly humid (80%) environment for 15 days [156]. Lead-free PVK film formation is also achieved with PLD. $CsSnI_3$ film was recently reported by Kiyek *et al.* [157]. The thickness-optimized film shows a stabilized black phase with a sharp absorption edge. About the deposition of organic-inorganic hybrid PVKs, another method named resonance infrared matrix-assisted pulsed laser evaporation [159] should be mentioned, showing low laser-induced damage of organic material. A detailed description of the new pulsed laser-based method can be found in Soto-Montero's review [160]. Based on the film quality as well as stability mentioned above, PLD has a potential application for scalable deposition of PVKs, especially in terms of fully inorganic PVK deposition.

2.2.3. Hybrid chemical vapor deposition

Hybrid chemical vapour deposition (HCVD) method can avoid solvent-related complications, which are challenging to control in industrial large-scale fabrication [163], such as fast solvent removal and wettability issues. This method combines chemical vapour deposition (CVD) and other scalable deposition methods, such as thermal evaporation [164] or spray coating [165]. A typical PVK-based HCVD process consists of two steps:

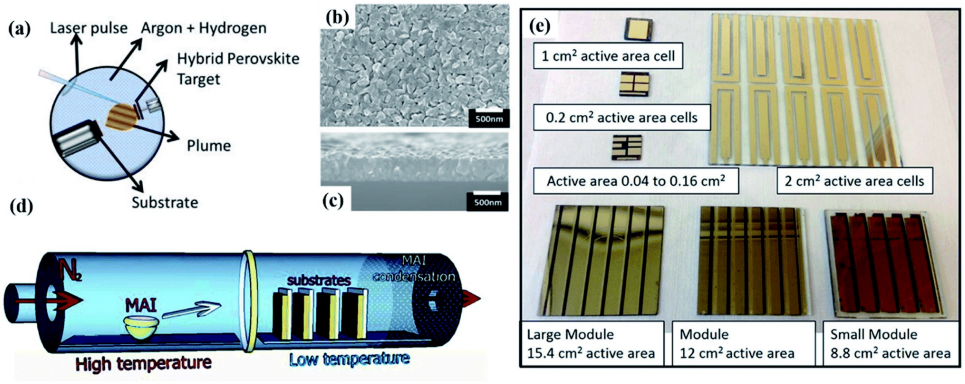

Figure 2.4: (a) Schematic diagram of the PLD configuration and deposition process [155]; (b) top view of PVK film on silicon wafer deposited with PLD [155]; (c) the cross-section of the PLD PVK film [155]; (d) schematic diagram of the HCVD configuration for MAI deposition onto PbI_2 coated substrates [161]; (e) image of cells and modules prepared with HCVD approach demonstrating the up-scaling process [162].

formation of inorganic film and organic/inorganic halide vapour deposition. The inorganic film is mainly deposited *via* thermal evaporation in reported works [166, 167]. As for the CVD process, the organic halide vapour is optimized by pressure and temperature to deposit on the inorganic film, following a gas-solid reaction and converting into uniform PVK films [168]. The HCVD configuration and vapour deposition process for $MAPbI_3$ are shown in Figure 2.4d. Several works have reported a successful formation of scalable PVK films by combining thermal evaporation and CVD [157, 162, 164]. Leyden *et al.* [161] firstly prepared a planar $MAPbCl_3$ device *via* HCVD method, achieving a PCE as high as 11.8%. Following the similar approach, Leyden *et al.*[162] again indicated the device upscaling process *via* HCVD. They fabricated $MAPbI_3$ based devices with a PCE of 9.5% (8.8 cm^2) and obtained a PCE of 9.0% (12 cm^2) for $FAPbI_3$ based devices, the corresponding up-scaling processes are shown in Figure 2.4e. However, similar to solution-based film formation, mixed-cations and mixed-halides play a critical role in film opto-electronic properties and stability [169]. Therefore, mixed cations/halides are commonly introduced in the first step by co-evaporation [170]. Different from this approach, Luo *et al.* [164] prepared a mixed-cation PVK film by optimizing the second step. They replaced pure FAI vapour with FAI/FACl mixed vapour to optimize the vapour-solid reaction, resulting in improved phase stability. Consequently, the large-sized PSC modules (active area of 41.25 cm^2) demonstrated champion PCE of 12.24%.

2.3. Challenges for device upscaling

The device PCEs, deposition approaches, and corresponding areas are summarized in Figure 2.5, which clearly shows that PCEs significantly decrease for large device areas. As for the methods not mentioned above (e.g. CVD, soft-cover deposition), detailed technical parameters can be found somewhere [165, 170–172]. The upscaling of PVK PV technology faces challenges toward commercialization. In this section, we review the most significant challenges for processing high PCE devices from lab-scale to fab-scale.

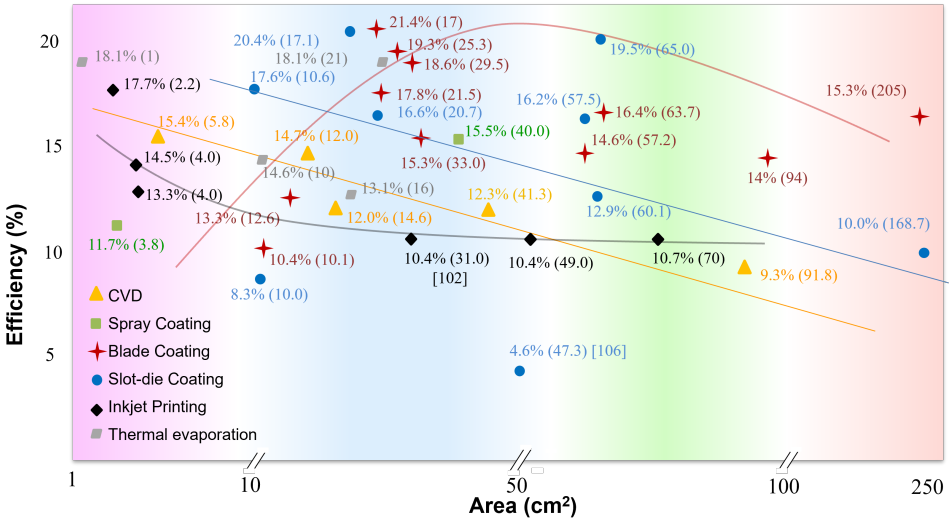

Figure 2.5: Summary of PCEs as a function of the device area for PSCs prepared by different fabrication methods [83, 93, 103, 111, 116, 117, 127, 129, 133, 135–137, 145, 148, 150, 152, 162–165, 170, 173–178, 178–187].

2.3.1. Precursors and absorber layer

Upscaling of PVK films emphasizes the suitable storage of precursors as well as film deposition process. For solution-based methods, the precursor solution ratio and storage may have impacts on film quality, influencing both the nucleation and the crystal growth. To address this question, many attempts have been performed to control the film morphology and photovoltaic performance starting from a non-stoichiometric precursor solution [188, 189]. As an example, excess of PbI_2 can lead to higher PCEs suggesting that unreacted PbI_2 improves the crystallinity of PVK films [190]. The reported precursor engineering may have some differences based on different solution deposition methods, but most of them are related to introducing of additives as stabilizer or mixing solvents to optimize the precursor viscosity as well as boiling point [191]. Table 2.1 briefly shows the reported requirements, approaches and corresponding solution-based deposition methods. Besides, the detailed PVK precursor solution chemistry is reviewed by Jung *et al.* [192] from fundamentals to industrialization.

Compared with solution-based methods, vacuum deposition can exactly control the deposited amount. However, one of the drawbacks is the lack of compatibility with additive engineering, which is an excellent approach to improve crystal quality, as shown in Table 2.2. Furthermore, this method shows less flexibility in the number of sources that can be incorporated in the final PVK material. For the deposition process, one of the most challenging part is to form a suitable interaction between substrate and precursors for both solution and vacuum related deposition approaches [209]. A better interaction not only depresses formation of non-radiative centres in the interfacial, but also has an influence on PVK crystal growth.

Table 2.1: Different requirements and strategies of precursor solution preparation/storage based on different solution-based methods

Methods	Requirement	Approaches
Blade coating	Purified organic precursor [193] high viscosity [93]	Reductant [194, 195] Moisture barrier [196] Material with synergistic effects [197]
Spray coating	Low viscosity [192] Suitable boiling point solvent [104]	Co-solvents [198] Low ink concentrations [108, 199] Material with synergistic effects [200]
Slot die coating	-	Co-solvents [201–203] Lewis base additives [127] Material with synergistic effects [120, 178]
Ink printing	Slow solvent evaporation [204]	Material with synergistic effects [136, 205–207] Co-solvents [208]

Table 2.2: Comparison of solution- and vacuum-based depositions

Approaches	advantages	disadvantages
solution-based	Simple Compatible with additives [214]	Solvent usage [215] Low material utilization [216]
Vacuum-based	Uniformity control on large area Non-toxic solvent Flexibility in substrate usage [217]	Number limitation of evaporation sources Long deposition process

2.3.2. Charge transporting layers

For large area film fabrication, charge transporting layers (CTLs) should not only have appropriate energy alignment, thickness as well as conductivity, but also be suitable for scalable deposition. Therefore, the selection of compatible materials and processes is important for PSC commercialization. In this section, CTLs will be briefly discussed focusing on challenges for both hole transporting layer (HTL) and electron transporting layer (ETL).

HTL

Organic materials, such as spiro-MeOTAD [210, 211] and poly(triarylamine) (PTAA) [212, 213], are widely used as hole transporting material for high-performance PSCs. Spiro-MeOTAD is the most common HTL material in lab-scale device preparation. There are some successful examples for large area device preparation with spiro-MeOTAD as HTL. Luo *et al.*[164] prepared PVK solar modules with spiro-MeOTAD, the device achieved a PCE of 12.24% and device area is 64 cm^2.

Following the spin coating method, Yang *et al.*[93] demonstrated a four-cell module (12.6 cm^2) with a stabilized efficiency output of 13.3%. Nevertheless, these pure organic HTL materials have low hole mobility, and dopants such as bis(trifluoromethane) sulfonimide lithium salt (LiTFSI) are required to improve the device PCE. Unfortunately, the introduction of the dopants can accelerate the degradation of PVK. Therefore, spiro-MeOTAD still has a gap between lab and fab due to its cost and the negative effect of dopant. In terms of inorganic materials, such as metal oxides, they are utilized not only

to improve device stability but also to simplify the deposition process in mass production. Nickel oxide (NiO_x) is a popular HTL with high material stability [218]. NiO_x film can be formed with a variety of approaches, such as screen printing [219], spin-coating [220], and spray deposition [221]. However, the carrier mobility in NiO_x is also not so high and the reported NiO_x based device area is only 3-5 cm^2 [222, 223]. Another commonly used metal oxide is molybdenum oxide (MoO_x) [224]. Different MoO_x film morphologies are obtained with different approaches, such as solution preparation [225], thermal evaporation [226], blade coating [227], and electrodeposition [228]. Thermally deposited MoO_x is commonly used in PSCs to realize energy level alignment and hole extraction [229, 230]. It is generally applied together with spiro-MeOTAD as a bilayer because the interface reaction between MoO_x and PVK may accelerate the degradation of PVK [231]. Several other inorganic materials are also researched for HTL application, for example, CuSCN [232] and VO_x [233, 234]. Even though small area devices based on CuSCN and VO_x have achieved excellent PV properties, PCEs drop dramatically with the increase of device area. Next to the abovementioned materials used as HTL in PSCs, some novel materials (such as TaTm:F6-TCNNQ, TaTm) are also applied as HTL and the details can be found in ref. [235]. Taking the cost and stability into consideration, inorganic materials show potential candidates for large area devices, further works focused on good film quality with high hole mobility should be achieved in near future.

ETL

SnO_2 [164, 170], C60 [143, 226], and PCBM [236, 237] are most frequently used as ETLs for high PCE devices because of their high carrier mobility and good conductivity. Those materials can also be used for large area ETL fabrication. For TiO_2 [117, 238, 239], several works show outstanding properties [240, 241]. Keremane *et al.* [241] printed in ambient atmosphere mesoporous TiO_2 enabling 11.55% PCE (70 cm^2). However, TiO_2 is reported to show a photocatalytic effect which may degrade the PVK absorber layer [242]. Atomic layer deposition (ALD)-based SnO_2 is also an excellent candidate demonstrating high *Voc*, small $J-V$ hysteresis, and negligible photocatalytic effect. Currently, the highest PCE of SnO_2-based PSCs has achieved 23.3% with an active area of 0.1 cm^2 [243]. However, SnO_2-based large-area device fabrication still needs to be further improved, because SnO_2 has a higher probability of pinhole formation during film fabrication compared with TiO_2 [170]. SnO_2 film needs to be thin while it is not easy to fully cover the substrate surface with extremely thin SnO_2 film. This problem is more critical for large area PSCs. Therefore, a trade-off between thickness and mobility needs to be carefully found. Up to now, the most successful example for SnO_2 film scaling up is by Qi's group [170]. By precise interface engineering, they demonstrated a PCE of 10% with a designated area of 91.8 cm^2 [170]. PCBM is also applied for scalable deposition, which is usually in combination with other materials such as C60 or BCP to form an efficient electron transporting bilayer [178, 236, 237]. Especially, C60 and BCP can be deposited by thermal evaporation, that makes these films easy to realize also on large area substrates, making it compatible with industrialization. The reported C60 and BCP based devices show PCEs of 14.6% (57.2 cm^2) [83] and 16.4% (63.7 cm^2) [180].

2.3.3. Back electrode

Thermally or e-beam evaporated metals (Au, Ag, Al) are the mostly used materials for the back electrode in PSCs. Analogous to the metal electrode in c-Si solar cells, a scalable and industrial process for metallization is a critical aspect to address in terms of material consumption for large-area devices. Cheaper materials are needed in replacement of noble metals when looking into commercialization. Nickel (Ni) film is also applied as back electrode for scalable PVK application [244]. One interesting aspect is that degraded PVK can be washed off from a device with Ni electrodes and then fresh PVK can be reloaded [244]. This unique recycling technology shows a new way for further development of low-cost PSCs. Besides, the direct contact between a metal and the CTL or PVK may lead to additional reactions. To address this issue, TCO films (for example, indium-doped tin oxide (ITO), aluminum-doped zinc oxide (AZO), indium-doped zinc oxide (IZO)) can be inserted between metal and CTL to prevent the undesired ion immigration. Lee *et al.* [245]. fabricated large-scale PVK solar modules with application of multi-layered transparent electrodes, demonstrating excellent thermal stability. Carbon has also been proposed as electrode due to several advantages, such as high stability, low cost, excellent conductivity, and environmental protection [246, 247]. A large-area (70 cm^2) PVK solar module with carbon electrode was fabricated, achieving a PCE of 10.74% (certified PCE 9.11%) [120]. Besides, graphene is also an excellent candidate as electrode due to its good conductivity, stability, and transparency [248, 249]. Thus, it is commonly applied as electrode for PSC, especially for semi-transparent [250, 251] or flexible PSCs [252, 253]. Based on the above discussion, carbon electrodes show a potential application in PSC commercialization, especially because of their stability and low cost.

2.3.4. Stability of large area PVK devices

Sources of instability

The instability of PVK and degradation mechanisms have been systematically studied based on experiments and simulations [75, 254]. Lab-scale devices show improved stability *via* different optimization steps, such as introducing inorganic cations [163, 166], surface modification and using 2-dimensional (2D) materials [167, 255, 256]. However, to make PVK competitive to c-Si, the issues related to device lifetime still need to be addressed. The instability of PVK film comes mainly from defects (ion migration) [257, 258], pinholes (lattice deformation) [259], and phase transition [260], which may accelerate the degradation in presence of water [261], high temperature [262], light [263], and electric field [264]. To estimate the potential lifetime of PSCs, the International Electrotechnical Commission (IEC) is normally used based on a series of strict tests, such as UV-light, thermal cycling, and damp heating [183]. The long-term operation of PSCs does not only depend on stability of PVK film, but also properties of CTLs and electrode, for example, the thermal instability of Spiro [265], UV-instability of TiO_2 (ref. [266]) and reaction between I^- and Ag [267].

Developments and strategies on long term device stability

Focusing on the instability problems mentioned above, some strategies are proposed to improve the stability of large area PSCs, which can be summarized into four main parts.

Table 2.3: The structure (light entering from the left-hand side), performance, and stability of large area (≥5.00 cm^2) PSCs

Approach	PCE (%)	Area (cm^2)	Stability	Ref
Glass/ITO/NiO_x/PVK/Nb_2O_5/Ag	11.20	5.00	98% for 150 min, N_2, 100 °C	[223]
Glass/FTO/TiO_2/PVK/spiro-MeOTAD/Au	14.60	12.00	96% for 1200 min, N_2, MPP	[163]
Glass/FTO/TiO_2/PVK/WBH/P3HT/Au	16.00	24.97	85% for 1370 h, RH 85%, room temperature	[89]
Glass/FTO/c-TiO_2/m-TiO_2/ZrO_2/PVK/carbon	10.40	49.00	30 days for RH 80%, 30 °C	[117]
Glass/FTO/c-TiO_2/m-TiO_2/ZrO_2/PVK/carbon	10.75	70.00	95% for 2000 h, RH 65-70%, 25-30 °C	[173]
Glass/FTO/c-TiO_2/m-TiO_2/ZrO_2/PVK/carbon	6.40	100.00	96% for 1046 h, full sun light illumination	[268]

Firstly, composition engineering. Inorganic cations such as Cs^+ and Rb^+ are introduced to stabilize the PVK cubic phase [269, 270]. Secondly, interfacial modification is useful to not only passivate non-radiative central defects, increase resistance to moisture, but also hinder I^- migration [271]. As an example, the use of 2D materials has been successfully extended to large-area PSC fabrication. It was reported that 2D material-based large-area PVK solar modules (PCE 13.4% for 108 cm^2 and 15.3% for 82 cm^2) showed excellent stability under thermal stress test at 65 °C (ISOSD2) for over 1000 h [256]. Thirdly, select other functional layer materials to replace susceptible CTLs and electrodes. Especially for the HTL, inorganic candidates such as NiOx [272], CuOx [273], and CuSCN [274] are introduced to substitute organic materials. Table 2.3 summarizes the structure, stability, and corresponding performance of PSCs with areas larger than 5 cm^2. Finally, encapsulation. It is the final step of device fabrication, which provides a physical barrier protecting against various outdoor environmental factors. The company Microquanta Semiconductor announced that their encapsulated PVK module (20 cm^2) showed degradation of less than 2% after a 100 kW h ultraviolet (UV) preconditioning test (6.5 times IEC standards) [275]. One thing need to be noted, we can observe a great variety of test conditions reported in the literature which makes a systematic comparison difficult. To solve this issue, a consensus statement [275] was given by many researchers for stability assessment. Based on the International Summit on Organic Photovoltaic Stability (ISOS) protocols, some other properties of PSCs are investigated, such as ion redistribution under electric fields, reversible degradation, and distinguishing ambient-induced degradation from other stress factors [275]. This section has a summary about strategies on PSC stability towards commercialization, the corresponding detailed information can be found in ref. [183, 183, 276–280].

2.4. Scaling up of two-terminal monolithic tandem devices

To overcome the SQ limit of single-junction solar cells, the multijunction (MJ) configuration has been developed. The MJ approach is certainly not new in the PV community. In fact, it has been intensively investigated for thin-film Si [281–293] and III-V PV technologies [294–302]. It consists of two or more sub-cells that absorb light of different energies. By tuning the bandgap (Eg) of these sub-cells, better utilization of solar photons can be achieved resulting in higher PCEs. The simplest example is a so-called 'tandem' device consisting of two sub-cells stacked one on top of the other with engineered absorber layers. In the monolithic configuration, also known as two-terminal (2T), the sub-cells are

electrically connected in series, meaning that the absorber properties must be carefully designed for 'current matching', namely each sub-cell should deliver an equal photocurrent. There are also other configurations, such as the four-terminal (4T) [303], which eliminates the current matching requirement and provides only a mechanical stacking, and the three-terminal (3T) [304], which is suitable for back-contacted bottom cell architectures [300, 305].

In this context, PVK/c-Si tandem device attracts much attention because of the stable and mature c-Si technology, the bandgap compatibility between the two absorbers, and the low processing temperature of the PVK top cell. Starting from the 1.12 eV of the Eg of c-Si and using a PVK top cell of 1.70 eV, the theoretical limit of PCE for PVK/c-Si monolithic tandem device is 44.1%. Considering the great variety of PVK compositions and the ease of integration of new elements in the PVK lattice, Eg can be varied in a wide range of energies from 1.2 eV (ref. [306]) to 3.0 eV [307, 308]. Consequently, MJ solar cells fully consisting of PVK devices [84, 86] or combinations with CIGS bottom cells [20, 309, 310] have been demonstrated. Independent of the deployed hybrid technologies, MJ devices using PVKs have shown a rapid PCE increase which can contribute to the acceleration towards the commercialization of PVK devices.

This section focuses on progress and challenges for PCE and stability, which is based on large area (≥ 1 cm^2) PVK/c-Si two-terminal monolithic tandem devices. The detailed discussion based on material, technical, and device levels of small area PVK/c-Si tandem devices can be found somewhere else [311–315].

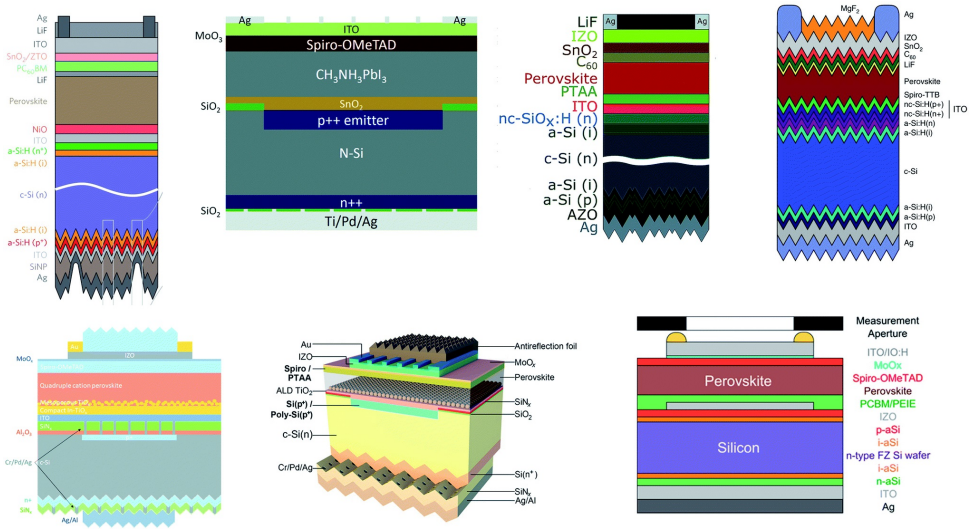

Figure 2.6: A summary of different 2T tandem structures for large area PVK-based tandem devices [85, 144, 316–321].

2.4.1. Conversion efficiency

The efficiency of tandem devices is related to the properties of bottom cell, top cell, and various anti-reflective, recombination, and contact layers. Homojunction and heterojunction silicon (SHJ) can be used as the bottom cell for both 4T [318, 322] and 2T tandem devices [144, 316]. SHJ solar cells are commonly chosen due to their high *Voc* and PCE, which have a positive effect on the tandem device performance. Homojunction cells are also excellent candidates because they currently dominate most parts of the PV market. Up to now, works reported on efficiency improvement of large area tandem devices can be classified into three areas: PVK sub-cell optimization, recombination layer optimization, and optical design. Figure 2.6 shows a summary of different tandem structures, which were reported to be used for large area tandem devices.

PVK sub-cell

For 2T large area tandem solar cells, the PVK film quality strongly determines the top cell photovoltaic properties. It is a big challenge to form high-quality large area PVK film on a textured surface to enable integration with industry-relevant textured c-Si bottom cells. Hou *et al.* [323] demonstrated a solution processed PVK top cell with fully textured c-Si bottom cell by employing an µm-thick PVK layer. In recent work, a two-step sequential vacuum process was applied for PVK deposition on textured surface [324]. Consequently, 100 cm^2 textured silicon substrate was perfectly covered by a PVK film via sputtering and CVD. In addition, interface modification, as well as composition engineering, have a huge influence on the whole device efficiency. Low-temperature (70 °C) slot-die coating was applied with a combination of modification strategy for top cell preparation [325]. A PVK/textured silicon monolithic 2T tandem device achieved a PCE of 23.8% with an area of 1 cm^2 [325]. Besides, Cs^+ and FA^+ were also applied to tune the PVK bandgap and high device stability was obtained. The mixed-cation based PVK/c-Si solar cell achieved a PCE of 23.6% with an area of 1 cm^2 [317]. Current matching cannot be ignored to obtain a high PCE for tandem device, and the most common method is to optimize the bandgap of the top cell. The bandgap optimization can be realized by composition engineering.

Recombination layer

Improvements in PCE are also driven by selection and optimization of the recombination layer between the two sub-cells. A thorough analysis of many aspects related to the recombination junction for tandem devices was recently published by Bastiani *et al* [344]. Most commonly, TCO materials are used as recombination layers because they can fulfill both optical and electrical interconnection requirements. Up to now, recombination layers such as ITO, IZO, AZO have been generally applied for large area 2T tandem devices and excellent outcomes have been obtained. With optimization of the IZO thickness, Werner *et al.* [318] achieved a stable PCE of 19.2% over an aperture area of 1.22 cm^2. A PCE of 22.6% (area 57.4 cm^2) was achieved with a sputtered ITO recombination layer [332]. Apart from TCO layers, doped hydrogenated nanocrystalline silicon (nc-Si:H) has also been employed as a recombination layer. For example, Sahli *et al.* [144] introduced a nc-Si:H recombination junction to the tandem device with an effective decrease of the parasitic absorption and optical reflection, demonstrating a certified

Table 2.4: Parameters and properties of PVK-based large area 2T tandem devices. Reported results are sorted by date.

Silicon	Perovskite	Top cell bandgap (eV)	Recombination layer	Efficiency (%)	Area (cm^2)	Insitution	Year	Ref
Homo-junction	$MAPbI_3$	1.55	n^{++}/p^{++} Si	13.7	1.00	MIT/stanford	2015	[326]
	$MAPbI_3$	1.55	ZTO	16.3	1.43	EPFL/CSEM	2016	[327]
	$CsRbFAMAPbI_{3-x}Br_x$	1.62	ITO	22.5	1.00	ANU	2017	[320]
	$MAPbI_3$	1.58	-	21.0	4.00	UNSW	2018	[319]
	$MAPbI_3$	1.58	-	17.6	16.00	UNSW	2018	[319]
	$(FAPbI_3)_{0.83}(MAPbBr_3)_{0.17}$	1.59	-	21.8	16.00	UNSW	2018	[319]
	$CsRbFAMAPbI_{3-x}Br_x$	1.62	-	23.2	1.00	ANU	2018	[316]
	$FAMAPbI_{3-x}Br_x$	1.61	-	23.1	4.00	UNSW	2019	[328]
SHJ	$MAPbI_3$	1.55	IZO	19.2	1.22	EPFL/CSEM	2015	[318]
	$MAPbI_3$	1.55	IZO	20.5	1.43	EPFL/CSEM	2016	[318]
	$CsFAPbI_{3-x}Br_x$	1.63	ITO	23.6	1.00	Stanford/ASU	2017	[317]
	$CsFAPbI_{3-x}Br_x$	1.63	nc-Si: H	21.2	1.43	EPFL/CSEM	2017	[329]
	$CsFAPbI_{3-x}Br_x$	1.63	nc-Si: H	18.0	12.96	EPFL/CSEM	2017	[329]
	$CsFAPbI_{3-x}Br_x$	1.63	nc-Si: H	25.2	1.419	EPFL/CSEM	2018	[144]
	$CsRbFAMAPbI_{3-x}Br_x$	1.62	-	24.1	1.00	ANU	2018	[316]
	$CsFAPbI_{3-x}Br_x$	1.68	ITO	25.0	1.00	Stanford/ASU	2018	[330]
	$CsFAPbI_{3-x}Br_x$	1.63	nc-Si: H	25.4	1.43	EPFL	2019	[331]
	$Cs_xFA_{1-x}PbI_yBr_{3-y}$	1.63	ITO	22.6	57.4	CSEM/EPFL	2019	[332]
	$Cs_{0.05}(FA_{0.77}MA_{0.23})_{0.95}Pb(I_{0.77}Br_{0.23})_3$	1.68	ITO	29.1	1.06	HZB	2020	[333]
	$(FA_{0.65}MA_{0.2}Cs_{0.15})Pb(I_{0.8}Br_{0.2})_3$	1.68	ITO	26.2	1.00	KAIST	2020	[334]
	$FA_{0.75}Cs_{0.25}Pb(I_{0.8}Br_{0.2})_3$	1.67	ITO	27.1	1.00	CU-Boulder	2020	[335]
	$(Cs_{0.06}FA_{0.78}MA_{0.16})Pb(Br_{0.17}I_{0.83})_3$	1.64	ITO	26.3	1.43	C.H.O.S.E	2020	[336]
	$MAPb(I_{0.75}Br_{0.25})_3$	1.68	ITO	23.8	1.00	KSC	2020	[325]
	$Cs_{0.05}FA_{0.73}MA_{0.27}PbI_{0.77}Br_{0.23}$	1.68	ITO	29.8	1.016	HZB	2021	[337]
	$Cs_{0.18}FA_{0.82}Pb(I,Br)_3$	1.7	ITO	31.3	1.1677	EPFL/CSEM	2022	[338]
	$Cs_{0.22}FA_{0.78}PbI_{2.55}Br_{0.45}$	1.68	ITO	32.5	1.014	HZB	2023	[339]
	-	-	ITO	33.2	0.9977	KAUST	2023	[340]
	-	-	-	34.6	-	LongGi	2024	[88]
	$Cs_{0.05}FA_{0.8}MA_{0.15}Pb(I_{2.265}Br_{0.765}$	1.68	IZO	33.7	1.00	KAUST	2024	[341]
	$Cs_xFA_{1-x}PbI_yBr_{3-y}$	1.67	ITO	31.5	1.015	NCU	2024	[342]
	$Cs_{0.22}FA_{0.63}MA_{0.37}PbI_{2.49}Br_{0.42}Cl_{0.09}$	1.68	ITO	29.7	1.055	KAUST	2024	[343]

PCE of 25.2% with an active area of 1.419 cm^2 [144]. Following a similar approach, PCE of 18.0% and 25.1% were obtained with areas of 12.96 cm^2 and 1.42 cm^2, respectively [329]. The use of nc-Si:H as the recombination layer for large area monolithic tandem devices has been mainly reported by EPFL until now. Another unique structure was reported by Zheng *et al.* [319]: the tandem device shows a recombination contact between SnO_2 and a p-doped region, as illustrated in Figure 2.6. Compared with the common structure with an interfacial layer, SnO_2 serves not only as an ETL for the top cell, but also a recombination contact. As a result, PCEs of 17.6% (area 16.00 cm^2) and 21% (area 4.00 cm^2) were achieved [319].

Optical design

Optical design is an efficient approach to further improve the device's short current density (J_{sc}) and to achieve current matching. Currently, optical design for PVK-based tandem devices deals with three aspects: light trapping, reflection losses, and parasitic absorption [345]. Regarding light trapping, a rear-side textured bottom cell can effectively improve light trapping and increase its near-infrared spectral response [346]. In addition, textured structures can also be applied for light management at the front side of tandem devices [318, 330, 347]. As an example, Jošt *et al.* [348] employed a textured foil on the planar front-side of a tandem solar cell, significantly improving J_{sc} from 17.3 mA/cm^2 to 18.5 mA/cm^2. As for the reduction of reflection losses, introducing an optical interlayer between the sub-cells can significantly decrease the reflection losses resulting from large differences in optical refractive index of Si and PVK. Mazzarella *et al.* [349] employed hydrogenated nanocrystalline silicon oxide (nc-SiOx: H) with optimized refractive index and thickness as an optical interlayer of a tandem device resulting in 1.4 mA/cm^2 current gain with a device area of 1 cm^2. Besides, nc-Si: H replacing ITO as a recombination layer improves the optical properties of monolithic tandem device [329], shown in Figure 2.6. Based on comparison with ITO, the nc-Si: H recombination junction was demonstrated to mitigate reflection at the sub-cell interface and increase the light transmittance to the bottom cell, consequently, the bottom cell photocurrent increased by more than 1 mA/cm^2 [329]. In addition, thinner front ITO can also improve light-harvesting due to a lower parasitic absorption as well as reflection. Focusing on decreasing parasitic absorption, spectrum down-conversion materials can convert high energetic photons into visible light, which can be used to avoid the parasitic absorption of CTLs for tandem devices. Zheng *et al.* [328] employed $(Ba, Sr)_2SiO_4Eu_2^+$ phosphor at the front of the monolithic tandem cells to realize PCE as high as 23.1% for an area of 4 cm^2. It should be noted that J_{sc} has been dramatically improved from 14.1 mA/cm^2 to 16.5 mA/cm^2. Besides, a thinner transparent electrode and inorganic HTL can effectively decrease the parasitic absorption and further improve the device J_{sc}. Current progress in terms of parameters and properties of PVK-based large area 2T tandem devices are summarized in Table 2.4.

2.4.2. Stability of large area PVK-based monolithic tandem devices

Currently, there are some works based on the stability of large-area monolithic tandem devices. The stability of PVK-based monolithic tandem devices is mainly determined by the PVK sub-cell. c-Si is stable enough to operate consistently for many years in ambi-

Table 2.5: Summary of stability for large area PVK-based 2T tandem devices sorted per device area from the smallest to the largest.

Structure	PCE (%)	Area (cm^2)	Stability	Ref
$CsFAPbI_{3-x}Br_x$ PVK/SHJ Si	23.6	1.00	80% for 1000 h, 85% RH, 85 °C	[317]
$FA_{0.75}Cs_{0.25}Pb(I_{0.8}Br_{0.2})_3$ PVK/SHJ Si	27.1	1.00	96% for 1000 h, MPP operation, 60 °C	[335]
$Cs_{0.05}(MA_{0.17}FA_{0.83})_{0.95}Pb(I_{0.83}Br_{0.17})_3$ PVK/CIGS	23.3	1.03	97% for 11 h, MPP operation, 40 °C	[350]
$CsFAPbI_{3-x}Br_x$ PVK/SHJ Si	25.2	1.42	90% for 270 h, MPP operation	[144]
$FAMAPbI_{3-x}Br_x$ PVK/homojunction Si	23.1	4.00	90% for 288 h, UV exposure	[328]
$(FAPbI_3)_{0.83}(MAPbBr_3)_{0.17}$ PVK/homojunction Si	21.8	16.00	91% for 31 days, N_2, room temperature	[351]

ent conditions. Therefore, the research based on large-area tandem device stability is mainly focused on the top-cell stability improvement. According to recent studies, pinholes are among the factors responsible for device instability. The existence of pinholes leads to film instability because of a decrease in carrier lifetime and mobility [334]. To solve this problem, Bush *et al.* [317] applied a bilayer SnO_2/ZTO by ALD or pulsed-CVD deposition to prevent the formation of pinholes. The double-layer enables the device to withstand a 1000 hour damp heat test at 85 °C and 85% relative humidity. Another factor is the reaction between the electrode (Ag) and halogens in PVK. Reducing the reaction between PVK and the Ag electrode can also improve the device stability [335]. Sahli *et al.* [144] pointed out that buffer layers, as well as a transparent conductive electrode, can efficiently prevent ion migration and suppress the reaction of PVK with the Ag electrode. Besides, a stable carbon or gold electrode can largely improve the device's stability. A third factor impacting stability is moisture/light/temperature-induced environmental degradation. Inorganic materials can be applied to improve thermal stability, such as Cs^+ for PVK [317] and NiO_x for the HTL. As for water, dense buffer layers or transparent polymer layers are introduced to realize a moisture barrier [144, 328]. In addition, spectrum down-conversion materials are employed to transfer high-energy photons into low energy photons, realizing a device UV stability [328]. Table 2.5 summarizes the large area device stabilities in detail. Compared to c-Si solar cells, the stability of PVK-based large area 2T tandem solar cells still needs to be improved further.

2.5. Conclusion and outlook

In this chapter, the developments and challenges for PSCs from lab-to-fab are systematically discussed focusing on different relevant aspects. In the past years, key material processing, scalable device fabrication, and PSC properties have been investigated in depth. However, compared with other well-established PV technologies, both the efficiency and stability of PSCs show a large gap between small-area cells and large-area modules. To achieve the goals of PSCs upscaling and further industrialization, many issues need to be addressed, including not only the efficiency, but also stability, costs, reproducibility, and fabrication techniques. At present, the main challenges involving PSCs commercialization are: (1) long term stability. Modules should ensure durable outdoor operation under operative conditions such as long-term illumination and heat; (2) cost issues. More efforts should be devoted to identify alternative low-cost raw materials for each layer composing the cell, as well as simplifying the device process; (3) further applications.

Broad the PSCs application market, for example, tandem device, flexible device, and indoor PV technology. Finally, we are still at the early stage of the PSCs industrialization. In the long term, can PVK realistically become a competitive candidate in the PV market to uptake silicon technology? How the research community will be able to come up with new ideas and solutions aiming at addressing the key challenges/problems we discussed in this review, will indicate the future paths, and define the success of the emerging PVK technology.

3

Crystallization process for high-quality CsFAPbIBr film deposited *via* simplified sequential vacuum evaporation

This chapter was published in ACS Applied Energy Materials*

Abstract

Multiple-source thermal evaporation is emerging as an excellent technique to obtain perovskite (PVK) materials for solar cell applications due to its solvent-free processing, accurate control of stoichiometric ratio, and potential for scalability. Nevertheless, the currently reported layer-by-layer deposition approach is afflicted by long processing times caused by the multiple repetitions of thin films, which hinder industrial uptake. On the other hand, the co-evaporation entails higher complexity due to the challenges of controlling the sublimation of multiple sources simultaneously. In this work, we propose a simplified approach consisting of a single-cycle deposition (SCD) of three thick precursor layers to obtain high-quality $Cs_{0.15}FA_{0.85}PbI_{2.85}Br_{0.15}$(CsFAPbIBr) films. After annealing, the optimized PVK film exhibits comparable properties to the one deposited by multicycle deposition in terms of crystal structure, in-depth uniformity, and opto-electrical properties. Also, the formation and evolution of SCD PVK during annealing are investigated. We found that, in the competitive processes of precursor diffusion and reaction, the presence of cesium bromide can assist precursor mixing driven by the

*This chapter is based on the following publication: **J. Yan**, J. Zhao, H. Wang, M. Kerklaan, L. J. Bannenberg, B. Ibrahim, T. J. Savenije,* L. Mazzarella,* and O. Isabella, *Crystallization Process for High-Quality $Cs_{0.15}FA_{0.85}PbI_{2.85}Br_{0.15}$ Film Deposited via Simplified Sequential Vacuum Evaporation*, ACS Appl. Energy Mater. 2023, 6, 20, 10265-10273

annealing treatment, demonstrating a reaction-limited process in the PVK conversion. With this simplified SCD approach, a PVK film is obtained with expected optical and opto-electronic properties, providing an appealing way for future thermally evaporated PSCs preparation.

3.1. Introduction

As a new absorber material for next-generation solar cells, metal halide PVKs have attracted intensive attention due to their high absorption coefficients [352], long carrier diffusion lengths [353], and apparent defect tolerance [354]. The rapid developments in material optimization and fabrication techniques have led to an unprecedented fast increase of the PCE of PVK solar cells (PSCs) exceeding 25% within a decade [355]. One of the key advancements in device PCE originates from the development of mixed-cation and mixed-halide PVKs, which improve the crystal structure and phase stability [356]. Nevertheless, some well-developed solution-based methods are still limited with respect to scalability because of low reproducibility and the use of hazardous solvents [300]. Vacuum deposition methods are possibly more attractive for device upscaling considering that they are widely employed in the semiconductor and silicon PV industries. Moreover, thermal evaporation is compatible with textured substrates [300]. Nevertheless, challenges still exist for high-quality PVK film preparation based on co-evaporation, such as the realization of a stoichiometric composition [357] and achieving stable deposition rates for the methylammonium halide (MAX) precursors [358], especially for multi-source co-evaporation. It has been shown that deposition of MAX and formamidinium halide (FAX) can lead to chamber pressure fluctuations during evaporation, affecting the deposition rate of other precursors and eventually the quality of the final PVK material. Li *et al.* [359] recently reported that the ratio of PbI_2 to methylammonium iodide (MAI) progressively increases with deposition time during co-evaporation, resulting in a gradually changing composition as the PVK film grows. Instead of simultaneously controlling the rates of two or even more precursors during deposition, sequential deposition is less complex and allows for better stoichiometric control. Feng *et al.* [148] used sequential deposition for the preparation of PVK films, and the resulting devices reached a PCE of 21.32% (0.1 cm^2). However, regarding thermally evaporated mixed-cation, mixed-halide PVK thin films, most of the reports are based on co-evaporation [147, 360], while only a few sequential deposition studies based on three or more precursors have been reported [148]. In using sequential thermal evaporation, individual layers of the precursors are deposited. This can be done in a multicycle approach yielding an array of precursor layers or in a single-cycle approach yielding thick films of each individual precursor (see Figure 3.1a). Although the latter is a straightforward and cost-effective method, in particular, the nonuniform elemental distribution across the film might lead to local non-stoichiometry [359]. A post-annealing treatment is yet expected to enhance the inter-diffusion and improve the element distribution. However, as mentioned above, little information regarding this method of deposition is available. Therefore, it is meaningful to investigate the opto-electronic properties of PVK films prepared from precursors varying in thickness, during and after the post-deposition annealing.

The mixed-cation, mixed-halide PVK $Cs_xFA_{1-x}PbI_{3-x}Br_x$ exhibits good thermal and phase stability [361]. In this work, we propose to use the single-cycle deposition (SCD)

procedure to prepare high-quality and uniform CsFAPbIBr PVK films. The impact of PVK thickness as well as annealing is systematically investigated in terms of crystallinity, in-depth uniformity, and opto-electronic properties. Also, the conversion from precursors to PVK during post-deposition annealing is also studied in detail with grazing incidence X-ray diffraction (GI-XRD). We find that, by applying an optimized annealing treatment, CsFAPbIBr deposited with SCD shows comparable opto-electronic properties to the one deposited by multicycle deposition (MCD) when the PVK thickness reach even 250 nm. Moreover, we found that cesium bromide (CsBr) accelerates the interdiffusion of formamidinium iodide (FAI) over the different layers, supporting the crystallization of PVK. With this straightforward approach, the 250 nm SCD PVK film's half-intensity lifetime ($\tau_{1/2}$) reaches around 650 ns with carrier mobility close to 10 cm^2 V^{-1} s^{-1}. This work demonstrates that precursors can be deposited by SCD and that relatively thick precursor layers can still react to fully convert into PVK through the film. The understanding of the influence of the post-deposition annealing treatment on the precursor diffusion and on the reaction mechanism provides directions for further improving the thermally evaporated PVK deposition.

3.2. Experimental details

3.2.1. Material and film preparation

$CH(NH_2)_2I$ (FAI) (99.9%),CsBr, and PbI_2 (99.999%) were purchased from Sigma-Aldrich and used as received. Quartz and Corning glass substrates were cleaned according to a standard procedure consisting of acetone, ethanol, and an ozone treatment for 5 min. After cleaning, the substrates were directly transferred into a N_2-filled glovebox and loaded into the deposition chamber (AJA). The chamber was evacuated reaching a base pressure of 5×10^{-6} mbar before the sources were heated. During film preparation, precursors were sequentially deposited forming one stack. The deposition order was PbI_2, FAI, and CsBr for $Cs_xFA_{1-x}PbI_{3-x}Br_x$, while it was PbI_2, FAI for $FAPbI_3$. The target thickness was obtained by repeating the stack number (N), where N = 20 for MCD and N = 1 for SCD. The PbI_2 was evaporated at the temperature of about 240 °C, and the corresponding deposition rate was stabilized at 0.4-0.5 Å/s. FAI was evaporated on top of the as-deposited PbI_2 film, and the evaporation rate of FAI reached 0.3-0.4 Å/s with the crucible temperature of around 100 °C. As for CsBr, the source was evaporated with a rate of 0.08-0.10 Å/s at around 380 °C. Evaporation rates and film thicknesses were monitored by one quartz crystal microbalance. Taking into consideration different tooling factors, the target PVK film thicknesses were set to reach 100, 250, and 400 nm by adapting the N or thickness of each precursor layer in one stack (shown in Table A.1). The detailed processing information (such as evaporating temperature, chamber pressure, and deposition rates) is shown in Table A.2. The as-deposited PVKs were then annealed under 100 °C for 30 min in the glovebox before characterization.

3.2.2. Characterization

XRD patterns were measured with a Bruker D8 Advance diffractometer equipped with a Cu–Kα X-ray source that has a wavelength of 1.54 Å. Grazing incident XRD (GIXRD, Bruker D8 Discover, Cu Kα) was performed with incident angles of 0.25°, 0.5°, 1°, 3°, and

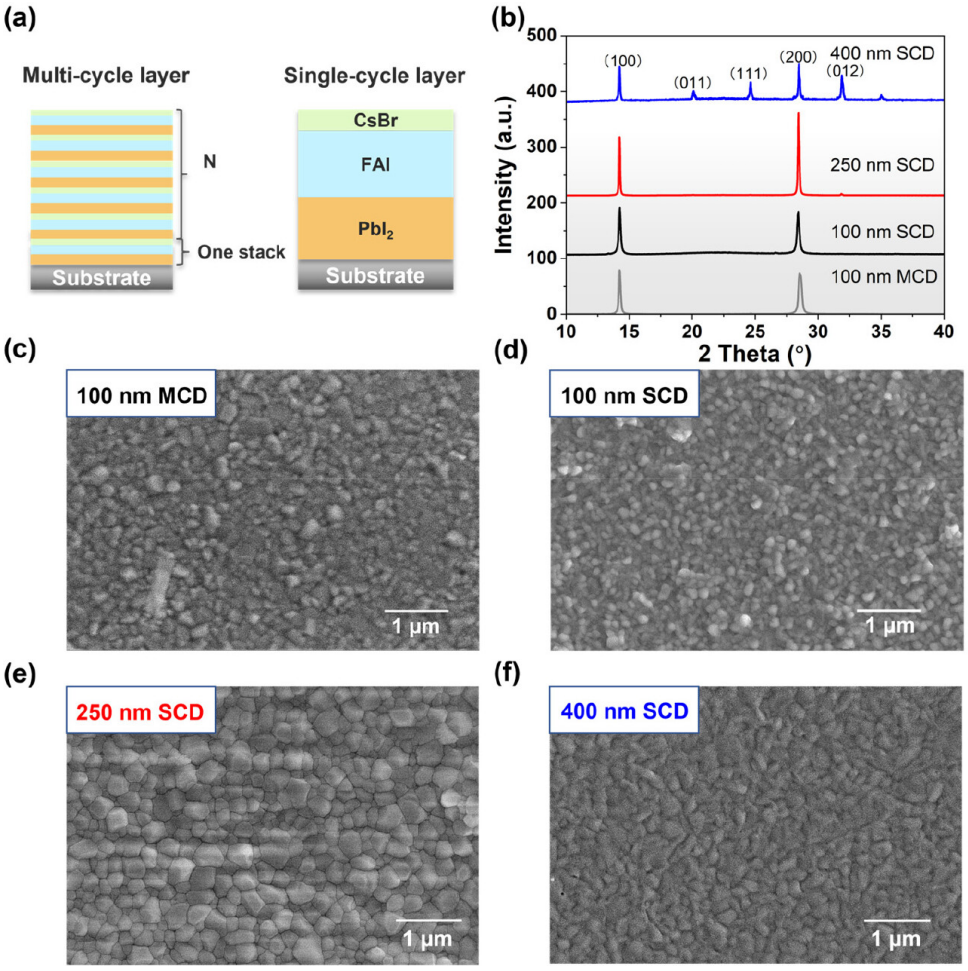

Figure 3.1: (a) Schematic illustration of the preparation procedure of PVK films by MCD and SCD; (b) XRD patterns of the MCD precursor film (gray) and SCD film; (c-f) Top-view SEM images of samples reported in panel; (b) with different thicknesses. All the films are annealed at 100 °C for 30 min.

5°to vary the information depth. The measurements were carried out in vacuum at 10^{-4} mbar inside an Anton Paar XRK900 Reactor Chamber equipped with Be windows. On the primary side, a Goebel mirror was used together with a fixed slit of 0.1, 0.1, 0.2, 0.6, and 1.0 mm, respectively, for the incident angles to control the footprint on the film. On the secondary side, a Soller 2.5°slit was used, and the LYNXEYE XE detector was operated in 0D high-resolution mode. The elemental composition of the PVK films was analyzed by X-ray photoelectron spectroscopy using a ThermoScientific K-Alpha spectrometer. The spectrometer is equipped with a focused monochromatic AlKα X-ray source (1486.6 eV) operating at 36 W (12 kV, 3 mA). The spot-size is approximately 800 × 400 μm^2. The pass energy of the analyzer was set to 50 eV. A flood gun was operated at 1 V, 100 μA to prevent charging of the sample. The base pressure in the analysis chamber was approximately 2 × 10^{-9} mbar. Depth profiling was performed by etching the sample with argon ions. The voltage of the ion gun was set to 1000 eV for in-depth etching for both 100 and 250 nm-thick samples, while a higher voltage of 2000 eV was applied to the 400 nm-thick sample, due to protection of the XPS machine with shortened etching time. Detailed analysis was performed with the Avantage software. Atomic percentages were calculated based on the fitted peak areas and the corresponding sensitivity factors of the detailed scans. The binding energy was corrected for the charge shift by taking the done relative to the primary C 1s hydrocarbon peak at BE = 284.8 eV as a reference. The surface morphology of the PVK films were measured by the scanning electron microscope (SEM, JEOL) under an accelerating voltage of 8 keV. The absorptance spectra of samples were measured by ultraviolet–visible spectroscopy (UV/vis, PerkinElmer, Lambda 1050) within a wavelength range of 300-800 nm. The photoluminescence spectra of the samples were investigated by the steady-state photoluminescence setup (PL, FLS 980) with an excitation wavelength of 420 nm, while the emission light was filtered by a 550 nm filter. The time-resolved photoluminescence was measured with the setup (Lifespec) with an excitation wavelength of 405 nm. The detailed measurement was described in ref. [362]. Time-resolved microwave conductance (TRMC) was applied to learn about the carrier lifetime, mobility, and trap densities. All the measurement parameters can be found in ref. [363].

3.3. Results and discussion

Figure 3.1a shows the schematic cross sections of the PVK film preparation process based on MCD and SCD thermal evaporation to produce CsFAPbIBr.

3.3.1. Thickness effects on SCD layers

To learn about the thickness-related PVK film properties, we measured crystal structure, in-depth uniformity, and opto-electronic properties of samples with different target thicknesses (100, 250, and 400 nm). Figure 3.1b shows the XRD patterns of the 100 nm-thick CsFAPbIBr reference layer obtained with MCD and three CsFAPbIBr films obtained using SCD with thicknesses from 100 to 400 nm. For the MCD layer, we observe the presence of two main peaks at 2θ = 14.08 °and 2θ = 28.32 °corresponding to the (100) and (200) planes of the PVK. As no other intense reflections are present, this indicates a preferable crystal growth [229]. Both the 100 and 250 nm-thick SCD films share a similar

pattern with the reference film, and the detailed peak information is provided in Table A.1. The presence of two main peaks in both the 100 and 250 nm-thick SCD PVK films highlight the preferential orientation of the grains [360]. Interestingly, this kind of orientation disappears as the thickness increases to 400 nm for the SCD sample [364]. When we focus on the (100) peak of the samples with different thicknesses (Figure A.1 and Table A.1), we notice no shift in peak position, which is consistent with a constant I/Br ratio across the film thickness [365]. To investigate the film morphology as a function of the thicknesses and deposition process, we report SEM top-view images in Figure 3.1c-f. Looking at the two 100 nm-thick samples, the SCD layer shows an average grain size of around 100 nm, which is slightly smaller than the reference MCD layer, which is around 130 nm. The corresponding grain size statistics are shown in Figure A.2. The decreased grain size for the SCD film could be attributed to the increased number of nucleation sites during deposition [366]. Note that in the single-cycle approach, PbI_2 forms the substrate on which the FAI layer is deposited, as shown in Figure 3.1a. Differently, the mixed precursor/PVK already formed in MCD, which is shown as the template layer for the subsequent stack.

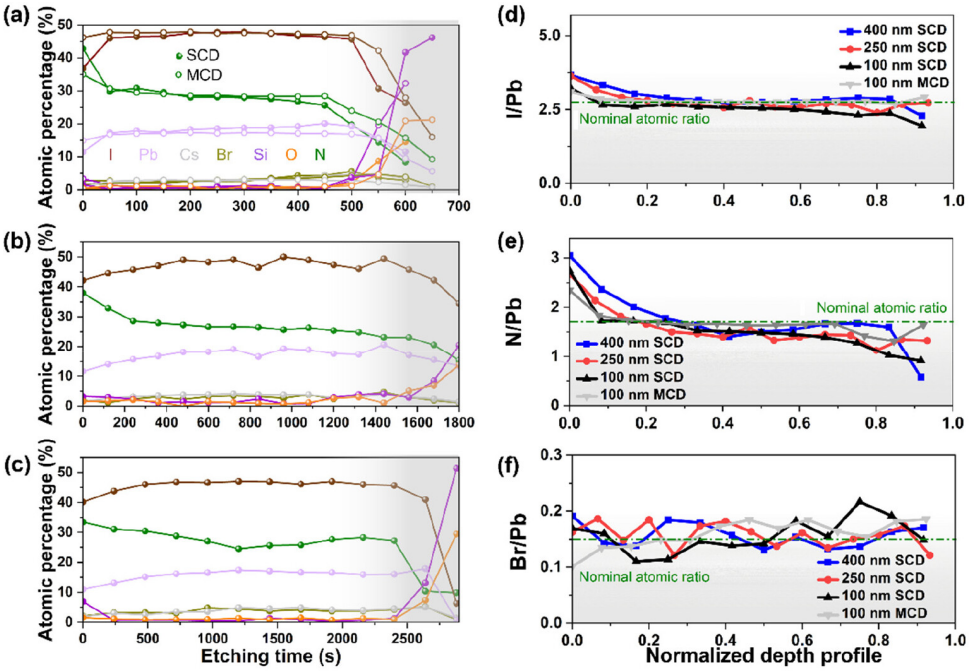

Figure 3.2: XPS depth atomic percentage profile of PVK films with different thicknesses: (a) 100 nm MCD layer (open symbols) and SCD samples (full symbols); (b) 250 nm SCD sample; (c) 400 nm SCD sample; (d-f) Corresponding XPS depth atomic ratios of PVK films with different thicknesses for (d) I/Pb, (e) N/Pb, and (f) Br/Pb. The green dashed line indicates the nominal ratio.

Furthermore, we observed in Figures 3.1c-f (and Figure A.2) that the grain size gradually increases as the film thickness increases from 100 to 250 nm, while the grain shapes show a small change. The increased grain size mainly comes from improved crystallinity

[367]. Differently, the grain shape is observed elongated in the horizontal direction for the 400 nm-thick sample, which originates from the changing of crystal orientation growth, resulting from the degree of precursor reaction [368]. Furthermore, we studied the role of annealing time on the crystal growth by looking at the evolution of film's microstructure for various annealing times (30 s, 1 min, and 30 min) by SEM inspection as shown in Figure A.6. For the 250 nm-thick sample, there is no apparent grain shape change, while the grain size shows a slight increase from a 30 s to 30 min annealing time, in agreement with the XRD results in Figure A.3a calculated from Scherrer equation [369]. Differently, the 400 nm-thick sample shows an apparent grain shape change from 30 s to 1 min, which comes from the formation of non-orientation-preferred PVK polycrystalline.

To examine the chemical composition across the film, we measured samples with different thicknesses by XPS after specific periods of etching as shown in Figure 3.2. The atomic percentages and element ratios through the film are plotted as a function of the etching time. The XPS high-resolution spectra of Pb $4f_{7/2}$, C 1s, N 1s, Cs $3d_{5/2}$, I $3d_{5/2}$, and Br 3d can be found in Figure A.7 for the 100 nm-thick SCD sample as an example to show the fitting and extraction of raw data. The averaged atomic percentage of different elements for all samples extracted from Figure 3.2 are summarized in Table A.2. In Figure 3.2a, we note that both MCD and SCD layers with a thickness of 100 nm show similar atomic percentage trends for N, Cs, Br, Pb, and I, indicating comparable element depth-dependent uniformity irrespective of the preparation procedure used. With increased film thickness, we observe an almost stable composition along the film for the 250 nm-thick sample (Figure 3.2b), while the 400 nm-thick one exhibits atomic percentage variation, as shown in Figure 3.2c. In particular, the N (Pb) atomic percentage shows a clear drop (increase) for etching times longer than 1200 s. This phenomenon may suggest that for the thicker layer, FAI is unable to uniformly diffuse under 100 °C and a 30 min annealing due to the thicker layer. Therefore, a longer annealing time is applied to the film, and the corresponding XRD patterns are shown in Figure A.4. Clearly, the samples with 45 and 60 min of annealing indicate the appearance of the PbI_2 peak compared with the ones with shorter annealing times, showing partcially sample thermal degradation. Thus, the SCD 400 nm-thick PVK film exhibits a problem with the balance between FAI uniform distribution and thermal degradation during annealing optimization. To compare the in-depth precursor ratios, we report in Figure 3.2d-f, the calculated atomic ratios I/Pb, N/Pb, and Br/Pb as a function of the normalized in-depth profile. The N/Pb gives an indication of the FAI distribution along the film thickness, and the Br/Pb ratio is related to the bandgap variation. The nominal atomic ratio for I/Pb (N/Pb, Br/Pb) is equal to 2.85 (1.7 and 0.15) in the CsFAPbIBr PVK structure, and it is shown as dashed lines in Figure 3.2d-f. The I/Pb ratio shows similar trends for 100 nm SCD samples compared with the 100 nm-thick MCD sample, while the 400 nm-thick SCD sample exhibits a high I/Pb ratio and slow I/Pb drop at the top of the film compared with the ratio of the 100 nm-thick samples (Figure 3.2d). Similarly, an initial high FA is observed for a 400 nm-thick SCD sample in Figure 3.2e, which further indicates a nonuniform distribution of FAI. Different trends are found for Br/Pb in Figure 3.2f, proving different diffusion lengths of FAI and CsBr precursors in PbI_2, which can be explained as the FAI molecular size being larger compared with CsBr [370].

As annealing drives molecular diffusion, we characterized the 400 nm-thick samples by XPS before annealing to evaluate the impact of the annealing treatment on the elemental distribution (Figure A.8). In the as-deposited 400 nm-thick sample, we observed noticeable distribution variations with a gradual drop of the N/Pb (from 2 to 0.2) calculated by the atomic profile as etching goes from the PVK surface toward the PVK/quartz interface. In addition, the I/Pb ratio at the bottom of the film is equal to 2, showing that FAI can hardly penetrate through the bottom of the film. These results indicate the hampering of the FAI diffusion into the PbI_2 during deposition (without annealing). On the contrary, both Br and Cs are detected across the entire PVK film thickness even though the Br/Pb ratio gradually decreases when approaching the PVK/quartz interface. This finding further confirms the longer diffusion length of CsBr in PbI_2 compared to FAI.

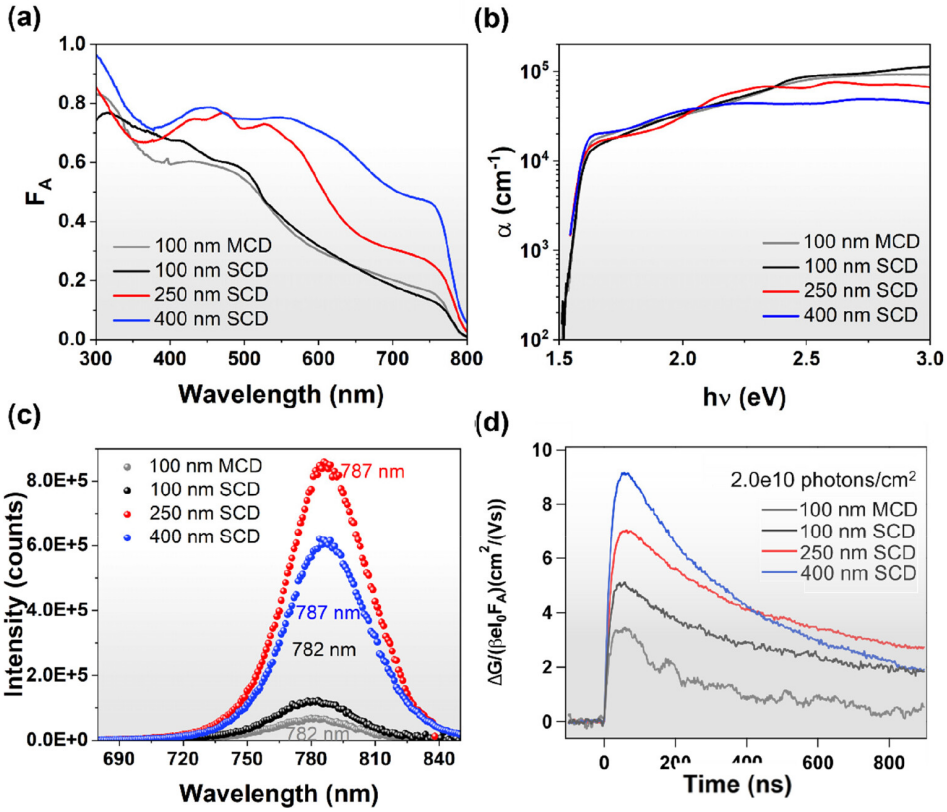

Figure 3.3: Optical and opto-electronic properties of 100 nm MCD and SCD layers with different thicknesses. (a) Fraction of light absorbed (F_A); (b) semilogarithmic plot of the absorption coefficients; (c) steady-state PL, and (d) TRMC measurement with photon intensity of $2e^{10}$ cm^2 per pulse.

In addition to the crystal structure, morphology, and uniformity, we carried out more investigations to probe the opto-electrical properties of CsFAPbIBr films fabricated *via* SCD. Figure 3.3a and 3.3b show different optical properties with varying film thicknesses. Specifically, the spectra in Figure 3.3a of the PVKs show improved absorptance at the

long wavelength range due to increased thickness. The absorption coefficients (α) are compared in Figure 3.3b. The absorption coefficient of 100 nm-thick SCD samples overlaps well with the one of the 100 nm-thick MCD sample. All the films show an α at the level of 10^4 cm^{-1}. Also, all these samples present a sharp absorption edge corresponding to a bandgap of 1.58 eV as determined by the Tauc plot of Figure A.9a. These values are in agreement with published work on PVKs having a similar composition [170]. To investigate the thickness-related film opto-electrical properties, carrier lifetime, mobility, and trap densities are determined by applying steady-state PL, TRPL, and TRMC. Figure 3.3c reports the steady-state PL spectra of all samples. The spectra are symmetric and can be well-fitted by a single Gaussian peak. In addition, the peak positions show a slight red shift from 782 nm (1.58 eV) to 787 nm (1.57 eV) as the film thickness increases. This kind of peak shift is related to the variation of precursor composition, as indicated by the increased d-value in Table A.3. The dynamics of the charge carrier recombination are analyzed by TRPL as shown in Figure A.9b. Interestingly, the 250 nm-thick sample shows an even longer lifetime compared to the 400 nm-thick sample, benefiting from its better crystal orientation [371].

In contrast to TRPL, TRMC gives information regarding the free charge carrier mobility and lifetime (Figure 3.3d). In view of the low exciton binding energy of CsFA-based PVK, we can assume that the free charge carrier generation yield, is close to unity at room temperature. Therefore, we conclude that the sum of the effective electron and hole mobilities, $\sum\mu$, increases from 5 to 9 cm^2 V^{-1} s^{-1} with increasing the film thickness. This improvement can be explained by the increased crystal size, verified by the SEM results in Figure 3.1c-f [372]. Nevertheless, the lifetime of 400 nm-thick film is shorter than the 250 nm one, which is in accordance with the TRPL. One reason is that the orientation growth of 250 nm film can suppress trap recombination. Compared to the TRPL results, TRMC verified that the 400 nm-thick PVK film needs further annealing treatment to improve the crystallization. Moreover, the TRMC with various incident light intensities is shown in Figure A.10 based on samples with different thicknesses. It should be noted that both the 250 and 400 nm-thick samples exhibit comparable carrier mobility and lifetime to other published works, which are based on thermal co-evaporation methods [359, 373]; the detailed data are summarized in Table A.4. Therefore, we conclude that the variation of thickness in SCD affects the film opto-electronic properties performance because of the precursor diffusion, reaction (Figure 3.2), and crystal growth (Figure 3.1).

3.3.2. Crystallization of the single-cycle thermally evaporated PVK during annealing

The results discussed above indicate that the SCD process can reach comparable film properties with MCD for 100 nm-thick film, and it can be expanded to thicker layers up to 250 nm. However, the precursor diffusion and reaction process during annealing is still not fully understood. Therefore, it is meaningful to study the conversion of PVK during annealing. To this end, 400 nm-thick samples subjected to annealing times ranging from 30 s to 30 min are monitored by GIXRD. By increasing the incident angle stepwise from 0.25 °to 5 °, we increase the information depth of the XRD measurement to obtain depth-dependent structural information regarding the PVK and PbI_2 phases. The GIXRD patterns of a 400 nm-thick CsFAPbIBr film shown in Figure 3.4a-c exhibit five main peaks

at 2θ of 14.2 °, 20.0 °, 24.6 °, 28.4 °, and 31.8 °, which can be assigned to the (100), (011), (111), (200), and (012) planes of cubic PVK [360]. The additional two diffraction peaks at 11.8 °and 12.7 °correspond to the δ-phase PVK and the (100) peak of PbI_2, respectively [374]. Even at only 30 s of annealing at 100 °C, the appearance of the PVK peaks in Figure 3.4a shows that a substantial amount of the precursors has already converted into PVK, although unreacted PbI_2 is still visible, in particular at large incident angles. These results show that the top region has fully converted into PVK, while the bottom part exhibits a mixture of PbI_2 and PVK. With a longer annealing period of 1 min, a weak PbI_2 peak is only observed at large incident angles, indicating the presence of unreacted precursor in the bottom of the PVK layer, as shown in Figure 3.4b. After 30 min of annealing, no PbI_2 peak is detected at any incident angle (Figure 3.4c), showing that PbI_2 has completely converted into PVK.

To further understand the crystallization process as well as the role of CsBr in the conversion during annealing, 400 nm-thick $FAPbI_3$ layers are prepared by SCD. The samples are annealed at 100 °C for 30 s, 1 min, 10 min, 30 min and measured by GIXRD. The $FAPbI_3$ sample annealed for 30 s resulted to be particularly unstable during the sample transfer, which comes from the conversion from $FAPbI_3$ PVK into yellow phase. Thus, this result is not included in Figure 3.4. The $FAPbI_3$ film annealed for 1 min shown in Figure 3.4d exhibits a high relative intensity of PbI_2/PVK (100) at incident angles of both 3 °and 5 °, while no peak is spotted at lower incident angles, indicating relatively large amounts of unreacted PbI_2 at the bottom of film. Furthermore, even after 10 min of annealing, the PbI_2 peak is still visible at 5 °, as shown in Figure 3.4e, indicating there is still some unreacted PbI_2 at the bottom. Only for the longest annealing time of 30 min is no PbI_2 peak detected (Figure 3.4f). From this comparison, we can conclude that the presence of CsBr accelerates the precursor conversion into PVKs. The fact that after 10 min of post-annealing thermal treatment, there is still PbI_2 at the bottom of the $FAPbI_3$ film suggests that, in the absence of CsBr, mixing of the precursors limits the complete PVK conversion. To further classify the CsBr induced difference between CsFAPbIBr and $FAPbI_3$ during annealing, the I_{PbI_2}/I_{PVK} ratios from Figure 3.4a-f are plotted as a function of the incident angle for both CsFAPbIBr and $FAPbI_3$ to visualize the in-depth reaction process as shown in Figure 3.4g. The I_{PbI_2}/I_{PVK} ratios increase going deeper into the film for both PVK materials investigated and all annealing times, but their slopes are very different from each other's. The steep slope change for CsFAPbIBr from 30 s annealing to 1 min annealing in Figure 3.4g visually indicates that the presence of CsBr assists precursor mixing and accelerates PVK conversion during annealing. We note that in general interpreting GIXRD measurements of samples with preferred orientation is difficult and should be taken with the necessary precautions, as both depth-dependence and preferred orientation can cause a variation of the (relative) peak intensity with incident angle. Although the preferential orientation of the PbI_2 phase complicates also here the interpretation, we believe that the consistent trends among the different samples with different annealing times and in particular the different ratios of I_{PbI_2}/I_{PVK} of the different samples strongly indicate that the variations of the PbI_2 peak intensity also reflect a depth-dependence of the PbI_2 concentration. Apart from the PVK crystal formation, the evolution of film opto-electronic properties upon annealing is also analyzed. We measure TRPL on 100, 250, and 400 nm-thick SCD samples with different annealing times

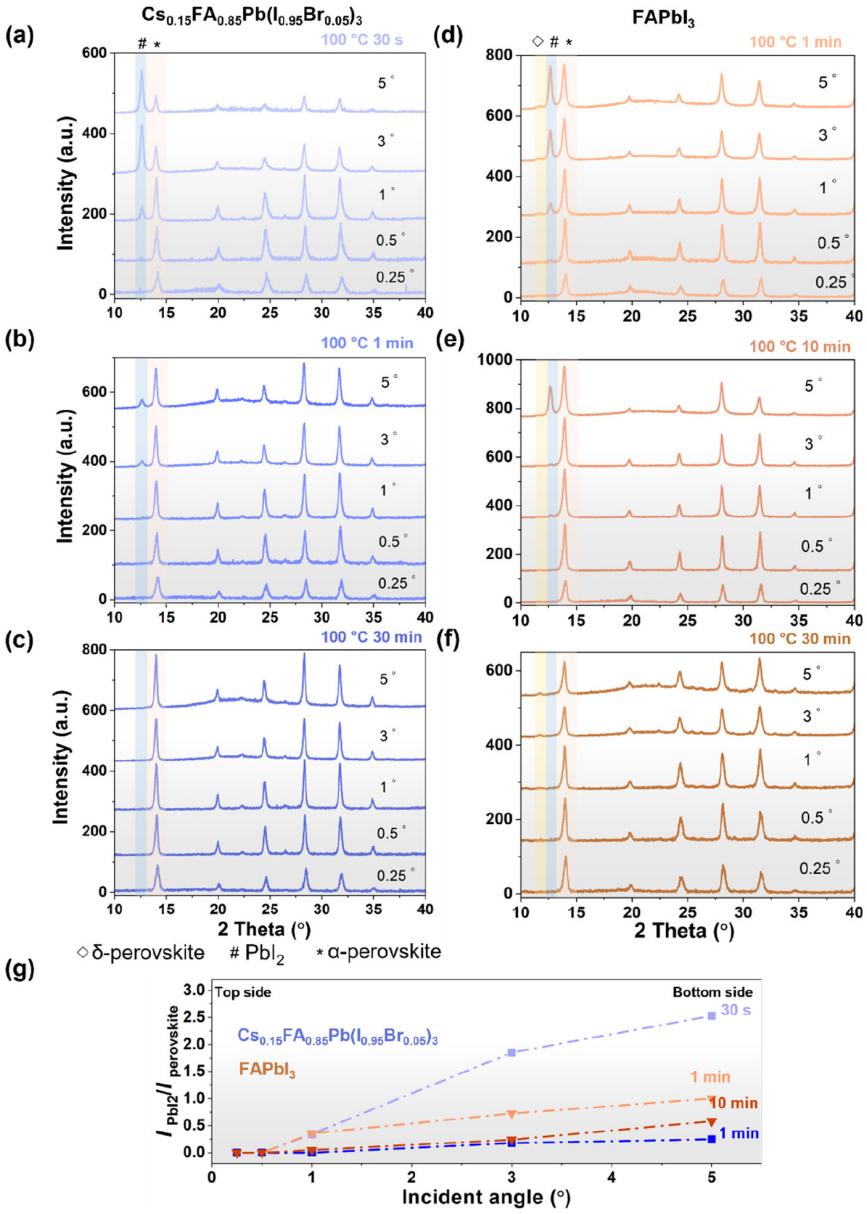

Figure 3.4: (a-c) GIXRD measurements on 400 nm-thick CsFAPbIBr films with different annealing times: (a) 30 s, (b) 1 min, and (c) 30 min. (d-f) GIXRD measurements on 400 nm-thick $FAPbI_3$ with different annealing times: (d) 1 min, (e) 10 min, and (f) 30 min. The δ-phase PVK peak is highlighted in yellow; the PbI_2 (100) peak is highlighted in light blue; and the PVK (100) peak is highlighted in light brown. (g) Dependence of the I_{PbI_2}/I_{PVK} (100) ratio extracted from Figure 3.4(a-f) as a function of incident angle for CsFAPbIBr and $FAPbI_3$ at different annealing times.

(30 s, 1 min, and 30 min), as shown in Figure 3.5a-c. All these samples show annealing time-dependent PL decay, and the lifetime is extended by longer annealing time due to higher crystallinity. For the 100 nm sample, the initial part of the TRPL signal of the 1 min overlays with the one of 30 min annealing. In contrast, for the 400 nm-thick sample, the initial part of the TRPL signal of the 1 min overlays with the 30 s annealed signal. For the 250 nm-thick sample, an intermediate behavior is found.

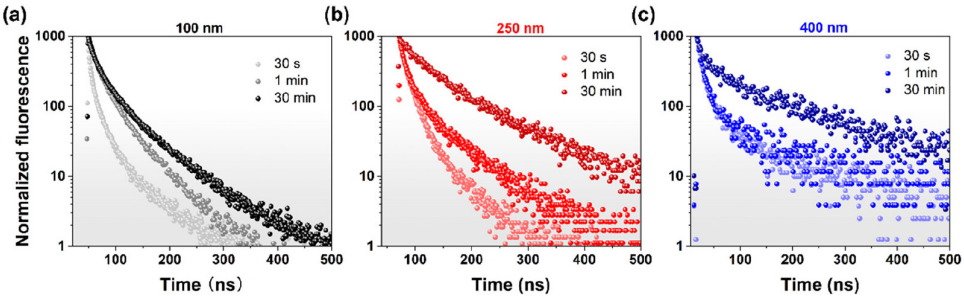

Figure 3.5: Evolution of opto-electrical properties of SCD $Cs_xFA_{1-x}PbI_{3-x}Br_x$ annealed at 100 °C and variable time. (a-c) TRPL of 100, 250, and 400 nm SCD samples annealed at 30 s, 1 min, and 30 min.

From the above, for the 400 nm-thick sample, a 30 min annealing time is required to obtain long TRPL lifetimes, even though from structural (Figure A.4) and optical (Figure A.5) measurements, the PVK conversion seems to be complete even after only 1 min of annealing. In contrast, for the 100 nm-thick sample, 1 min of thermal treatment seems sufficient to reach optimal opto-electronic properties. It indicates that the structural and optical properties are asynchronous with electrical properties during annealing, and this phenomenon is strongly dependent on film thickness. As confirmed by GIXRD, the precursors exhibit a reaction-limited process during annealing. To look further into this process, we measured the opto-electronic properties of the 400 nm-thick CsFAPbIBr with different annealing times in Figures A.11. The PVK conversion can also be examined by measuring the evolution of opto-electronic properties during annealing. The PVK absorption onset starts to form after 30 s of annealing, and a continuous increase of the absorptance was observed from 300 to 800 nm for longer annealing times. In contrast to the 400 nm-thick sample, the 250 nm-thick samples show a similar absorptance for 1 and 30 min annealing (Figure A.3b), especially at longer wavelengths. This implies that the conversion into PVK has already finished, in line with the XRD results shown in Figure A.3a. PL spectra were also recorded as a function of the annealing time by illuminating through the quartz substrate (back) and PVK surface (front) of the 400 nm-thick SCD sample as shown in Figure A.11. The peak shape and position are altered by illuminating from different sides for both 30 s and 1 min annealed samples, suggesting that there are compositional changes through the cross section of the film.

3.3.3. Role of CsBr in PVK conversion in SCD films during post-deposition annealing

Combining the information obtained by GIXRD, XPS, UV-vis, and PL measurements during the annealing of the SCD film, we propose the following mechanism for the forma-

tion of CsFAPbIBr. Three stages take place during the entire process as depicted in Figure 3.6 for both CsFAPbIBr and $FAPbI_3$. In the as-deposited film (stage I in Figure 3.6), FAI and PbI_2 almost keep as individual stacks for $FAPbI_3$ film, while FAI shows concentration driving gradient distribution in PbI_2 film for CsFAPbIBr, as indicated in the XPS profile in Figure A.8. Furthermore, signals of both Cs and Br were detected through the film and even at the bottom of the as-deposited CsFAPbIBr layer (Figure A.8). As annealing time goes on, precursors partially convert into PVKs through the film for both CsFAPbIBr and $FAPbI_3$, as shown in stage II in Figure 3.6. Compared with $FAPbI_3$, the existence of CsBr assists the precursor mixing and leads to the fast formation of CsFAPbIBr, which only takes a few minutes to realize a full conversion of PVK through the film (Figure 3.4). We attribute this difference to the role of CsBr that is already uniformly distributed through the film (Figure A.8). As for stage III at the end of annealing, unreacted precursors are detected at the bottom of the $FAPbI_3$ film, while unreacted PbI_2 exists through the CsFAPbIBr film because of the different precursor mixing levels.

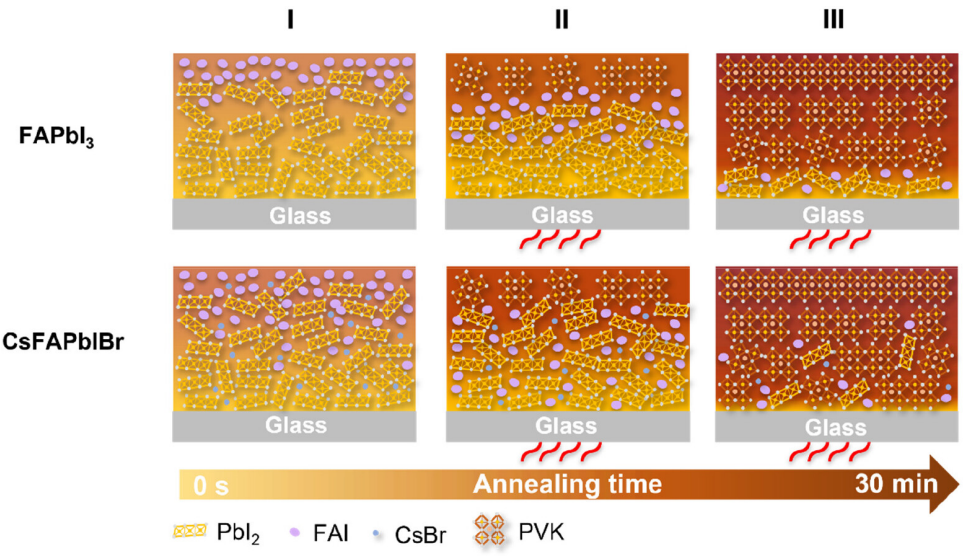

Figure 3.6: Schematic of the PVK conversion process for both CsFAPbIBr and $FAPbI_3$ during annealing.

3.4. Conclusions

We demonstrated a simple sequential evaporation technique to prepare high-quality PVK films based on multisource deposition. By sequentially depositing the precursors into a single stack, highly crystalline $Cs_{0.15}FA_{0.85}PbI_{2.85}Br_{0.15}$ is obtained after optimized annealing treatment. This single-cycle deposition film shows thickness-dependent opto-electronic properties. As the target thickness increases to 400 nm, the film shows a drop in opto-electronic properties even though it structurally shows a PVK diffraction peak with optimized annealing. This phenomenon might be explained by the limited diffusion length of these precursors in single-cycle deposited 400 nm-thick PVK film.

To improve the composition uniformity for thick samples, further strategies could be explored: (1) Change the deposition order; (2) First layer morphology optimization (annealing or atmosphere treatment); (3) Introducing small-sized cations and halides in as-deposited films. We also studied the precursor reaction during postdeposition annealing, the crystal structure, and opto-electronic properties as a function of different annealing times. The structural and optical properties are asynchronous with electrical properties during annealing, which is strongly dependent on film thickness, resulting from precursor mixing and reacting. In addition, the presence of CsBr can assist the precursor mixing during annealing, which is beneficial to the fast precursor reaction and PVK conversion. The strategy used in this work provides an alternative way for uniform and large-scale vacuum deposition for PVK-based photovoltaic technology.

4

Vacuum deposited perovskites with a controllable crystal orientation

This chapter was published in The Journal of Physical Chemistry Letters [*]

Abstract

The preferential orientation of the perovskite (PVK) is typically accomplished by manipulation of the mixed cation/halide composition of the solution used for wet processing. However, for PVKs grown by thermal evaporation, this has been rarely addressed. It is unclear how variation in crystal orientation affects the opto-electronic properties of thermally evaporated films, including the charge carrier mobility, lifetime, and trap densities. In this study, we use different intermediate annealing temperatures T_{inter} between two sequential evaporation cycles to control the $Cs_{0.15}FA_{0.85}PbI_{2.85}Br_{0.15}$ orientation of the final PVK layer. XRD and 2D-XRD measurements reveal that when using no intermediate annealing primarily the (110) orientation is obtained, while when using T_{inter} = 100 °C a nearly isotropic orientation is found. Most interestingly for $T_{inter} \geq 130$ °C a highly oriented PVK (100) is formed. We found that although bulk electronic properties like photoconductivity are independent of the preferential orientation, surface related properties differ substantially. The highly oriented PVK (100) exhibits improved photoluminescence in terms of yield and lifetime. In addition, high spatial resolution mappings of the contact potential difference (CPD) as measured by KPFM for the highly oriented PVK show a more homogeneous surface potential distribution than those of

[*]This chapter is based on the following publication: **J. Yan**, L. Stickel, L. van den Hengel, H. Wang, P. Ravi Anusuyadevi, A. Kooijman, X. Liu, B. Ibrahim, A. Mol, P. Taheri, L. Mazzarella, O. Isabella, T. J. Savenije, *Vacuum Deposited Perovskites with a Controllable Crystal Orientation*, J. Phys. Chem. Lett. 2023, 14, 39, 8787–8795

the non-oriented PVK. These observations suggest that a highly oriented growth of thermally evaporated PVK is preferred to improve the charge extraction at the device level.

4.1. Introduction

Metal halide PVK solar cells have attracted an extensive amount of attention due to the rapid enhancement of the PCE reaching 25% within a decade [375]. The most explored approach to deposit high-quality PVK films is wet chemical processing including spin-coating, which has demonstrated excellent performing devices with relatively small areas of about 0.1-1 cm^2 [300]. Various strategies have been reported to improve the PCE of spin-coated PSCs, including structure design [376], interface modification [377], and composition replacement for each functional layer [37]. Among them, controlling the growth of PVK crystals is critical to obtain high-quality absorber materials that exhibit high absorption coefficients, high charge carrier mobilities, and long lifetimes [36, 378]. To date, several main techniques are commonly applied to control the PVK growth, such as additive engineering [379], solvent engineering [43], and gradient annealing [380]. The main goal of these approaches is to slow down solvent evaporation to enhance the crystal grain size [216]. Moreover, various groups have reported highly selective growth using template modulated PVK growth [381, 382], or composition engineering, such as MA/FA mixed cations in precursor solution in ref. [383]. In these works, preferential crystal growth has been claimed to suppress nonradiative recombination and to improve the free carrier lifetime in spin-coated PVK layers [383, 384]. Therefore, manipulation of the PVK preferential crystal orientation is an interesting and effective method to improve the PCE of PSCs [385, 386].

Unlike spin coating, thermal evaporation of PVKs does not require the use of harmful solvents and is compatible with textured substrates [387]. Besides, it has very good potential toward upscaling due to the exact precursor control [388] and uniform deposition [389]. Recently, Li *et al.* [145] prepared minimodules based on thermally evaporated PVKs, with a champion PCE above 18% with an active area of 22 cm^2. However, manipulating the preferential orientation of the PVK crystal growth in layers prepared by thermal evaporation has hardly been addressed [390, 391]. To date, only two papers have been reported on the control of the preferential growth of thermally evaporated PVKs. Abzieher *et al.* [364] investigated the effects of substrate material on the orientation of methylammonium lead iodide ($MAPbI_3$) crystals and identified few organic hole transport materials as ideal candidates for the fabrication of efficient fully evaporated PSCs [364]. Similarly, Klipfel *et al.* [392] highlighted the importance of the underlying material selection. Furthermore, both studies stressed that the deposition rate of co-evaporated lead(II) iodide (PbI_2) and methylammonium iodide (MAI) can achieve fine-tuning of preferred crystal orientation [392]. However, these studies mainly focused on the influence of substrate material on $MAPbI_3$ orientation growth and discussed opto-electrical properties at the device level. A systematic study of the influence of the preferential orientation on charge carrier mobility, lifetime, and trap densities is lacking [393]. Besides, no strategies to manipulate the crystal orientation of thermally evaporated $Cs_xFA_{1-x}PbI_{3-y}Br_y$ have been reported. Therefore, it is important to manipulate the crystal orientation of thermally evaporated $Cs_xFA_{1-x}PbI_{3-y}Br_y$ and investigate the effects of the crystal orientation on its opto-electronic properties.

In this work, PVK films are fabricated using sequential deposition comprising two cycles, each consisting of three thick precursor layers, i.e., PbI_2, FAI, and CsBr [394]. By applying different intermediate annealing temperatures between the first and second cycles, we can fabricate 450 nm-thick $Cs_{0.15}FA_{0.85}PbI_{2.85}Br_{0.15}$ films with a different preferable crystal orientation, as demonstrated by both X-ray diffraction (XRD) and two-dimensional XRD (2D-XRD). In addition, we explain the underlying mechanism of the controllable crystal orientation by XRD. Furthermore, we investigate how the PVK crystal orientation influences the opto-electronic properties in the bulk and at the surface of the film by performing photoluminescence (PL) measurements, time-resolved microwave conductivity (TRMC) measurements, and Kelvin probe force microscopy (KPFM). Our findings suggest that the preferential growth along (100) shows less variation in the surface potential/lower trap densities on the film surface compared with the (110)/(100) mixed one. On the other hand, the variation of crystal orientation shows no effects on the bulk opto-electrical properties for the thermally evaporated $Cs_{0.15}FA_{0.85}PbI_{2.85}Br_{0.15}$ PVK.

4.2. Experimental details

4.2.1. Material and film preparation

$CH(NH_2)_2I$ (FAI) (99%, Sigma-Aldrich), CsBr (99.999%, Sigma-Aldrich), and PbI_2 (99.999%, Thermal Scientific) precursors were used as received. Before sample preparation, the bare quartz sheet was cleaned with acetone and ethanol and then treated in UV plasma cleaning for 5 min. PVK films were fabricated using a simplified approach consisting of a single-cycle deposition method described elsewhere [394]. The schematic illustration of the sequential thermal evaporation process is depicted in Figure 4.1a. During the deposition of the $Cs_{0.15}FA_{0.85}PbI_{2.85}Br_{0.15}$ film, three precursors were sequentially evaporated with the order of PbI_2, FAI, and CsBr into one stack with a total thickness of 250 nm. Afterward, the second stack is deposited repeating the same sequenced three-layer precursors stack to reach a target thickness of 450 nm. Between the two deposition cycles, we applied different intermediate annealing (T_{inter}) treatments on a hot plate for 5 min (without annealing (*w/o*-A); 50, 100, 130, and 160 °C) in a nitrogen-filled glovebox. The final PVK layer consisting of two stacks was annealed at 130 °C for 5 min, named T_{final}, also in a N_2-filled glovebox.

4.2.2. Characterization

X-ray diffraction (XRD) patterns were measured with a Bruker D8 Advance diffractometer equipped with a Cu Kα X-ray source that has a wavelength of 1.54 Å.

Two-dimensional X-ray diffraction (2D-XRD, Bruker D8 Discover, Cu Kα) was performed with an incident angle of 5 °to analyze the crystallinity and orientation within the PVK films. The X-ray generator shows a voltage of 40 kV and a current of 25 mA. The beam size is 2.0 mm in diameter. The intensity of the peaks is integrated with DIFFRAC.EVA software.

The elemental compositions of the PVK films were analyzed by X-ray photoelectron spectroscopy (XPS) using a ThermoScientific K-Alpha spectrometer. The spectrometer was equipped with a focused monochromatic Al-kα X-ray source (1486.6 eV) operating

at 36 W (12 kV, 3 mA). The samples were transferred in a N_2 box for XPS measurements but were exposed to air during sample loading. Peak fitting was performed with Avantage software using a Gaussian function. The binding energy was corrected for the charge shift by taking the primary C 1s hydrocarbon peak at BE = 284.8 eV as a reference.

The morphology of the PVK surfaces was measured by a scanning electron microscope (SEM, Thermo Scientific, Verios G4 UC) at an accelerating voltage of 5 kV.

The absorptance of samples were measured by ultraviolet–visible spectroscopy (UV/vis, PerkinElmer, Lambda 950) with a wavelength range of 300-850 nm.

The photoluminescence spectra of the samples were investigated by steady-state photoluminescence (PL, HORIBA, FL3-111) with an excitation wavelength of 405 nm; besides, the emission light was filtered by a 550 nm filter.

Time-resolved microwave conductance (TRMC) was applied to learn about the carrier lifetime, mobility, and trap densities. All the measurement parameters can be found in ref. [363]. The effective electron and hole mobilities ($\sum \mu$) are derived from the maximum signal height (ΔG_{max}), which is normalized by the absorptance at an excitation wavelength of 650 nm. The charge carrier half-lifetime is obtained from the photoconductance decay.

Kelvin probe force microscopy (KPFM, Bruker, Dimension Edge scanning probe microscope) measurements were performed in an enclosure provided by the manufacturer at ambient pressure, temperature, and humidity conditions. The requisite CPD distribution over the scan area (1 × 1 μm^2) of the samples studied was determined by applying an AC voltage and plus a DC voltage to the AFM tip. To ensure the appropriate electrical conductivity between the tip and the sample, copper tape was attached between the film and the AFM holder. The contact potential difference (CPD) between the tip and sample was measured simultaneously with the topography of the region studied. The CPD/VPD distribution maps and topographical maps were collected with a similar pixel density of about 256 × 256 pixels per image and a scan rate of 0.6 µm/s. The data were analyzed with the Gwyddion software. To remove high-frequency noise, the KPFM figures were processed with a low pass filter.

4.3. Results and discussion

4.3.1. Effect of intermediate annealing temperature on PVK orientation growth

After finishing both cycles and a final annealing step at T_{final} = 130 °C, we investigated the influence of the intermediate annealing temperature (T_{inter}) in terms of crystallography. Figure 4.1b shows visual images of the unit cell with crystal orientation along the (100) and (110) planes. The XRD patterns of the final $Cs_{0.15}FA_{0.85}PbI_{2.85}Br_{0.15}$ films with different T_{inter} values are plotted in Figure 4.1c. The major peaks are located 2ϑ at 14.05°, 20.08°, 28.16°, 31.88°, and 40.43°, which are assigned to the (100), (110), (200), (012), and (220) crystal planes of PVK, respectively [360]. Apparently, the (100) peak intensity (highlighted in light gray in Figure 4.1c) gradually increases with higher T_{inter}. This trend is indicative of improved crystallization and crystal orientation of (100) direction for a higher thermal budget. On the contrary, by increasing the T_{inter} from *w/o*-A to 160 °C, the (110) peak intensity (highlighted in light brown) decreases to almost zero.

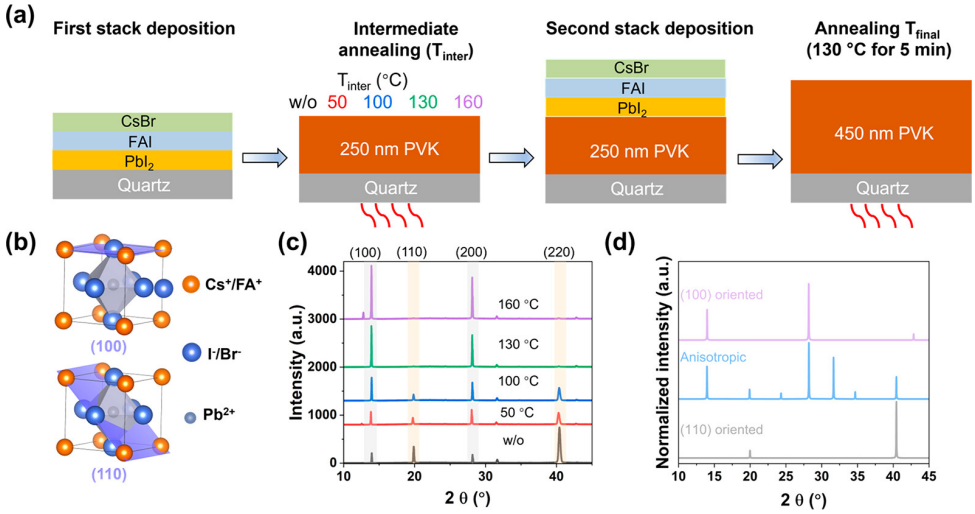

Figure 4.1: (a) Schematic illustration of the sequential thermal evaporation with various T_{inter}; (b) Illustrations of the (100) and (110) planes in a unit cell; (c) XRD patterns of final PVK films grown with different T_{inter} values and constant final annealing (T_{final}); (d) Simulated XRD patterns of non-oriented PVK and PVK with orientations along the (110) or (100) direction.

To analyze the orientation of the prepared samples, simulated XRD patterns are provided in Figure 4.1d, which either are isotropic or have a preferred growth along the (110) or (100) direction. On comparison of the experimental patterns (Figure 4.1c) with the simulated results (Figure 4.1d), we note that intermediate annealing can control the crystal orientation ranging from (1) no annealing: some preferential orientation along the 110 direction; (2) T_{inter} = 100 °C annealing: near isotropic orientation; and (3) T_{inter} = 160 °C annealing: preferential orientation mostly along the (100) direction. The difference in full width at half-maximum (FWHM) of the (100) and (110) peaks is negligible as T_{inter} increased, as shown in Table B.1, suggesting a comparable crystallite size in all samples. The top-view SEM images of these samples are shown in Figure B.1. In agreement with the XRD results, there is no clear grain size variation as the crystal orientation changes. We show in Figure B.2 the grain size distribution for samples with T_{inter} of *w/o*-A((110)/(100)-mixed) and 160 °C ((100)-oriented). Thus, an apparent preferable growth along the (100) and (200) crystallographic planes for PVKs by increasing the T_{inter} is concluded.

To further assess the controllable crystal orientations, we measured 2D-XRD of PVK samples *w/o*-A at 130 °C as shown in Figure 4.2. The two samples are selected based on their clear different preferential crystal orientations of mixed (110)/(100) and (100). In the 2D-XRD images of Figure 4.2a,b, the azimuthal intensity distribution correlates to the orientation of the planes [395]. Therefore, uniform intensity along the Debye-Scherrer ring indicates no preferable crystal orientation [396]. In contrast, the brighter parts compared with the dark region suggest specific out-of-plane orientations. The Debye-Scherrer ring shown in Figure 4.2a,b is the diffraction pattern of the (100) crystal plane for samples of *w/o*-A and 130 °C [395]. It is observed that diffraction intensities of

the preferential (100) plane varied significantly with different T_{inter}, according to Figures 4.2a and 4.2b. To better visualize and compare the difference, we integrate the intensity of the (100) crystal plane along different azimuth angles (χ), as shown in Figures 4.2c and 4.2d. More details about the integration process can be found in Figure B.3. The peak position reflects the angle of the (100) plane with respect to the substrate, while the peak intensity and width stand for the distribution [397]. For sample *w/o*-A (Figure 4.2c), two broad peaks appear at 88°-93°and 134°-135°with relatively low peak intensities, suggesting that the (100) plane is oriented along two different directions with azimuth values of 88°-93°and 134°-135°, as visualized in the inset. In contrast, the sample with a T_{inter} of 130 °C (Figure 4.2d) shows an increased peak intensity with a narrower distribution of the (100) plane oriented along 89°-90°, as shown by the cubes in the inset. Apparently, as T_{inter} increases, the orientation of the (100) plane is intensified along $\chi \approx 90°$, which is perpendicular to the substrate surface. It confirms that the preferred facet orientation along the (100) crystal plane is achieved by applying a high T_{inter}.

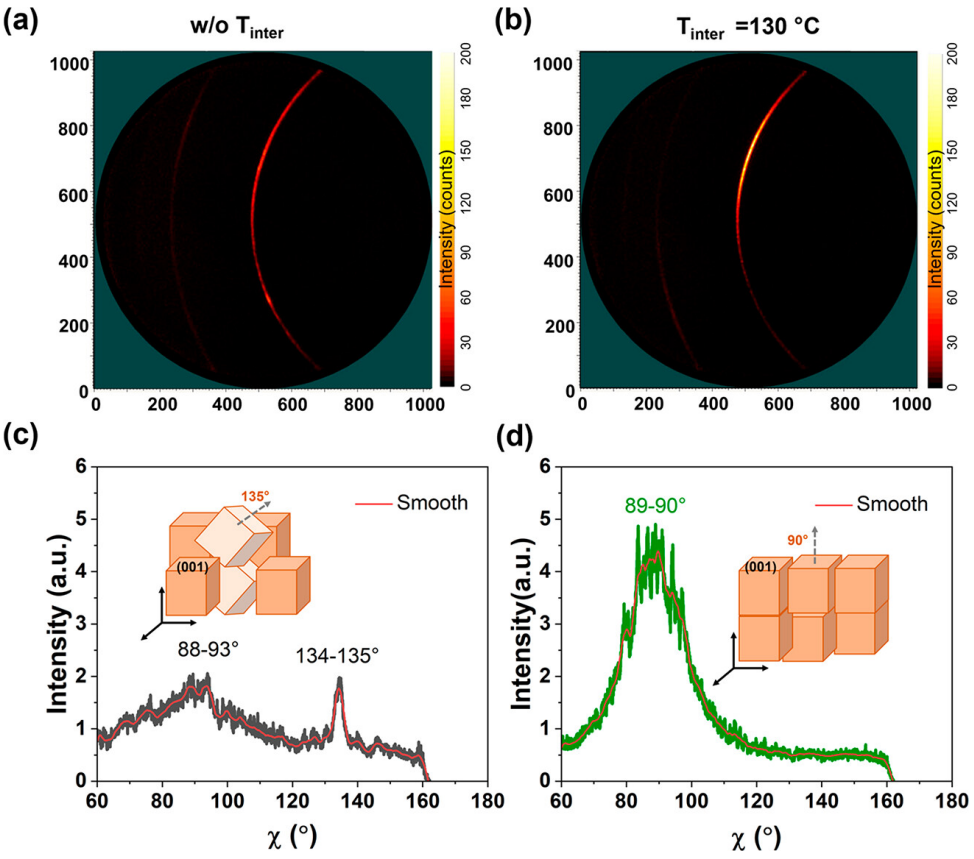

Figure 4.2: (a, b) 2D-XRD of samples with T_{inter} values of (a) *w/o*-A and (b) 130 °C. (c, d) Integration of the azimuthal intensity along the (100) reflex in 2D-XRD for samples with T_{inter} of (a) *w/o*-A and (b) 130 °C. The insets in (c) and (d) depict the preferred crystal orientation.

4.3.2. Understanding the orientation growth of PVK films

To analyze the influence of the stack from the first cycle on PVK growth, XRD characterization is performed on the first stack after the different annealing temperatures, as shown in Figure 4.3a. For the samples *w/o*-A and T_{inter} = 50 °C, XRD patterns show a high PbI_2 peak at 2ϑ = 12.7°, indicating a low conversion of the deposited precursors into PVK. With the increase of T_{inter} to 100 °C and higher, the PbI_2 peak disappears, and the PVK peak gradually increases in intensity. Then we deposited the second stack on these various samples and applied a final annealing step for all samples at 130 °C. The diffraction patterns of these double-cycle deposited PVKs are shown in Figure 4.3b. The (110) and (220) plane diffraction signals in Figure 4.3b gradually disappear as T_{inter} increases, while the (100) and (200) PVK diffraction peaks become more intense. The I_{PVK} (sum of peak intensities of (100) and (110)) of the first stack and the (100)/(110) ratios of the PVK films are plotted in Figure 4.3c as a function of T_{inter}. For T_{inter} < 100 °C the I_{PVK} *vs* T_{inter} is nearly constant. When T_{inter} is around 100 °C, the ratio quickly increases, confirming the nearly complete PVK formation. A T_{inter} of 100 °C seems to be a threshold temperature to obtain substantial precursor conversion which is in line with other works on vacuum deposited PVKs [142, 357, 398]. Interestingly, the trend for the (100)/(110) ratio for the final PVK with increasing T_{inter} follows the same trend as the I_{PVK} obtained from the first stack. For low T_{inter}, the (100)/(110) ratio remains below 1, while for a high T_{inter}, a (100)/(110) ratio ≥ 10 is found, demonstrating a substantial change in the preferred PVK orientation.

To analyze the preferential orientation of the grown PVK layers with different values of T_{inter}, the peak intensities for layers with different orientations were simulated and can be found in Figure B.4 and Table B.2. These X-ray diffraction patterns have increasing preferential ordering along the (100) or (110) directions as defined by the March-Dollase parameter (MDP) [399] with a MDP of 1 corresponding to the absolute random orientation and a lower MDP value corresponding to increasing preferential orientation [399]. The sample with T_{inter} = 100 °C shows peak intensities comparable to those of the simulation with no preferential oriented PVK (MDP = 1). From our analysis, we can conclude that the degree of preferential PVK growth is in line with the conversion of the precursors in the first stack. We ascribe the crystal orientation dependency on the T_{inter} to a template-guided PVK growth process. In other words, the ratio of unreacted precursors/converted PVK at the surface of the first stack dictates the preferential ordering of the second stack PVK. This finally leads to the manipulation of PVK orientation from a mixed (100) and (110) to a preferential (100).

To further confirm this explanation, XPS is applied to the first stacks *w/o*-A and with T_{inter} = 160 °C. Full XPS spectra for the first stack samples *w/o*-A and 160 °C can be found in Figure B.5, while the high-resolution spectra of Pb $4f_{7/2}$, I $3d_{5/2}$, Cs $3d_{5/2}$, and Br 3d are shown in Figure B.6. The corresponding peak positions and atomic percentages are given in Tables B.3 and B.4. The peak position of Pb $4f_{7/2}$ shows 138.5 eV for sample *w/o*-A, while it shifts to 139.1 eV for the sample with 160 °C (Table B.4). These peak positions are all calibrated by C 1s spectra at 284.8 eV [400]. Interestingly, the reported binding energy of Pb $4f_{7/2}$ in PbI_2 for the literature value is 138.5 eV, indicating that the Pb still exists in the form of PbI_2 on the surface of the sample *w/o*-A. To support this conclusion, we also recorded high-resolution XPS spectra of Pb $4f_{7/2}$, I $3d_{5/2}$, Cs $3d_{5/2}$, and Br 3d of

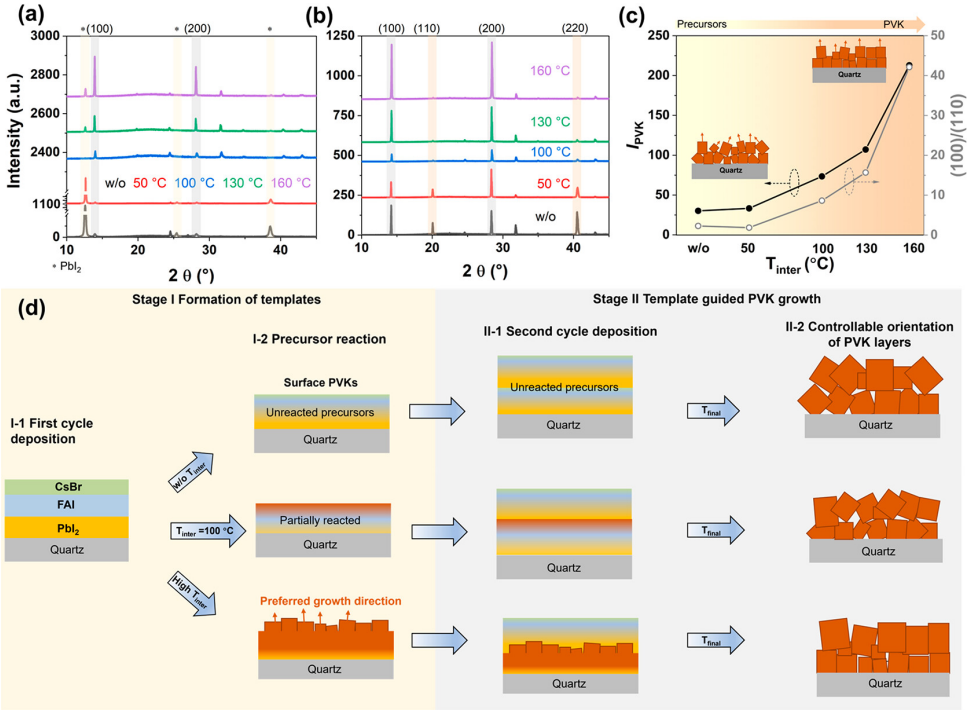

Figure 4.3: (a) XRD patterns of the first stack PVKs with different T_{inter}. Note that the y-axis contains two gaps to improve clarity. (b) XRD patterns of the double-cycle deposited samples which are continued with the first-cycle deposited samples shown in Figure 4.3a. (c) PVK peak intensity (I_{PVK}, which is the sum of intensities of peak (100) and (110)) of the first stack and the (100)/(110) ratio of the corresponding double-cycle deposited films as a function of T_{inter}. (d) Mechanism of template-guided PVK crystal orientation growth for different T_{inter}.

the individual precursors shown in Figure B.7. Furthermore, the ratio of FAI/PbI_2 at the film surface can be obtained by calculating the (I-2Pb)/Pb ratio, which is 1.71 and 0.91 for the samples *w/o*-A and T_{inter} = 160 °C, respectively (Table B.3). Apparently, the difference in (I-2Pb)/Pb for these two samples provides different templates for the growth of the next stack. Hence, the degree of PVK formation of the first stack directly influences the growth and crystal orientation of the entire PVK film.

Based on the XRD, 2D-XRD, and XPS results, we relate the crystal orientation dependency on the T_{inter} to a template-guided PVK growth process, as shown in Figure 4.3d. Different intermediate stages are achieved using T_{inter} from *w/o*-A to 160 °C. For the case without T_{inter}, the unreacted precursors in the film provide a disordered template for the deposition of the second stack and lead to a PVK film with mixed orientations as shown. On the contrary, the samples with high T_{inter} combined with nearly complete PVK conversion provide a template for the deposition of the second stack leading to a PVK film with a highly preferential orientation along the (100) direction.

4.3.3. Effects of orientation growth on opto-electronic properties

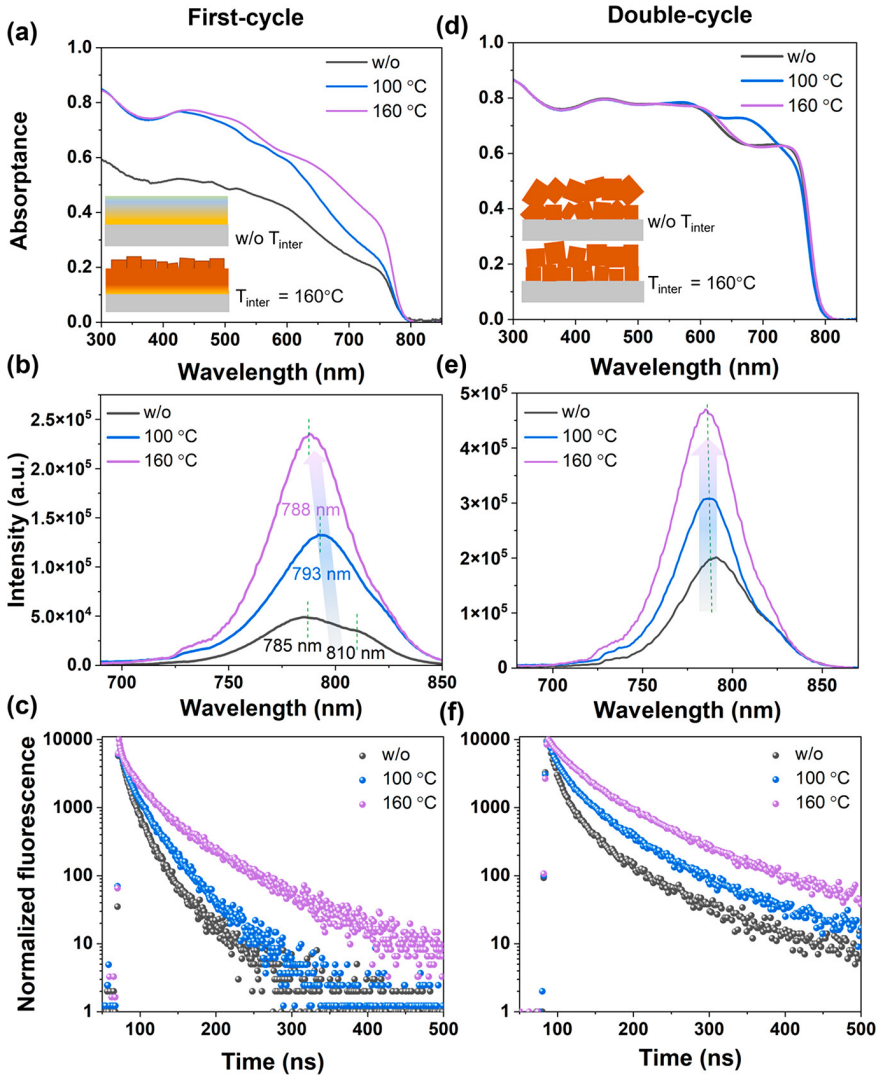

Figure 4.4: Opto-electronic properties of the first stack (left column) and double-stacked (right column) samples with different T_{inter}: (a, d) absorbance spectra, (b, e) steady-state PL, and (c, f) TRPL.

As reported in several publications [390, 401, 402], solution-based PVKs show opto-electronic properties dependent on crystal orientation. Hereby, we investigate the influence of orientation growth on opto-electronic properties based on thermally evaporated PVKs. Specifically, we choose samples with a T_{inter} of *w/o*-A, T_{inter} = 100 °C, and T_{inter} = 160 °C to study the opto-electronic properties. UV-vis and PL results of the first stacks with different T_{inter} values are shown in Figure 4.4a-c. In Figure 4.4a. The first stack *w/o*-A shows relatively low absorptance compared to the other samples because of the

limited PVK conversion, as confirmed by XRD in Figure 4.3a. Both steady-state PL and time-resolved PL measurements are performed to study the radiative band-to-band recombination at an excitation wavelength of 405 nm. The appearance of two peaks for samples *w/o*-A in Figure 4.4b could be explained from the initial formation of different PVK compositions [396] or trap-assisted emission [403]. Because the (100) PVK peak in the XRD pattern can be fitted using a single Gaussian as shown in Figure B.8, it is expected that the PVK composition is rather uniform. This is in line with the very similar absorption onsets shown in Figure 4.4a for different values of T_{inter}. Hence, it is likely that the presence of unreacted precursors might lead to the formation of shallow emissive states [404], resulting in the appearance of the shoulder in the PL spectrum at 810 nm. The position of maximum PL in Figure 4.4b shows a gradual blue-shift with increasing T_{inter} as evidence of the precursor reaction, which is consistent with the conclusion from Figure 4.3. Similarly, the longer lifetime in TRPL decay of the first stack with 160 °C shows a more complete conversion. The first stacks treated with different T_{inter} (Figures 4.4a-c) are then completed with the second cycle and final annealing step as shown in Figures 4.4d-f. The onset of absorptance in Figure 4.4d is identical for all three samples, implying that the bandgap is identical for the PVKs with different preferential orientation. From the increased PL with higher values for T_{inter}, the radiative electron-hole recombination increases as shown in Figure 4.4e. In addition, the TRPL measurements shown in Figure 4.4f exhibit a slower decay over time with increasing T_{inter}. All the TRPL spectra are fitted by mono-exponential decays, and the corresponding lifetimes and deviation (χ^2) are summarized in Table B.5. These PL measurements indicate that at least the surface of the PVKs prepared using different values for T_{inter} develops different surface properties.

TRMC gives information regarding charge carrier mobilities and lifetimes. Figures B.9a-c show the photoconductance (ΔG) as a function of time on pulsed excitation for the samples *w/o*-A, T_{inter} = 100 °C, and T_{inter} = 160 °C. Given the low exciton binding energy of CsFA-based PVKs, we can assume that the charge carrier generation yield, Φ, is close to unity at room temperature [405]. No significant differences in both the lifetime and mobility are observed between samples with different orientations, as summarized in Figure 4.5a. The recombination dynamics are also investigated by probing the sample with different laser intensities, as shown in Figures B.9a-c. The decay of ΔG under low photon intensities ($10^9/cm^2$) is attributed to the immobilization of excess charge carriers *via* trapping or recombination [363], indicated by process 1 in Figure B.9d. As the photon intensity increases to $10^{10}/cm^2$, the decay curve shows a clear difference with the low photon intensity for all samples (Figures B.9a-c), demonstrating enhanced second-order electron-hole recombination, as shown by process 2 in Figure B.9d. Therefore, we conclude that all samples with different preferable crystal growth share a comparable trap density. We find similar mobility values of 30 $cm^2\ V^{-1}\ s^{-1}$ and $\tau_{1/2}$ values of 780 ns using photon intensities of $10^{10}/cm^2$ for all samples, as summarized in Figure 4.5a. In view of the excitation wavelength used for the TRMC measurements (650 nm), resulting in a rather homogeneous excitation profile, we conclude that the bulk properties of the different PVKs are very similar. This is agreement with the comparable grain size for the different samples, as verified by both SEM (Figures B.1 and B.2) and XRD (Table B.1). Therefore, the comparable charge carrier mobilities and lifetimes of samples with

different values for T_{inter} imply that the bulk opto-electronic properties for thermally evaporated PVKs crystals are crystal orientation independent.

According to DFT calculations reported by Li *et al.* [391], the (100) planes show less dangling bonds as compared to the (110) planes in accordance with our observations. In this work, the reduced standard deviation for the sample with T_{inter} = 160 °C agrees with the fact that at the surface, only a single plane is exposed. For the sample *w/o*-A the different planes lead to larger variations in measured CPD values.

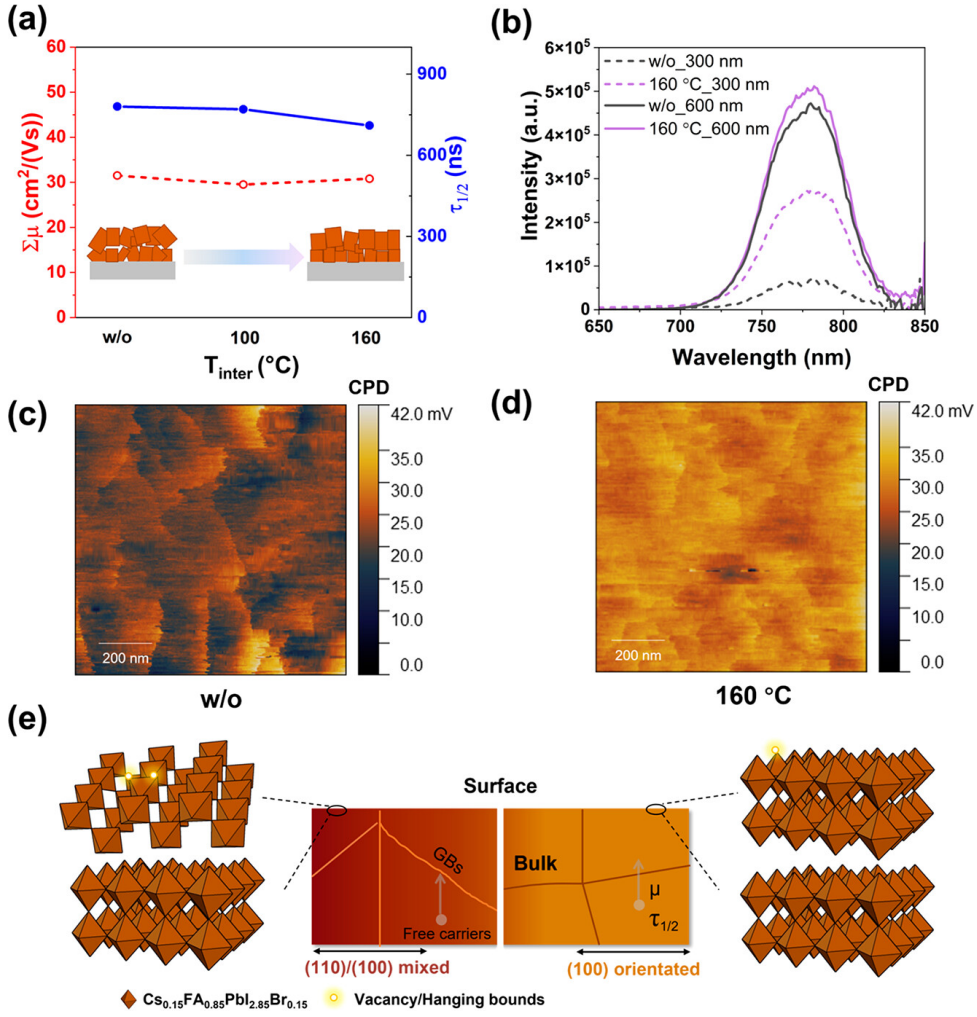

Figure 4.5: (a) Mobility (left axis) and half-lifetime (right axis) extracted from TRMC traces in Figure B.9 as a function of T_{inter} for different samples. (b) PL spectra of samples *w/o* A and T_{inter} = 160 °C with excitation wavelengths of 300 and 600 nm. (c, d) 2D CPD distribution maps of double-stacked PVK films with T_{inter} of (c) *w/o*-A, and (d) 160 °C. (e) Schematic illustration of the relationship between crystal orientation and the corresponding bulk/surface opto-electrical properties.

In order to examine how the extent of preferential ordering affects the opto-electronic properties, PL spectra are recorded using different excitation wavelengths (λ = 300 nm or λ = 600 nm) of the samples *w/o*-A and with T_{inter} = 160 °C, as shown in Figure 4.5b. The penetration depths are very different going from tens of nanometers to hundreds of nanometers. While the PL spectra are similar for both samples using λ = 600 nm, at λ = 300 nm the intensity for the sample *w/o*-A is a factor of 4 lower than that of the sample with T_{inter} = 160 °C. This implies that the surface properties of the sample *w/o*-A lead to more radiationless decay. To further confirm our conclusion, we performed additional Kelvin probe force microscopy (KPFM) measurements to specifically study the laterally resolved contact potential difference distribution. Figures 4.5c and 4.5d show KPFM images of the contact potential difference (CPD) distribution for the samples *w/o*-A and T_{inter} = 160 °C, respectively. The sample *w/o*-A exhibits a low averaged CPD of 22.8 mV combined with a large standard deviation of ±0.95 mV. On the contrary, the sample with T_{inter} = 160 °C shown in Figure 4.5d shows a large and quite uniform averaged CPD of 29.7 mV and a standard deviation of ±0.47 mV. The CPD distributions of both images are converted into histograms in Figure B.10. The increased average CPD is related to a reduced concentration of surface defects caused by the dangling bonds [406]. According to DFT calculations reported by Li *et al.* [391], the (100) planes show less dangling bonds as compared to the (110) planes in accordance with our observations. In this work, the reduced standard deviation for the sample with T_{inter} = 160 °C agrees with the fact that at the surface only a single plane is exposed. For the sample with *w/o*-A the different planes lead to larger variations in measured CPD values.

Combining the results of measurements probing the bulk and surface, the influence of thermal evaporated PVK crystal orientation on film opto-electrical properties is schematically illustrated in Figure 4.5e. In terms of bulk properties, variation in the preferable crystal growth has little effect on the bulk opto-electronic properties. Reasons lay in the similar grain boundaries, as confirmed by the comparable grain size in Figure B.2. On the contrary, the effect of different crystal orientations on the opto-electronic properties is observed at the surface of the film. The mixed crystal orientations expose different facets at the film surface, affecting the number of surface vacancies and dangling bonds and further exhibiting differences in surface potential. A uniform ordering of the PVK crystals might lead to improved charge extraction at the interface of PVK and transporting layers and less interfacial recombination [407].

4.4. Conclusions

We propose an intermediate annealing approach to manipulate the crystal orientation of thermally evaporated $Cs_{0.15}FA_{0.85}PbI_{2.85}Br_{0.15}$ PVK films fabricated by using a simplified sequential layer deposition method. By optimizing the intermediate annealing temperature, we demonstrate that the crystal orientation can be tailored ranging from primarily (110) to near isotropic to predominantly (100). Our results indicate that the degree of precursor reaction upon different intermediate annealing temperatures of the first stack influences the preferred crystal orientation of the entire PVK film by providing different templates for the subsequent deposition. Moreover, we reveal how thermally evaporated PVK crystal orientation influences the film opto-electronic properties by applying PL, TRMC, and KPFM measurements. We found that the preferable growth along

both directions have comparable bulk properties in terms of charge carrier mobility, lifetime, and trap densities, which is dominated by the grain size and grain boundaries. On the contrary, the (100) oriented growth exhibits higher surface potential/lower trap densities at the film surface compared to the primarily (110) to near isotropic PVK layers, which plays a decisive role in charge carrier extraction. Therefore, realizing uniform PVK layers with a highly preferential (100) orientation is expected to show improved charge extraction and transportation at the device level.

5

Scalable and simplified sequential vacuum deposition for perovskite solar cells

This chapter was submitted in Solar Energy Materals and Solar Cells *

Abstract

Sequential thermal evaporation is an emerging technique to obtain PVK photoactive materials for solar cell application. Advantages include solvent-free processing, accurate stoichiometry control, and scalable processing. Nevertheless, the PCE of PSCs fabricated by evaporation still lags behind compared to solution-processed PSCs. Here, based on multi-cycle sequential thermal evaporation, we systematically investigate the effects of the post-deposition annealing temperature on the PVK properties in terms of surface morphology, opto-electronic properties, and device performance. We find that the average grain size increases to 1 μm and charge carrier mobilities exceed 50 cm^2 V^{-1} s^{-1} when the annealing temperature is increased up to 170 °C. We introduce a trace of $PbCl_2$ to the multi-cycle sequential deposition to improve the absorber crystallinity at lower annealing temperature, as evidenced by the XRD and PL. The resulting PSC yields a PCE of 18.5% with a cell area of 0.09 cm^2. With the same deposition parameters, the cell area is scaled up to 0.36 cm^2, and 1 cm^2, achieving champion PCEs of 17.3% and 11% , respectively, with no significant open-circuit voltage drop. This indicates the great potential of this technology for commercialization of PSCs in the future.

*This chapter is based on the manuscript: **J.Yan**, J. Nespoli, R. Boekhoff, H. Wang, T. Gort, X. Liu, B. Ibrahim, T. J. Savenije, O. Isabella, L. Mazzarella., *Scalable and simplified sequential vacuum deposition for perovskite solar cells*, which has been submitted in Solar Energy Materials and Solar Cells.

5.1. Introduction

Thermal evaporation is a promising technique for the commercialization of perovskite (PVK) solar cells (PSCs), which is attributed to its numerous advantages, including controllable thickness, solvent-free processing, and compatibility with textured substrates [216, 300, 408]. Since the first work was reported in 2013 [53], remarkable progress has been achieved in this field. To date, PSCs based on vapor-deposited PVK have achieved a record power conversion efficiency (PCE) of 24.4% [149]. Additionally, fully evaporated PSCs have demonstrated a PCE of 20% [149]. Despite these significant advancements, several challenges hinder the steps toward industrial application of vacuum-based PSCs, including the control of organic ammonium compound [409] and the complexity associated with multisource deposition processes involving more than two precursors [147]. In contrast to co-evaporation, sequential thermal evaporation demonstrates compatibility with in-line fabrication [410], and it exhibits enhanced reproducibility due to the absence of cross-influence among the sources during deposition [411]. However, constrained by precursor mixing and interdiffusion, it is crucial to optimize the thickness of each layer during deposition. Conversely, an excessive number of layers in sequential deposition is time-consuming compared to co-evaporation process. As a result, there are limited reports on multi-cycle sequential vacuum deposition processes [142, 412, 413]. Unlike solution-based PVK, the crystal growth of thermally evaporated PVK can hardly be modulated through solvent engineering [414]. Therefore, the thermally deposited films commonly exhibit lower charge carrier mobility limited by grain size and shorter lifetime because of traps during film preparation [56, 415]. These defects lead to non-radiative recombination and photovoltage loss, which detrimentally affect the device efficiency and stability [55, 397]. To address these challenges, incorporating lead chloride ($PbCl_2$) into the precursors has emerged as a promising strategy. This approach has been explored first in solution-based [416, 417] but also in vacuum-based methods [397, 418] to influence crystallization dynamics and enhance the opto-electronic properties of the PVKs. Specifically, mixed cations, mixed halide perovskite, $Cs_xFA_{1-x}PbI_{3-x}Br_x$ exhibit thermal stability [419], phase stability [420], and tunable bandgap [421], which satisfy the requirements for top cells in tandem devices by ensuring current matching. To date, studies on sequential multi-cycle vacuum deposited $Cs_xFA_{1-x}PbI_{3-x}Br_x$ are rarely reported. Numerous studies have been reported focusing on the formation of PVKs by co-evaporation [300, 357, 360, 422]. In contrast, PVKs deposited by sequential vacuum deposition are converted mainly during the post-annealing process, highlighting the crucial role of annealing. Based on the process proposed in our previous work [394, 423], we demonstrate here efficient PSCs based on multi-cycle thermally deposited $Cs_xFA_{1-x}PbI_{3-x}Br_x$. In this work, the impact of post-deposition annealing is systematically investigated in terms of crystallinity, morphology, and opto-electrical properties and performance. We find that the grain size increases on average from 500 nm to 1 μm as the annealing temperature increases from 130 °C to 170 °C. Using the optimized annealing temperature and time, PVKs including $PbCl_2$ precursor are investigated at both film and device levels. We demonstrate that $PbCl_2$ improves PCE by enhancing the open circuit voltage (*Voc*) and fill factor (*FF*), which are attributed to the improved absorber crystallinity. With these optimized parameters, 0.09 cm^2 PSCs show PCE of 18.5% with a *Voc* of 1.01 V, a short circuit-current (*Jsc*) of 23.95 mA/cm^2, and *FF* of 78.5%. Further-

more, cells with different area are fabricated, ranging from 0.09 cm^2 to 1 cm^2. The best PSC gives the highest PCE of 17.3% and 11% for 0.36 cm^2 and 1 cm^2, respectively, with no losses observed in *Voc* when the active area is scaled up to 1 cm^2. Our findings provide an alternative approach for thermal evaporated absorber preparation and scaling up in PSCs application.

5.2. Experimental details

5.2.1. Material and device preparation

Indium tin oxide (ITO) coated glass substrates and PTAA were purchased from Yokou. CsBr, Fullerene (C60) and BCP were purchased from Sigma Aldrich. $CH(NH_2)_2I$ (FAI) and PbI_2 were purchased from Greatcell Solar Materials. All the chemicals are used as received. ITO coated glass substrates were cleaned with acetone, ethanol, and oxygen plasma for 5-10 mins respectively. As a hole-extraction layer, 1.5 mg/mL PTAA was spin coated with 6000 rpm (acceleration 2000 rpm), and then was annealed with 100 °C for 10 mins. Then, the samples were transferred to the vacuum chamber (Perovap, CreaPhys) for PVK deposition at a base pressure of 10^{-6} mbar. PVK films are prepared with a simplified approach consisting of a multi-cycle sequential thermal deposition method described by our previous works [394, 423]. To obtain $Cs_{0.15}FA_{0.85}PbI_{2.85}Br_{0.15}$ film, three precursors were sequentially evaporated, PbI_2, FAI, and CsBr, into one stack with a total thickness of 200-250 nm. Afterwards, two additional stacks are deposited repeating the same sequenced three-layer precursors stack to reach a target thickness of about 600 nm. As for the case with introducing of $PbCl_2$, 1.5% molar ratio of $PbCl_2$ to 1 of PbI_2 is thermally deposited between PbI_2 and FAI layers in every stack. Figure 5.1a shows a schematic illustration the sequential evaporation process. The final PVK layers consisting of three stacks were annealed on a hot plate with different annealing temperature (130 °C, 150 °C, and 170 °C) and time (10 min, 15 min, and 20 min). Afterwards, the samples were transferred into a second vacuum chamber (Optivap 2, CreaPhys) for the thermal evaporation of 20-nm thick of C60, and 2-nm thick of BCP, followed by a 100-nm thick Ag electrode (Optivap 1, CreaPhys) using metal masks to define the cell area.

5.2.2. Characterization

X-ray diffraction patterns (XRD) were measured with a Bruker D8 Advance diffractometer equipped with a Cu-Kα X-ray source with a wavelength of 1.54 Å. The top-view morphology and cross-section of PVK films and devices were measured by the scanning electron microscope (SEM, Thermo scientific, Verios G4 UC) with an accelerating voltage of 5 kV. The absorption of samples was measured by Ultraviolet-visible spectroscopy (UV/Vis, Perkin-Elmer, Lambda 950) with a wavelength range of 300-850 nm. The photoluminescence spectra of the samples were investigated by the Steady-state Photoluminescence (PL, HORIBA, FL3-111) with an excitation wavelength of 405 nm; besides, the emission light was filtered by a 550 nm filter. Time-resolved photoluminescence spectra were carried out using an Edinburgh LifeSpec spectrometer equipped with a single-photon counter. The films were excited at 405 nm with a filter of 550 nm for emission light. The current density-voltage (*J-V*) characteristics were recorded using a Keithley 2400 source measure unit using a solar simulator type (company). The active area of the

solar cells was determined using top metal contact to be 0.09 cm^2, 0.36 cm^2, and 1 cm^2.

5.3. Results and discussion

5.3.1. Effects of lead chloride on film structural and opto-electrical properties

Based on the sequential thermal deposition approach described above, we investigated the impact of $PbCl_2$ on the film properties for different annealing temperatures, including crystal structure, morphology, and opto-electrical properties. Samples *without* $PbCl_2$ are denoted as *w/o*, while those *with* $PbCl_2$ are referred to *w/* in the subsequent texts and figures. Figure 5.1b presents the X-ray diffraction (XRD) patterns of the sample *w/o* and *w/*$PbCl_2$ annealed at temperatures in the range between 130 °C and 170 °C. The major peaks of the PVK films are located at 14.05°and 28.16°, which are assigned to the (100), and (200) crystal planes of cubic PVK, respectively. The absence of significant peak shifts across different conditions implies identical lattice constants even with the introduction of trace amounts of $PbCl_2$. However, the increasing peak intensities indicate improved crystallinity with higher annealing temperatures for both *w/o* and *w/* $PbCl_2$. This observation is consistent with both the top-view (Figure C.1) and cross-sectional-view (Figure 5.1c) SEM images. In Figure 5.1c, the grain size shows a strong dependence on the annealing temperature. For both *w/o* and *w/* $PbCl_2$ samples, large grains form when temperature exceeds 150 °C, whereas annealing conditions at lower temperature (≤150 °C) result in smaller grains throughout the film. To further investigate the effect of $PbCl_2$, the full width at half maximum (FWHM) and the peak intensities of the *w/o* and *w/* $PbCl_2$ samples are reported in Figure 5.1d as function of the annealing temperature. Interestingly, the *w/* $PbCl_2$ samples annealed at 130 °C show a similar intensity and FWHM to the *w/o* $PbCl_2$ samples annealed at 150 °C (highlighted in light orange and light blue bar in Figure 5.1d), reflecting improved crystallinity in the presence of $PbCl_2$. Furthermore, both *w/* $PbCl_2$ samples annealed at 150 °C and 170 °C exhibit almost columnar grain growth, as shown in the cross-sectional SEM (Figure 5.1c). This columnar growth has been reported to be beneficial for efficient charge carrier collection [424–426], as evidenced by the high *FF* in cell performance (Figure C.2). In additional to the cross-sectional SEM, the grain size distribution statistics are summarized in Figure 5.1e for samples *w/* $PbCl_2$ at different annealing temperatures. These data are extracted from the top-view SEM shown in Figure C.1. Like the observations made in Figure 5.1d, the grain size distribution confirms that in the presence of $PbCl_2$, an annealing temperature of 150 °C is sufficient to convert the precursors into a dense PVK film with large grain sizes. This enhancement is consistent with published works on both solution-processed and co-evaporated PSCs [418, 425, 427, 428].

Following the structural and morphological analysis, Figure 5.2 shows the comparison on opto-electronic properties based on samples *w/o* and *w/* $PbCl_2$ annealed at 150 °C. The UV-vis absorption spectra of the PVK films are shown in Figure 5.2a. Higher absorption measured for sample *w/o* $PbCl_2$ compared to the *w/* $PbCl_2$ one can be related to small thickness variation. Figure C.3 shows the evolution of absorption with increasing annealing temperature for both *w/o* and *w/* $PbCl_2$ samples, together with a zoomed-in view of the absorption edge in the inset. Different with the samples of *w/o* $PbCl_2$ shown

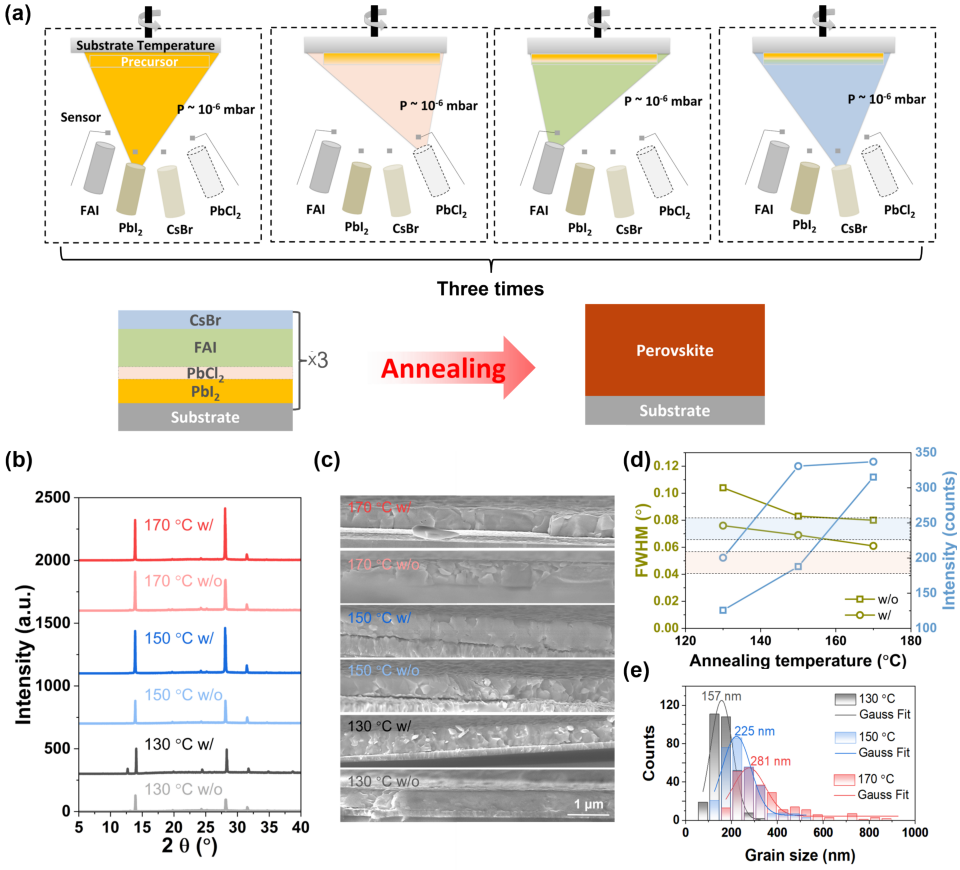

Figure 5.1: (a) Schematic illustration of the sequential thermal evaporation to prepare a PVK absorber; (b) XRD patterns of PVK films *w/o* and *w/* $PbCl_2$ subjected to different annealing temperatures; (c) Cross-sectional SEM of PVKs with varying annealing temperatures for both *w/o* and *w/* $PbCl_2$ samples; (d) FWHM and absolute peak intensity of the (100) crystal plane of *w/o* and *w/* $PbCl_2$ samples as a function of annealing temperatures; (e) Grain size distribution of PVK *w/* $PbCl_2$ with different annealing temperatures. Grain sizes were measured using ImageJ software and data were extracted from top view SEM images in Figure C.1.

in C.3a, there is almost no change in the absorption edge for the samples *w/* $PbCl_2$ in Figure C.3b. This indicates that the PVK has already fully converted at 130 °C in the presence of $PbCl_2$, consistent with the results shown in XRD and SEM discussed above. Figure 5.2b displays the steady-state photoluminescent (PL) spectra of the two types of films. Compared to the *w/o* $PbCl_2$ film, no significant peak position shift is observed in the PL spectrum of the $PbCl_2$-based film. This aligns with the XRD peak position shown in Table C.1, suggesting that Cl is not incorporated into the PVK lattice but rather enhances the crystallization and precursor reactions during annealing [427]. To support the above conclusion, XPS spectra at different etching times are recorded to investigate the elemental composition of the $PbCl_2$-based film, as shown in Figure C.4. Interestingly, both

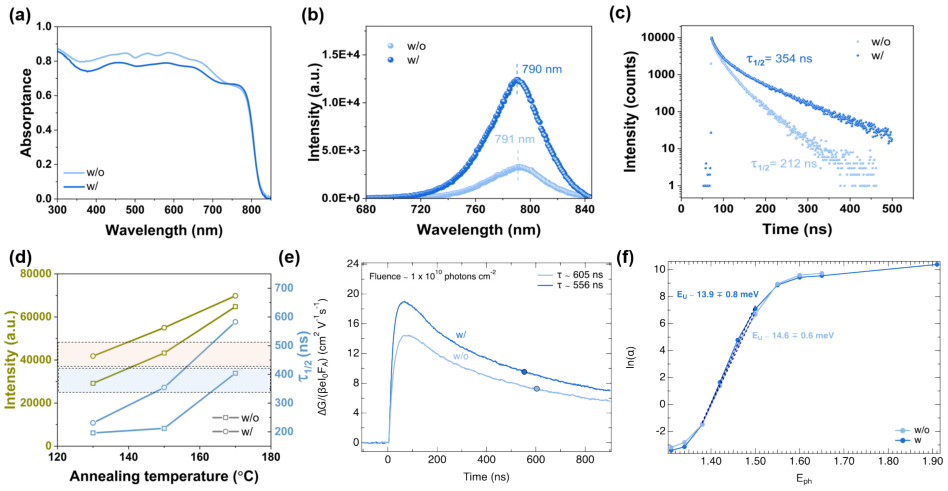

Figure 5.2: Opto-electrical properties of the *w/o* and *w/* $PbCl_2$ samples annealed at 150 °C. (a) Absorption spectra; (b) Steady state PL; (c) TRPL decay; (d) PL intensity and half-lifetime as a function of annealing temperature, the comparison of PL intensity and half-lifetime are highlighted in light orange and light blue bars; (e) TRMC traces recorded under laser pulses at 650 nm; (f) Urbach energies for *w/o* and *w/* $PbCl_2$ sample.

the surface and bulk show no Cl signal. This could result from either a Cl content below the detection limit or from the fact that Cl evaporates in the form of an organic salt. However, the improved PL intensity with introducing of $PbCl_2$ indicates that the $PbCl_2$-based film has less non-radiative recombination centre. Similarly, the TRPL decays are shown in Figure 5.2c for both samples. The *w/* $PbCl_2$ PVK film shows a longer half-lifetime compared to the *w/o* $PbCl_2$ film, indicating improved crystalline quality in the $PbCl_2$-based films. To further verify the role of $PbCl_2$, PL intensities and half-lifetimes are summarized in Figure 5.2d as a function of annealing temperature for both *w/o* and *w/* $PbCl_2$ samples. Similar to Figure 5.1d, the samples of *w/* $PbCl_2$ annealed at 130 °C show similar PL intensity and even a higher half lifetime compared to the *w/o* $PbCl_2$ sample annealed at 150 °C, highlighted in light orange and light blue bars. This result indicates that introducing $PbCl_2$ has similar effects as the increasing annealing temperature, with is related to increased film crystallinity and decreased trap states. Given that $PbCl_2$ improves PVK crystallization as evidenced by XRD and PL, we applied time-resolved microwave conductivity (TRMC) to study the electronic properties and charge-carrier dynamics. An enhancement in the charge-carrier mobility by a factor of about 1.3 from 14.5 $cm^2\ V^{-1}\ s^{-1}$ to 19.0 $cm^2\ V^{-1}\ s^{-1}$ was observed, implying a significantly improved diffusion length for the *w/* $PbCl_2$ PVK. (Figure 5.2e). The increased mobility in the *w/* $PbCl_2$ sample can be related to the larger grains, as observed by SEM. Finally, the Urbach energies (Eu), defining the sub-band gap tail states in the PVKs, were obtained by using TRMC for both samples. Figure 5.2f shows the logarithmic absorption coefficient, $\ln(\alpha)$ as a function of the photon energy, Eph. From the resulting slope near the offset, the Urbach energy (Eu) can be derived amounting to 14.5 and 13.9 meV for the *w/o* $PbCl_2$ and *w/* $PbCl_2$ PVK films, respectively. These relatively low Eu values for both samples are indicative of a low

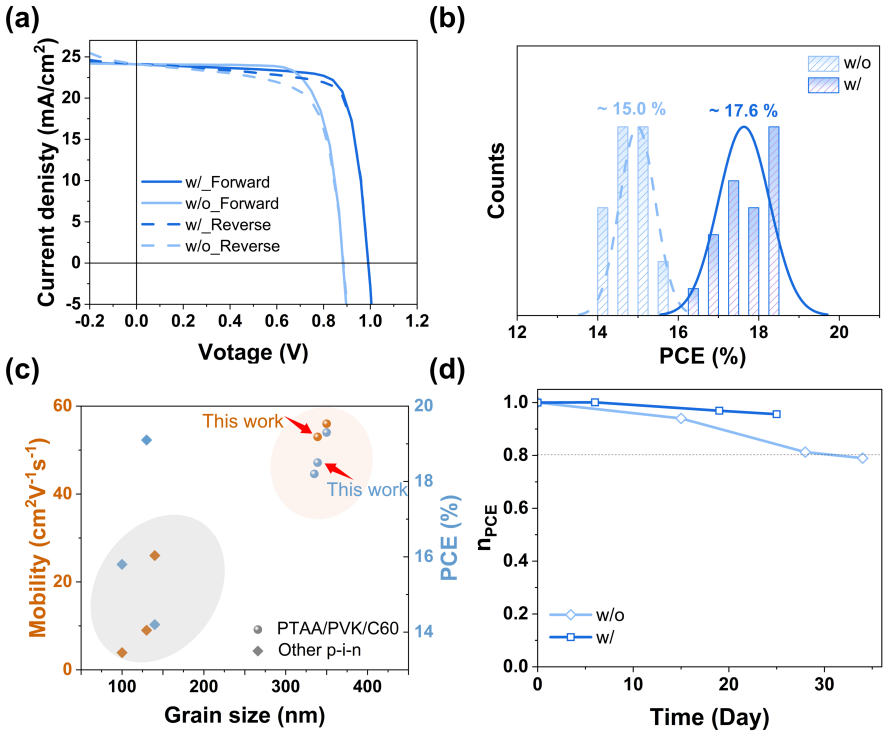

Figure 5.3: Photovoltaic performance of solar cells *w/o* and *w/* $PbCl_2$ annealed at 150 °C. (a) *J-V* curves in forward and reverse scan modes of the champion PSC; (b) PCE distribution of 20 cells for each condition, extracted from Figure C.2; (c) Recently reported mobilities and PCEs as a function of grain size based on PSCs with thermally deposited absorbers. Sphere symbols represent the PTAA/PVK/C60 architecture, identical to the structure used in this study, while square symbols represent solar cells with other HTL/PVK/ETL;(d) Normalized PCE (n_{PCE}) versus time over nearly 30 days with the solar cells are stored in N_2 filled glovebox in between measurements. The solar cells area is 0.09 cm^2.

degree of energetic disorder, implying a low concentration of sub gap tail states.

5.3.2. Effects of Lead Chloride on device performance

Next, we investigated the influence of the annealing on the performance of solar cells first *w/o* $PbCl_2$ and later-on *w/* $PbCl_2$. The cell configuration is illustrated in Figure C.5. Doubling the annealing time from 10 to 20 minutes at 150 °C shows negligible impact on the photovoltaic parameters of the cell, as indicated in Figure C.6. This result suggests that higher annealing temperatures are necessary to achieve improved PVK crystallization and enhanced cell efficiency. However, PTAA is not thermally stable when the temperature increases up to 170 °C, even though such a temperature is optimal for the absorber, as evidenced by Figure C.7. Figure C.7 shows the *J-V* curve of solar cells annealed at 170 °C, showing a significantly reduced PCE of below 10% compared to around 15% for the reference case annealed at 150 °C. Therefore, most of the discussion in the following part is limited to PVK annealed at 150 °C.

The record solar cells with $PbCl_2$-based PVK achieved instead a PCE of 18.5% in forward bias scan (*Voc* = 1.01 V; *Jsc* = 24.5 mA/cm^2; *FF* = 78.5%), compared to 15.8% in case of the sample *w/o* $PbCl_2$ (*Voc* = 0.85 V; *Jsc* = 24.2 mA/cm^2; *FF* = 76.3%). As evidenced by the film crystallinity and opto-electrical properties, the champion cell *w/* $PbCl_2$ shows improved *Voc* and *FF* compared to the sample of *w/o* $PbCl_2$ (Figure 5.3a), benefiting from the enhanced passivation and the extended carrier diffusion length (lifetime and mobility).The PCE statistics distribution are summarized in Figure 5.3b based on 20 solar cells for each condition, where the average PCEs are approximately 15.0% and 17.6% for the samples of *w/o* and *w/* $PbCl_2$, respectively. The corresponding statistical distributions of the photovoltaic parameters (*Voc*, *Jsc*, and *FF*) are reported in Figure C.2. Moreover, the statistic of *FF* in reverse and forward scan are summarized in Figure C.8 for PSCs *w/o* and *w/* $PbCl_2$. In contrast to the *w/o* $PbCl_2$ samples, the $PbCl_2$-based PSCs show comparable *FF* values for reverse and forward scans, demonstrating that $PbCl_2$ effectively reduces the hysteresis, in agreement with findings in spin-coated PSCs [429, 430]. The reason of this improvement in the hysteretic behavior could be attributed to fewer defect states near the surface of PVK/transporting layers [431].

To further link the film morphology and opto-electrical properties to cell-level performance, we plotted the PCE and carrier mobility as functions of grain size in Figure 5.3c, including data reported in literature based on similar cell structures (HTL/PVK/ETL) and fabricated with thermally deposited absorbers. The data distribution clearly delineates two main regions, indicating that both PCE and carrier mobility are both largely influenced by the grain size. Profiting from the reduced trap states, stability tests (Figure 5.3d) of the PSCs stored for 30 days in glovebox proved that both PSCs *w/o* and *w/* $PbCl_2$, retained 77% and 88% of their initial efficiency, respectively (Figure 5.3d).

5.3.3. Up-scaling of cell area

The PCE values of the PSCs reported above are all based on cell area of 0.09 cm^2. While it has been reported in literature that the increase of area generally leads to a significant reduction of PCE and *Voc* because of pinholes, we proceeded to scale up the *w/* $PbCl_2$ devices up to 1 cm^2. Figures 5.4a-c show the dark and illuminated current density-voltage (*J-V*) curves in forward, and reverse scan direction of the champion PSCs with cell areas of 0.09 cm^2, 0.36 cm^2, and 1 cm^2, all annealed at 150 °C. The corresponding external parameters measured in the reverse/forward scans and the corresponding hysteresis values are reported in Table C.2. From the *J-V* curves, it is evident that the *FF* drops as cell area increases. Despite similar dark *J-V* characteristics, there is a marked difference in the slope of light *J-V* curve at the 0 bias-voltage region, indicating significant photon-shunt as the cells area increases. This is due to problems in carrier transport and interfacial accumulation rather than pinholes. This observation suggests the feasibility of preparing large-area cells without pinholes using this deposition technology. To further explore the impact of annealing temperature on cell performance as cell area varies, we applied annealing temperature of 130 °C, 150 °C, and 170 °C to the absorber for cells with areas of 0.09 cm^2, 0.36 cm^2, and 1 cm^2. The corresponding cell statistics are summarized in Figure 5.4d-g. Similar as reported in literature, Figure 5.4d demonstrates a decrease in PCE as cell area increases. However, this drop mainly comes from reductions in both *Jsc*

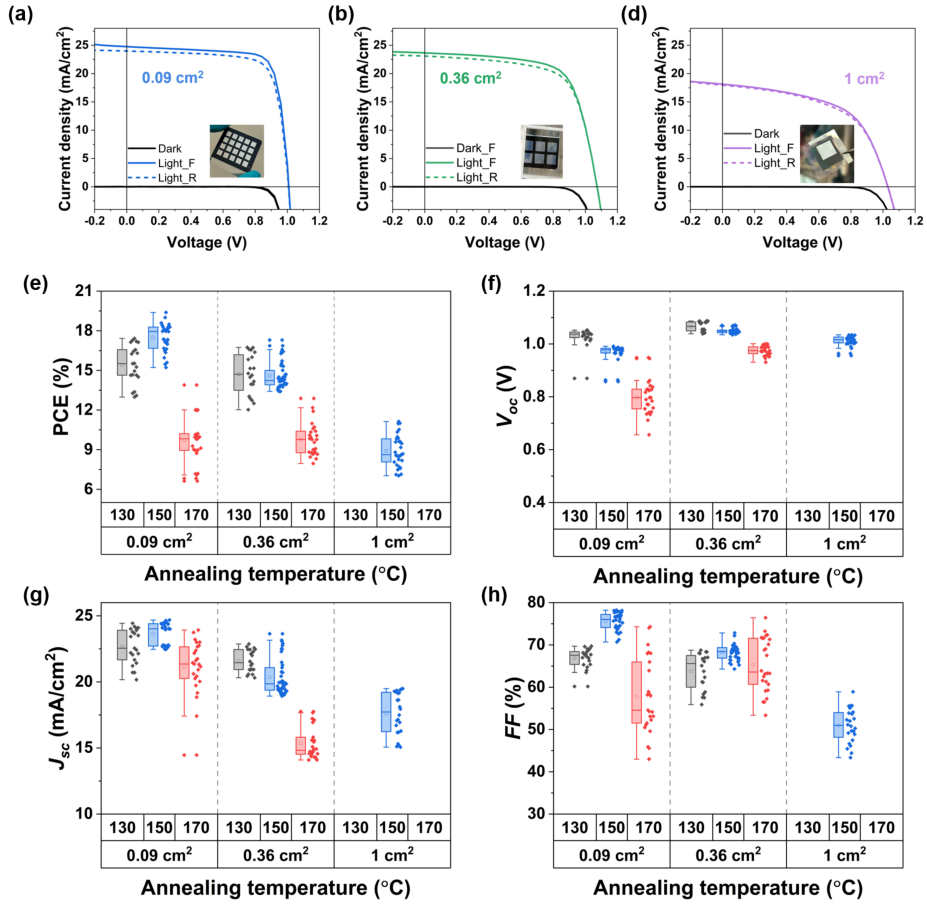

Figure 5.4: Influence of the annealing temperature on *J-V* curves and external parameters of *w/* $PbCl_2$ PSCs. (a)-(c) Dark, forward, and reverse *J-V* curves of PSCs with active areas ranging from 0.09 to 1 cm^2; (d)-(g) Distribution of external parameters (PCE, *Voc*, *Jsc*, and *FF*) of PSCs as a function of annealing temperature and cell area. Data of more than 20 cells are collected for each variation. The cells of 0.09 cm^2 and 0.36 cm^2 reported here are prepared in the same batch, while the 1 cm^2 cells are prepared in another batch with the same deposition parameters.

and *FF* because of carrier transport issues, as discussed in Figure 5.4a-c. Notably, when increasing the active area from 0.09 cm^2 to 0.36 cm^2 and 1 cm^2, the *Voc* remains mostly unaffected, especially in cases of low annealing temperature to exclude the PTAA degradation influence. The *Voc* for increasing cell area shows relative variations between 1% and 2% as compared with the 0.09 cm^2 PSCs. These findings further confirm the reduced trap densities and high uniformity of the thermally evaporated PVK thin films over large areas. Moreover, it indicates that PCE losses over large areas are primarily attributable to the increased electrode resistance.

To assess the uniformity of large-area PVKs deposited *via* sequential evaporation, a

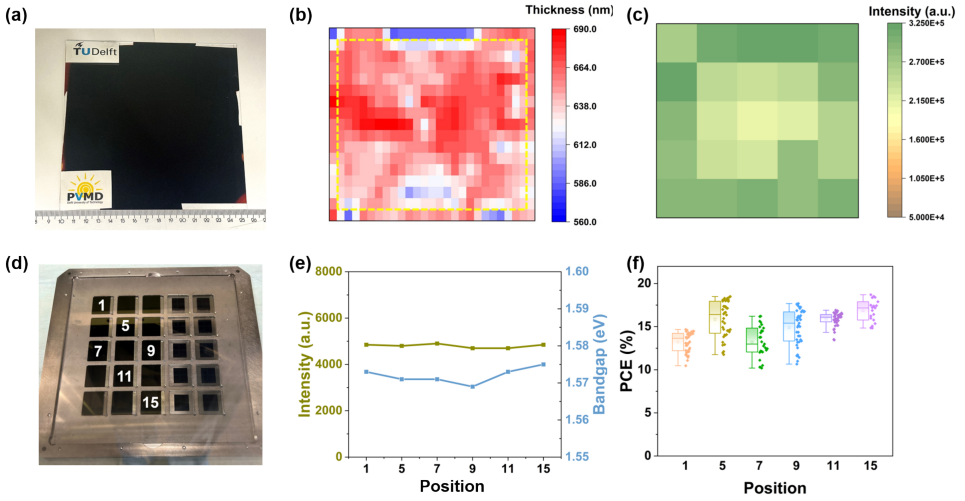

Figure 5.5: Uniformity test of the large area PVK film in terms of thickness, crystal structure, opto-electronic, and device performance. PVK films shown here are fabricated with $PbCl_2$ and annealed at 150 °C for 20 mins. (a) Photo of the sequentially thermal deposited PVK film. The substrate size in photo is 15.6×15.6 cm^2; (b) Thickness mapping of the film shown in Figure 5.5a; (c) PL mapping of film shown in Figure 5.5a; (d) Photo of PVK films at different positions for measurement of crystal structure, opto-electronic, and device performance; (e) Absolute peak intensity for (100) crystal plane and bandgap as a function of samples at different positions on the large area film as shown in Figure 5.5d; (f) Boxplot distribution of PCEs at 6 different locations, with each location having 20 cells with cell area of 0.09 cm^2, as shown in Figure 5.4a.

15.6×15.6 cm^2 film (Figure 5.5a) was deposited on glass and evaluated in terms of homogeneity of thickness, PL, and device performance. The thickness mapping of sample in Figure 5.5b indicates that the PVK layer thickness varies by less than 15% between the center and edges, confirming the potential application of this deposition technique for fabricating highly efficient large-area devices. Besides, the dis-uniformity decreases to less than 9% when excluding the external edges, as shown in the yellow dash line in Figure 5.5b. In Figure 5.5c, the PL distribution reveals rather comparable signal intensities, indicating uniform emission properties across the film. In addition to full area test, specific samples were selected from different regions for both film and device-level measurements. Figure 5.5d shows the selected positions of the large-area PVK film (1, 5, 7, 9, 11 and 15) for PL and XRD investigations. It was found that the peak intensities of the (100) plane from XRD and bandgap values extracted from PL in different regions are comparable, as provided in Figure 5.5e. This result suggests a uniform crystallization and composition throughout the large-area PVK films. Figure 5.5f and Figure C.9 present the performance of 0.09 cm^2 solar cells, demonstrating that all photovoltaic parameters exhibit less than 10% variation across different positions, affirming the uniformity and reliability of the fabricated large-area PVK devices.

5.4. Conclusions

In conclusion, we fabricated and characterized perovskite films and p-i-n devices using sequential thermal evaporation. The grain size increases significantly from less than 200 nm to almost 1 μm as the annealing temperature increase from 130 °C to 170 °C. The introduction of minor amounts of $PbCl_2$ improves the perovskite crystallinity. The champion efficiency is observed in devices with $PbCl_2$ and annealed at 150 °C, achieving a maximum power conversion efficiency of 18.5% and exhibiting *Voc* and *FF* equal to 1.01 V and 78.5%, respectively, for 0.09 cm^2 cell area. Building on these optimized parameters, we scaled the device size up from 0.09 cm^2 to 0.36 cm^2, and 1 cm^2. Despite the increase in cell area, larger area devices showcase almost *Voc* (≥ 1 V). Besides, 15.6×15.6 cm^2 perovskite films are prepared with uniform crystallization and comparable photovoltaic parameters, showing less than 10% variation across different positions. These results indicate the potential application of this technology for commercialization of perovskite solar cells.

6

Conclusions and outlook

6.1. Conclusions

This thesis describes the development of sequential thermally deposited perovskite (PVK) films for solar cell applications, and how to make use of them for scaling up purpose. The main conclusions are summarized below.

Firstly, we have written a literature review focusing on the recent progress in large-scale PSCs and the challenges for commercialization. In Chapter 2, we firstly summarize several high-volume manufacturing technologies which are suitable for scalable deposition of PVK film. Afterwards, we discuss the challenges for scaling up different PVK layers. Finally, an overview of efficiency and stability of large area PVK-based monolithic tandem solar cells is provided.

Secondly, we have developed a simplified approach consisting of a single-cycle deposition (SCD) of three thick layers of precursors to obtain thermally deposited perovskite films by means of an optimized post-annealing treatment. In Chapter 3, we optimize the thermally deposited PVK films with a simplified single-cycle deposition. By varying the film thickness and post-annealing time, we indicated that the maximum precursor mixing/diffusion thickness is roughly 250 nm based on the single cycle deposition consisting of the three precursors layers. As the target thickness increases to 400 nm, the film shows a drop in opto-electronic properties even though it structurally shows a PVK diffraction peak with optimized annealing. This phenomenon might be explained by the limited diffusion length of these precursors in single-cycle deposited 400-nm thick PVK film. An optimized 250-nm thick PVK film was obtained with comparable properties (μ of 10 cm^2 V^{-1} s^{-1} and $\tau_{1/2}$ of 300 ns) as the one with multi-cycle deposition. Besides, the structural and optical properties are asynchronous with electrical properties during annealing, which is strongly dependent on film thickness, resulting from precursor mixing and reacting. In addition, we noticed that the presence of CsBr can assist the precursor mixing during annealing, which is beneficial to the fast precursor reaction and PVK conversion.

Thirdly, we have repeated the single cycle deposited perovskite with intermediate annealing to manipulate the crystal orientation. In Chapter 4, we present a method

to manipulate the crystal orientation of the thermally deposited layers by applying an intermediate annealing treatments at different temperature between two subsequent deposition cycles. Through analyses on the crystal structure, surface morphology, optical properties and intermediate annealing temperature-dependent electrical properties, the template guided different perovskite preferrable crystal growth were proposed. By optimizing the intermediate annealing temperature, we demonstrate that the crystal orientation can be tailored ranging from primarily (110) to near isotropic to predominantly (100). Our results indicate that the degree of precursor reaction upon different intermediate annealing temperatures of the first stack influences the preferred crystal orientation of the entire PVK film by providing different templates for the subsequent deposition. In addition, We found that although bulk electronic properties like photoconductivity are independent from the preferential orientation, surface related properties differ substantially. Therefore, realizing uniform PVK layers with a highly preferential (100) orientation is expected to show improved charge extraction and transportation at the device level.

Finally, we have implemented the abovementioned techniques to prepare thermally deposited perovskites for devices scaling up. In Chapter 5, we fabricate and characterize perovskite films and devices with the sequential thermal evaporation approach as reported in Chapter 3. By varying the annealing temperature, the grain size increases significantly from less than 500 nm to almost 1 μm as the annealing temperature increase from 130 °C to 170 °C. Moreover, a trance of $PbCl_2$ is introduced as precursor, improving the perovskite crystallinity as evidenced by XRD, SEM, PL, and device performance. The champion efficiency is observed based on device with $PbCl_2$ and annealed at 150 °C, achieving a maximum power conversion efficiency of 18.5% with V_{oc} and *FF* equal to 1.01 V and 78.5%, respectively, for 0.09 cm^2 cell area. Building on these optimized parameters, we scaled the device size up from 0.09 cm^2 to 0.36 cm^2, and 1 cm^2, while keeping almost unaffected open circuit voltage of above 1 V. Besides, 15.6×15.6 cm^2 perovskite films are prepared with uniform crystallization and comparable photovoltaic parameters over the whole area, showing less than 10% thickness variation across different positions. These results indicate the potential application of this technology for commercialization of perovskite solar cells.

6.2. Limitations of this work

In many experiments, various limitations are encountered, such as small details within the experiment, the stability of materials used, and the reliability of the equipment. This work is no different and this section covers the manner in which such limitations influence the outcomes reported in the experimental chapters.

Reproducibility. The issue of reproducibility remains of importance in the field of perovskites and is a key parameter across experiments toward commercialization. In this thesis, sequential thermal evaporation shows good reproducibility as long as attention is paid to some small details. The most important of them is to control the overshoot of temperature. Especially for the organic salt, a thermal overshoot will mostly result in a chemical vapor, which will influence film properties. Besides, cooling down of the source is needed to wait for the next source shutter open. As for the powder reuse, it has not been seen much difference for batch-to-batch variation with the reused powder, even

for the organic ones. However, it is better to further investigate the impact of precursor aging in the future.

Degradation of HTL. Improved perovskite quality (grain size and mobility) has been observed at high annealing temperature (170 °C). However, PTAA will partially degrade with too high annealing temperature, leading to traps at the HTL/perovskite interface. Therefore, it is better to replace the PTAA with more stable HTLs such as NiOx/SAMs for higher efficiency solar cell .

Device stability. It has been noticed that the perovskite film shows good stability in air but poor moisture stability for device level. This mainly comes from the reaction of Ag and I in perovskite. The C60/BCP are very thin, 20 nm and 2 nm, respectively. The C60 is not very dense film, which lead to easy diffusion of Ag through the ETL. For the future work, thicker BCP (8 nm) or ALD deposited SnOx or Al_2O_3 should be applied for improved cell stability.

Long processing time. The optimized sequential evaporation process on our laboratory scale evaporation chamber takes more than 12 hours to deposit 500 to 600-nm thick perovskite films. The deposition of precursors is very quick, but the temperature ramping up of each sources takes an extended period of time. In the longer term, line-based sources with moving substrates does not require alternate ramp up of sources making this technology industrially appealing.

6.3. Outlook

Several areas relevant to the development of thermally deposited perovskite solar cells are described in this thesis. This section elaborate further on crucial aspects that are expected to become the focus of the future research.

Balance between V_{oc} and *FF*. As discussed in Chapter 3, we evidenced the presence of diffusion limitation of PVK precursors when attempting to increase the thickness of the layers of the unit PVK stack, as also evidenced at the cell level. If there is obvious non-reacted PbI_2 precursors in bulk, related PSCs will show obvious S-shape curve. Besides, we noticed a very obvious trade-of between V_{oc} and *FF* of the cells during optimization, high probably attributed from the level of precursor reaction. Therefore, it is advised to target a thinner unit stack and repeat the cycle to obtain the final PVK thickness. With that approach, a larger process window is avaliable for introducing other lead halide PbX_2 for sequential depositions.

Bi-HTL layers. In our works, we have noticed substrate influenced perovskite composition change during thermal evaporation. Even though the PbI_2 serves as template layer, there is still composition change when the substrate property changes, for example, the level of substrate crystallization (HTL here in HTL/PVK/ETL structure), and chemical composition (metal oxide or organic materials). In this respect, bi-HTL metal oxide/organic materials such as NiO_x/SAMs, MoO_x/TaTm can be good options. The metal oxide keeps good thermal stability and high work function. On the other hand, organic surface will block the interaction (coordination effects) between metal oxide and Pb^{2+}, which could accelerate the degradation of perovskite at interface.

Development of solar cells with area above 1 cm^2. To fabricate PVK PV on an industrial scale, the focus needs to be on (1) highly efficient absorber materials; (2) industrially viable throughput rates (dynamic deposition rates in industrial terminology); and (3) the

lowest possible complexity of the deposition process [432]. Aiming at these targets, the following aspects are proposed and discussed as follows:

1) *Control the quality of the absorber layers and bottom transporting layer.* PSCs deposited with thermal evaporation technique still need to reduce non-radiative recombination and improve charge transport to achieve the highest possible V_{oc} and *FF*. Even though thermal evaporation demonstrated to be a suitable technology to fabricate pinhole-free PVK films, as reported in Chapter 5, shunting problem still dominates the efficiency drop when cell area increases. Therefore, it is crucial to control the crystallinity of perovskite and control the quality of the bottom transporting layer to ensure cracks-free films. Besides, interfacial traps are also one crucial factor influence the power conversion efficiency, traps at interface can be suppressed by controlling the grain growth and applying interfacial modification/passivation.

2) *Increasing deposition rate.* Sequential thermal evaporation is compatible with in line production of PVK films compared to co-evaporation. In our laboratory scale process, the PVK film deposition with a thickness around 600 nm takes more than 12 hours, which is way longer compared to co-evaporation. The long-time processing results from the slow source temperature ramping up and the low deposition rate. Two actions are proposed to mitigate this issue. Firstly, increasing the deposition rate of each precursor depositions can accelerate the full process. Recently, few research works [433, 434] demonstrated a stable soler cell performance for co-evaporated $MAPbI_3$ films down to less than 30 mins. We expect an increase of the deposition speed up to 1-3 nm/s which can reduce the sequential process down to 20 mins. Secondly, the further reduction of the number of precursor cycles. Currently in our work we demonstrated a minimum of two cycle of precursors (see Chapter 3). Further process optimization and the use of seed layers is expected to lead to an even simpler process with only one precursor cycle. This further reduction is attractive for the in line-deposition in industrial environment where only 3-4 sequential precursor depositions are needed.

3) *Reliability test study.* One key issue of the large-area PSCs is the long-term stability. The reliability test is still a not completely explored topic, which is crucial for perovskite large area industrial upscaling. As reported from Oxford PV, the thermally evaporated PVK cells are superior to the solution-based ones, when tested for hundreds of hours under different illumination conditions and 85 °C, the degradation mechanism and the control of the performance under operative conditions are not conclusive yet.

Perovskite solar cell for application in tandem device. PVK/c-Si tandem device attracts much attention because of the stable and mature c-Si technology, and tunable bandgap of the PVK top cell. Based on the ITRPV roadmap [435], the tandem cell is expected in the marker already in 2028. Aiming at this target, following aspects are proposed for further investigation:

1) *Exploring texture in the tandem cells.* For PVK/c-Si tandem solar cells industrialization, the use of a commercially available c-Si bottom cells without deep modifications of their production is preferable. This requirement implicates the growth of PVK subcells on pyramidal textured substrates. Few groups have proposed strategies to control the PVK deposition on rough substrates as we reviewed in Chapter 2. Thermal evaporation or hybrid approach demonstrated a conformal growth of the PVK absorber (see also Chapter 2). However, the substrate effects can strongly influence the perovskite com-

position, which leads to poor crystallization and increase of trap densities. Therefore, introducing surface modification layers on textured surface will minims the substrate effects and ensure the conformal growth of absorber layer. Besides, manipulation of the PVK crystal orientation by introducing seed/template layers is also beneficial to the carrier transportation and collection.

2) *Thermal evaporation of wide-bandgap perovskite.* To exploit the highest efficiency possible of a tandem device the current matching requirement is crucial. As discussed in Chapter 2, the optimal PVK band gap is around 1.7 eV. Practically, in most of the reported works, as discussed in Chapter 2, PVK bandgaps are slightly lower in the range of 1.65-1.68 eV clearly indicating a limitation in the electrical quality of larger bandgap PVK absorbers. To reach the suitable bandgap, higher Br/I ratio is needed by incorporating more Br, which leads to low carrier mobility and high trap densities, and therefore results in reduced carrier diffusion length. Besides, the photon induced phase segregation will accelerate the formation of traps in these wide-bandgap perovskite films. To minimize the perovskite phase segregation, it is important to suppress the mobile ion under bias or light. In our previous work (unpublished), we investigated sequential evaporation for wide-bandgap PVK by subsequently depositing PbI_2, $PbBr_2$, FAI and CsBr to form one stack. Here, we noticed comparable phase segregation as reported for perovskite films with the same composition but deposited *via* spin coating. To further progress in the application of wide-bandgap perovskites, the distribution of Br/I in the bulk of the PVK film needs to be carefully kept uniform to slow down the likelihood of phase segregation. Therefore, possible approaches could consist in co-evaporating PbI_2 and $PbBr_2$ firstly followed by the organic evaporation. In fact, similarly to what we observed for CsBr in Chapter 3, the presence of $PbBr_2$ could be beneficial to the precursor mixing and promote the subsequent FAI diffusion. An alternative option consists in introducing a 2D PVK layer at the interface with HTL in pin configuration to partially block ion diffusion. This result can be obtained with phenethylammonium iodide that is also compatible with thermal evaporation.

A

Crystallization process for high-quality CsFAPbIBr film deposited *via* simplified sequential vacuum evaporation

This appendix provides supporting information of Chapter 3, which was included in the publication of ACS Appl. Energy Mater *.

A.1. X-ray diffraction patterns of the (100) PVK peak for different samples.

Table A.1: XRD analysis for samples with different thickness for peak (100).

Samples	(100)Peak position (°)	FWHM (°)	Intensity (a.u.)	d-value (Å)
100 nm MCD	14.26	0.163	80.5	6.259
100 nm SCD	14.25	0.186	82.4	6.263
250 nm SCD	14.24	0.096	197.8	6.267
400 nm SCD	14.24	0.145	58.79	6.267

Figure A.1 shows the XRD patterns zooming in of the (100) PVK peak for samples with different thickness. With respect to the multi-cycle layer PVK film, the single-cycle deposited layers show similar crystallinity. To have a detailed comparison, the peak position, FWHM, intensity and d-values can are listed in Table A.1. The similar peak information in peak position is also consistent with a constant I/Br ratio across the film thickness.

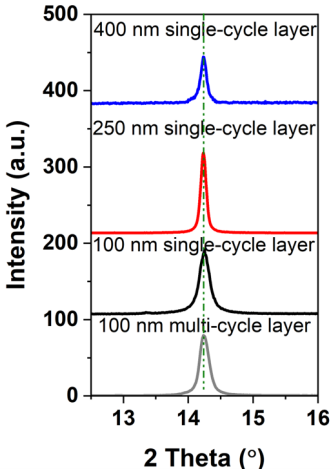

Figure A.1: X-ray diffraction patterns zooming in of the (100) PVK peak for samples produced by SCD and MCD with different thicknesses.

A.2. The grain size distribution and top view SEM of all samples

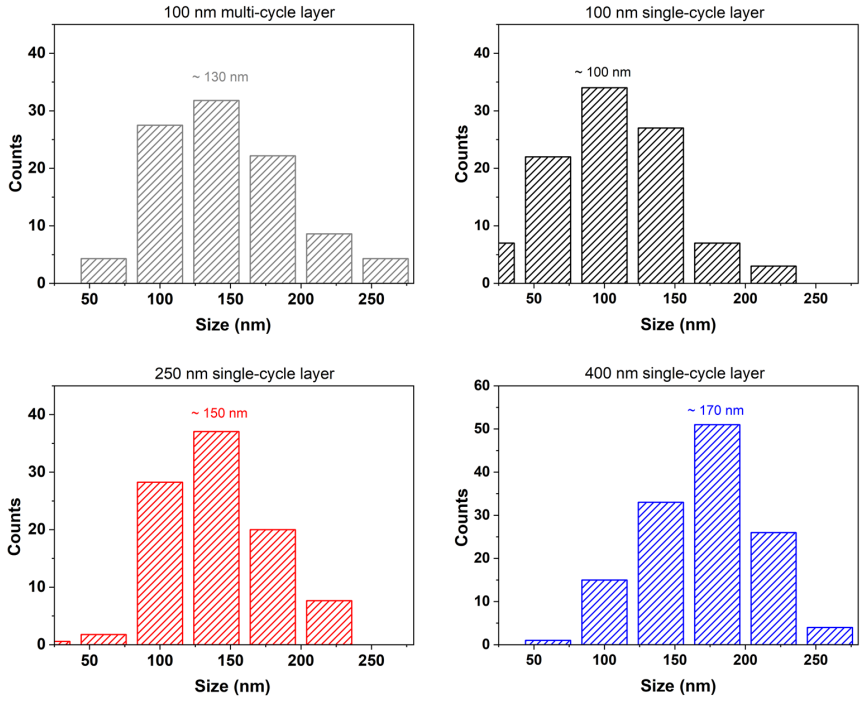

Figure A.2: The grain size distribution of all samples reported in Figure 3.1c-f. The grain sizes are collected from the top-view SEM images by using *ImageJ* software.

Looking at Figure A.2 about the two 100-nm thick samples, the SCD layer shows an average grain size of ~100 nm, which is slightly smaller than the reference MCD layer, which is around ~130 nm. The decreased grain size for the SCD film could be attributed to the increased number of nucleation sites during deposition. Furthermore, the grain size gradually increases as the film thickness increases from 100 to 250 nm. The increased grain size mainly comes from improved crystallinity.

A

A.3. Structural and optical evolution during annealing of 250 nm SCD PVK

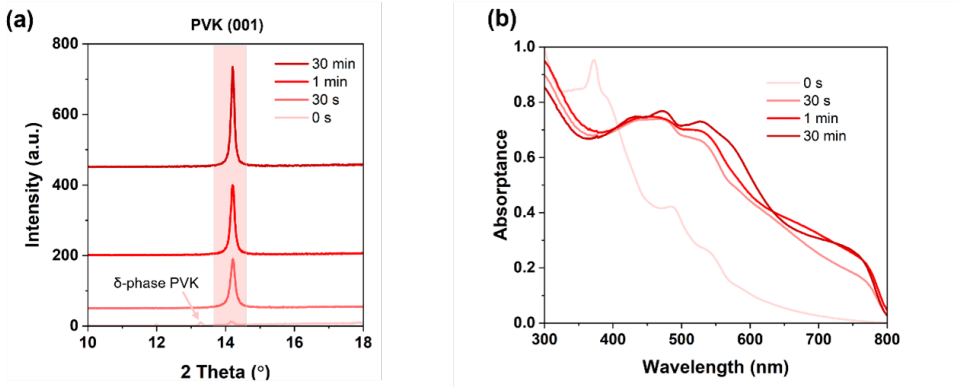

Figure A.3: Crystal structure and optical properties of 250-nm thick CsFAPbIBr layers as-deposited and annealed at 100 °C for different annealing time. (a) Zooming in of the (100) XRD peak and (b) Absorptance spectra as a function of wavelength.

For the 250-nm thick sample, there is no apparent grain shape change, while the grain size shows a slight increase from a 30 s to 30 min annealing time, in agreement with the XRD results in Figure A.3a calculated from Scherrer equation. We observe an almost stable composition along the film for the 250 nm thick sample.

A.4. Structural and optical evolution during annealing of 400 nm SCD PVK

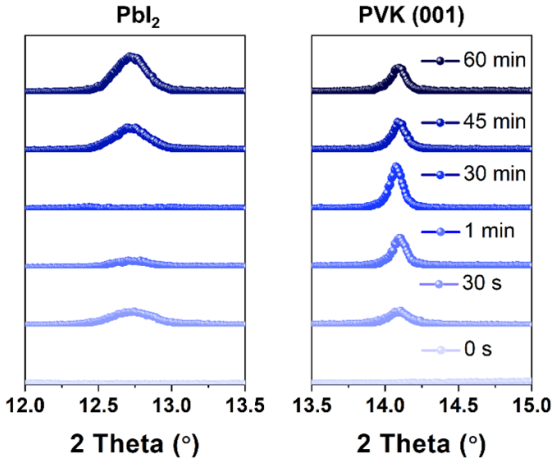

Figure A.4: Close-up diffraction patterns of PbI_2 and PVK (100) peak for 400-nm thick CsFAPbIBr annealed at 100 °C for different times between 30 s and 60 min.

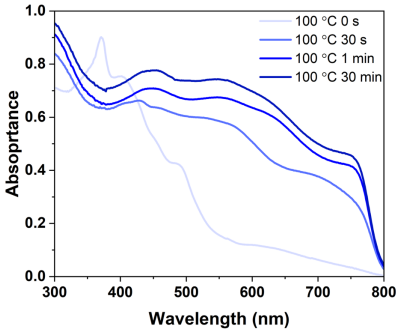

Figure A.5: Absorptance as a function of wavelength of 400-nm thick PVK.

The samples with 45 and 60 min of annealing indicate the appearance of the PbI_2 peak compared with the ones with shorter annealing times, showing some thermal degradation. Thus, the SCD 400-nm thick PVK film exhibits a problem with the balance between FAI uniform distribution and thermal degradation during annealing optimization. The PVK absorption onset starts to form after 30 s of annealing, and a continuous increase of the absorption was observed from 300 to 800 nm for longer annealing times.

A.5. Morphology evolution during annealing for SCD PVKs with different thickness

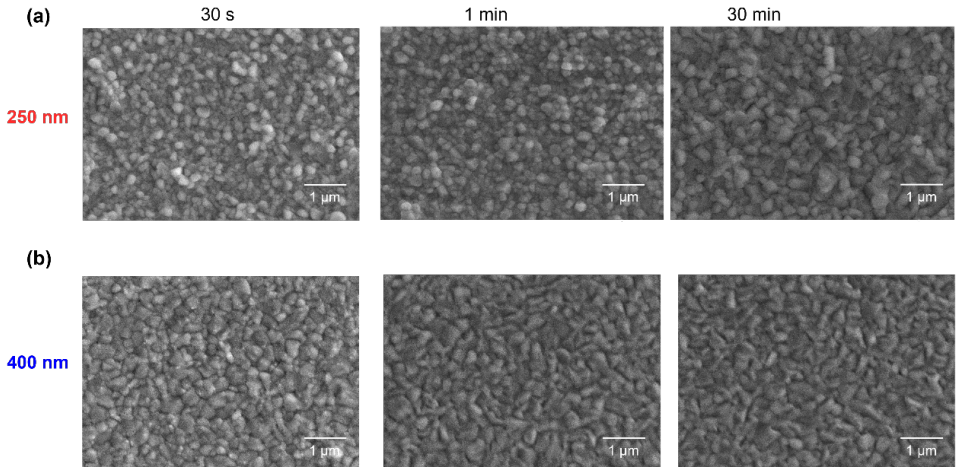

Figure A.6: The grain size distribution of all samples reported in Figure 3.1c-f. The grain sizes are collected from the top-view SEM images by using ImageJ software.

For the 250-nm thick sample, there is no apparent grain shape change, while the grain size shows a slight increase from a 30 s to 30 min annealing time. Differently, the 400-nm thick sample shows an apparent grain shape change from 30 s to 1 min, which comes from the formation of non-orientation-preferred PVK polycrystalline.

A.6. XPS data analysis and the summary of atomic percentage for different elements

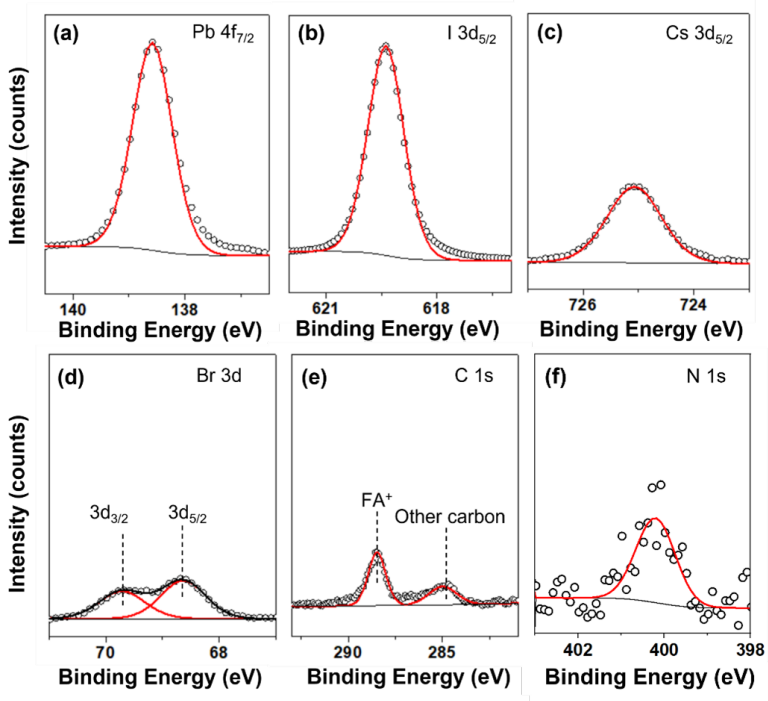

Figure A.7: XPS raw data analysis and fitting for different spectra. The red line indicates the fit to the data.

Table A.2: The averaged atomic percentage of different elements for all samples extracted from (Figure 3.2).

Samples	Cs	N (FA)	Pb	I	Br
100 nm MCD	2.62	27.34	16.25	45.48	3.12
100 nm SCD	3.20	27.59	17.52	44.67	3.08
250 nm SCD	2.84	26.92	17.11	46.82	3.28
400 nm SCD	3.05	27.88	17.08	49.42	3.30

The XPS high-resolution spectra of Pb $4f_{7/2}$, C 1s, N 1s, Cs $3d_{5/2}$, I $3d_{5/2}$, and Br 3d can be found in Figure A.7 for the 100-nm thick SCD sample as an example to show the fitting and extraction of raw data. The averaged atomic percentage of different elements for all samples extracted from Figure 3.2 are summarized in Table A.2.

A

A.7. XPS in depth element distribution

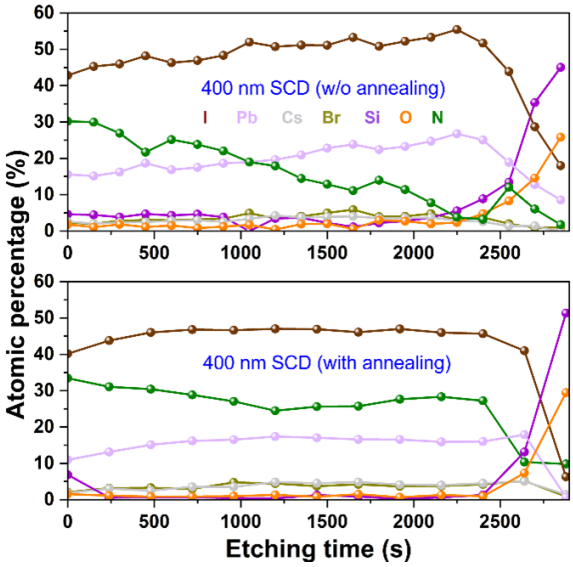

Figure A.8: XPS in-depth element distribution profile for 400-nm thick PVK films before and after annealing (100 °C, 30 min).

In the as-deposited 400-nm thick sample, we observed noticeable distribution variations with a gradual drop of the N/Pb (from ~2 to ~0.2) calculated by the atomic profile as etching goes from the PVK surface toward the PVK/quartz interface. In addition, the I/Pb ratio at the bottom of the film is equal to 2, showing that FAI can hardly penetrate through the bottom of the film. These results indicate the hampering of the FAI diffusion into the PbI_2 during deposition (without annealing). On the contrary, both Br and Cs are detected across the entire PVK film thickness even though the Br/Pb ratio gradually decreases when approaching the PVK/quartz interface. This finding further confirms the longer diffusion length of CsBr in PbI_2 compared to FAI.

A.8. Optoelectrical properties of SCD samples with different thickness

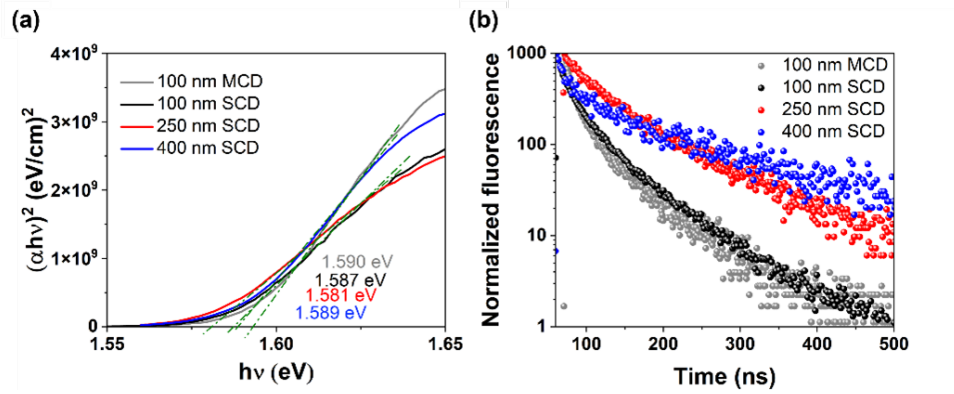

Figure A.9: Optoelectrical properties of 100-nm MCD and SCD layers with different thicknesses. (a) Tauc plot and (b) TRPL decays.

Table A.3: The fitting of TRPL and corresponding decay lifetime for all samples

Samples	τ_1	τ_2	χ^2
100 nm MCD	7.07	42.82	0.997
100 nm SCD	11.36	50.34	0.999
250 nm SCD	31.30	96.88	0.995
400 nm SCD	10.85	129.91	0.088

All these samples present a sharp absorption edge corresponding to a bandgap of ~1.58 eV as determined by the Tauc plot of Figure A.9a. These values are in agreement with published work on PVKs having a similar composition.

The dynamics of the charge carrier recombination are analyzed by TRPL as shown in Figure A.9b. Interestingly, the 250-nm thick sample shows an even longer lifetime compared to the 400-nm thick sample, benefiting from its better crystal orientation.

A

A.9. TRMC of SCD samples with different thickness

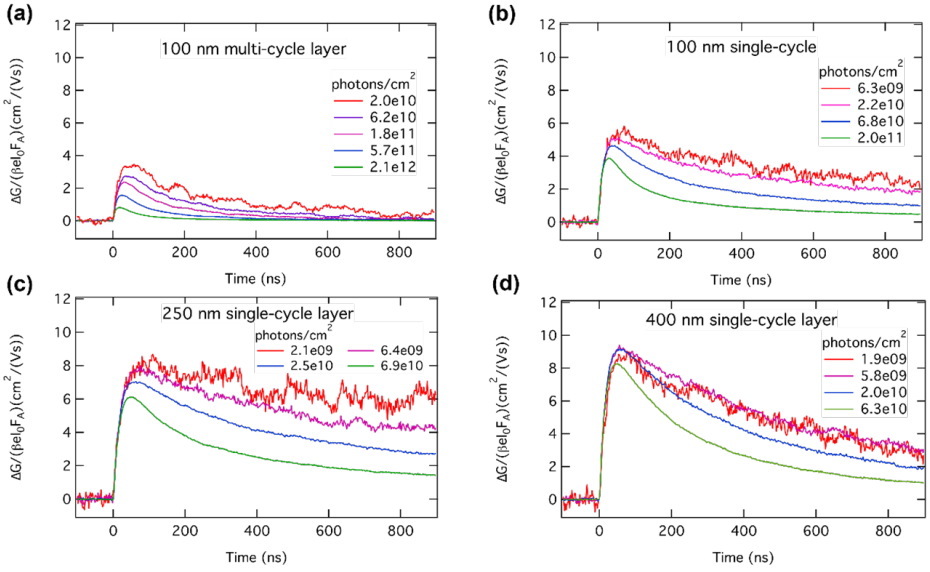

Figure A.10: TRMC with various incident light intensities based on samples with different thickness.

Table A.4: The averaged atomic percentage of different elements for all samples extracted from (Figure 3.2)

Sample	$\tau_{1/2}$ (ns)	**Mobility (cm^2/Vs)**	**Ref.**
100 nm MCD	360	3.6	-
100 nm SCD	410	5.2	-
250 nm SCD	650	7.3	-
400 nm SCD	400	8.8	-
100 nm $MAPbI_3$	280	7.5	[1]
300 nm $MAPbI_3$	210	4.0	[2]
400 nm $FAPbI_3$	2.8	31	[3]

The TRMC with various incident light intensities is shown in Figure A.10 based on samples with different thicknesses. It should be noted that both the 250 and 400-nm thick samples exhibit comparable carrier mobility and lifetime to other published works, which are based on thermal coevaporation methods; the detailed data are summarized in Table A.4. Therefore, we conclude that the variation of thickness in SCD affects the film optoelectronic properties performance because of the precursor diffusion, reaction (Figure 3.2), and crystal growth (Figure 3.1).

A.10. PL as a function of wavelength of 400-nm thick PVK

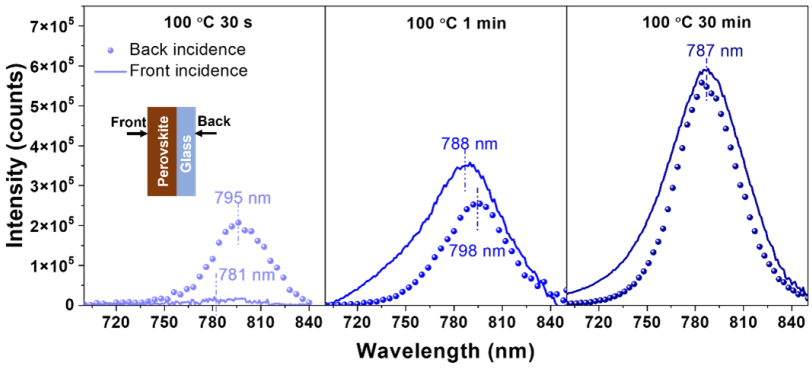

Figure A.11: Absorptance as a function of wavelength of 400-nm thick PVK.

PL spectra were also recorded as a function of the annealing time by illuminating through the quartz substrate (back) and PVK surface (front) of the 400-nm thick SCD sample as shown in Figure A.11. The peak shape and position are altered by illuminating from different sides for both 30 s and 1 min annealed samples, suggesting that there are compositional changes through the cross section of the film.

B

Vacuum deposited perovskites with a controllable crystal orientation

This appendix provides supporting information of chapter 4, which was included in the publication of J. Phys. Chem. Lett. *

B.1. XRD pattern information of samples with different T_{inter}.

Table B.1: Full-width half-maximum (FWHM) of (100) and (110) peaks for samples with different T_{inter}.

T_{inter} (°C)	FWHM (100)	FWHM (110)
w/o A	0.130	0.170
50	0.148	0.191
100	0.154	0.191
130	0.148	-
160	0.145	-

The difference in full width at half-maximum (FWHM) of the (100) and (110) peaks is negligible as T_{inter} increased, as shown in Table B.1, suggesting a comparable crystallite size in all samples.

B.2. Top view SEM and grain size distribution of samples with different T_{inter}

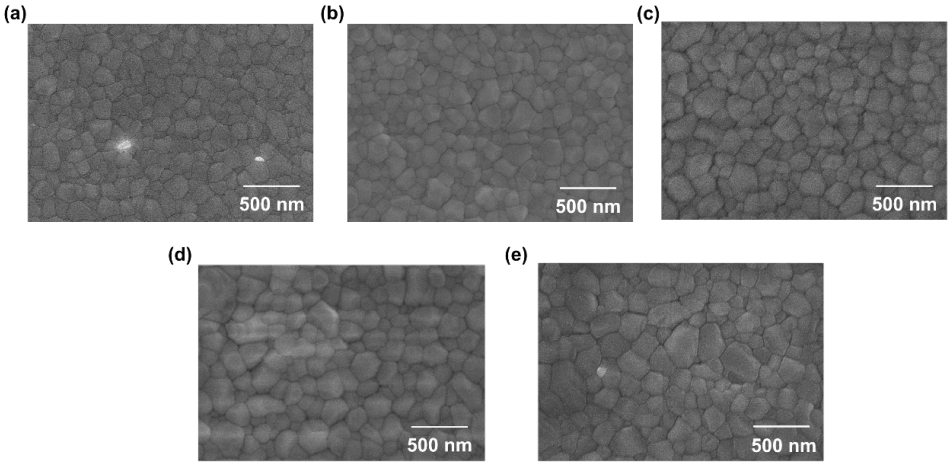

Figure B.1: Top-view SEM of $Cs_{0.15}FA_{0.85}PbI_{2.85}Br_{0.15}$ samples with different T_{inter} (a) *w/o*-A, (b) 50 °C, (c) 100 °C, (d) 130 °C and (e) 160 °C.

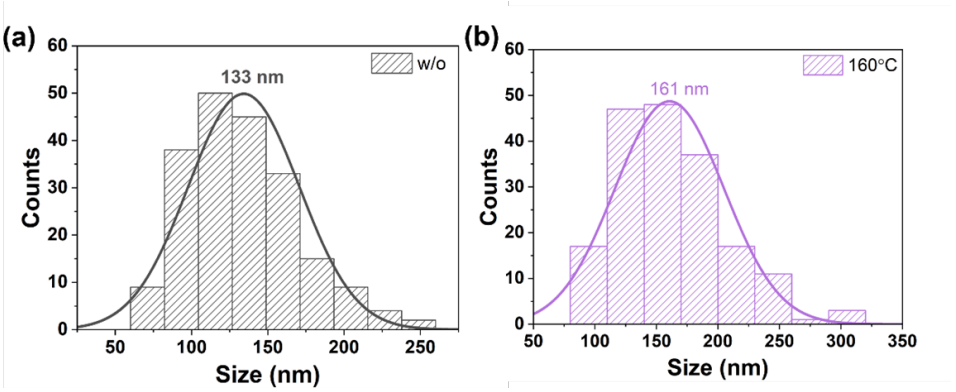

Figure B.2: Grain size distribution of $Cs_{0.15}FA_{0.85}PbI_{2.85}Br_{0.15}$ samples (a) *w/o*-A and (b) T_{inter} of 160 °C reported in figure B.1. The grain sizes are collected by using ImageJ software.

The top-view SEM images of these samples are shown in Figure B.1. In agreement with the XRD results, there is no clear grain size variation as the crystal orientation changes. We show in Figure B.2 the grain size distribution for samples with T_{inter} of *w/o*-A((110)/(100)-mixed) and 160 °C ((100)-oriented).

B.3. Intergration of (100) diffraction pattern of 2D XRD.

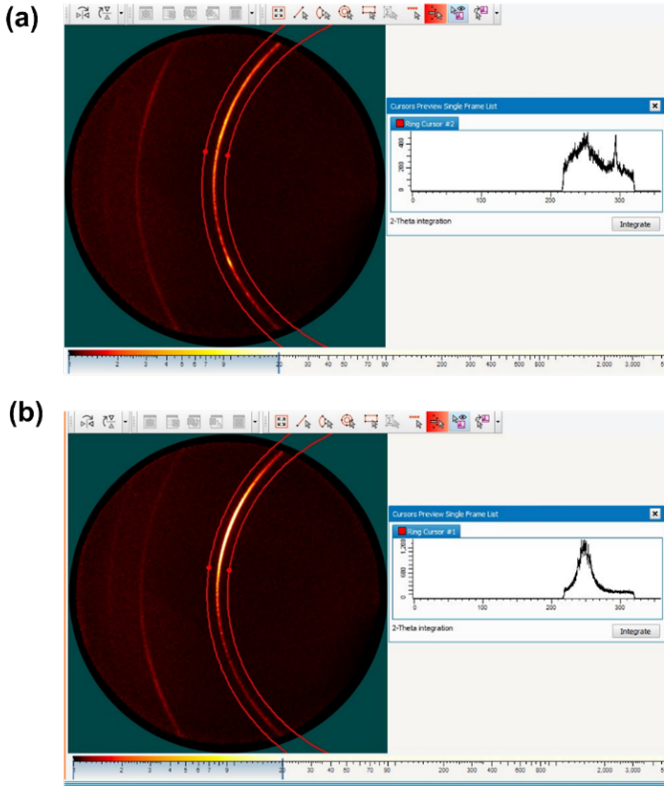

Figure B.3: Integration of the (100) diffraction ring of 2D XRD pattern with software (DIFFRAC.EVA). (a) *w/o*-A (b) 130 °C.

Details about the integration process can be found in Figure B.3.

B.4. Simulated XRD patterns with varying degrees of texture.

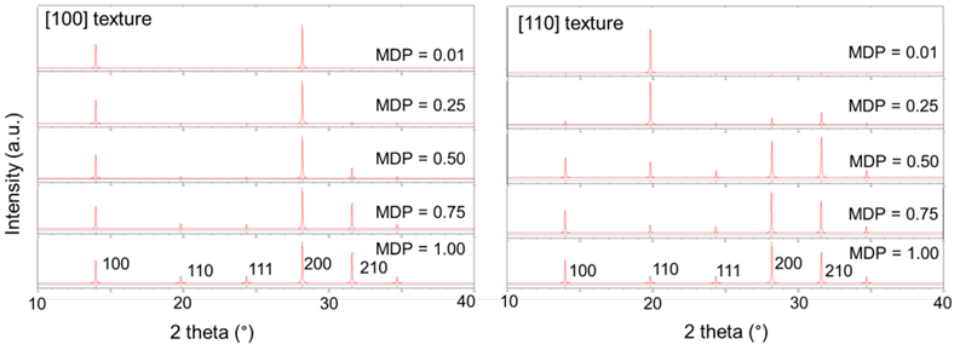

Figure B.4: XRD pattern simulation of samples textured along (100) and (110) orientation with varying degrees of texture defined by the March–Dollase parameter (MDP). Software named PowderCell2.4 was used.

Table B.2: Simulated peak intensity with different preferred orientation/MDP value.

2 Theta (°C)	**hkl**	**Intensity (a.u.) with [100] texture**				
		MDP 1.00	MDP 0.75	MDP 0.50	MDP 0.25	MDP 0.01
13.99	100	100.00	100.00	100.00	100.00	100.00
19.83	110	30.72	23.58	7.16	0.39	0.00
24.35	111	29.41	21.53	6.01	0.31	0.00
2 Theta (°C)	**hkl**	**Intensity (a.u.) with [110] texture**				
		MDP 1.00	MDP 0.75	MDP 0.50	MDP 0.25	MDP 0.01
13.99	100	100.00	100.00	100.00	8.18	0.00
19.83	110	30.72	34.38	78.73	100.00	100.00
24.35	111	29.41	31.29	36.26	3.30	0.00

To analyze the preferential orientation of the grown PVK layers with different values of T_{inter}, the peak intensities for layers with different orientations were simulated and can be found in Figure B.4 and Table B.2. These X-ray diffraction patterns have increasing preferential ordering along the (100) or (110) directions as defined by the March-Dollase parameter (MDP) with a MDP of 1 corresponding to the absolute random orientation and a lower MDP value corresponding to increasing preferential orientation. The sample with T_{inter} = 100 °C shows peak intensities comparable to those of the simulation with no preferential oriented PVK (MDP = 1).

B.5. Wide XPS image and list of atomic percentages for samples with T_{inter} of *w/o*-A and 160 °C.

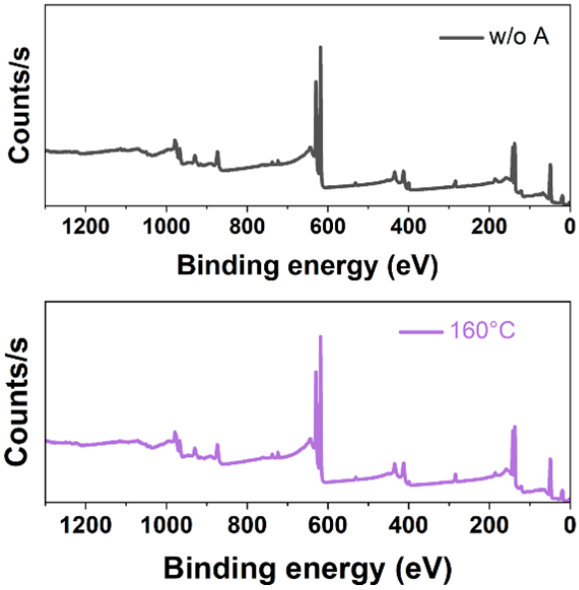

Figure B.5: Wide XPS image of the samples with T_{inter} of *w/o*-A and 160 °C.

Table B.3: Atomic percentage of Pb, I, Cs, and Br for samples with T_{inter} of *w/o*-A and 160 (°C).

Atomic percentage	***w/o*-A**	**160 (°C)**
Pb	19.43	24.18
I	72.08	70.54
Cs	3.23	2.91
Br	5.26	2.37

Full XPS spectra for the first stack samples *w/o*-A and 160 °C. the ratio of FAI/PbI_2 at the film surface can be obtained by calculating the (I-2Pb)/Pb ratio, which is 1.71 and 0.91 for the samples *w/o*-A and T_{inter} = 160 °C, respectively (Table B.3). Apparently, the difference in (I-2Pb)/Pb for these two samples provides different templates for the growth of the next stack.

B.6. Fine XPS information for samples with T_{inter} of *w/o*-A and 160 °C.

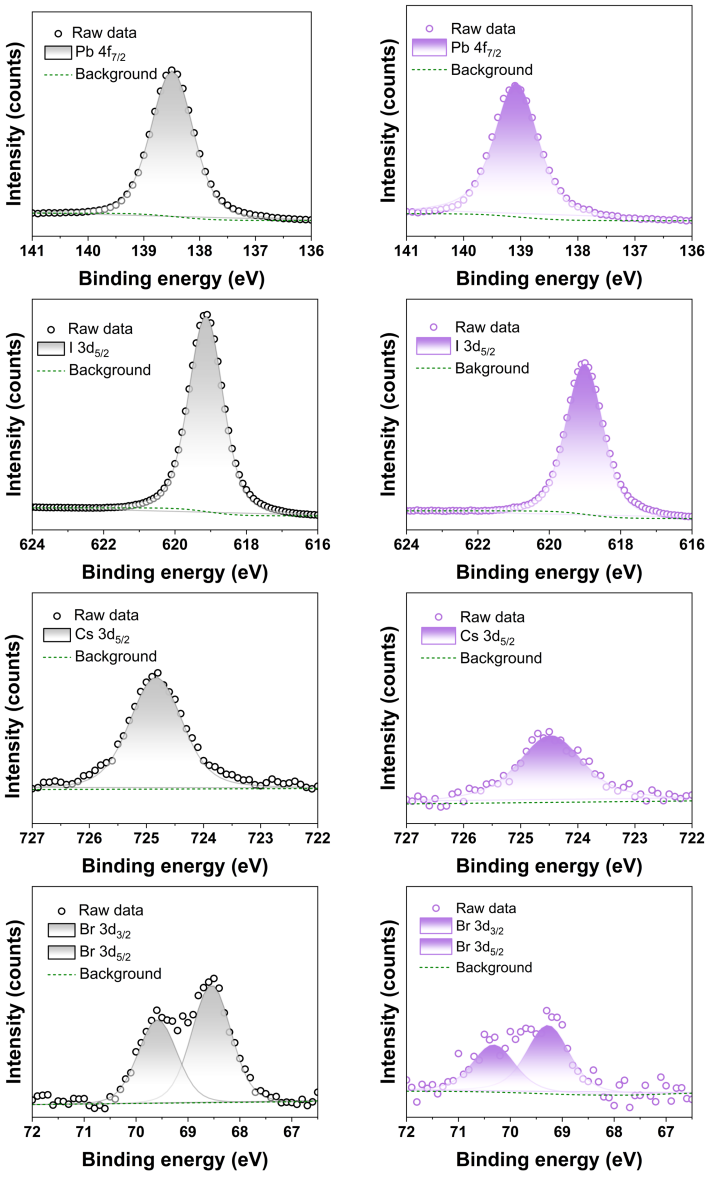

Figure B.6: Fine XPS images of Pb $4f_{7/2}$, I $3d_{5/2}$, Cs $3d_{5/2}$, Br $3d_{5/2}$, and Br $3d_{3/2}$ peaks with different T_{inter} for first stacks.

The high-resolution spectra of Pb $4f_{7/2}$, I $3d_{5/2}$, Cs $3d_{5/2}$, and Br 3d are shown in Figure B.6. The corresponding peak positions and atomic percentages are given in Tables

Table B.4: Peak positions of cores in XPS spectra for samples with T_{inter} of *w/o*-A and 160 °C.

XPS	***w/o*-A**	**160 °C**	**Ref**
Pb $4f_{7/2}$	138.5	139.1	138
I $3d_{5/2}$	619.1	619.0	619
Cs $3d_{5/2}$	724.8	724.5	724
Br $3d_{5/2}$	68.5	69.3	69

B.3 and B.4. The peak position of Pb $4f_{7/2}$ shows 138.5 eV for sample *w/o*-A, while it shifts to 139.1 eV for the sample with 160 °C. These peak positions are all calibrated by C 1s spectra at 284.8 eV. Interestingly, the reported binding energy of Pb $4f_{7/2}$ in PbI_2 for the literature value is 138.5 eV, indicating that the Pb still exists in the form of PbI_2 on the surface of the sample *w/o*-A.

B.7. XPS spectrum of the pure precursors

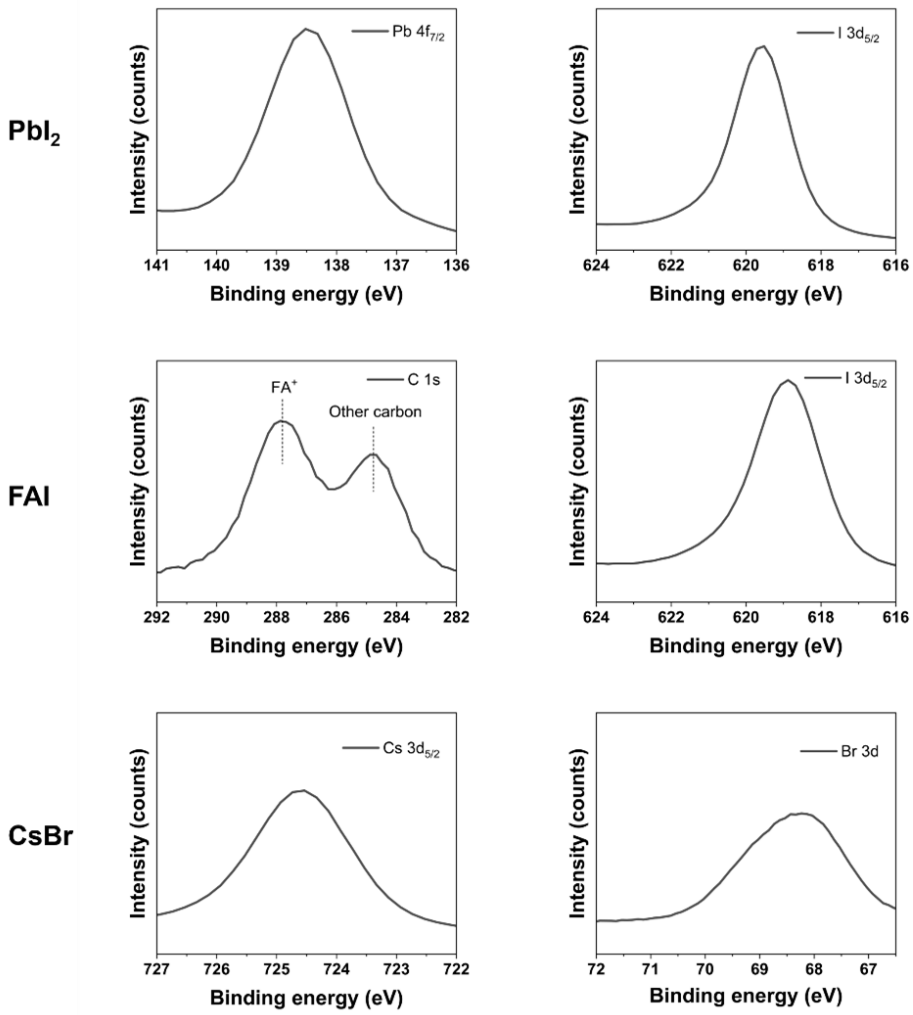

Figure B.7: XPS spectrum of the pure precursor (PbI_2, FAI, and CsBr) with surface scan.

The high-resolution spectra of Pb $4f_{7/2}$, I $3d_{5/2}$, Cs $3d_{5/2}$, and Br 3d measured with XPS for pure precursors.

B.8. Gaussian fitting of XRD patterns and PL spectrum

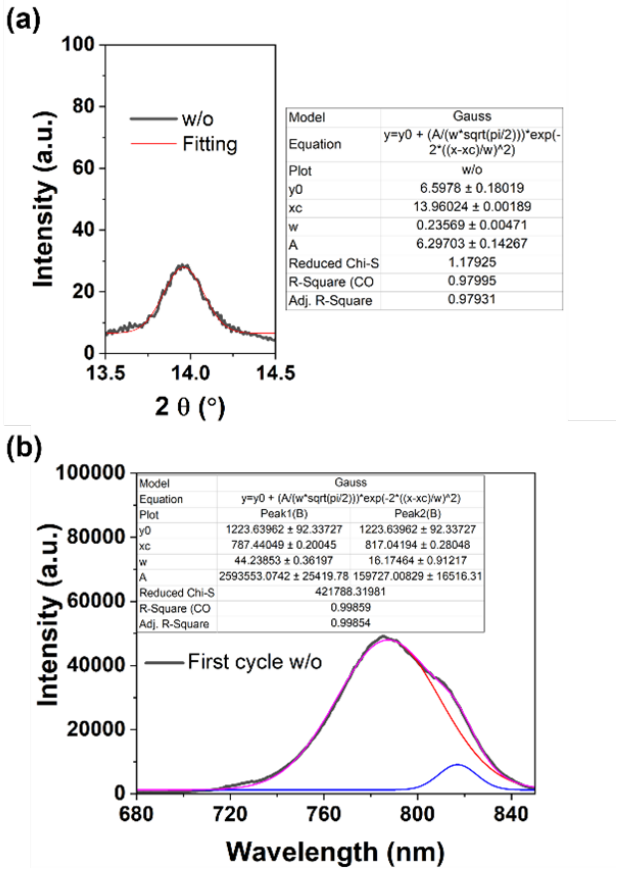

Figure B.8: Gaussian fitting of (a) XRD pattern and (b) PL spectrum of the first cycle-deposited sample *w/o*-A.

Because the (100) PVK peak in the XRD pattern can be fitted using a single Gaussian as shown in Figure B.8, it is expected that the PVK composition is rather uniform. It is likely that the presence of unreacted precursors might lead to the formation of shallow emissive states, resulting in the appearance of the shoulder in the PL spectrum at 810 nm.

B.9. Optoelectrical properties of samples with different T_{inter}

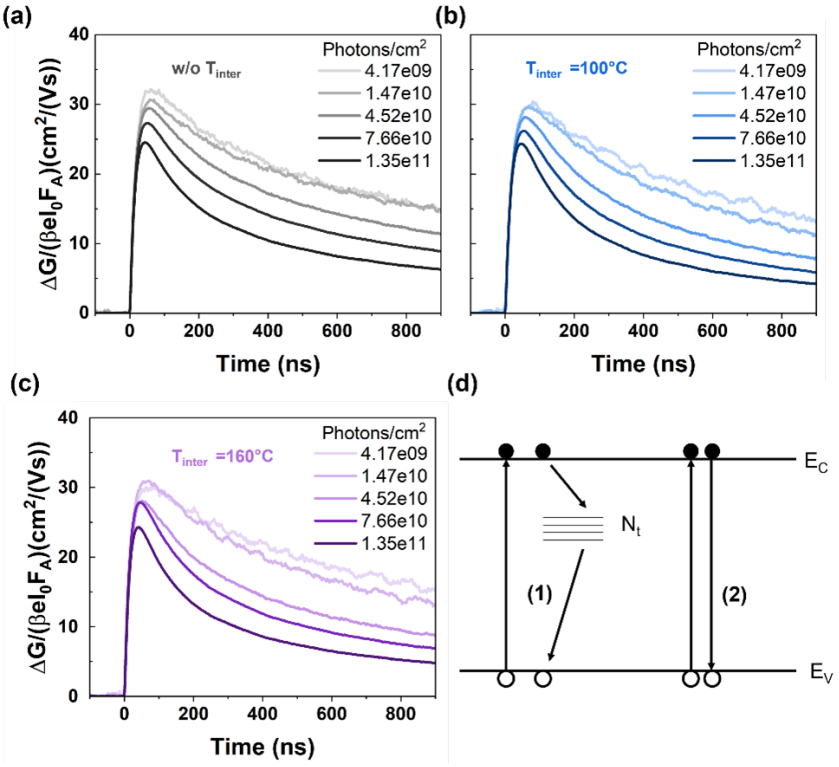

Figure B.9: TRMC of samples measured under different photon intensities for different T_{inter}: (a) *w/o*-A, (b) 100 °C, and (c) 160 °C. (d) Kinetic model of the charge-carrier processes.

Table B.5: Decay times obtained from TRPL and fitted by mono-exponential decay equation.

Samples	$\tau_{1/2}$	χ^2
w/o-A	45.98	0.998
100 (°C)	59.85	0.999
160 (°C)	83.14	0.999

All the TRPL spectra are fitted by mono-exponential decays, and the corresponding lifetimes and deviation (χ^2) are summarized in Table B.5. These PL measurements indicate that at least the surface of the PVKs prepared using different values for T_{inter} develops different surface properties. TRMC gives information regarding charge carrier mobilities and lifetimes. Figures B.9a-c show the photoconductance (ΔG) as a function of time on pulsed excitation for the samples *w/o*-A, T_{inter} = 100 °C, and T_{inter} = 160 °C.

B.10. CPD distribution for PVKs with T_{inter} of *w/o*-A and 160 °C

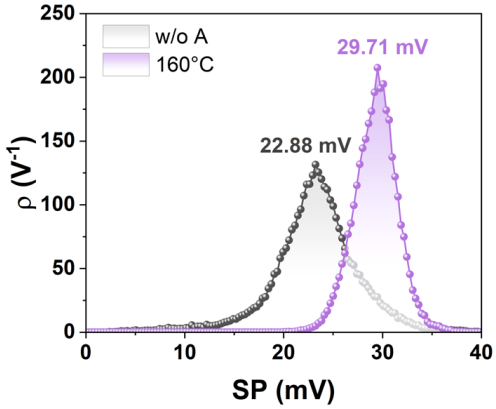

Figure B.10: Histogram of the contact potential difference (CPD) distribution for PVKs with (100) preferable and (110)/(100) mixed orientation.

The sample *w/o*-A exhibits a low averaged CPD of 22.8 mV combined with a large standard deviation of ±0.95 mV. On the contrary, the sample with T_{inter} = 160 °C shown in Figure 4.5d shows a large and quite uniform averaged CPD of 29.7 mV and a standard deviation of ±0.47 mV. The CPD distributions of both images are converted into histograms in Figure B.10.

C

Scalable and simplified sequential vacuum deposition for perovskite solar cells

This appendix provides supporting information of Chapter 5, which was included in the manuscript in preparation.

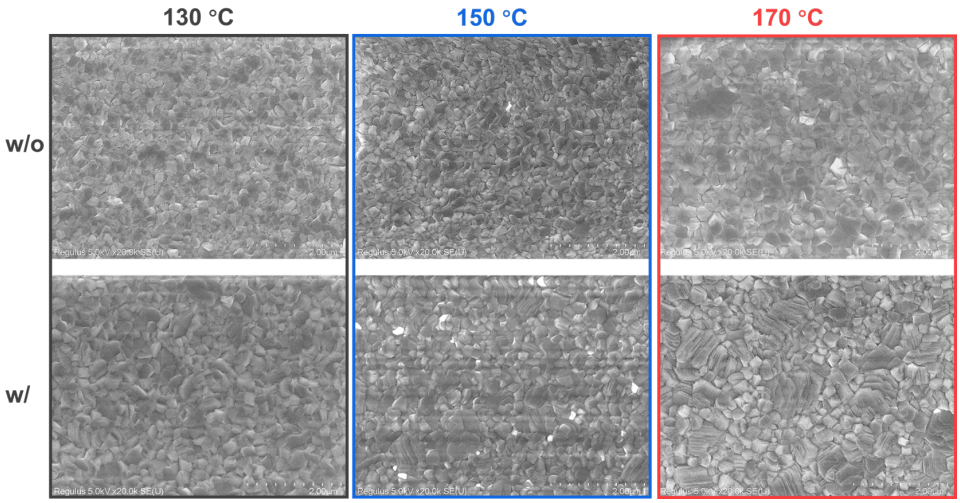

Figure C.1: Top-view SEM of samples *w/o* and *w/* $PbCl_2$ annealed at different temperatures.

Table C.1: Peak position of (100) for samples *w/o* and *w/* $PbCl_2$ annealed at different temperature.

Annealing temperature (°C)	***w/o* $PbCl_2$**	***w/* $PbCl_2$**
130	13.927	13.889
150	13.891	13.885
170	13.878	13.871

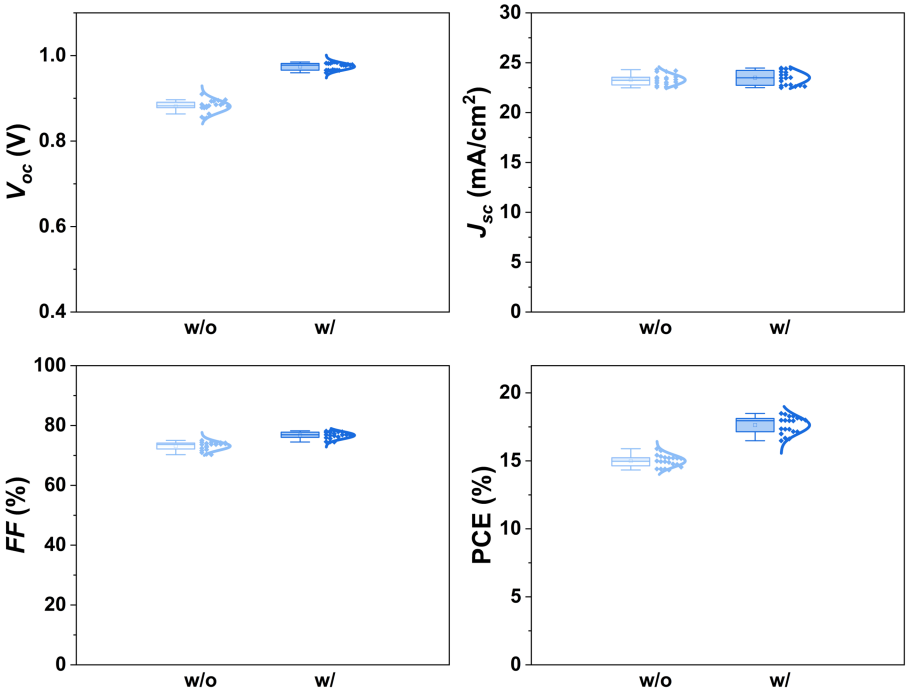

Figure C.2: Statistical distributions of the photovoltaic parameters (V_{oc}, J_{sc}, *FF*, and PCE) of solar cells *w/*- and *w/o*- $PbCl_2$. Each condition includes 20 solar cells.

Table C.2: The photovoltaic parameters and *hysteresis index* for the PSCs shown in Figure 5.4a-c.

Cell area (cm^2)	V_{oc} (V)	J_{sc} (mA/cm^2)	*FF* (%)	PCE (%)
0.09 Forward	1.001	24.77	78.24	19.4
0.09 Reverse	0.999	23.98	76.74	18.4
0.36 Forward	1.07	23.64	68.32	17.29
0.36 Reverse	1.07	23.06	67.14	16.57
1 Forward	1.030	19.14	55.64	10.97
1 Reverse	1.033	19.35	55.63	11.13

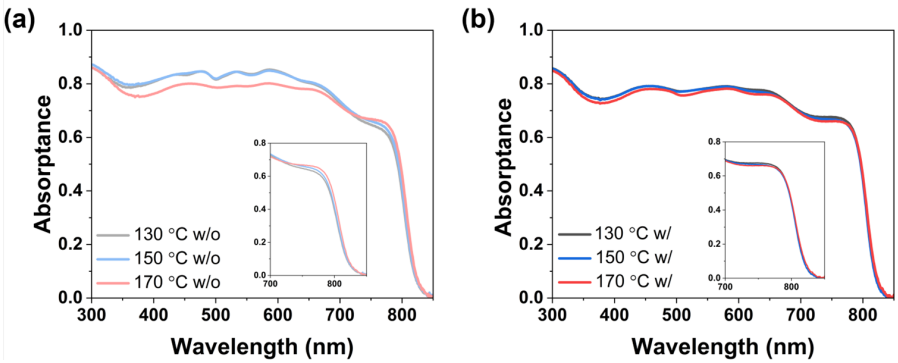

Figure C.3: Absorption spectra of samples *w/o*- and *w/*- $PbCl_2$ annealed at different temperatures. The inserted figure is the detailed curves by zooming in the figure in the wavelength range of 700-850 nm.

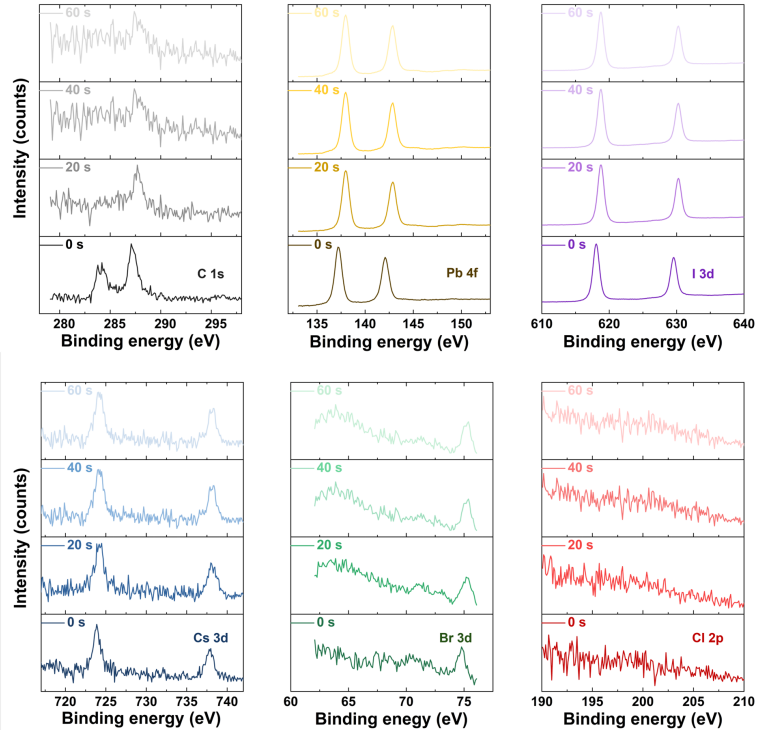

Figure C.4: Fine XPS images of C 1s, Pb 4f, I 3d, Cs 3d, Br 3d, and Cl 2p peaks with different etching time (in-depth).

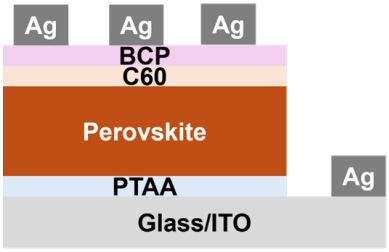

Figure C.5: Schematic structure of the solar cell.

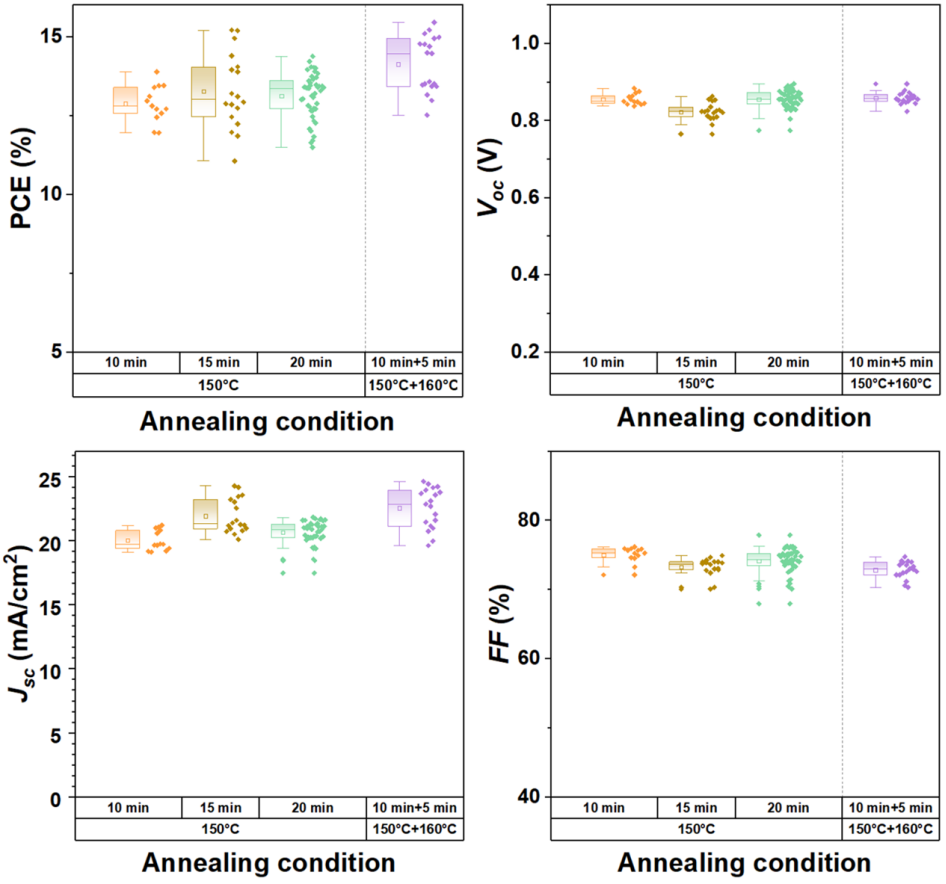

Figure C.6: Statistical distribution of PSCs *w/o*- $PbCl_2$ based on different annealing temperature and time. To classify, the purple distribution box means that the samples are annealed at 150 °C for 10 mins and afterwards 160 °C for 5 mins.

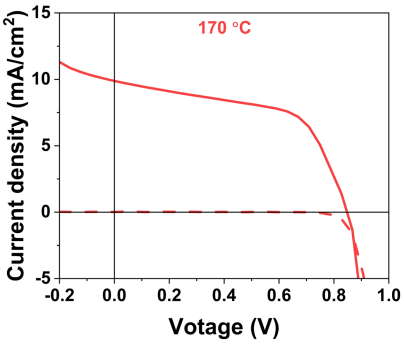

Figure C.7: *J-V* curve of the cell with 170 °C annealing for 10 mins.

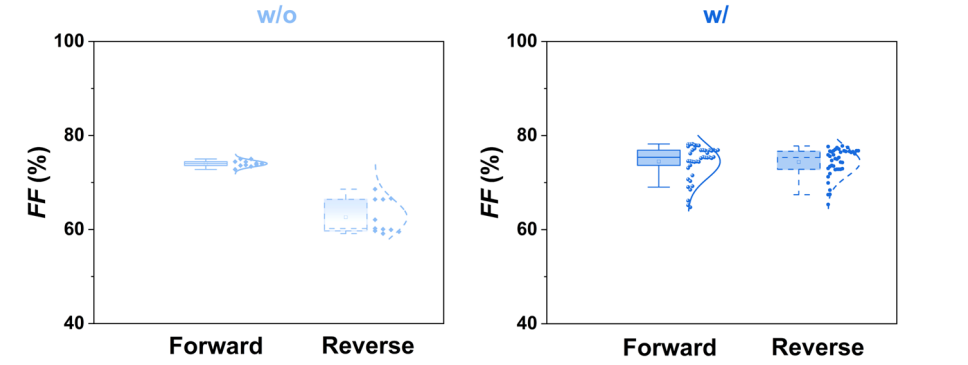

Figure C.8: Statistic distribution of *FF* with forward and reverse scan mode of the samples *w/-* and *w/o-* $PbCl_2$.

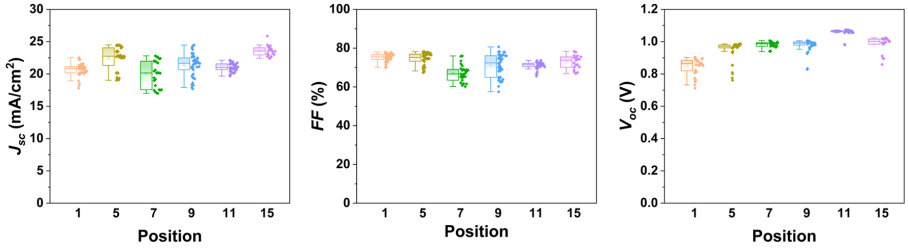

Figure C.9: Statistical distributions of the V_{oc}, J_{sc}, and *FF* based on the samples at different position shown on Figure 5.5d.

References

[1] J. G. Olivier, K. Schure, J. Peters, *et al., Trends in global CO_2 and total greenhouse gas emissions,* PBL Netherlands Environmental Assessment Agency **5**, 1 (2017).

[2] A. F. Ghoniem, *Needs, resources and climate change: Clean and efficient conversion technologies,* Progress in energy and combustion science **37**, 15 (2011).

[3] S. M. trust holdings, *Aiming to limit temperature increase,* (2020).

[4] Z. Şen, *Solar energy in progress and future research trends,* Progress in Energy and Combustion Science **30**, 367 (2004).

[5] S. A. Kalogirou, *Solar energy engineering: processes and systems* (Elsevier, 2023).

[6] R. Pujahari, *Solar cell technology,* in *Energy Materials* (Elsevier, 2021) pp. 27–60.

[7] C. Battaglia, A. Cuevas, and S. De Wolf, *High-efficiency crystalline silicon solar cells: status and perspectives,* Energy & Environmental Science **9**, 1552 (2016).

[8] Z. Yu, *Silicon-Based Tandem Solar Cells with Silicon Heterojunction Bottom Cells*, Ph.D. thesis, Arizona State University (2018).

[9] L. Duan, D. Walter, N. Chang, J. Bullock, D. Kang, S. P. Phang, K. Weber, T. White, D. Macdonald, K. Catchpole, *et al., Stability challenges for the commercialization of perovskite–silicon tandem solar cells,* Nature Reviews Materials **8**, 261 (2023).

[10] J. H. Werner, *Second and third generation photovoltaics–dreams and reality,* in *Advances in Solid State Physics* (Springer, 2004) pp. 51–66.

[11] U. P. Singh and S. P. Patra, *Progress in polycrystalline thin-film cu (in, ga) se2 solar cells,* International Journal of Photoenergy **2010**, 468147 (2010).

[12] B. E. McCandless and J. R. Sites, *Cadmium telluride solar cells,* Handbook of photovoltaic science and engineering , 600 (2011).

[13] C. Becker, D. Amkreutz, T. Sontheimer, V. Preidel, D. Lockau, J. Haschke, L. Jogschies, C. Klimm, J. J. Merkel, P. Plocica, *et al., Polycrystalline silicon thin-film solar cells: Status and perspectives,* Solar Energy Materials and Solar Cells **119**, 112 (2013).

[14] U. Gangopadhyay, S. Jana, and S. Das, *State of art of solar photovoltaic technology,* in *Conference papers in science*, Vol. 2013 (Wiley Online Library, 2013) p. 764132.

[15] A. Hagfeldt, G. Boschloo, L. Sun, L. Kloo, and H. Pettersson, *Dye-sensitized solar cells,* Chemical reviews **110**, 6595 (2010).

[16] A. J. Nozik, *Quantum dot solar cells,* Physica E: Low-dimensional Systems and Nanostructures **14**, 115 (2002).

[17] Z. Pan, H. Rao, I. Mora-Seró, J. Bisquert, and X. Zhong, *Quantum dot-sensitized solar cells,* Chemical Society Reviews **47**, 7659 (2018).

[18] H. Hoppe and N. S. Sariciftci, *Organic solar cells: An overview,* Journal of Materials Research **19**, 1924 (2004).

[19] H. S. Jung and N.-G. Park, *Perovskite solar cells: from materials to devices,* Small **11**, 10 (2015).

[20] NREL, *Best research-cell efficiency chart,* (2024).

[21] A. Jodlowski, D. Rodríguez-Padrón, R. Luque, and G. de Miguel, *Alternative perovskites for photovoltaics,* Advanced Energy Materials **8**, 1703120 (2018).

[22] F. J. Iftikhar, Q. Wali, S. Yang, Y. Iqbal, R. Jose, S. Munir, I. A. Gondal, and M. E. Khan, *Structural and optoelectronic properties of hybrid halide perovskites for solar cells,* Organic Electronics **91**, 106077 (2021).

[23] I. E. Castelli, K. S. Thygesen, and K. W. Jacobsen, *Calculated optical absorption of different perovskite phases,* Journal of Materials Chemistry A **3**, 12343 (2015).

[24] Z. Yang, Z. Yu, H. Wei, X. Xiao, Z. Ni, B. Chen, Y. Deng, S. N. Habisreutinger, X. Chen, K. Wang, *et al.*, *Enhancing electron diffusion length in narrow-bandgap perovskites for efficient monolithic perovskite tandem solar cells,* Nature Communications **10**, 4498 (2019).

[25] D. Luo, R. Su, W. Zhang, Q. Gong, and R. Zhu, *Minimizing non-radiative recombination losses in perovskite solar cells,* Nature Reviews Materials **5**, 44 (2020).

[26] W. Tress, *Physics of perovskite solar cells: Efficiency, open-circuit voltage, and recombination,* Perovskite Photovoltaics and Optoelectronics: From Fundamentals to Advanced Applications , 127 (2022).

[27] A. Kojima, K. Teshima, Y. Shirai, and T. Miyasaka, *Organometal halide perovskites as visible-light sensitizers for photovoltaic cells,* Journal of the American Chemical Society **131**, 6050 (2009).

[28] Y. Rong, L. Liu, A. Mei, X. Li, and H. Han, *Beyond efficiency: the challenge of stability in mesoscopic perovskite solar cells,* Advanced Energy Materials **5**, 1501066 (2015).

[29] J. Burschka, A. Dualeh, F. Kessler, E. Baranoff, N.-L. Cevey-Ha, C. Yi, M. K. Nazeeruddin, and M. Grätzel, *Tris (2-(1 h-pyrazol-1-yl) pyridine) cobalt (iii) as p-type dopant for organic semiconductors and its application in highly efficient solid-state dye-sensitized solar cells,* Journal of the American Chemical Society **133**, 18042 (2011).

[30] Y. Rong, Y. Hu, A. Mei, H. Tan, M. I. Saidaminov, S. I. Seok, M. D. McGehee, E. H. Sargent, and H. Han, *Challenges for commercializing perovskite solar cells,* Science **361**, eaat8235 (2018).

[31] D. Zhou, T. Zhou, Y. Tian, X. Zhu, and Y. Tu, *Perovskite-based solar cells: materials, methods, and future perspectives,* Journal of Nanomaterials **2018**, 8148072 (2018).

[32] T. Wu, Z. Qin, Y. Wang, Y. Wu, W. Chen, S. Zhang, M. Cai, S. Dai, J. Zhang, J. Liu, *et al., The main progress of perovskite solar cells in 2020–2021,* Nano-Micro Letters **13**, 1 (2021).

[33] N. S. Kumar and K. C. B. Naidu, *A review on perovskite solar cells (pscs), materials and applications,* Journal of Materiomics **7**, 940 (2021).

[34] J. Shi, X. Xu, D. Li, and Q. Meng, *Interfaces in perovskite solar cells,* Small **11**, 2472 (2015).

[35] Z. Fang, Q. Zeng, C. Zuo, L. Zhang, H. Xiao, M. Cheng, F. Hao, Q. Bao, L. Zhang, Y. Yuan, *et al., Perovskite-based tandem solar cells,* Science Bulletin **66**, 621 (2021).

[36] N.-G. Park, *Perovskite solar cells: an emerging photovoltaic technology,* Materials Today **18**, 65 (2015).

[37] N. J. Jeon, J. H. Noh, W. S. Yang, Y. C. Kim, S. Ryu, J. Seo, and S. I. Seok, *Compositional engineering of perovskite materials for high-performance solar cells,* Nature **517**, 476 (2015).

[38] F. Wang, S. Bai, W. Tress, A. Hagfeldt, and F. Gao, *Defects engineering for high-performance perovskite solar cells,* npj Flexible Electronics **2**, 22 (2018).

[39] H. Lu, A. Krishna, S. M. Zakeeruddin, M. Grätzel, and A. Hagfeldt, *Compositional and interface engineering of organic-inorganic lead halide perovskite solar cells,* Iscience **23** (2020).

[40] M. Ye, C. He, J. Iocozzia, X. Liu, X. Cui, X. Meng, M. Rager, X. Hong, X. Liu, and Z. Lin, *Recent advances in interfacial engineering of perovskite solar cells,* Journal of Physics D: Applied Physics **50**, 373002 (2017).

[41] Z. Yang, B. H. Babu, S. Wu, T. Liu, S. Fang, Z. Xiong, L. Han, and W. Chen, *Review on practical interface engineering of perovskite solar cells: from efficiency to stability,* Solar RRL **4**, 1900257 (2020).

[42] E. Rezaee, W. Zhang, and S. R. P. Silva, *Solvent engineering as a vehicle for high quality thin films of perovskites and their device fabrication,* Small **17**, 2008145 (2021).

[43] N. J. Jeon, J. H. Noh, Y. C. Kim, W. S. Yang, S. Ryu, and S. I. Seok, *Solvent engineering for high-performance inorganic–organic hybrid perovskite solar cells,* Nature Materials **13**, 897 (2014).

[44] R. Liu and K. Xu, *Solvent engineering for perovskite solar cells: A review,* Micro & Nano Letters **15**, 349 (2020).

[45] Z. Hu, Z. Lin, J. Su, J. Zhang, J. Chang, and Y. Hao, *A review on energy band-gap engineering for perovskite photovoltaics,* Solar RRL **3**, 1900304 (2019).

[46] N. K. Elangovan, R. Kannadasan, B. Beenarani, M. H. Alsharif, M.-K. Kim, and Z. H. Inamul, *Recent developments in perovskite materials, fabrication techniques, band gap engineering, and the stability of perovskite solar cells,* Energy Reports **11**, 1171 (2024).

[47] M. Cheng, C. Zuo, Y. Wu, Z. Li, B. Xu, Y. Hua, and L. Ding, *Charge-transport layer engineering in perovskite solar cells,* Sci. Bull **65**, 1237 (2020).

[48] F. Azri, A. Meftah, N. Sengouga, and A. Meftah, *Electron and hole transport layers optimization by numerical simulation of a perovskite solar cell,* Solar Energy **181**, 372 (2019).

[49] J. Suo, B. Yang, E. Mosconi, D. Bogachuk, T. A. Doherty, K. Frohna, D. J. Kubicki, F. Fu, Y. Kim, O. Er-Raji, *et al.*, *Multifunctional sulfonium-based treatment for perovskite solar cells with less than 1% efficiency loss over 4,500-h operational stability tests,* Nature Energy **9**, 172 (2024).

[50] H. Su, Z. Xu, X. He, Y. Yao, X. Zheng, Y. She, Y. Zhu, J. Zhang, and S. Liu, *Surface energy engineering of buried interface for highly stable perovskite solar cells with efficiency over 25%,* Advanced Materials **36**, 2306724 (2024).

[51] V. V. Ozerova, N. A. Emelianov, L. A. Frolova, Y. S. Fedotov, S. I. Bredikhin, S. M. Aldoshin, and P. A. Troshin, *Impact of hole-transport layer materials on the field-induced degradation of pin perovskite solar cells,* Sustainable Energy & Fuels **8**, 997 (2024).

[52] F. Ruf, *Excitonic Effects and Bandgap Instabilities in Perovskite Solar Cells* (KIT Scientific Publishing, 2020).

[53] M. Liu, M. B. Johnston, and H. J. Snaith, *Efficient planar heterojunction perovskite solar cells by vapour deposition,* Nature **501**, 395 (2013).

[54] L. Gil-Escrig, I. Susic, İ. Doğan, V. Zardetto, M. Najafi, D. Zhang, S. Veenstra, S. Sedani, B. Arikan, S. Yerci, *et al.*, *Efficient and thermally stable wide bandgap perovskite solar cells by dual-source vacuum deposition,* Advanced Functional Materials **33**, 2214357 (2023).

[55] L. Gil-Escrig, C. Dreessen, I. C. Kaya, B.-S. Kim, F. Palazon, M. Sessolo, and H. J. Bolink, *Efficient vacuum-deposited perovskite solar cells with stable cubic perovskite,* ACS Energy Letters **5**, 3053 (2020).

[56] A. Babaei, W. Soltanpoor, M. A. Tesa-Serrate, S. Yerci, M. Sessolo, and H. J. Bolink, *Preparation and characterization of mixed halide perovskite thin films by three-source vacuum deposition,* Energy Technology **8**, 1900784 (2020).

[57] I. Susic, L. Gil-Escrig, F. Palazon, M. Sessolo, and H. J. Bolink, *Quadruple-cation wide-bandgap perovskite solar cells with enhanced thermal stability enabled by vacuum deposition,* ACS Energy Letters **7**, 1355 (2022).

[58] N. Rodkey, K. P. Zanoni, M. Piot, C. Dreessen, R. Grote, P. Carroy, J. E. Sebastian Alonso, A. Paliwal, D. Muñoz, and H. J. Bolink, *Efficient micrometer thick bifacial perovskite solar cells,* Advanced Energy Materials **14**, 2400058 (2024).

[59] K. Yoshikawa, H. Kawasaki, W. Yoshida, T. Irie, K. Konishi, K. Nakano, T. Uto, D. Adachi, M. Kanematsu, H. Uzu, *et al.*, *Silicon heterojunction solar cell with interdigitated back contacts for a photoconversion efficiency over 26%,* Nature energy **2**, 1 (2017).

[60] F. Haase, C. Hollemann, S. Schäfer, A. Merkle, M. Rienäcker, J. Krügener, R. Brendel, and R. Peibst, *Laser contact openings for local poly-si-metal contacts enabling 26.1%-efficient polo-ibc solar cells,* Solar Energy Materials and Solar Cells **186**, 184 (2018).

[61] N. T. Energy, *Best research-cell efficiency chart,* (2020).

[62] S. Agarwal and P. R. Nair, *Pinhole induced efficiency variation in perovskite solar cells,* Journal of Applied Physics **122** (2017).

[63] J. Yan, N. Li, Y. Ai, Z. Wang, W. Yang, M. Zhao, C. Shou, B. Yan, J. Sheng, and J. Ye, *Enhanced perovskite crystallization by the polyvinylpyrrolidone additive for high efficiency solar cells,* Sustainable Energy & Fuels **3**, 3448 (2019).

[64] G. Divitini, S. Cacovich, F. Matteocci, L. Cinà, A. Di Carlo, and C. Ducati, *In situ observation of heat-induced degradation of perovskite solar cells,* Nature Energy **1**, 1 (2016).

[65] K. Domanski, E. A. Alharbi, A. Hagfeldt, M. Grätzel, and W. Tress, *Systematic investigation of the impact of operation conditions on the degradation behaviour of perovskite solar cells,* Nature Energy **3**, 61 (2018).

[66] J. Yang, B. D. Siempelkamp, D. Liu, and T. L. Kelly, *Investigation of perovskite degradation rates and mechanisms in controlled humidity environments using in situ techniques,* ACS Nano **9**, 1955 (2015).

[67] M. Shirayama, M. Kato, T. Miyadera, T. Sugita, T. Fujiseki, S. Hara, H. Kadowaki, D. Murata, M. Chikamatsu, and H. Fujiwara, *Degradation mechanism of perovskite materials upon exposure to humid air,* Journal of Applied Physics **119** (2016).

[68] R. K. Misra, S. Aharon, B. Li, D. Mogilyansky, I. Visoly-Fisher, L. Etgar, and E. A. Katz, *Temperature-and component-dependent degradation of perovskite photovoltaic materials under concentrated sunlight,* The journal of physical chemistry letters **6**, 326 (2015).

[69] X. Tang, M. Brandl, B. May, I. Levchuk, Y. Hou, M. Richter, H. Chen, S. Chen, S. Kahmann, A. Osvet, *et al.*, *Photoinduced degradation of methylammonium lead triiodide perovskite semiconductors,* Journal of Materials Chemistry A **4**, 15896 (2016).

[70] J. Wei, Q. Wang, J. Huo, F. Gao, Z. Gan, Q. Zhao, and H. Li, *Mechanisms and suppression of photoinduced degradation in perovskite solar cells,* Advanced Energy Materials **11**, 2002326 (2021).

[71] S. Sun, A. Tiihonen, F. Oviedo, Z. Liu, J. Thapa, Y. Zhao, N. T. P. Hartono, A. Goyal, T. Heumueller, C. Batali, *et al.*, *A data fusion approach to optimize compositional stability of halide perovskites,* Matter **4**, 1305 (2021).

[72] T. A. Berhe, W.-N. Su, C.-H. Chen, C.-J. Pan, J.-H. Cheng, H.-M. Chen, M.-C. Tsai, L.-Y. Chen, A. A. Dubale, and B.-J. Hwang, *Organometal halide perovskite solar cells: degradation and stability,* Energy & Environmental Science **9**, 323 (2016).

[73] C. C. Boyd, R. Cheacharoen, K. A. Bush, R. Prasanna, T. Leijtens, and M. D. McGehee, *Barrier design to prevent metal-induced degradation and improve thermal stability in perovskite solar cells,* ACS Energy Letters **3**, 1772 (2018).

[74] J. Carolus, T. Merckx, Z. Purohit, B. Tripathi, H.-G. Boyen, T. Aernouts, W. De Ceuninck, B. Conings, and M. Daenen, *Potential-induced degradation and recovery of perovskite solar cells,* Solar RRL **3**, 1900226 (2019).

[75] C. C. Boyd, R. Cheacharoen, T. Leijtens, and M. D. McGehee, *Understanding degradation mechanisms and improving stability of perovskite photovoltaics,* Chemical Reviews **119**, 3418 (2018).

[76] J. Li, J. Huang, A. Zhao, Y. Li, and M. Wei, *An inorganic stable sn-based perovskite film with regulated nucleation for solar cell application,* Journal of Materials Chemistry C **8**, 8840 (2020).

[77] A. X. Chen, A. Chhabra, H.-H. G. Song, H. E. Fleming, C. S. Chen, and S. N. Bhatia, *Controlled apoptosis of stromal cells to engineer human microlivers,* Advanced Functional Materials **30**, 1910442 (2020).

[78] G. Tong, D.-Y. Son, L. K. Ono, Y. Liu, Y. Hu, H. Zhang, A. Jamshaid, L. Qiu, Z. Liu, and Y. Qi, *Scalable fabrication of 90 cm^2 perovskite solar modules with more than 1000 h operational stability based on the intermediate phase strategy,* Advanced Energy Materials **11**, 2003712 (2021).

[79] S. Xiong, T. Hao, Y. Sun, J. Yang, R. Ma, J. Wang, S. Gong, X. Liu, L. Ding, M. Fahlman, *et al.*, *Defect passivation by nontoxic biomaterial yields 21% efficiency perovskite solar cells,* Journal of Energy Chemistry **55**, 265 (2021).

[80] M. C. Brennan, S. Draguta, P. V. Kamat, and M. Kuno, *Light-induced anion phase segregation in mixed halide perovskites,* ACS Energy Letters **3**, 204 (2017).

[81] L. T. E. G. N. NK and S. Habisreutinger, *Petrozza a. snaith hj adv,* Energy Mater **5**, 1500963 (2015).

[82] M. Jeong, I. W. Choi, E. M. Go, Y. Cho, M. Kim, B. Lee, S. Jeong, Y. Jo, H. W. Choi, J. Lee, *et al.*, *Stable perovskite solar cells with efficiency exceeding 24.8% and 0.3-v voltage loss,* Science **369**, 1615 (2020).

[83] Y. Deng, X. Zheng, Y. Bai, Q. Wang, J. Zhao, and J. Huang, *Surfactant-controlled ink drying enables high-speed deposition of perovskite films for efficient photovoltaic modules,* Nature Energy **3**, 560 (2018).

[84] K. Xiao, J. Wen, Q. Han, R. Lin, Y. Gao, S. Gu, Y. Zang, Y. Nie, J. Zhu, J. Xu, *et al.*, *Solution-processed monolithic all-perovskite triple-junction solar cells with efficiency exceeding 20%,* ACS Energy Letters **5**, 2819 (2020).

[85] K. Xiao, R. Lin, Q. Han, Y. Hou, Z. Qin, H. T. Nguyen, J. Wen, M. Wei, V. Yeddu, M. I. Saidaminov, *et al.*, *All-perovskite tandem solar cells with 24.2% certified efficiency and area over 1 cm2 using surface-anchoring zwitterionic antioxidant,* Nature Energy **5**, 870 (2020).

[86] J. Wang, V. Zardetto, K. Datta, D. Zhang, M. M. Wienk, and R. A. Janssen, *16.8% monolithic all-perovskite triple-junction solar cells via a universal two-step solution process,* Nature Communications **11**, 5254 (2020).

[87] Z. Zhou, Q. Chen, and P. Bermel, *Prospects for high-performance thermophotovoltaic conversion efficiencies exceeding the shockley–queisser limit,* Energy Conversion and Management **97**, 63 (2015).

[88] LongGi, *34.6% record-breaker longi once again sets a new world efficiency for silicon-perovskite tandem solar cells,* (2024).

[89] E. H. Jung, N. J. Jeon, E. Y. Park, C. S. Moon, T. J. Shin, T.-Y. Yang, J. H. Noh, and J. Seo, *Efficient, stable and scalable perovskite solar cells using poly (3-hexylthiophene),* Nature **567**, 511 (2019).

[90] S. Chen, X. Dai, S. Xu, H. Jiao, L. Zhao, and J. Huang, *Stabilizing perovskite-substrate interfaces for high-performance perovskite modules,* Science **373**, 902 (2021).

[91] J.-X. Zhong, W.-Q. Wu, L. Ding, and D.-B. Kuang, *Blade-coating perovskite films with diverse compositions for efficient photovoltaics,* Energy & Environmental Materials **4**, 277 (2021).

[92] S. Razza, F. Di Giacomo, F. Matteocci, L. Cina, A. L. Palma, S. Casaluci, P. Cameron, A. D'epifanio, S. Licoccia, A. Reale, *et al.*, *Perovskite solar cells and large area modules (100 cm2) based on an air flow-assisted pbi2 blade coating deposition process,* Journal of Power Sources **277**, 286 (2015).

[93] M. Yang, Z. Li, M. O. Reese, O. G. Reid, D. H. Kim, S. Siol, T. R. Klein, Y. Yan, J. J. Berry, M. F. Van Hest, *et al.*, *Perovskite ink with wide processing window for scalable high-efficiency solar cells,* Nature Energy **2**, 1 (2017).

[94] A. T. Mallajosyula, K. Fernando, S. Bhatt, A. Singh, B. W. Alphenaar, J.-C. Blancon, W. Nie, G. Gupta, and A. D. Mohite, *Large-area hysteresis-free perovskite solar cells via temperature controlled doctor blading under ambient environment,* Applied Materials Today **3**, 96 (2016).

[95] Y. Zhong, R. Munir, J. Li, M.-C. Tang, M. R. Niazi, D.-M. Smilgies, K. Zhao, and A. Amassian, *Blade-coated hybrid perovskite solar cells with efficiency> 17%: an in situ investigation,* ACS Energy Letters **3**, 1078 (2018).

[96] M.-C. Tang, Y. Fan, D. Barrit, X. Chang, H. X. Dang, R. Li, K. Wang, D.-M. Smilgies, S. F. Liu, S. De Wolf, *et al., Ambient blade coating of mixed cation, mixed halide perovskites without dripping: in situ investigation and highly efficient solar cells,* Journal of materials chemistry A **8**, 1095 (2020).

[97] J. Li, R. Munir, Y. Fan, T. Niu, Y. Liu, Y. Zhong, Z. Yang, Y. Tian, B. Liu, J. Sun, *et al., Phase transition control for high-performance blade-coated perovskite solar cells,* Joule **2**, 1313 (2018).

[98] J. Yin, Y. Lin, C. Zhang, J. Li, and N. Zheng, *Growth-dynamic-controllable rapid crystallization boosts the perovskite photovoltaics' robust preparation: From blade coating to painting,* ACS applied materials & interfaces **10**, 23103 (2018).

[99] J. H. Kim, S. T. Williams, N. Cho, C.-C. Chueh, and A. K.-Y. Jen, *Enhanced environmental stability of planar heterojunction perovskite solar cells based on blade-coating,* Advanced energy materials **5**, 1401229 (2015).

[100] L.-H. Chou, X.-F. Wang, I. Osaka, C.-G. Wu, and C.-L. Liu, *Scalable ultrasonic spray-processing technique for manufacturing large-area ch3nh3pbi3 perovskite solar cells,* ACS applied materials & interfaces **10**, 38042 (2018).

[101] N.-G. Park and K. Zhu, *Scalable fabrication and coating methods for perovskite solar cells and solar modules,* Nature Reviews Materials **5**, 333 (2020).

[102] Z. Ouyang, M. Yang, J. B. Whitaker, D. Li, and M. F. van Hest, *Toward scalable perovskite solar modules using blade coating and rapid thermal processing,* ACS Applied Energy Materials **3**, 3714 (2020).

[103] T. Bu, L. K. Ono, J. Li, J. Su, G. Tong, W. Zhang, Y. Liu, J. Zhang, J. Chang, S. Kazaoui, *et al., Modulating crystal growth of formamidinium–caesium perovskites for over 200 cm2 photovoltaic sub-modules,* Nature Energy **7**, 528 (2022).

[104] A. T. Barrows, A. J. Pearson, C. K. Kwak, A. D. Dunbar, A. R. Buckley, and D. G. Lidzey, *Efficient planar heterojunction mixed-halide perovskite solar cells deposited via spray-deposition,* Energy & Environmental Science **7**, 2944 (2014).

[105] H. Chen, X. Ding, X. Pan, T. Hayat, A. Alsaedi, Y. Ding, and S. Dai, *Comprehensive studies of air-brush spray deposition used in fabricating high-efficiency ch3nh3pbi3 perovskite solar cells: combining theories with practices,* Journal of Power Sources **402**, 82 (2018).

[106] H. Ishihara, S. Sarang, Y.-C. Chen, O. Lin, P. Phummirat, L. Thung, J. Hernandez, S. Ghosh, and V. Tung, *Nature inspiring processing route toward high throughput production of perovskite photovoltaics,* Journal of Materials Chemistry A **4**, 6989 (2016).

[107] C. Girotto, D. Moia, B. P. Rand, and P. Heremans, *High-performance organic solar cells with spray-coated hole-transport and active layers,* Advanced Functional Materials **21**, 64 (2011).

[108] M. Habibi, A. Rahimzadeh, I. Bennouna, and M. Eslamian, *Defect-free large-area (25 cm2) light absorbing perovskite thin films made by spray coating,* Coatings **7**, 42 (2017).

[109] Y.-S. Chou, L.-H. Chou, A.-Z. Guo, X.-F. Wang, I. Osaka, C.-G. Wu, and C.-L. Liu, *Ultrasonic spray-coated mixed cation perovskite films and solar cells,* ACS sustainable chemistry & engineering **7**, 14217 (2019).

[110] M. Park, W. Cho, G. Lee, S. C. Hong, M.-c. Kim, J. Yoon, N. Ahn, and M. Choi, *Highly reproducible large-area perovskite solar cell fabrication via continuous megasonic spray coating of ch3nh3pbi3,* Small **15**, 1804005 (2019).

[111] Z. Liang, S. Zhang, X. Xu, N. Wang, J. Wang, X. Wang, Z. Bi, G. Xu, N. Yuan, and J. Ding, *A large grain size perovskite thin film with a dense structure for planar heterojunction solar cells via spray deposition under ambient conditions,* RSC advances **5**, 60562 (2015).

[112] Z. Bi, Z. Liang, X. Xu, Z. Chai, H. Jin, D. Xu, J. Li, M. Li, and G. Xu, *Fast preparation of uniform large grain size perovskite thin film in air condition via spray deposition method for high efficient planar solar cells,* Solar energy materials and solar cells **162**, 13 (2017).

[113] J. E. Bishop, J. A. Smith, and D. G. Lidzey, *Development of spray-coated perovskite solar cells,* ACS Applied Materials & Interfaces **12**, 48237 (2020).

[114] J. H. Heo, F. Zhang, C. Xiao, S. J. Heo, J. K. Park, J. J. Berry, K. Zhu, and S. H. Im, *Efficient and stable graded cspbi3- xbrx perovskite solar cells and submodules by orthogonal processable spray coating,* Joule **5**, 481 (2021).

[115] D. Mohamad, B. Freestone, R. Masters, M. Reinhardt, S. Canning, C. Rodenburg, and D. Lidzey, *Optimized organometal halide perovskite solar cell fabrication through control of nanoparticle crystal patterning,* Journal of Materials Chemistry C **5**, 2352 (2017).

[116] M. Xu, W. Ji, Y. Sheng, Y. Wu, H. Cheng, J. Meng, Z. Yan, J. Xu, A. Mei, Y. Hu, *et al.*, *Efficient triple-mesoscopic perovskite solar mini-modules fabricated with slot-die coating,* Nano Energy **74**, 104842 (2020).

[117] Y. Hu, S. Si, A. Mei, Y. Rong, H. Liu, X. Li, and H. Han, *Stable large-area (10 × 10 cm^2) printable mesoscopic perovskite module exceeding 10% efficiency,* Solar RRL **1**, 1600019 (2017).

[118] E. Bi, W. Tang, H. Chen, Y. Wang, J. Barbaud, T. Wu, W. Kong, P. Tu, H. Zhu, X. Zeng, *et al.*, *Efficient perovskite solar cell modules with high stability enabled by iodide diffusion barriers,* Joule **3**, 2748 (2019).

[119] M. Fievez, P. J. S. Rana, T. M. Koh, M. Manceau, J. H. Lew, N. F. Jamaludin, B. Ghosh, A. Bruno, S. Cros, S. Berson, *et al.*, *Slot-die coated methylammonium-free perovskite solar cells with 18% efficiency,* Solar Energy Materials and Solar Cells **230**, 111189 (2021).

[120] G. Cotella, J. Baker, D. Worsley, F. De Rossi, C. Pleydell-Pearce, M. Carnie, and T. Watson, *One-step deposition by slot-die coating of mixed lead halide perovskite for photovoltaic applications,* Solar Energy Materials and Solar Cells **159**, 362 (2017).

[121] Solliance, *Solliance sets more world records for roll-to-roll perovskite solar cells and modules,* (2017).

[122] F. Di Giacomo, H. Fledderus, H. Gorter, G. Kirchner, I. de Vries, I. Dogan, W. Verhees, V. Zardetto, M. Najafi, D. Zhang, *et al.*, *Large area over 140 cm^2 perovskite solar modules made by sheet to sheet and roll to roll fabrication with 14.5% efficiency,* in *2018 IEEE 7th World Conference on Photovoltaic Energy Conversion (WCPEC)(A Joint Conference of 45th IEEE PVSC, 28th PVSEC & 34th EU PVSEC)* (IEEE, 2018) pp. 2795–2798.

[123] F. Xu, J. Liu, A. S. Subbiah, W. Liu, J. Kang, G. T. Harrison, X. Yang, F. H. Isikgor, E. Aydin, M. De Bastiani, *et al.*, *Potassium thiocyanate-assisted enhancement of slot-die-coated perovskite films for high-performance solar cells,* Small Science **1**, 2000044 (2021).

[124] I. Zimmermann, M. Provost, S. Mejaouri, M. Al Atem, A. Blaizot, A. Duchatelet, S. Collin, and J. Rousset, *Industrially compatible fabrication process of perovskite-based mini-modules coupling sequential slot-die coating and chemical bath deposition,* ACS Applied Materials & Interfaces **14**, 11636 (2022).

[125] J. Wang, M. R. Squillante, S. Sidhik, A. Mohite, and M. S. Marshall, *Large scale flexible perovskite solar cells fabricated by slot die coating,* in *2021 IEEE 48th Photovoltaic Specialists Conference (PVSC)* (IEEE, 2021) pp. 1128–1130.

[126] I. Zimmermann, M. Al Atem, O. Fournier, S. Bernard, S. Jutteau, L. Lombez, and J. Rousset, *Sequentially slot-die-coated perovskite for efficient and scalable solar cells,* Advanced Materials Interfaces **8**, 2100743 (2021).

[127] Z. Yang, W. Zhang, S. Wu, H. Zhu, Z. Liu, Z. Liu, Z. Jiang, R. Chen, J. Zhou, Q. Lu, *et al.*, *Slot-die coating large-area formamidinium-cesium perovskite film for efficient and stable parallel solar module,* Science Advances **7**, eabg3749 (2021).

[128] M. Mercuri, K. Pierpauli, M. G. Bellino, and C. L. Berli, *Complex filling dynamics in mesoporous thin films,* Langmuir **33**, 152 (2017).

[129] T. Bu, J. Li, H. Li, C. Tian, J. Su, G. Tong, L. K. Ono, C. Wang, Z. Lin, N. Chai, *et al.*, *Lead halide–templated crystallization of methylamine-free perovskite for efficient photovoltaic modules,* Science **372**, 1327 (2021).

[130] C.-F. Li, H.-C. Huang, S.-H. Huang, Y.-H. Hsiao, P. Chaudhary, C.-Y. Chang, F.-Y. Tsai, W.-F. Su, and Y.-C. Huang, *High-performance perovskite solar cells and modules fabricated by slot-die coating with nontoxic solvents,* Nanomaterials **13**, 1760 (2023).

[131] K. Hwang, Y.-S. Jung, Y.-J. Heo, F. H. Scholes, S. E. Watkins, J. Subbiah, D. J. Jones, D.-Y. Kim, and D. Vak, *Toward large scale roll-to-roll production of fully printed perovskite solar cells,* Advanced materials **27**, 1241 (2015).

[132] L. Gao, K. Huang, C. Long, F. Zeng, B. Liu, and J. Yang, *Fully slot-die-coated perovskite solar cells in ambient condition,* Applied Physics A **126**, 1 (2020).

[133] F. Di Giacomo, S. Shanmugam, H. Fledderus, B. J. Bruijnaers, W. J. Verhees, M. S. Dorenkamper, S. C. Veenstra, W. Qiu, R. Gehlhaar, T. Merckx, *et al.*, *Up-scalable sheet-to-sheet production of high efficiency perovskite module and solar cells on 6-in. substrate using slot die coating,* Solar Energy Materials and Solar Cells **181**, 53 (2018).

[134] R. Patidar, D. Burkitt, K. Hooper, D. Richards, and T. Watson, *Slot-die coating of perovskite solar cells: An overview,* Materials Today Communications **22**, 100808 (2020).

[135] P. Li, C. Liang, B. Bao, Y. Li, X. Hu, Y. Wang, Y. Zhang, F. Li, G. Shao, and Y. Song, *Inkjet manipulated homogeneous large size perovskite grains for efficient and large-area perovskite solar cells,* Nano Energy **46**, 203 (2018).

[136] Z. Li, P. Li, G. Chen, Y. Cheng, X. Pi, X. Yu, D. Yang, L. Han, Y. Zhang, and Y. Song, *Ink engineering of inkjet printing perovskite,* ACS Applied Materials & Interfaces **12**, 39082 (2020).

[137] C. Liang, K. M. Salim, P. Li, Z. Wang, T. M. Koh, H. Gu, B. Wu, J. Xia, Z. Zhang, K. Wang, *et al.*, *Controlling the film structure by regulating two-dimensional ruddlesden–popper perovskite formation enthalpy for efficient and stable tri-cation perovskite solar cells,* Journal of materials chemistry A **8**, 5874 (2020).

[138] L. Gil-Escrig, M. Roß, J. Sutter, A. Al-Ashouri, C. Becker, and S. Albrecht, *Fully vacuum-processed perovskite solar cells on pyramidal microtextures,* Solar RRL **5**, 2000553 (2021).

[139] L. Cojocaru, K. Wienands, T. W. Kim, S. Uchida, A. J. Bett, S. Rafizadeh, J. C. Goldschmidt, and S. W. Glunz, *Detailed investigation of evaporated perovskite absorbers with high crystal quality on different substrates,* ACS Applied Materials & Interfaces **10**, 26293 (2018).

[140] P. S. Schulze, K. Wienands, A. J. Bett, S. Rafizadeh, L. E. Mundt, L. Cojocaru, M. Hermle, S. W. Glunz, H. Hillebrecht, and J. C. Goldschmidt, *Perovskite hybrid evaporation/spin coating method: From band gap tuning to thin film deposition on textures,* Thin Solid Films **704**, 137970 (2020).

[141] C. Gao, J. Liu, C. Liao, Q. Ye, Y. Zhang, X. He, X. Guo, J. Mei, and W. Lau, *Formation of organic–inorganic mixed halide perovskite films by thermal evaporation of lead chloride and mai compounds,* RSC Advances **5**, 26175 (2015).

[142] C.-W. Chen, H.-W. Kang, S.-Y. Hsiao, P.-F. Yang, K.-M. Chiang, and H.-W. Lin, *Efficient and uniform planar-type perovskite solar cells by simple sequential vacuum deposition.* Advanced Materials (Deerfield Beach, Fla.) **26**, 6647 (2014).

[143] J. Borchert, R. L. Milot, J. B. Patel, C. L. Davies, A. D. Wright, L. Martńez Maestro, H. J. Snaith, L. M. Herz, and M. B. Johnston, *Large-area, highly uniform evaporated formamidinium lead triiodide thin films for solar cells,* ACS Energy Letters **2**, 2799 (2017).

[144] F. Sahli, J. Werner, B. A. Kamino, M. Bräuninger, R. Monnard, B. Paviet-Salomon, L. Barraud, L. Ding, J. J. Diaz Leon, D. Sacchetto, *et al.*, *Fully textured monolithic perovskite/silicon tandem solar cells with 25.2% power conversion efficiency,* Nature Materials **17**, 820 (2018).

[145] J. Li, H. Wang, X. Y. Chin, H. A. Dewi, K. Vergeer, T. W. Goh, J. W. M. Lim, J. H. Lew, K. P. Loh, C. Soci, *et al.*, *Highly efficient thermally co-evaporated perovskite solar cells and mini-modules,* Joule **4**, 1035 (2020).

[146] J. Werner, F. Sahli, F. Fu, J. J. Diaz Leon, A. Walter, B. A. Kamino, B. Niesen, S. Nicolay, Q. Jeangros, and C. Ballif, *Perovskite/perovskite/silicon monolithic triple-junction solar cells with a fully textured design,* ACS Energy Letters **3**, 2052 (2018).

[147] L. Gil-Escrig, C. Dreessen, F. Palazon, Z. Hawash, E. Moons, S. Albrecht, M. Sessolo, and H. J. Bolink, *Efficient wide-bandgap mixed-cation and mixed-halide perovskite solar cells by vacuum deposition,* ACS energy letters **6**, 827 (2021).

[148] J. Feng, Y. Jiao, H. Wang, X. Zhu, Y. Sun, M. Du, Y. Cao, D. Yang, and S. F. Liu, *High-throughput large-area vacuum deposition for high-performance formamidine-based perovskite solar cells,* Energy & Environmental Science **14**, 3035 (2021).

[149] J. Zhou, L. Tan, Y. Liu, H. Li, X. Liu, M. Li, S. Wang, Y. Zhang, C. Jiang, R. Hua, *et al.*, *Highly efficient and stable perovskite solar cells via a multifunctional hole transporting material,* Joule (2024).

[150] J. Tavakoli, H. Abbasi, A. Zarei Jelyani, and A. Mousavi Khaneghah, *The use of salvia macrosiphon and lepidium sativum linn. seed gums in nanoencapsulation processes: Improving antioxidant activity of potato skin extract,* Journal of Food Quality **2021**, 1 (2021).

[151] Y. Choi, D. Koo, M. Jeong, G. Jeong, J. Lee, B. Lee, K. J. Choi, C. Yang, and H. Park, *Toward all-vacuum-processable perovskite solar cells with high efficiency, stability, and scalability enabled by fluorinated spiro-ometad through thermal evaporation,* Solar RRL **5**, 2100415 (2021).

[152] T. Lei, F. Li, X. Zhu, H. Dong, Z. Niu, S. Ye, W. Zhao, J. Xi, B. Jiao, L. Ding, *et al.*, *Flexible perovskite solar modules with functional layers fully vacuum deposited,* Solar RRL **4**, 2000292 (2020).

[153] H. M. Christen and G. Eres, *Recent advances in pulsed-laser deposition of complex oxides,* Journal of Physics: Condensed Matter **20**, 264005 (2008).

[154] S. Hoffmann-Urlaub, Y. Zhang, Z. Wang, B. Kressdorf, and T. Meyer, *Fabrication of tin-based halide perovskites by pulsed laser deposition,* Applied Physics A **126**, 1 (2020).

[155] U. Bansode and S. Ogale, *On-axis pulsed laser deposition of hybrid perovskite films for solar cell and broadband photo-sensor applications,* Journal of Applied Physics **121** (2017).

[156] H. Wang, Y. Wu, M. Ma, S. Dong, Q. Li, J. Du, H. Zhang, and Q. Xu, *Pulsed laser deposition of cspbbr3 films for application in perovskite solar cells,* ACS Applied Energy Materials **2**, 2305 (2019).

[157] V. M. Kiyek, Y. A. Birkhölzer, Y. Smirnov, M. Ledinsky, Z. Remes, J. Momand, B. J. Kooi, G. Koster, G. Rijnders, and M. Morales-Masis, *Single-source, solvent-free, room temperature deposition of black γ-cssni3 films,* Advanced Materials Interfaces **7**, 2000162 (2020).

[158] W. A. Dunlap-Shohl, Y. Zhou, N. P. Padture, and D. B. Mitzi, *Synthetic approaches for halide perovskite thin films,* Chemical reviews **119**, 3193 (2018).

[159] R. Pate and A. Stiff-Roberts, *The impact of laser-target absorption depth on the surface and internal morphology of matrix-assisted pulsed laser evaporated conjugated polymer thin films,* Chemical Physics Letters **477**, 406 (2009).

[160] T. Soto-Montero, W. Soltanpoor, and M. Morales-Masis, *Pressing challenges of halide perovskite thin film growth,* APL Materials **8** (2020).

[161] M. R. Leyden, L. K. Ono, S. R. Raga, Y. Kato, S. Wang, and Y. Qi, *High performance perovskite solar cells by hybrid chemical vapor deposition,* Journal of Materials Chemistry A **2**, 18742 (2014).

[162] M. R. Leyden, Y. Jiang, and Y. Qi, *Chemical vapor deposition grown formamidinium perovskite solar modules with high steady state power and thermal stability,* Journal of Materials Chemistry A **4**, 13125 (2016).

[163] Y. Jiang, M. R. Leyden, L. Qiu, S. Wang, L. K. Ono, Z. Wu, E. J. Juarez-Perez, and Y. Qi, *Combination of hybrid cvd and cation exchange for upscaling cs-substituted mixed cation perovskite solar cells with high efficiency and stability,* Advanced Functional Materials **28**, 1703835 (2018).

[164] L. Luo, Y. Zhang, N. Chai, X. Deng, J. Zhong, F. Huang, Y. Peng, Z. Ku, and Y.-B. Cheng, *Large-area perovskite solar cells with csfapbibr thin films deposited by a vapor–solid reaction method,* Journal of Materials Chemistry A **6**, 21143 (2018).

[165] Y. Jiang, M. Remeika, Z. Hu, E. J. Juarez-Perez, L. Qiu, Z. Liu, T. Kim, L. K. Ono, D.-Y. Son, Z. Hawash, *et al.*, *Negligible-pb-waste and upscalable perovskite deposition technology for high-operational-stability perovskite solar modules,* Advanced Energy Materials **9**, 1803047 (2019).

[166] N. A. N. Ouedraogo, Y. Chen, Y. Y. Xiao, Q. Meng, C. B. Han, H. Yan, and Y. Zhang, *Stability of all-inorganic perovskite solar cells,* Nano Energy **67**, 104249 (2020).

[167] J. Liu, Y. Xue, Z. Wang, Z.-Q. Xu, C. Zheng, B. Weber, J. Song, Y. Wang, Y. Lu, Y. Zhang, *et al.*, *Two-dimensional ch3nh3pbi3 perovskite: synthesis and optoelectronic application,* ACS nano **10**, 3536 (2016).

[168] X. Liu, L. Cao, Z. Guo, Y. Li, W. Gao, and L. Zhou, *A review of perovskite photovoltaic materials' synthesis and applications via chemical vapor deposition method,* Materials **12**, 3304 (2019).

[169] F. Bella, G. Griffini, J.-P. Correa-Baena, G. Saracco, M. Grätzel, A. Hagfeldt, S. Turri, and C. Gerbaldi, *Improving efficiency and stability of perovskite solar cells with photocurable fluoropolymers,* Science **354**, 203 (2016).

[170] L. Qiu, S. He, Y. Jiang, D.-Y. Son, L. K. Ono, Z. Liu, T. Kim, T. Bouloumis, S. Kazaoui, and Y. Qi, *Hybrid chemical vapor deposition enables scalable and stable cs-fa mixed cation perovskite solar modules with a designated area of 91.8 cm^2 approaching 10% efficiency,* Journal of Materials Chemistry A **7**, 6920 (2019).

[171] H. Chen, F. Ye, W. Tang, J. He, M. Yin, Y. Wang, F. Xie, E. Bi, X. Yang, M. Grätzel, *et al.*, *A solvent-and vacuum-free route to large-area perovskite films for efficient solar modules,* Nature **550**, 92 (2017).

[172] F. Ye, H. Chen, F. Xie, W. Tang, M. Yin, J. He, E. Bi, Y. Wang, X. Yang, and L. Han, *Soft-cover deposition of scaling-up uniform perovskite thin films for high cost-performance solar cells,* Energy & Environmental Science **9**, 2295 (2016).

[173] A. Priyadarshi, L. J. Haur, P. Murray, D. Fu, S. Kulkarni, G. Xing, T. C. Sum, N. Mathews, and S. G. Mhaisalkar, *A large area (70 cm^2) monolithic perovskite solar module with a high efficiency and stability,* Energy & Environmental Science **9**, 3687 (2016).

[174] J. Tait, S. Manghooli, W. Qiu, L. Rakocevic, L. Kootstra, M. Jaysankar, C. M. De La Huerta, U. W. Paetzold, R. Gehlhaar, D. Cheyns, *et al.*, *Rapid composition screening for perovskite photovoltaics via concurrently pumped ultrasonic spray coating,* Journal of Materials Chemistry A **4**, 3792 (2016).

[175] H. Huang, J. Shi, L. Zhu, D. Li, Y. Luo, and Q. Meng, *Two-step ultrasonic spray deposition of perovskite for efficient and large-area perovskite solar cell,* Nano Energy **27**, 352 (2016).

[176] J. Hyuck Heo, M. Ho Lee, M. Hyeok Jang, and S. Hyuk Im, *Highly efficient ch3nh3pbi3àxclx mixed halide perovskite solar cells prepared by re-dissolution and crystal grain growth via spray coating,* J. Mater. Chem. A **4**, 17636 (2016).

[177] L. Cai, L. Liang, J. Wu, B. Ding, L. Gao, and B. Fan, *Large area perovskite solar cell module,* Journal of Semiconductors **38**, 014006 (2017).

[178] D. Lee, Y.-S. Jung, Y.-J. Heo, S. Lee, K. Hwang, Y.-J. Jeon, J.-E. Kim, J. Park, G. Y. Jung, and D.-Y. Kim, *Slot-die coated perovskite films using mixed lead precursors for highly reproducible and large-area solar cells,* ACS applied materials & interfaces **10**, 16133 (2018).

[179] D. Vak, K. Hwang, A. Faulks, Y.-S. Jung, N. Clark, D.-Y. Kim, G. J. Wilson, and S. E. Watkins, *Solar cells: Three-dimensional printer based slot-die coater as a lab-to-fab translation tool for solution-processed solar cells (adv. energy mater. 4/2015).* Advanced energy materials **5** (2015).

[180] Y. Deng, C. H. Van Brackle, X. Dai, J. Zhao, B. Chen, and J. Huang, *Tailoring solvent coordination for high-speed, room-temperature blading of perovskite photovoltaic films,* Science advances **5**, eaax7537 (2019).

[181] Y. Deng, Z. Ni, A. F. Palmstrom, J. Zhao, S. Xu, C. H. Van Brackle, X. Xiao, K. Zhu, and J. Huang, *Reduced self-doping of perovskites induced by short annealing for efficient solar modules,* Joule **4**, 1949 (2020).

[182] Y. Deng, S. Xu, S. Chen, X. Xiao, J. Zhao, and J. Huang, *Defect compensation in formamidinium–caesium perovskites for highly efficient solar mini-modules with improved photostability,* Nature Energy **6**, 633 (2021).

[183] Z. Yang, S. Zhang, L. Li, and W. Chen, *Research progress on large-area perovskite thin films and solar modules,* Journal of Materiomics **3**, 231 (2017).

[184] M. A. Uddin, P. J. S. Rana, Z. Ni, X. Dai, Z. Yu, Z. Shi, H. Jiao, and J. Huang, *Blading of conformal electron-transport layers in p–i–n perovskite solar cells,* Advanced Materials **34**, 2202954 (2022).

[185] P. J. S. Rana, B. Febriansyah, T. M. Koh, B. T. Muhammad, T. Salim, T. J. Hooper, A. Kanwat, B. Ghosh, P. Kajal, J. H. Lew, *et al.*, *Alkali additives enable efficient large area (> 55 cm2) slot-die coated perovskite solar modules,* Advanced Functional Materials **32**, 2113026 (2022).

[186] S. You, H. Zeng, Y. Liu, B. Han, M. Li, L. Li, X. Zheng, R. Guo, L. Luo, Z. Li, *et al.*, *Radical polymeric p-doping and grain modulation for stable, efficient perovskite solar modules,* Science **379**, 288 (2023).

[187] F. Jafarzadeh, L. A. Castriotta, F. De Rossi, J. Ali, F. Di Giacomo, A. Di Carlo, F. Matteocci, and F. Brunetti, *All-blade-coated flexible perovskite solar cells & modules processed in air from a sustainable dimethyl sulfoxide (dmso)-based solvent system,* Sustainable Energy & Fuels **7**, 2219 (2023).

[188] Y. Rong, S. Venkatesan, R. Guo, Y. Wang, J. Bao, W. Li, Z. Fan, and Y. Yao, *Critical kinetic control of non-stoichiometric intermediate phase transformation for efficient perovskite solar cells,* Nanoscale **8**, 12892 (2016).

[189] G. Longo, A. Wong, M. Sessolo, and H. J. Bolink, *Effect of the precursor's stoichiometry on the optoelectronic properties of methylammonium lead bromide perovskites,* Journal of Luminescence **189**, 120 (2017).

[190] C. Roldán-Carmona, P. Gratia, I. Zimmermann, G. Grancini, P. Gao, M. Graetzel, and M. K. Nazeeruddin, *High efficiency methylammonium lead triiodide perovskite solar cells: the relevance of non-stoichiometric precursors,* Energy & Environmental Science **8**, 3550 (2015).

[191] D. H. Kim, J. B. Whitaker, Z. Li, M. F. van Hest, and K. Zhu, *Outlook and challenges of perovskite solar cells toward terawatt-scale photovoltaic module technology,* Joule **2**, 1437 (2018).

[192] M. Jung, S.-G. Ji, G. Kim, and S. I. Seok, *Perovskite precursor solution chemistry: from fundamentals to photovoltaic applications,* Chemical Society Reviews **48**, 2011 (2019).

[193] Y. Deng, E. Peng, Y. Shao, Z. Xiao, Q. Dong, and J. Huang, *Scalable fabrication of efficient organolead trihalide perovskite solar cells with doctor-bladed active layers,* Energy & Environmental Science **8**, 1544 (2015).

[194] Q. Wang, M. Eslamian, T. Zhao, and A. K.-Y. Jen, *Achieving fully blade-coated ambient-processed perovskite solar cells by controlling the blade-coater temperature,* IEEE Journal of Photovoltaics **8**, 1662 (2018).

[195] S. Chen, X. Xiao, H. Gu, and J. Huang, *Iodine reduction for reproducible and high-performance perovskite solar cells and modules,* Science Advances **7**, eabe8130 (2021).

[196] W.-Q. Wu, Z. Yang, P. N. Rudd, Y. Shao, X. Dai, H. Wei, J. Zhao, Y. Fang, Q. Wang, Y. Liu, *et al., Bilateral alkylamine for suppressing charge recombination and improving stability in blade-coated perovskite solar cells,* Science Advances **5**, eaav8925 (2019).

[197] Z. Xu, R. Chen, Y. Wu, R. He, J. Yin, W. Lin, B. Wu, J. Li, and N. Zheng, *Br-containing alkyl ammonium salt-enabled scalable fabrication of high-quality perovskite films for efficient and stable perovskite modules,* Journal of Materials Chemistry A **7**, 26849 (2019).

[198] J. Su, H. Cai, J. Yang, X. Ye, R. Han, J. Ni, J. Li, and J. Zhang, *Perovskite ink with an ultrawide processing window for efficient and scalable perovskite solar cells in ambient air,* ACS applied materials & interfaces **12**, 3531 (2019).

[199] J. E. Bishop, T. J. Routledge, and D. G. Lidzey, *Advances in spray-cast perovskite solar cells,* The journal of physical chemistry letters **9**, 1977 (2018).

[200] J. H. Heo, M. H. Lee, M. H. Jang, and S. H. Im, *Highly efficient perovskite mixed halide perovskite solar cells prepared by re-dissolution and crystal grain growth via spray coating,* Journal of Materials Chemistry A **4**, 17636 (2016).

[201] J. Li, J. Dagar, O. Shargaieva, M. A. Flatken, H. Köbler, M. Fenske, C. Schultz, B. Stegemann, J. Just, D. M. Többens, *et al.*, *20.8% slot-die coated perovskite solar cells by optimal solvent-content and age of precursor inks,* Advanced Energy Materials **11**, 2003460 (2021).

[202] Y. Galagan, F. Di Giacomo, H. Gorter, G. Kirchner, I. de Vries, R. Andriessen, and P. Groen, *Roll-to-roll slot die coated perovskite for efficient flexible solar cells,* Advanced Energy Materials **8**, 1801935 (2018).

[203] D. Burkitt, R. Patidar, P. Greenwood, K. Hooper, J. McGettrick, S. Dimitrov, M. Colombo, V. Stoichkov, D. Richards, D. Beynon, *et al.*, *Roll-to-roll slot-die coated p–i–n perovskite solar cells using acetonitrile based single step perovskite solvent system,* Sustainable Energy & Fuels **4**, 3340 (2020).

[204] F. Mathies, T. Abzieher, A. Hochstuhl, K. Glaser, A. Colsmann, U. W. Paetzold, G. Hernandez-Sosa, U. Lemmer, and A. Quintilla, *Multipass inkjet printed planar methylammonium lead iodide perovskite solar cells,* Journal of Materials Chemistry A **4**, 19207 (2016).

[205] C. Zuo, D. Vak, D. Angmo, L. Ding, and M. Gao, *One-step roll-to-roll air processed high efficiency perovskite solar cells,* Nano Energy **46**, 185 (2018).

[206] Z. Li, T. Ma, H. Yang, L. Lu, and R. Wang, *Transparent and colored solar photovoltaics for building integration,* Solar RRL **5**, 2000614 (2021).

[207] A. Giuri, E. Saleh, A. Listorti, S. Colella, A. Rizzo, C. Tuck, and C. Esposito Corcione, *Rheological tunability of perovskite precursor solutions: From spin coating to inkjet printing process,* Nanomaterials **9**, 582 (2019).

[208] B. Dou, J. B. Whitaker, K. Bruening, D. T. Moore, L. M. Wheeler, J. Ryter, N. J. Breslin, J. J. Berry, S. M. Garner, F. S. Barnes, *et al.*, *Roll-to-roll printing of perovskite solar cells,* ACS Energy Letters **3**, 2558 (2018).

[209] L. Qiu, S. He, L. K. Ono, S. Liu, and Y. Qi, *Scalable fabrication of metal halide perovskite solar cells and modules,* ACS Energy Letters **4**, 2147 (2019).

[210] M.-H. Li, C.-W. Hsu, P.-S. Shen, H.-M. Cheng, Y. Chi, P. Chen, and T.-F. Guo, *Novel spiro-based hole transporting materials for efficient perovskite solar cells,* Chemical Communications **51**, 15518 (2015).

[211] Z. Hawash, L. K. Ono, and Y. Qi, *Recent advances in spiro-meotad hole transport material and its applications in organic–inorganic halide perovskite solar cells,* Advanced Materials Interfaces **5**, 1700623 (2018).

[212] D. Luo, W. Yang, Z. Wang, A. Sadhanala, Q. Hu, R. Su, R. Shivanna, G. F. Trindade, J. F. Watts, Z. Xu, *et al.*, *Enhanced photovoltage for inverted planar heterojunction perovskite solar cells,* Science **360**, 1442 (2018).

[213] M. M. Tavakoli and R. Tavakoli, *All-vacuum-processing for fabrication of efficient, large-scale, and flexible inverted perovskite solar cells,* physica Status Solidi (RRL)–Rapid Research Letters **15**, 2000449 (2021).

[214] D.-K. Lee, K.-S. Lim, J.-W. Lee, and N.-G. Park, *Scalable perovskite coating via anti-solvent-free lewis acid–base adduct engineering for efficient perovskite solar modules,* Journal of Materials Chemistry A **9**, 3018 (2021).

[215] M. Zhang, D. Xin, X. Zheng, Q. Chen, and W.-H. Zhang, *Toward greener solution processing of perovskite solar cells,* ACS Sustainable Chemistry & Engineering **8**, 13126 (2020).

[216] Y. Vaynzof, *The future of perovskite photovoltaics—thermal evaporation or solution processing?* Advanced Energy Materials **10**, 2003073 (2020).

[217] C. Roldán-Carmona, O. Malinkiewicz, A. Soriano, G. M. Espallargas, A. Garcia, P. Reinecke, T. Kroyer, M. I. Dar, M. K. Nazeeruddin, and H. J. Bolink, *Flexible high efficiency perovskite solar cells,* Energy & Environmental Science **7**, 994 (2014).

[218] A. C. Nkele, A. C. Nwanya, N. M. Shinde, S. Ezugwu, M. Maaza, J. S. Shaikh, and F. I. Ezema, *The use of nickel oxide as a hole transport material in perovskite solar cell configuration: Achieving a high performance and stable device,* International Journal of Energy Research **44**, 9839 (2020).

[219] K. Cao, Z. Zuo, J. Cui, Y. Shen, T. Moehl, S. M. Zakeeruddin, M. Grätzel, and M. Wang, *Efficient screen printed perovskite solar cells based on mesoscopic architecture,* Nano Energy **17**, 171 (2015).

[220] X. Yin, M. Que, Y. Xing, and W. Que, *High efficiency hysteresis-less inverted planar heterojunction perovskite solar cells with a solution-derived nio x hole contact layer,* Journal of Materials Chemistry A **3**, 24495 (2015).

[221] W. J. Scheideler, N. Rolston, O. Zhao, J. Zhang, and R. H. Dauskardt, *Rapid aqueous spray fabrication of robust niox: a simple and scalable platform for efficient perovskite solar cells,* Advanced Energy Materials **9**, 1803600 (2019).

[222] T. Abzieher, S. Moghadamzadeh, F. Schackmar, H. Eggers, F. Sutterlüti, A. Farooq, D. Kojda, K. Habicht, R. Schmager, A. Mertens, *et al.*, *Electron-beam-evaporated nickel oxide hole transport layers for perovskite-based photovoltaics,* Advanced Energy Materials **9**, 1802995 (2019).

[223] X. Liu, Y. Xiao, Q. Zeng, J. Jiang, and Y. Li, *Large-area organic-free perovskite solar cells with high thermal stability,* The Journal of Physical Chemistry Letters **10**, 6382 (2019).

[224] B.-S. Kim, T.-M. Kim, M.-S. Choi, H.-S. Shim, and J.-J. Kim, *Fully vacuum–processed perovskite solar cells with high open circuit voltage using moo3/npb as hole extraction layers,* Organic Electronics **17**, 102 (2015).

[225] B. Xie, Y. Zhang, Y. Li, W. Chen, X. Hu, and S. Zhang, *Solution preparation of molybdenum oxide on graphene: A hole transport layer for efficient perovskite solar cells with a 1.12 volt high open-circuit voltage,* Journal of Materials Science: Materials in Electronics **31**, 6248 (2020).

[226] A. M. Igual-Muñoz, J. Ávila, P. P. Boix, and H. J. Bolink, *A narrow bandgap perovskite synthesized through evaporation methods for solar cell applications,* Solar RRL **4**, 1900283 (2020).

[227] Q. Zeng, Z. Xu, C. Zheng, Y. Liu, W. Chen, T. Guo, F. Li, C. Xiang, Y. Yang, W. Cao, *et al.*, *Improving charge injection via a blade-coating molybdenum oxide layer: toward high-performance large-area quantum-dot light-emitting diodes,* ACS Applied Materials & Interfaces **10**, 8258 (2018).

[228] W. Zhang, H. Li, C. J. Firby, M. Al-Hussein, and A. Y. Elezzabi, *Oxygen-vacancy-tunable electrochemical properties of electrodeposited molybdenum oxide films,* ACS Applied Materials & Interfaces **11**, 20378 (2019).

[229] A. Ng, Z. Ren, Q. Shen, S. H. Cheung, H. C. Gokkaya, G. Bai, J. Wang, L. Yang, S. K. So, A. B. Djurišić, *et al.*, *Efficiency enhancement by defect engineering in perovskite photovoltaic cells prepared using evaporated multilayers,* Journal of Materials Chemistry A **3**, 9223 (2015).

[230] Y. Zhao, A. M. Nardes, and K. Zhu, *Effective hole extraction using moox-al contact in perovskite solar cells,* Applied Physics Letters **104** (2014).

[231] P. Schulz, J. O. Tiepelt, J. A. Christians, I. Levine, E. Edri, E. M. Sanehira, G. Hodes, D. Cahen, and A. Kahn, *High-work-function molybdenum oxide hole extraction contacts in hybrid organic–inorganic perovskite solar cells,* ACS Applied Materials & Interfaces **8**, 31491 (2016).

[232] I. S. Yang, M. R. Sohn, S. Do Sung, Y. J. Kim, Y. J. Yoo, J. Kim, and W. I. Lee, *Formation of pristine cuscn layer by spray deposition method for efficient perovskite solar cell with extended stability,* Nano Energy **32**, 414 (2017).

[233] J. A. Raiford, R. A. Belisle, K. A. Bush, R. Prasanna, A. F. Palmstrom, M. D. McGehee, and S. F. Bent, *Atomic layer deposition of vanadium oxide to reduce parasitic absorption and improve stability in n–i–p perovskite solar cells for tandems,* Sustainable Energy & Fuels **3**, 1517 (2019).

[234] S. Chu, R. Zhao, R. Liu, Y. Gao, X. Wang, C. Liu, J. Chen, and H. Zhou, *Atomic-layer-deposited ultra-thin vox film as a hole transport layer for perovskite solar cells,* Semiconductor Science and Technology **33**, 115016 (2018).

[235] D. Forgács, D. Pérez-del Rey, J. Ávila, C. Momblona, L. Gil-Escrig, B. Dänekamp, M. Sessolo, and H. J. Bolink, *Efficient wide band gap double cation–double halide perovskite solar cells,* Journal of Materials Chemistry A **5**, 3203 (2017).

[236] Y. Zheng, J. Kong, D. Huang, W. Shi, L. McMillon-Brown, H. E. Katz, J. Yu, and A. D. Taylor, *Spray coating of the pcbm electron transport layer significantly improves the efficiency of pin planar perovskite solar cells,* Nanoscale **10**, 11342 (2018).

[237] Z. Yang, C.-C. Chueh, F. Zuo, J. H. Kim, P.-W. Liang, and A. K.-Y. Jen, *High-performance fully printable perovskite solar cells via blade-coating technique under the ambient condition,* Advanced Energy Materials **5**, 1500328 (2015).

[238] L.-L. Jiang, S. Cong, Y.-H. Lou, Q.-H. Yi, J.-T. Zhu, H. Ma, and G.-F. Zou, *Interface engineering toward enhanced efficiency of planar perovskite solar cells,* Journal of Materials Chemistry A **4**, 217 (2016).

[239] Y. Yang, K. Ri, A. Mei, L. Liu, M. Hu, T. Liu, X. Li, and H. Han, *The size effect of tio 2 nanoparticles on a printable mesoscopic perovskite solar cell,* Journal of Materials Chemistry A **3**, 9103 (2015).

[240] B. Su, H. A. Caller-Guzman, V. Koerstgens, Y. Rui, Y. Yao, N. Saxena, G. Santoro, S. V. Roth, and P. Mueller-Buschbaum, *Macroscale and nanoscale morphology evolution during in situ spray coating of titania films for perovskite solar cells,* ACS Applied Materials & Interfaces **9**, 43724 (2017).

[241] K. S. Keremane, S. Prathapani, L. J. Haur, A. Bruno, A. Priyadarshi, A. V. Adhikari, and S. G. Mhaisalkar, *Improving the performance of carbon-based perovskite solar modules (70 cm^2) by incorporating cesium halide in mesoporous titanium oxide,* ACS Applied Energy Materials **4**, 249 (2020).

[242] P. Chen, Z. Wang, S. Wang, M. Lyu, M. Hao, M. Ghasemi, M. Xiao, J.-H. Yun, Y. Bai, and L. Wang, *Luminescent europium-doped titania for efficiency and uv-stability enhancement of planar perovskite solar cells,* Nano Energy **69**, 104392 (2020).

[243] Q. Jiang, Y. Zhao, X. Zhang, X. Yang, Y. Chen, Z. Chu, Q. Ye, X. Li, Z. Yin, and J. You, *Surface passivation of perovskite film for efficient solar cells,* Nature Photonics **13**, 460 (2019).

[244] Z. Ku, X. Xia, H. Shen, N. H. Tiep, and H. J. Fan, *A mesoporous nickel counter electrode for printable and reusable perovskite solar cells,* Nanoscale **7**, 13363 (2015).

[245] S. H. Lee, G. Kim, J. W. Lim, K.-S. Lee, and M. G. Kang, *High-performance zno: Ga/ag/zno: Ga multilayered transparent electrodes targeting large-scale perovskite solar cells,* Solar Energy Materials and Solar Cells **186**, 378 (2018).

[246] C. Tian, A. Mei, S. Zhang, H. Tian, S. Liu, F. Qin, Y. Xiong, Y. Rong, Y. Hu, Y. Zhou, *et al.*, *Oxygen management in carbon electrode for high-performance printable perovskite solar cells,* Nano Energy **53**, 160 (2018).

[247] H. Chen and S. Yang, *Carbon-based perovskite solar cells without hole transport materials: The front runner to the market?* Advanced materials **29**, 1603994 (2017).

[248] T. Mahmoudi, Y. Wang, and Y.-B. Hahn, *Graphene and its derivatives for solar cells application,* Nano Energy **47**, 51 (2018).

[249] E. L. Lim, C. C. Yap, M. H. H. Jumali, M. A. M. Teridi, and C. H. Teh, *A mini review: can graphene be a novel material for perovskite solar cell applications?* Nano-micro letters **10**, 1 (2018).

[250] Z. Liu, P. You, C. Xie, G. Tang, and F. Yan, *Ultrathin and flexible perovskite solar cells with graphene transparent electrodes,* Nano Energy **28**, 151 (2016).

[251] H. Sung, N. Ahn, M. S. Jang, J.-K. Lee, H. Yoon, N.-G. Park, and M. Choi, *Transparent conductive oxide-free graphene-based perovskite solar cells with over 17% efficiency,* Advanced Energy Materials **6**, 1501873 (2016).

[252] J. Yoon, H. Sung, G. Lee, W. Cho, N. Ahn, H. S. Jung, and M. Choi, *Superflexible, high-efficiency perovskite solar cells utilizing graphene electrodes: towards future foldable power sources,* Energy & Environmental Science **10**, 337 (2017).

[253] C. Zhang, S. Wang, H. Zhang, Y. Feng, W. Tian, Y. Yan, J. Bian, Y. Wang, S. Jin, S. M. Zakeeruddin, *et al.*, *Efficient stable graphene-based perovskite solar cells with high flexibility in device assembling via modular architecture design,* Energy & Environmental Science **12**, 3585 (2019).

[254] M. I. Asghar, J. Zhang, H. Wang, and P. D. Lund, *Device stability of perovskite solar cells–a review,* Renewable and Sustainable Energy Reviews **77**, 131 (2017).

[255] Y. Wang, Y. Zhou, T. Zhang, M.-G. Ju, L. Zhang, M. Kan, Y. Li, X. C. Zeng, N. P. Padture, and Y. Zhao, *Integration of a functionalized graphene nano-network into a planar perovskite absorber for high-efficiency large-area solar cells,* Materials Horizons **5**, 868 (2018).

[256] A. Agresti, S. Pescetelli, A. L. Palma, B. Martin-Garcia, L. Najafi, S. Bellani, I. Moreels, M. Prato, F. Bonaccorso, and A. Di Carlo, *Two-dimensional material interface engineering for efficient perovskite large-area modules,* ACS Energy Letters **4**, 1862 (2019).

[257] J. Wu, J. Shi, Y. Li, H. Li, H. Wu, Y. Luo, D. Li, and Q. Meng, *Quantifying the interface defect for the stability origin of perovskite solar cells,* Advanced Energy Materials **9**, 1901352 (2019).

[258] X. Ren, L. Zhang, Y. Yuan, L. Ding, *et al.*, *Ion migration in perovskite solar cells,* J. Semicond **42**, 010201 (2021).

[259] H. Yu, Q. Sun, T. Zhang, X. Zhang, Y. Shen, and M. Wang, *Is the strain responsible to instability of inorganic perovskites and their photovoltaic devices?* Materials Today Energy **19**, 100601 (2021).

[260] E. Zheng, Z. Niu, G. A. Tosado, H. Dong, Y. Albrikan, and Q. Yu, *Revealing stability of inverted planar ma-free perovskite solar cells and electric field-induced phase instability,* The Journal of Physical Chemistry C **124**, 18805 (2020).

[261] K. J. Xu, R. T. Wang, A. F. Xu, J. Y. Chen, and G. Xu, *Hysteresis and instability predicted in moisture degradation of perovskite solar cells,* ACS Applied Materials & Interfaces **12**, 48882 (2020).

[262] M. Wang, V. Vasudevan, S. Lin, J. Jasieniak, S. P. Russo, N. Birbilis, and N. V. Medhekar, *Molecular mechanisms of thermal instability in hybrid perovskite light absorbers for photovoltaic solar cells,* Journal of Materials Chemistry A **8**, 17765 (2020).

[263] S. Fang, W. Yao, Z. Hu, L. Huang, X. Liu, H. Zhang, J. Zhang, and Y. Zhu, *Stability in photoinduced instability in mixed-halide perovskite materials and solar cells,* The Journal of Physical Chemistry C **125**, 21370 (2021).

[264] S. Bae, S. Kim, S.-W. Lee, K. J. Cho, S. Park, S. Lee, Y. Kang, H.-S. Lee, and D. Kim, *Electric-field-induced degradation of methylammonium lead iodide perovskite solar cells,* The journal of physical chemistry letters **7**, 3091 (2016).

[265] W. Song, L. Rakocevic, R. Thiruvallur Eachambadi, W. Qiu, J. P. Bastos, R. Gehlhaar, Y. Kuang, A. Hadipour, T. Aernouts, and J. Poortmans, *Improving the morphology stability of spiro-ometad films for enhanced thermal stability of perovskite solar cells,* ACS Applied Materials & Interfaces **13**, 44294 (2021).

[266] F. Wan, X. Qiu, H. Chen, Y. Liu, H. Xie, J. Shi, H. Huang, Y. Yuan, Y. Gao, and C. Zhou, *Accelerated electron extraction and improved uv stability of titanium oxide based perovskite solar cells by tin oxide based surface passivation,* Organic Electronics **59**, 184 (2018).

[267] W. Ming, D. Yang, T. Li, L. Zhang, and M.-H. Du, *Formation and diffusion of metal impurities in perovskite solar cell material: implications on solar cell degradation and choice of electrode,* Advanced Science **5**, 1700662 (2018).

[268] A. Mei, X. Li, L. Liu, Z. Ku, T. Liu, Y. Rong, M. Xu, M. Hu, J. Chen, Y. Yang, *et al.*, *A hole-conductor–free, fully printable mesoscopic perovskite solar cell with high stability,* Science **345**, 295 (2014).

[269] Z. Tang, T. Bessho, F. Awai, T. Kinoshita, M. M. Maitani, R. Jono, T. N. Murakami, H. Wang, T. Kubo, S. Uchida, *et al.*, *Hysteresis-free perovskite solar cells made of potassium-doped organometal halide perovskite,* Scientific Reports **7**, 12183 (2017).

[270] S. Tang, S. Huang, G. J. Wilson, and A. Ho-Baillie, *Progress and opportunities for cs incorporated perovskite photovoltaics,* Trends in Chemistry **2**, 638 (2020).

[271] G. Wu, J. Zhou, J. Zhang, R. Meng, B. Wang, B. Xue, X. Leng, D. Zhang, X. Zhang, S. Bi, *et al.*, *Management of the crystallization in two-dimensional perovskite solar*

cells with enhanced efficiency within a wide temperature range and high stability, Nano Energy **58**, 706 (2019).

[272] J. You, L. Meng, T.-B. Song, T.-F. Guo, Y. Yang, W.-H. Chang, Z. Hong, H. Chen, H. Zhou, Q. Chen, *et al., Improved air stability of perovskite solar cells via solution-processed metal oxide transport layers,* Nature Nanotechnology **11**, 75 (2016).

[273] W. Sun, Y. Li, S. Ye, H. Rao, W. Yan, H. Peng, Y. Li, Z. Liu, S. Wang, Z. Chen, *et al., High-performance inverted planar heterojunction perovskite solar cells based on a solution-processed cuo x hole transport layer,* Nanoscale **8**, 10806 (2016).

[274] S. Ye, W. Sun, Y. Li, W. Yan, H. Peng, Z. Bian, Z. Liu, and C. Huang, *Cuscn-based inverted planar perovskite solar cell with an average pce of 15.6%,* Nano Letters **15**, 3723 (2015).

[275] M. V. Khenkin, E. A. Katz, A. Abate, G. Bardizza, J. J. Berry, C. Brabec, F. Brunetti, V. Bulović, Q. Burlingame, A. Di Carlo, *et al., Consensus statement for stability assessment and reporting for perovskite photovoltaics based on isos procedures,* Nature Energy **5**, 35 (2020).

[276] N. Li, X. Niu, Q. Chen, and H. Zhou, *Towards commercialization: the operational stability of perovskite solar cells,* Chemical Society Reviews **49**, 8235 (2020).

[277] Q. Wali, F. J. Iftikhar, M. E. Khan, A. Ullah, Y. Iqbal, and R. Jose, *Advances in stability of perovskite solar cells,* Organic Electronics **78**, 105590 (2020).

[278] S. Zhang, Z. Liu, W. Zhang, Z. Jiang, W. Chen, R. Chen, Y. Huang, Z. Yang, Y. Zhang, L. Han, *et al., Barrier designs in perovskite solar cells for long-term stability,* Advanced Energy Materials **10**, 2001610 (2020).

[279] M. K. Rao, D. Sangeetha, M. Selvakumar, Y. Sudhakar, and M. Mahesha, *Review on persistent challenges of perovskite solar cells' stability,* Solar Energy **218**, 469 (2021).

[280] U. Krishnan, M. Kaur, M. Kumar, and A. Kumar, *Factors affecting the stability of perovskite solar cells: a comprehensive review,* Journal of Photonics for Energy **9**, 021001 (2019).

[281] H. Tan, E. Moulin, F. T. Si, J.-W. Schüttauf, M. Stuckelberger, O. Isabella, F.-J. Haug, C. Ballif, M. Zeman, and A. H. Smets, *Highly transparent modulated surface textured front electrodes for high-efficiency multijunction thin-film silicon solar cells,* Progress in Photovoltaics: Research and Applications **23**, 949 (2015).

[282] T. Matsui, K. Maejima, A. Bidiville, H. Sai, T. Koida, T. Suezaki, M. Matsumoto, K. Saito, I. Yoshida, and M. Kondo, *High-efficiency thin-film silicon solar cells realized by integrating stable a-si: H absorbers into improved device design,* Japanese Journal of Applied Physics **54**, 08KB10 (2015).

[283] J. Cashmore, M. Apolloni, A. Braga, O. Caglar, V. Cervetto, Y. Fenner, S. Goldbach-Aschemann, C. Goury, J. Hötzel, T. Iwahashi, *et al., Improved conversion efficiencies of thin-film silicon tandem (micromorph™) photovoltaic modules,* Solar Energy Materials and Solar Cells **144**, 84 (2016).

[284] S. Kim, J.-W. Chung, H. Lee, J. Park, Y. Heo, and H.-M. Lee, *Remarkable progress in thin-film silicon solar cells using high-efficiency triple-junction technology,* Solar Energy Materials and Solar Cells **119**, 26 (2013).

[285] B. Liu, L. Bai, Z. Chen, X. Zhang, D. Zhang, J. Ni, Q. Huang, C. Wei, J. Sun, X. Chen, *et al., High efficiency triple junction thin film silicon solar cells with optimized electrical structure,* Progress in Photovoltaics: Research and Applications **23**, 1313 (2015).

[286] K. Söderström, G. Bugnon, R. Biron, C. Pahud, F. Meillaud, F.-J. Haug, and C. Ballif, *Thin-film silicon triple-junction solar cell with 12.5% stable efficiency on innovative flat light-scattering substrate,* Journal of Applied Physics **112** (2012).

[287] B. Yan, G. Yue, L. Sivec, J. Yang, S. Guha, and C.-S. Jiang, *Innovative dual function nc-siox: H layer leading to a> 16% efficient multi-junction thin-film silicon solar cell,* Applied Physics Letters **99** (2011).

[288] H. Sai, T. Matsui, and K. Matsubara, *Stabilized 14.0%-efficient triple-junction thin-film silicon solar cell,* Applied Physics Letters **109** (2016).

[289] F.-J. Haug and C. Ballif, *Light management in thin film silicon solar cells,* Energy & Environmental Science **8**, 824 (2015).

[290] O. Isabella, A. H. M. Smets, and M. Zeman, *Thin-film silicon-based quadruple junction solar cells approaching 20% conversion efficiency,* Solar Energy Materials and Solar Cells **129**, 82 (2014).

[291] F. T. Si, D. Y. Kim, R. Santbergen, H. Tan, R. A. van Swaaij, A. H. Smets, O. Isabella, and M. Zeman, *Quadruple-junction thin-film silicon-based solar cells with high open-circuit voltage,* Applied Physics Letters **105** (2014).

[292] O. Isabella, R. Vismara, D. Linssen, K. Wang, S. Fan, and M. Zeman, *Advanced light trapping scheme in decoupled front and rear textured thin-film silicon solar cells,* Solar Energy **162**, 344 (2018).

[293] K. Nakada, T. Nishimura, N. Suyama, and A. Yamada, *Cathode luminescence analysis of solar cells treated with thiourea solution,* Japanese Journal of Applied Physics **60**, 031001 (2021).

[294] F. Fan, *Development of advanced solar cells-Contribution to the HCSC on InP and to the III-V onto Si monolithic tandem cells*, Ph.D. thesis, INSA de Rennes (2022).

[295] N. Jain, K. L. Schulte, J. F. Geisz, D. J. Friedman, R. M. France, E. E. Perl, A. G. Norman, H. L. Guthrey, and M. A. Steiner, *High-efficiency inverted metamorphic 1.7/1.1 ev gainasp/gainas dual-junction solar cells,* Applied Physics Letters **112** (2018).

[296] F. Dimroth, T. N. Tibbits, M. Niemeyer, F. Predan, P. Beutel, C. Karcher, E. Oliva, G. Siefer, D. Lackner, P. Fuß-Kailuweit, *et al.*, *Four-junction wafer-bonded concentrator solar cells,* IEEE Journal of Photovoltaics **6**, 343 (2015).

[297] J. F. Geisz, M. A. Steiner, N. Jain, K. L. Schulte, R. M. France, W. E. McMahon, E. E. Perl, and D. J. Friedman, *Building a six-junction inverted metamorphic concentrator solar cell,* IEEE Journal of Photovoltaics **8**, 626 (2017).

[298] K. Sasaki, T. Agui, K. Nakaido, N. Takahashi, R. Onitsuka, and T. Takamoto, *Development of ingap/gaas/ingaas inverted triple junction concentrator solar cells,* in *AIP conference proceedings*, Vol. 1556 (American Institute of Physics, 2013) pp. 22–25.

[299] P. Chiu, D. Law, R. Woo, S. Singer, D. Bhusari, W. Hong, A. Zakaria, J. Boisvert, S. Mesropian, R. King, *et al.*, *Ieee 40th photovolt,* in *Spec. Conf. PVSC*, Vol. 2014 (2014) pp. 11–13.

[300] J. Yan, T. J. Savenije, L. Mazzarella, and O. Isabella, *Progress and challenges on scaling up of perovskite solar cell technology,* Sustainable Energy & Fuels **6**, 243 (2022).

[301] N. N. Demonstrates, *45.7% efficiency for concentrator solar cell new design for ultra-efficient iii-v multijunction cell pushes the limits of solar conversion, news release nr-4514. 2014 [updated 2014 december 16; cited 2015 june 17],* (2015).

[302] D. Wilt and M. Stan, *High efficiency multijunction photovoltaic development,* Industrial & Engineering Chemistry Research **51**, 11931 (2012).

[303] Z. J. Yu, M. Leilaeioun, and Z. Holman, *Selecting tandem partners for silicon solar cells,* Nature Energy **1**, 1 (2016).

[304] E. L. Warren, W. E. McMahon, M. Rienacker, K. T. VanSant, R. C. Whitehead, R. Peibst, and A. C. Tamboli, *A taxonomy for three-terminal tandem solar cells,* ACS Energy Letters **5**, 1233 (2020).

[305] M. Rienäcker, E. L. Warren, M. Schnabel, H. Schulte-Huxel, R. Niepelt, R. Brendel, P. Stradins, A. C. Tamboli, and R. Peibst, *Back-contacted bottom cells with three terminals: Maximizing power extraction from current-mismatched tandem cells,* Progress in Photovoltaics: Research and Applications **27**, 410 (2019).

[306] T. C.-J. Yang, P. Fiala, Q. Jeangros, and C. Ballif, *High-bandgap perovskite materials for multijunction solar cells,* Joule **2**, 1421 (2018).

[307] R. Comin, G. Walters, E. S. Thibau, O. Voznyy, Z.-H. Lu, and E. H. Sargent, *Structural, optical, and electronic studies of wide-bandgap lead halide perovskites,* Journal of Materials Chemistry C **3**, 8839 (2015).

[308] N. Y. Nia, D. Saranin, A. L. Palma, and A. Di Carlo, *Perovskite solar cells,* in *Solar Cells and Light Management* (Elsevier, 2020) pp. 163–228.

[309] H. Shen, J. Peng, D. Jacobs, N. Wu, J. Gong, Y. Wu, S. K. Karuturi, X. Fu, K. Weber, X. Xiao, *et al.*, *Mechanically-stacked perovskite/cigs tandem solar cells with efficiency of 23.9% and reduced oxygen sensitivity,* Energy & Environmental Science **11**, 394 (2018).

[310] T. J. Jacobsson, A. Hultqvist, S. Svanström, L. Riekehr, U. B. Cappel, E. Unger, H. Rensmo, E. M. Johansson, M. Edoff, and G. Boschloo, *2-terminal cigs-perovskite tandem cells: A layer by layer exploration,* Solar Energy **207**, 270 (2020).

[311] Y. Cheng and L. Ding, *Perovskite/si tandem solar cells: Fundamentals, advances, challenges, and novel applications,* SusMat **1**, 324 (2021).

[312] S. Chauhan and R. Singh, *A review on perovskite/silicon tandem solar cells,* (2021).

[313] Q. Hou, D. Bacal, A. N. Jumabekov, W. Li, Z. Wang, X. Lin, S. H. Ng, B. Tan, Q. Bao, A. S. Chesman, *et al.*, *Back-contact perovskite solar cells with honeycomb-like charge collecting electrodes,* Nano Energy **50**, 710 (2018).

[314] L. Yan, C. Han, B. Shi, Y. Zhao, and X. Zhang, *A review on the crystalline silicon bottom cell for monolithic perovskite/silicon tandem solar cells,* Materials Today Nano **7**, 100045 (2019).

[315] Q. Wali, N. K. Elumalai, Y. Iqbal, A. Uddin, and R. Jose, *Tandem perovskite solar cells,* Renewable and Sustainable Energy Reviews **84**, 89 (2018).

[316] H. Shen, S. T. Omelchenko, D. A. Jacobs, S. Yalamanchili, Y. Wan, D. Yan, P. Phang, T. Duong, Y. Wu, Y. Yin, *et al.*, *In situ recombination junction between p-silicon and titanium dioxide enables high-efficiency monolithic perovskite/si tandem cells,* Science Advances **4**, eaau9711 (2018).

[317] K. A. Bush, A. F. Palmstrom, Z. J. Yu, M. Boccard, R. Cheacharoen, J. P. Mailoa, D. P. McMeekin, R. L. Hoye, C. D. Bailie, T. Leijtens, *et al.*, *23.6%-efficient monolithic perovskite/silicon tandem solar cells with improved stability,* Nature Energy **2**, 1 (2017).

[318] J. Werner, C.-H. Weng, A. Walter, L. Fesquet, J. P. Seif, S. De Wolf, B. Niesen, and C. Ballif, *Efficient monolithic perovskite/silicon tandem solar cell with cell area> 1 cm2,* The journal of physical chemistry letters **7**, 161 (2016).

[319] J. Zheng, C. F. J. Lau, H. Mehrvarz, F.-J. Ma, Y. Jiang, X. Deng, A. Soeriyadi, J. Kim, M. Zhang, L. Hu, *et al.*, *Large area efficient interface layer free monolithic perovskite/homo-junction-silicon tandem solar cell with over 20% efficiency,* Energy & Environmental Science **11**, 2432 (2018).

[320] Y. Wu, D. Yan, J. Peng, Y. Wan, S. P. Phang, H. Shen, N. Wu, C. Barugkin, X. Fu, S. Surve, *et al.*, *Monolithic perovskite/silicon-homojunction tandem solar cell with over 22% efficiency,* Energy & Environmental Science **10**, 2472 (2017).

[321] E. Köhnen, M. Jošt, A. B. Morales-Vilches, P. Tockhorn, A. Al-Ashouri, B. Macco, L. Kegelmann, L. Korte, B. Rech, R. Schlatmann, *et al.*, *Highly efficient monolithic perovskite silicon tandem solar cells: analyzing the influence of current mismatch on device performance,* Sustainable Energy & Fuels **3**, 1995 (2019).

[322] Z. Wang, X. Zhu, S. Zuo, M. Chen, C. Zhang, C. Wang, X. Ren, Z. Yang, Z. Liu, X. Xu, *et al.*, *27%-efficiency four-terminal perovskite/silicon tandem solar cells by sandwiched gold nanomesh,* Advanced Functional Materials **30**, 1908298 (2020).

[323] Y. Hou, E. Aydin, M. De Bastiani, C. Xiao, F. H. Isikgor, D.-J. Xue, B. Chen, H. Chen, B. Bahrami, A. H. Chowdhury, *et al.*, *Efficient tandem solar cells with solution-processed perovskite on textured crystalline silicon,* Science **367**, 1135 (2020).

[324] J.-K. Hwang, S.-W. Lee, W. Lee, S. Bae, K. Cho, S. Kim, S. Lee, J. Y. Hyun, Y. Kang, H.-S. Lee, *et al.*, *Conformal perovskite films on 100 cm^2 textured silicon surface using two-step vacuum process,* Thin Solid Films **693**, 137694 (2020).

[325] A. S. Subbiah, F. H. Isikgor, C. T. Howells, M. De Bastiani, J. Liu, E. Aydin, F. Furlan, T. G. Allen, F. Xu, S. Zhumagali, *et al.*, *High-performance perovskite single-junction and textured perovskite/silicon tandem solar cells via slot-die-coating,* ACS Energy Letters **5**, 3034 (2020).

[326] J. P. Mailoa, C. D. Bailie, E. C. Johlin, E. T. Hoke, A. J. Akey, W. H. Nguyen, M. D. McGehee, and T. Buonassisi, *A 2-terminal perovskite/silicon multijunction solar cell enabled by a silicon tunnel junction,* Applied Physics Letters **106** (2015).

[327] J. Werner, A. Walter, E. Rucavado, S.-J. Moon, D. Sacchetto, M. Rienaecker, R. Peibst, R. Brendel, X. Niquille, S. De Wolf, *et al.*, *Zinc tin oxide as high-temperature stable recombination layer for mesoscopic perovskite/silicon monolithic tandem solar cells,* Applied Physics Letters **109** (2016).

[328] J. Zheng, H. Mehrvarz, C. Liao, J. Bing, X. Cui, Y. Li, V. R. Gonçales, C. F. J. Lau, D. S. Lee, Y. Li, *et al.*, *Large-area 23%-efficient monolithic perovskite/homojunction-silicon tandem solar cell with enhanced uv stability using down-shifting material,* ACS Energy Letters **4**, 2623 (2019).

[329] F. Sahli, B. A. Kamino, J. Werner, M. Bräuninger, B. Paviet-Salomon, L. Barraud, R. Monnard, J. P. Seif, A. Tomasi, Q. Jeangros, *et al.*, *Improved optics in monolithic perovskite/silicon tandem solar cells with a nanocrystalline silicon recombination junction,* Advanced Energy Materials **8**, 1701609 (2018).

[330] K. A. Bush, S. Manzoor, K. Frohna, Z. J. Yu, J. A. Raiford, A. F. Palmstrom, H.-P. Wang, R. Prasanna, S. F. Bent, Z. C. Holman, *et al.*, *Minimizing current and voltage losses to reach 25% efficient monolithic two-terminal perovskite–silicon tandem solar cells,* ACS Energy Letters **3**, 2173 (2018).

[331] G. Nogay, F. Sahli, J. Werner, R. Monnard, M. Boccard, M. Despeisse, F. Haug, Q. Jeangros, A. Ingenito, and C. Ballif, *25.1%-efficient monolithic perovskite/silicon tandem solar cell based on a p-type monocrystalline textured silicon wafer and high-temperature passivating contacts,* ACS Energy Letters **4**, 844 (2019).

[332] B. A. Kamino, B. Paviet-Salomon, S.-J. Moon, N. Badel, J. Levrat, G. Christmann, A. Walter, A. Faes, L. Ding, J. J. Diaz Leon, *et al.*, *Low-temperature screen-printed metallization for the scale-up of two-terminal perovskite–silicon tandems,* ACS Applied Energy Materials **2**, 3815 (2019).

[333] A. Al-Ashouri, E. Köhnen, B. Li, A. Magomedov, H. Hempel, P. Caprioglio, J. A. Márquez, A. B. Morales Vilches, E. Kasparavicius, J. A. Smith, *et al.*, *Monolithic perovskite/silicon tandem solar cell with> 29% efficiency by enhanced hole extraction,* Science **370**, 1300 (2020).

[334] D. Kim, H. J. Jung, I. J. Park, B. W. Larson, S. P. Dunfield, C. Xiao, J. Kim, J. Tong, P. Boonmongkolras, S. G. Ji, *et al.*, *Efficient, stable silicon tandem cells enabled by anion-engineered wide-bandgap perovskites,* Science **368**, 155 (2020).

[335] J. Xu, C. C. Boyd, Z. J. Yu, A. F. Palmstrom, D. J. Witter, B. W. Larson, R. M. France, J. Werner, S. P. Harvey, E. J. Wolf, *et al.*, *Triple-halide wide–band gap perovskites with suppressed phase segregation for efficient tandems,* Science **367**, 1097 (2020).

[336] E. Lamanna, F. Matteocci, E. Calabrò, L. Serenelli, E. Salza, L. Buschbaumini, F. Menchini, M. Izzi, A. Agresti, S. Pescetelli, *et al.*, *Mechanically stacked, two-terminal graphene-based perovskite/silicon tandem solar cell with efficiency over 26%,* Joule **4**, 865 (2020).

[337] P. Tockhorn, J. Sutter, A. Cruz, P. Wagner, K. Jäger, D. Yoo, F. Lang, M. Grischek, B. Li, J. Li, *et al.*, *Nano-optical designs for high-efficiency monolithic perovskite–silicon tandem solar cells,* Nature Nanotechnology **17**, 1214 (2022).

[338] X. Y. Chin, D. Turkay, J. A. Steele, S. Tabean, S. Eswara, M. Mensi, P. Fiala, C. M. Wolff, A. Paracchino, K. Artuk, *et al.*, *Interface passivation for 31.25%-efficient perovskite/silicon tandem solar cells,* Science **381**, 59 (2023).

[339] S. Mariotti, E. Köhnen, F. Scheler, K. Sveinbjörnsson, L. Zimmermann, M. Piot, F. Yang, B. Li, J. Warby, A. Musiienko, *et al.*, *Interface engineering for high-performance, triple-halide perovskite–silicon tandem solar cells,* Science **381**, 63 (2023).

[340] KAUST, *Kaust breaks the tandem photovoltaic world record,* (2023).

[341] E. Ugur, A. A. Said, P. Dally, S. Zhang, C. E. Petoukhoff, D. Rosas-Villalva, S. Zhumagali, B. K. Yildirim, A. Razzaq, S. Sarwade, *et al.*, *Enhanced cation interaction in perovskites for efficient tandem solar cells with silicon,* Science **385**, 533 (2024).

[342] Z. Liu, Z. Xiong, S. Yang, K. Fan, L. Jiang, Y. Mao, C. Qin, S. Li, L. Qiu, J. Zhang, *et al.*, *Strained heterojunction enables high-performance, fully textured perovskite/silicon tandem solar cells,* Joule (2024).

[343] A. S. Subbiah, L. V. Torres Merino, A. R. Pininti, V. Hnapovskyi, S. Mannar, E. Aydin, A. Razzaq, T. G. Allen, and S. De Wolf, *Enhancing the performance of blade-coated perovskite/silicon tandems via molecular doping and interfacial energy alignment,* ACS Energy Letters **9**, 727 (2024).

[344] M. De Bastiani, A. S. Subbiah, E. Aydin, F. H. Isikgor, T. G. Allen, and S. De Wolf, *Recombination junctions for efficient monolithic perovskite-based tandem solar cells: physical principles, properties, processing and prospects,* Materials Horizons **7**, 2791 (2020).

[345] M. Singh, R. Santbergen, I. Syifai, A. Weeber, M. Zeman, and O. Isabella, *Comparing optical performance of a wide range of perovskite/silicon tandem architectures under real-world conditions,* Nanophotonics **10**, 2043 (2021).

[346] D. A. Jacobs, M. Langenhorst, F. Sahli, B. S. Richards, T. P. White, C. Ballif, K. R. Catchpole, and U. W. Paetzold, *Light management: a key concept in high-efficiency perovskite/silicon tandem photovoltaics,* The journal of physical chemistry letters **10**, 3159 (2019).

[347] F. Hou, C. Han, O. Isabella, L. Yan, B. Shi, J. Chen, S. An, Z. Zhou, W. Huang, H. Ren, *et al.*, *Inverted pyramidally-textured pdms antireflective foils for perovskite/silicon tandem solar cells with flat top cell,* Nano energy **56**, 234 (2019).

[348] M. Jošt, E. Köhnen, A. B. Morales-Vilches, B. Lipovšek, K. Jäger, B. Macco, A. Al-Ashouri, J. Krč, L. Korte, B. Rech, *et al.*, *Textured interfaces in monolithic perovskite/silicon tandem solar cells: advanced light management for improved efficiency and energy yield,* Energy & Environmental Science **11**, 3511 (2018).

[349] L. Mazzarella, Y.-H. Lin, S. Kirner, A. B. Morales-Vilches, L. Korte, S. Albrecht, E. Crossland, B. Stannowski, C. Case, H. J. Snaith, *et al.*, *Infrared light management using a nanocrystalline silicon oxide interlayer in monolithic perovskite/silicon heterojunction tandem solar cells with efficiency above 25%,* Advanced Energy Materials **9**, 1803241 (2019).

[350] A. Al-Ashouri, A. Magomedov, M. Roß, M. Jošt, B. Talaikis, G. Chistiakova, T. Bertram, J. A. Márquez, E. Köhnen, E. Kasparavičius, *et al.*, *Conformal monolayer contacts with lossless interfaces for perovskite single junction and monolithic tandem solar cells,* Energy & Environmental Science **12**, 3356 (2019).

[351] J. Zheng, H. Mehrvarz, F.-J. Ma, C. F. J. Lau, M. A. Green, S. Huang, and A. W. Ho-Baillie, *21.8% efficient monolithic perovskite/homo-junction-silicon tandem solar cell on 16 cm^2,* ACS Energy Letters **3**, 2299 (2018).

[352] Y. Wang, Y. Zhang, P. Zhang, and W. Zhang, *High intrinsic carrier mobility and photon absorption in the perovskite,* Physical Chemistry Chemical Physics **17**, 11516 (2015).

[353] S. Bai, Z. Wu, X. Wu, Y. Jin, N. Zhao, Z. Chen, Q. Mei, X. Wang, Z. Ye, T. Song, *et al.*, *High-performance planar heterojunction perovskite solar cells: Preserving long charge carrier diffusion lengths and interfacial engineering,* Nano Research **7**, 1749 (2014).

[354] K. X. Steirer, P. Schulz, G. Teeter, V. Stevanovic, M. Yang, K. Zhu, and J. J. Berry, *Defect tolerance in methylammonium lead triiodide perovskite,* ACS Energy Letters **1**, 360 (2016).

[355] H. Min, D. Y. Lee, J. Kim, G. Kim, K. S. Lee, J. Kim, M. J. Paik, Y. K. Kim, K. S. Kim, M. G. Kim, *et al.*, *Perovskite solar cells with atomically coherent interlayers on tin oxide electrodes,* Nature **598**, 444 (2021).

[356] F. Xu, T. Zhang, G. Li, and Y. Zhao, *Mixed cation hybrid lead halide perovskites with enhanced performance and stability,* Journal of Materials Chemistry A **5**, 11450 (2017).

[357] B.-S. Kim, L. Gil-Escrig, M. Sessolo, and H. J. Bolink, *Deposition kinetics and compositional control of vacuum-processed perovskite,* The Journal of Physical Chemistry Letters **11**, 6852 (2020).

[358] B.-S. Kim, Y. Han, and J.-J. Kim, *Growth mechanism of perovskite in a vacuum processed perovskite,* Nanoscale Advances **2**, 3906 (2020).

[359] J. Li, H. A. Dewi, H. Wang, J. Zhao, N. Tiwari, N. Yantara, T. Malinauskas, V. Getautis, T. J. Savenije, N. Mathews, *et al.*, *Co-evaporated mapbi3 with graded fermi levels enables highly performing, scalable, and flexible p-i-n perovskite solar cells,* Advanced Functional Materials **31**, 2103252 (2021).

[360] R. Ji, Z. Zhang, C. Cho, Q. An, F. Paulus, M. Kroll, M. Löffler, F. Nehm, B. Rellinghaus, K. Leo, *et al.*, *Thermally evaporated methylammonium-free perovskite solar cells,* Journal of Materials Chemistry C **8**, 7725 (2020).

[361] W. Tan, A. R. Bowring, A. C. Meng, M. D. McGehee, and P. C. McIntyre, *Thermal stability of mixed cation metal halide perovskites in air,* ACS Applied Materials & Interfaces **10**, 5485 (2018).

[362] J. Zhao, V. M. Caselli, M. Bus, B. Boshuizen, and T. J. Savenije, *How deep hole traps affect the charge dynamics and collection in bare and bilayers of methylammonium lead bromide,* ACS Applied Materials & Interfaces **13**, 16309 (2021).

[363] E. M. Hutter, M. C. Gélvez-Rueda, A. Osherov, V. Bulović, F. C. Grozema, S. D. Stranks, and T. J. Savenije, *Direct–indirect character of the bandgap in methylammonium lead iodide perovskite,* Nature materials **16**, 115 (2017).

[364] T. Abzieher, T. Feeney, F. Schackmar, Y. J. Donie, I. M. Hossain, J. A. Schwenzer, T. Hellmann, T. Mayer, M. Powalla, and U. W. Paetzold, *From groundwork to efficient solar cells: On the importance of the substrate material in co-evaporated perovskite solar cells,* Advanced Functional Materials **31**, 2104482 (2021).

[365] S. A. Kulkarni, T. Baikie, P. P. Boix, N. Yantara, N. Mathews, and S. Mhaisalkar, *Band-gap tuning of lead halide perovskites using a sequential deposition process,* Journal of Materials Chemistry A **2**, 9221 (2014).

[366] P. Du, L. Wang, J. Li, J. Luo, Y. Ma, J. Tang, and T. Zhai, *Thermal evaporation for halide perovskite optoelectronics: Fundamentals, progress, and outlook,* Advanced Optical Materials **10**, 2101770 (2022).

[367] X. Ren, Z. Yang, D. Yang, X. Zhang, D. Cui, Y. Liu, Q. Wei, H. Fan, and S. F. Liu, *Modulating crystal grain size and optoelectronic properties of perovskite films for solar cells by reaction temperature,* Nanoscale **8**, 3816 (2016).

[368] Y. Zhou, M. Yang, A. L. Vasiliev, H. F. Garces, Y. Zhao, D. Wang, S. Pang, K. Zhu, and N. P. Padture, *Growth control of compact perovskite thin films via enhanced solid-state precursor reaction for efficient planar perovskite solar cells,* Journal of Materials Chemistry A **3**, 9249 (2015).

[369] Y. Wu, A. Islam, X. Yang, C. Qin, J. Liu, K. Zhang, W. Peng, and L. Han, *Retarding the crystallization of lead iodide for highly reproducible planar-structured perovskite solar cells via sequential deposition,* Energy & Environmental Science **7**, 2934 (2014).

[370] H. Tan, F. Che, M. Wei, Y. Zhao, M. I. Saidaminov, P. Todorović, D. Broberg, G. Walters, F. Tan, T. Zhuang, *et al.*, *Dipolar cations confer defect tolerance in wide-bandgap metal halide perovskites,* Nature Communications **9**, 3100 (2018).

[371] L. A. Muscarella, E. M. Hutter, S. Sanchez, C. D. Dieleman, T. J. Savenije, A. Hagfeldt, M. Saliba, and B. Ehrler, *Crystal orientation and grain size: do they determine optoelectronic properties of perovskite?* The journal of physical chemistry letters **10**, 6010 (2019).

[372] O. G. Reid, M. Yang, N. Kopidakis, K. Zhu, and G. Rumbles, *Grain-size-limited mobility in methylammonium lead iodide perovskite thin films,* ACS Energy Letters **1**, 561 (2016).

[373] C. Momblona, L. Gil-Escrig, E. Bandiello, E. M. Hutter, M. Sessolo, K. Lederer, J. Blochwitz-Nimoth, and H. J. Bolink, *Efficient vacuum deposited pin and nip perovskite solar cells employing doped charge transport layers,* Energy & Environmental Science **9**, 3456 (2016).

[374] H. Lu, Y. Liu, P. Ahlawat, A. Mishra, W. R. Tress, F. T. Eickemeyer, Y. Yang, F. Fu, Z. Wang, C. E. Avalos, *et al.*, *Vapor-assisted deposition of highly efficient, stable black-phase perovskite solar cells,* Science **370**, eabb8985 (2020).

[375] P. J. Dale and M. A. Scarpulla, *Efficiency versus effort: A better way to compare best photovoltaic research cell efficiencies,* Solar Energy Materials and Solar Cells **251**, 112097 (2023).

[376] J. Y. Kim, J.-W. Lee, H. S. Jung, H. Shin, and N.-G. Park, *High-efficiency perovskite solar cells,* Chemical reviews **120**, 7867 (2020).

[377] S. Bi, X. Leng, Y. Li, Z. Zheng, X. Zhang, Y. Zhang, and H. Zhou, *Interfacial modification in organic and perovskite solar cells,* Advanced Materials **31**, 1805708 (2019).

[378] D. Shi, V. Adinolfi, R. Comin, M. Yuan, E. Alarousu, A. Buin, Y. Chen, S. Hoogland, A. Rothenberger, K. Katsiev, *et al.*, *Low trap-state density and long carrier diffusion in organolead trihalide perovskite single crystals,* Science **347**, 519 (2015).

[379] F. Zhang and K. Zhu, *Additive engineering for efficient and stable perovskite solar cells,* Advanced Energy Materials **10**, 1902579 (2020).

[380] L. Huang, Z. Hu, J. Xu, K. Zhang, J. Zhang, and Y. Zhu, *Multi-step slow annealing perovskite films for high performance planar perovskite solar cells,* Solar energy materials and solar cells , 377 (2015).

[381] G. Uzurano, N. Kuwahara, T. Saito, A. Fujii, and M. Ozaki, *Orientation control of two-dimensional perovskite in two-dimensional/three-dimensional heterostructure by templated growth on 3d perovskite,* ACS Materials Letters **4**, 378 (2022).

[382] W. Zhao, M. Wu, Z. Liu, S. Yang, Y. Li, J. Wang, L. Yang, Y. Han, and S. Liu, *Orientation engineering via 2d seeding for stable 24.83% efficiency perovskite solar cells,* Advanced Energy Materials **13**, 2204260 (2023).

[383] Z. Xu, Z. Liu, N. Li, G. Tang, G. Zheng, C. Zhu, Y. Chen, L. Wang, Y. Huang, L. Li, *et al.*, *A thermodynamically favored crystal orientation in mixed formamidinium/methylammonium perovskite for efficient solar cells,* Advanced Materials **31**, 1900390 (2019).

[384] H. Zhang, M. Qin, Z. Chen, W. Yu, Z. Ren, K. Liu, J. Huang, Y. Zhang, Q. Liang, H. T. Chandran, *et al.*, *Bottom-up quasi-epitaxial growth of hybrid perovskite from solution process—achieving high-efficiency solar cells via template -guided crystallization,* Advanced Materials **33**, 2100009 (2021).

[385] G. Niu, H. Yu, J. Li, D. Wang, and L. Wang, *Controlled orientation of perovskite films through mixed cations toward high performance perovskite solar cells,* Nano Energy **27**, 87 (2016).

[386] G. Zheng, C. Zhu, J. Ma, X. Zhang, G. Tang, R. Li, Y. Chen, L. Li, J. Hu, J. Hong, *et al.*, *Manipulation of facet orientation in hybrid perovskite polycrystalline films by cation cascade,* Nature Communications **9**, 2793 (2018).

[387] P. Wu, J. He, and F. Zhang, *Vacuum thermal evaporation saved ma-free perovskite,* Joule **6**, 1394 (2022).

[388] Y.-H. Chiang, K. Frohna, H. Salway, A. Abfalterer, L. Pan, B. Roose, M. Anaya, and S. D. Stranks, *Vacuum-deposited wide-bandgap perovskite for all-perovskite tandem solar cells,* ACS Energy Letters **8**, 2728 (2023).

[389] F. U. Kosasih, E. Erdenebileg, N. Mathews, S. G. Mhaisalkar, and A. Bruno, *Thermal evaporation and hybrid deposition of perovskite solar cells and mini-modules,* Joule **6**, 2692 (2022).

[390] Z. Fang, N. Yan, and S. Liu, *Modulating preferred crystal orientation for efficient and stable perovskite solar cells-from progress to perspectives,* InfoMat **4**, e12369 (2022).

[391] B. Li, T. Shen, and S. Yun, *Recent progress of crystal orientation engineering in halide perovskite photovoltaics,* Materials Horizons **10**, 13 (2023).

[392] N. Klipfel, C. Momblona, H. Kanda, N. Shibayama, Y. Nakamura, M. D. Mensi, C. Liu, C. Roldaen-Carmona, and M. K. Nazeeruddin, *Crystallographically oriented hybrid perovskites via thermal vacuum codeposition,* Solar RRL **5**, 2100191 (2021).

[393] E. Raza and Z. Ahmad, *Review on two-terminal and four-terminal crystalline-silicon/perovskite tandem solar cells; progress, challenges, and future perspectives,* Energy Reports **8**, 5820 (2022).

[394] J. Yan, J. Zhao, H. Wang, M. Kerklaan, L. J. Bannenberg, B. Ibrahim, T. J. Savenije, L. Mazzarella, and O. Isabella, *Crystallization process for high-quality perovskite film deposited via simplified sequential vacuum evaporation,* ACS Applied Energy Materials **6**, 10265 (2023).

[395] H. Xiong, G. DeLuca, Y. Rui, Y. Li, E. Reichmanis, Q. Zhang, and H. Wang, *Solvent vapor annealing of oriented lead iodide films for improved crystallization of perovskite films in the air,* Solar Energy Materials and Solar Cells **166**, 167 (2017).

[396] G. Longo, C. Momblona, M.-G. La-Placa, L. Gil-Escrig, M. Sessolo, and H. J. Bolink, *Fully vacuum-processed wide band gap mixed-halide perovskite solar cells,* ACS energy letters **3**, 214 (2017).

[397] H. Li, J. Zhou, L. Tan, M. Li, C. Jiang, S. Wang, X. Zhao, Y. Liu, Y. Zhang, Y. Ye, *et al.*, *Sequential vacuum-evaporated perovskite solar cells with more than 24% efficiency,* Science Advances **8**, eabo7422 (2022).

[398] Y.-H. Chiang, M. Anaya, and S. D. Stranks, *Multisource vacuum deposition of methylammonium-free perovskite solar cells,* ACS Energy Letters **5**, 2498 (2020).

[399] W. L. Tan and C. R. McNeill, *X-ray diffraction of photovoltaic perovskites: Principles and applications,* Applied Physics Reviews **9** (2022).

[400] D. Fang, F. He, J. Xie, and L. Xue, *Calibration of binding energy positions with c1s for xps results,* Journal of Wuhan University of Technology-Mater. Sci. Ed. **35**, 711 (2020).

[401] J. Li, Y. Liu, X. Ren, Z. Yang, R. Li, H. Su, X. Yang, J. Xu, H. Xu, J.-Y. Hu, *et al.*, *Solution coating of superior large-area flexible perovskite thin films with controlled crystal packing,* Advanced Optical Materials **5**, 1700102 (2017).

[402] B. J. Foley, J. Girard, B. A. Sorenson, A. Z. Chen, J. S. Niezgoda, M. R. Alpert, A. F. Harper, D.-M. Smilgies, P. Clancy, W. A. Saidi, *et al.*, *Controlling nucleation, growth, and orientation of metal halide perovskite thin films with rationally selected additives,* Journal of Materials Chemistry A **5**, 113 (2017).

[403] T. Kirchartz, J. A. Maerquez, M. Stolterfoht, and T. Unold, *Photoluminescence-based characterization of halide perovskites for photovoltaics,* Advanced Energy Materials **10**, 1904134 (2020).

[404] S. Chen, J. Dong, J. Wu, S. Hou, J. Xing, H. Liu, and H. Hao, *Cesium bromide interface modification to improve the performance of perovskite solar cells prepared in ambient air,* Solar Energy Materials and Solar Cells **201**, 110110 (2019).

[405] T. J. Savenije, C. S. Ponseca Jr, L. Kunneman, M. Abdellah, K. Zheng, Y. Tian, Q. Zhu, S. E. Canton, I. G. Scheblykin, T. Pullerits, *et al.*, *Thermally activated exciton dissociation and recombination control the carrier dynamics in organometal halide perovskite,* The Journal of Physical Chemistry Letters **5**, 2189 (2014).

[406] Z. Kang, H. Si, M. Shi, C. Xu, W. Fan, S. Ma, A. Kausar, Q. Liao, Z. Zhang, and Y. Zhang, *Kelvin probe force microscopy for perovskite solar cells,* Sci. China Mater **62**, 776 (2019).

[407] J. Chen, Y. Zhou, Y. Fu, J. Pan, O. F. Mohammed, and O. M. Bakr, *Oriented halide perovskite nanostructures and thin films for optoelectronics,* Chemical Reviews **121**, 12112 (2021).

[408] S.-R. Bae, D. Heo, and S. Kim, *Recent progress of perovskite devices fabricated using thermal evaporation method: Perspective and outlook,* Materials Today Advances **14**, 100232 (2022).

[409] M. Kroll, S. D. Oez, Z. Zhang, R. Ji, T. Schramm, T. Antrack, Y. Vaynzof, S. Olthof, and K. Leo, *Insights into the evaporation behaviour of fai: material degradation and consequences for perovskite solar cells,* Sustainable Energy & Fuels **6**, 3230 (2022).

[410] M. Kam, Y. Zhu, D. Zhang, L. Gu, J. Chen, and Z. Fan, *Efficient mixed-cation mixed-halide perovskite solar cells by all-vacuum sequential deposition using metal oxide electron transport layer,* Solar RRL **3**, 1900050 (2019).

[411] J.-H. Lee, B. S. Kim, J. Park, J.-W. Lee, and K. Kim, *Opportunities and challenges for perovskite solar cells based on vacuum thermal evaporation,* Advanced Materials Technologies **8**, 2200928 (2023).

[412] Y. Zhang, L. Luo, J. Hua, C. Wang, F. Huang, J. Zhong, Y. Peng, Z. Ku, and Y.-b. Cheng, *Moisture assisted cspbbr3 film growth for high-efficiency, all-inorganic solar cells prepared by a multiple sequential vacuum deposition method,* Materials Science in Semiconductor Processing **98**, 39 (2019).

[413] M. M. Tavakoli, A. Simchi, X. Mo, and Z. Fan, *High-quality organohalide lead perovskite films fabricated by layer-by-layer alternating vacuum deposition for high efficiency photovoltaics,* Materials Chemistry Frontiers **1**, 1520 (2017).

[414] Y. Zhao, F. Ma, F. Gao, Z. Yin, X. Zhang, and J. You, *Research progress in large-area perovskite solar cells,* Photonics Research **8**, A1 (2020).

[415] H. Li, M. Liu, M. Li, H. Park, N. Mathews, Y. Qi, X. Zhang, H. J. Bolink, K. Leo, M. Graetzel, *et al.*, *Applications of vacuum vapor deposition for perovskite solar cells: A progress review,* IEnergy **1**, 434 (2022).

[416] X. Qi, G. Liu, D. Wang, N. Zhu, Y. Zhang, Z. Zhang, C. Wu, X. Li, W. Luo, Y. Li, *et al.*, *Stable power output (pce 19%) of planar perovskite solar cells with lead chloride modification at the interface of tin oxide/perovskite,* Organic Electronics **74**, 52 (2019).

[417] S. Chen, X. Yu, X. Cai, M. Peng, K. Yan, B. Dong, H. Hu, B. Chen, X. Gao, and D. Zou, *Lead chloride-assisted film formation for high-efficiency heterojunction perovskite solar cells,* RSC advances **6**, 648 (2016).

[418] K. B. Lohmann, S. G. Motti, R. D. Oliver, A. J. Ramadan, H. C. Sansom, Q. Yuan, K. A. Elmestekawy, J. B. Patel, J. M. Ball, L. M. Herz, *et al.*, *Solvent-free method for defect reduction and improved performance of pin vapor-deposited perovskite solar cells,* ACS Energy Letters **7**, 1903 (2022).

[419] L. Xie, P. Song, L. Shen, J. Lu, K. Liu, K. Lin, W. Feng, C. Tian, and Z. Wei, *Revealing the compositional effect on the intrinsic long-term stability of perovskite solar cells,* Journal of materials chemistry A **8**, 7653 (2020).

[420] R. Larciprete, A. Agresti, S. Pescetelli, H. Pazniak, A. Liedl, P. Lacovig, D. Lizzit, E. Tosi, S. Lizzit, and A. Di Carlo, *Mixed cation halide perovskite under environmental and physical stress,* Materials **14**, 3954 (2021).

[421] Y. Li, Y. Lu, X. Huo, D. Wei, J. Meng, J. Dong, B. Qiao, S. Zhao, Z. Xu, and D. Song, *Bandgap tuning strategy by cations and halide ions of lead halide perovskites learned from machine learning,* RSC advances **11**, 15688 (2021).

[422] B.-S. Kim, M.-H. Choi, M.-S. Choi, and J.-J. Kim, *Composition-controlled organometal halide perovskite via mai pressure in a vacuum co-deposition process,* Journal of Materials Chemistry A **4**, 5663 (2016).

[423] J. Yan, L. S. Stickel, L. van den Hengel, H. Wang, P. R. Anusuyadevi, A. Kooijman, X. Liu, B. Ibrahim, A. Mol, P. Taheri, *et al.*, *Vacuum deposited perovskites with a controllable crystal orientation,* The Journal of Physical Chemistry Letters **14**, 8787 (2023).

[424] J.-X. Zhong, W.-Q. Wu, J.-F. Liao, W. Feng, Y. Jiang, L. Wang, and D.-B. Kuang, *The rise of textured perovskite morphology: Revolutionizing the pathway toward high-performance optoelectronic devices,* Advanced Energy Materials **10**, 1902256 (2020).

[425] X. Cao, L. Zhi, Y. Li, F. Fang, X. Cui, L. Ci, K. Ding, and J. Wei, *Fabrication of perovskite films with large columnar grains via solvent-mediated ostwald ripening for efficient inverted perovskite solar cells,* ACS Applied Energy Materials **1**, 868 (2018).

[426] H. Eggers, F. Schackmar, T. Abzieher, Q. Sun, U. Lemmer, Y. Vaynzof, B. S. Richards, G. Hernandez-Sosa, and U. W. Paetzold, *Inkjet-printed micrometer-thick perovskite solar cells with large columnar grains,* Advanced Energy Materials **10**, 1903184 (2020).

[427] K. H. Stone, A. Gold-Parker, V. L. Pool, E. L. Unger, A. R. Bowring, M. D. McGehee, M. F. Toney, and C. J. Tassone, *Transformation from crystalline precursor to perovskite in $PbCl_2$-derived $mapbI_3$,* Nature communications **9**, 3458 (2018).

[428] X. Wang, J. Fang, S. Li, G. Xie, D. Lin, H. Li, D. Wang, N. Huang, H. Peng, and L. Qiu, *Lead iodide redistribution enables in situ passivation for blading inverted perovskite solar cells with 24.5% efficiency,* Small , 2404058 (2024).

[429] L. Li, P. Zhou, J. Li, Y. Mo, W. Huang, J. Xiao, W. Li, Z. Ku, J. Zhong, Y. Peng, *et al.*, *Suppressed hysteresis and enhanced performance of triple cation perovskite solar cell with chlorine incorporation,* Journal of Materials Chemistry C **6**, 13157 (2018).

[430] L. Fan, Y. Ding, J. Luo, B. Shi, X. Yao, C. Wei, D. Zhang, G. Wang, Y. Sheng, Y. Chen, *et al.*, *Elucidating the role of chlorine in perovskite solar cells,* Journal of Materials Chemistry A **5**, 7423 (2017).

[431] R. van Heerden, P. Procel, L. Mazzarella, R. Santbergen, and O. Isabella, *Slow shallow energy states as the origin of hysteresis in perovskite solar cells,* Frontiers in Photonics **3**, 889837 (2022).

[432] T. Abzieher, D. T. Moore, M. Roß, S. Albrecht, J. Silvia, H. Tan, Q. Jeangros, C. Ballif, M. T. Hoerantner, B.-S. Kim, *et al.*, *Vapor phase deposition of perovskite photovoltaics: short track to commercialization?* Energy & Environmental Science **17**, 1645 (2024).

[433] M. Piot, J. E. S. Alonso, K. P. Zanoni, N. Rodkey, F. Ventosinos, C. Roldán-Carmona, M. Sessolo, and H. Bolink, *Fast coevaporation of 1 μm thick perovskite solar cells,* ACS Energy Letters **8**, 4711 (2023).

[434] H. A. Dewi, E. Erdenebileg, D. De Luca, S. G. Mhaisalkar, and A. Bruno, *Accelerated mapbi3 co-evaporation: Productivity gains without compromising performance,* ACS Energy Letters **9**, 4319 (2024).

[435] ITRPV, *International technology roadmap for photovoltaic,* (2024).

Acknowledgements

During the four exceptional years I spent at both PVMD and OM group, I have met incredible and amazing people, and I would like to thank them all for their wonderful contributions to my works.

Olindo, I would not have started on this learning path in thermal deposition of perovskite without your help. I still remember the first day, you welcomed me into the PVMD Group, everything is so different and full of mystery to me. Special thanks to you, as you allowed me to develop my research with enough freedom but helped me in time when I get lost in the experiment. I enjoyed every meeting and discussion we had and learned a lot from you about the device level analysis. Besides, your passion for PV and renewable energies will continuously influence me, which I believe is very helpful to my future career. Although my PhD has been completed, I hope we can still find opportunities to collaborate in the future.

Tom, I remember that the first time we met is during lunch time at Applied Science. You asked me many questions on my previous work and future work plan. Some of these questions are so impressive to me because I have never thought about them before. In this four-year PhD journey, I really like the way you ask me questions, because it inspired me a lot to think deeper and start to be curious about the things happening behind a phenomenon. With this change, I have learned to appreciate the complexities of scientific research and to approach each challenge with curiosity and determination.

Luana, I feel so lucky that with you as my daily supervisor in the past four years. I am grateful that you spent so much time on guiding me step by step at the early stage of my PhD, allowing me to enter my research path faster and more smoothly. I appreciate how you always took the time to discuss my work in detail, providing constructive feedback, and encouraging me to refine my ideas. I still remember every moment we discuss questions in your office, at coffee break, and on WhatsApp even out of the working time. Moreover, I truly appreciate your emotional support as not only my daily supervisor but also a friend during some challenge times, and it helped me a lot to overcome the problems during my PhD journey.

Paul, "Shifu", thank you very much for giving me many supports when I need help. Your suggestions can always give me inspirations, and it helps me a lot when I feel puzzled. Besides, I still remember the time we together at London for HOPV conference, I really enjoyed these days. I have many photos in my phone that we took at that time with big smiles and Bubble tea holding in hands!

What I also really appreciate is the support and help from our technicians. **Bahiya**, **Jos**, **Martijn**, **Bernardus**, **Stefaan**, I would like to thank you all for your training and your tremendous help when problem arose in the lab. Without you, I would not have been able to complete my PhD smoothly. Besides, technicians for characterization, **Xiaohui**, **Lars**, **Bart**, **Marcel**, **Duco**, thank you for your training and support on data analysis. Your knowledge and patience make me more familiar with usage of many analysis setups.

My former students **Mels**, **Lennart**, **Timo**, **Lena**, and **Jasmine**, it has been a pleasure working with you and learning from each other. Thank you all for your contribution to my thesis and work during my PhD.

I am also feeling lucky to be one member of both PVMD and OM group, with all wonderful colleagues and such a comfort environment. **Valentina**, thank you for teaching me how to use the evaporator; it was the start of my PhD life. **Jiashang**, **Zimu**, and **Jasmeen**, I enjoyed a lot the time together with you all in office during my first two years. You all know a lot of my research and give me many valuable suggestions when I have problems. I also remember that we had fun together trying many times the hotpot and Chinese food. **Yifeng** and **Liqi**, thank you for sharing your valuable knowledge and experience on silicon solar cells, which is very helpful to me to understand the silicon research field. **Lara**, **Reinder**, and **Hua**, our overlap are so short due to different working hours, but I still learnt a lot from your research. I can feel your passion on the research and hope you enjoy your PhD journey for coming years. **Haoxu** and **Yingwen**, I really enjoyed the time we spent together on either hanging out or discussing experiments. **Haoxu**, thank you for organizing all kinds of activities, which makes my PhD time more colorful and interesting. **Yingwen**, I can remember every moment we spent together, for example, working in lab as buddy, cooking food, and dreaming of preparing the first "perovskite/IBC three terminal tandem device" in PVMD group. I wish you all the best of luck with the rest of your PhD journey.

My **dad** and **mom**, we have seen each other in person less than three weeks during the last four years. I miss you all very much and we will see each other soon when I'm back in China. I deeply grateful for your emotional support and unconditional love over these past four years, which gives me the courage to positively face any situations in life.

My boyfriend **Ershuai**, thank you for accompanying me on my PhD journey over the past four years. And I am grateful that you always unconditionally support any choice I want to go for. I enjoy every day we spent and look forward to experiencing more with you in the future.

Curriculum Vitæ

Jin YAN

Jin Yan was born on October 7, 1994 in Henan, China. In 2013, she started her bachelor in Chemical Engineering and Technology at Hefei University of Technology. Afterwards, in 2017, she went to University of Chinese Academy of Sciences in Beijing and continued to Ningbo Institute of Materials Technology and Engineering in 2018 to pursue a Master degree in Polymer Chemistry and Physics, where her graduation project focused on the fabrication of metal halide perovskite solar cells and investigating the large area perovskite film preparation. In 2020, she obtained her Master's degree under the supervision of Prof. Jiang Sheng and Prof. Jichun Ye.

Later on, she moved to the Netherlands persuing her PhD degree at Delft University of Technology, under the supervision of Pro. Olindo Isabella, Dr. Tom, J, Savenije, and Dr. Luana Mazzarella. She specialized in thermally deposited perovskite film and device preparation. Her research involved an in-depth exploration of the sequential thermal deposited perovskite in perspective of precursor reaction, tuning of crystal orientation, device preparation, and scaling up to 1 cm^2 of device toward fully thermal deposited perovskite solar cells.

List of Publications

Peer-reviewed journal articles

1. **J. Yan**, T. J. Savenije, L. Mazzarella, O. Isabella, *Progress and Challenges on Scaling up of Perovskite Solar Cell Technology*, Sustainable Energy and Fuels, 6, (2022). **(Chapter 2)**

2. **J. Yan**, J. Zhao, H. Wang, M. Kerklaan, L. J Bannenberg, B. Ibrahim, T. J. Savenije, L. Mazzarella, O. Isabella, *Crystallization Process for High-Quality* $Cs_{0.15}FA_{0.85}PbI_{2.85}Br_{0.15}$ *Film Deposited via Simplified Sequential Vacuum Evaporation*, ACS Appl. Energy Mater, 6 (20), (2023). **(Chapter 3)**

3. **J. Yan**, L. S. Stickel, L. van den Hengel, H. Wang, P. Ravi Anusuyadevi, A. Kooijman, X. Liu, B. Ibrahim, A. Mol, P. Taheri, L. Mazzarella, O. Isabella, T. J. Savenije, *Vacuum Deposited Perovskites with a Controllable Crystal Orientation*, J. Phys. Chem. Lett, 14(39), (2023). **(Chapter 4)**

4. **J. Yan**, J. Zhao, H. Wang, M. Kerklaan, L. J Bannenberg, B. Ibrahim, T. J. Savenije, L. Mazzarella, O. Isabella, *Scalable PVKs for PSCs via Simplified Sequential Vacuum Deposition*, Manuscript under preparation. **(Chapter 5)**

5. J. Zhao, L. M. van der Poll, S. L. Looman, **J. Yan**, J. Thieme, B. Ibrahim, and T. J. Savenije, *Long-Lived Charge Extraction in CsMAFA-Based Perovskites in n-i-p and p-i-n Structures*, ACS Energy Lett, 9, (2024).

Contribution to conferences and workshops

1. **J. Yan**, M. Kerklaan, L. Bannenberg, X Liu, B. Boshuizen, J. Zhao, V. Caselli, T. J. Savenije, L. Mazzarella, and O. Isabella, *A simplified deposition approach for sequential thermal evaporation of high-quality perovskite absorbers*, MRS Fall Meeting, online, poster, (2022).

2. **J. Yan**, L. S. Stickel, H. Wang, X. Liu, B. Ibrahim, T. J. Savenije, L. Mazzarella, O. Isabella, *Manipulation of the Preferential Growth in Thermally Evaporated Perovskites*, in 15th International Conference on Hybrid and Organic Photovoltaics, London, poster, (2023).

3. **J. Yan**, L. S. Stickel, L. van den Hengel, H. Wang, J. Zhao, B. Ibrahim, T. J. Savenije, L. Mazzarella, O. Isabella, *Perovskite orientation growth and bandgap optimization via thermal evaporation*, in the 7th international conference on perovskite solar cells and optoelectronics, Oxford, flash talk, (2023).

4. **J. Yan**, L. S. Stickel, L. van den Hengel, H. Wang, P. Anusuyadevi, A. Kooijman, X. Liu, B. Ibrahim, A. Mol, P. Taheri, L. Mazzarella, O. Isabella, T. J. Savenije, *Vacuum Deposited Perovskites with a Controllable Crystal Orientation* , in NWO Physics 2024, Veldhoven, oral presentation, (2024).

5. **J. Yan**, T. Gort, R. Boekhoff, H. Wang, T. J. Savenije, L. Mazzarella1, O. Isabella, *Sequential vacuum deposited perovskite for solar cell and upscaling* , in Next Gen PV Materials, Groningen, oral presentation, (2024).

Selected publications prior to the PhD study

1. **J. Yan**, N. Li, Y. Ai, Z. Wang, W. Yang, M. Zhao, C. Shou, B. Yan, J. Sheng, and J. Ye, *Enhanced perovskite crystallization by the polyvinylpyrrolidone additive for high efficiency solar cells*, Sustainable Energy Fuels, 3, (2019).

2. Z. Yang, **J. Yan**, W. Yang, Y. Zeng, J. Sun, X. Wang, X. Yang, J. Greer, J. Sheng, B. Yan, and J. Ye, *Back-contact structures for optoelectronic devices: Applications and perspectives*, Nano Energy, 78, (2020).

3. N. Li, **J. Yan**, Y. Ai, E. Jiang, L. Lin, C. Shou, B. Yan, J. Sheng, and J. Ye, *A low-temperature TiO_2/SnO_2 electron transport layer for high-performance planar perovskite solar cells*, Sci. China Mater, 63, (2020).

4. M. Zhao, **J. Yan**, G. Yu, W. Yang, J. Wu, Y. Zhang, J. Sheng, J. Sun, C. Shou, B. Yan, Z. Fu, and J. Ye, *Grain Boundary Defects Passivated with tert-Butyl Methacrylate for High-Efficiency Perovskite Solar Cells*, ACS Appl. Energy Mater, 10, (2021).